Synthetic Aperture Radar in Medium and Geosynchronous Earth Orbits: System Concepts and Analysis

Zur Erlangung des akademischen Grades eines

DOKTOR-INGENIEURS

von der KIT-Fakultät für
Elektrotechnik und Informationstechnik
des Karlsruher Instituts für Technologie (KIT)

genehmigte

DISSERTATION

von

M.Sc. Jalal Matar
geb. im Libanon

Tag der mündlichen Prüfung: 16.07.2025

Hauptreferent: Prof. Dr.-Ing. habil. Alberto Moreira
Korreferent: Prof. Dr. Antoni Broquetas Ibars

To my wife and best friend,
whose unwavering support and encouragement
have been my greatest strength—
this journey is as much yours as it is mine.

Acknowledgements

This dissertation is the result of research conducted during my tenure as a scientific researcher at the Microwaves and Radar Institute of the German Aerospace Center (DLR) in Oberpfaffenhofen, Germany. I would like to express my gratitude to Prof. Alberto Moreira, the institute's director and my thesis supervisor, for his invaluable support and guidance, which were instrumental in the successful completion of this work.

Special thanks to Prof. Antoni Broquetas Ibars, the co-examiner, for reviewing the manuscript and participating in the defense of the dissertation. I also thank Prof. John Jennolek, Prof. Peter Rost, and Prof. Michael Heizmann for serving as president and part of the jury, respectively.

I am deeply thankful to Dr. Marc Rodriguez-Cassola, head of the SAR Missions Group, and Prof. Gerhard Krieger, head of the Radar Concepts Department, for their roles as internal supervisors of this Ph.D. thesis. Their expertise, feedback, and mentorship played a central role in shaping the research presented here.

I would like to acknowledge the support and friendship of my current and former colleagues at DLR, including Andi, Maron, Eduardo, Daniel, Vinicius, Felipe, Reuben, Mariantonietta, Maria, Nicola, Michele, Pau, Paola, Marwan, Gianluca, Luca, Fairouz, Sandra, and many others, whose encouragement enriched both the professional and personal aspects of this journey.

A heartfelt thank you goes to my wife and family for their unwavering love, patience, and encouragement throughout this long and demanding process. Their support has been my foundation.

Minor language editing and partial translation assistance were provided by AI-based tools (GPT-4, Grammarly). All content was subsequently reviewed and verified by the author.

Munich, July 2025
Jalal Matar

Zusammenfassung

Die zunehmende Verfügbarkeit von satellitengestützten Erdbeobachtungsdaten hat unser Verständnis physikalischer, chemischer und biologischer Prozesse auf der Erde erheblich verbessert. Dennoch gibt es weiterhin erhebliche Lücken in der kontinuierlichen Datenerfassung, insbesondere im Hinblick auf den fortschreitenden Klimawandel und die zunehmenden anthropogenen Einflüsse.

Zur Bewältigung zahlreicher aktueller Herausforderungen im Bereich der Geowissenschaften werden Erdbeobachtungsdaten mit hoher räumlicher und zeitlicher Auflösung benötigt, damit auch sich schnell entwickelnde Prozesse auf der Erdoberfläche adäquat erfasst werden können. Die aktive Mikrowellenfernerkundung spielt hierbei eine zentrale Rolle, steht jedoch vor der Herausforderung, einen Kompromiss zwischen zeitlicher Wiederholung, räumlicher Auflösung und Abdeckung zu finden. So ermöglichen Scatterometer eine tägliche globale Beobachtung mit grober räumlicher Auflösung (in der Größenordnung von mehreren zehn Kilometern), während weltraumgestützte Radarsysteme mit synthetischer Apertur (engl. SAR - *Synthetic Aperture Radar*) hochauflösende Bilder (im Meterbereich) liefern, allerdings mit längeren Wiederholraten, die in der Regel mehr als zehn Tage betragen. SAR-Konstellationen können die Wiederholperioden auf wenige Tage verringern, erfordern jedoch im Low Earth Orbit (LEO) eine hohe Anzahl von Satelliten für eine großflächige Abdeckung.

Satelliten in Medium Earth Orbits (MEOs) und geosynchronen Earth Orbits (GEOs) bieten eine vielversprechende Alternative, um die bestehenden räumlichen und zeitlichen Abtastlücken entweder global oder zumindest für größere geographische Regionen zu schließen. In diesen Orbithöhen kann ein einziger Satellit die gesamte Erde in einem Rhythmus von wenigen Tagen erfassen oder regionale Gebiete–etwa Länder, Kontinente oder Ozeane–mehrmals täglich abbilden. Diese Fähigkeiten machen höher fliegende SAR-Plattformen zu guten Kandidaten für zukünftige wissenschaftliche Missionen, einschließlich solcher mit interferometrischen Anforderungen.

Diese Dissertation bietet eine umfassende quantitative Analyse von SAR-Missionen in höheren Orbits und beleuchtet zentrale Kompromisse zwischen den verschiedenen Missionsaspekten. Die detaillierten Analysen zeigen neue operative Möglichkeiten und Anwendungsbereiche auf, die durch MEO- und GEO-Konfigurationen ermöglicht werden. Beispiele sind die globale dreidimensionale Deformationsmessung mit einem einzigen MEO-Satelliten in rund 6.000 km Höhe und die mehrfach tägliche Abbildung Europas aus etwa 20.000 km Höhe. Entgegen gängiger Annahmen zeigt die Analyse, dass solche hochfliegenden Satellitenmissionen mit aktuellen Technologien realisiert werden können und kritische Erdbeobachtungsdaten mit (i) kontinentaler bis globaler Abdeckung, (ii) hoher zeitlicher Wiederholrate und (iii) moderater räumlicher Auflösung im Bereich von Dutzenden von Metern liefern können.

In dieser Dissertation werden zwei MEO-SAR-Missionskonzepte vorgeschlagen, die für ein globales und regionales Aufnahmeszenario mit möglichst kurzen Wiederholraten optimiert sind, sowie ein neuartiges Konzept für geosynchrone Orbits, das täglich mehrere interferometrische SAR-Akquisitionen ermöglicht. Darüber hinaus wird ein neues Modell zum Design von Akquisitionsszenarien für GEO-SAR-Missionen vorgestellt. Ein speziell entwickeltes Vergleichsmodell ermöglicht es, die relative Komplexität von SAR-Missionen in hohen Orbits gegenüber äquivalenten monostatischen LEO-SAR-Konstellationen zu bewerten. Dieser Vergleich wird durch beispielhafte Missionskonzepte und Strategien für die optimale Verteilung der LEO-Satelliten unterstützt.

Abstract

The increasing availability of Earth observation (EO) data from space has significantly advanced our understanding of Earth's physical, chemical, and biological systems. However, significant gaps remain as climate change and anthropogenic pressures intensify.

Addressing many of today's pressing Earth science challenges requires EO data with high temporal and spatial sampling to effectively capture rapidly evolving processes. Microwave remote sensing instruments are central to this effort but face trade-offs among temporal revisit, spatial coverage, and spatial resolution. For instance, scatterometers offer daily global observations with coarse spatial resolution (on the order of tens of kilometers), while synthetic aperture radar (SAR) systems provide high-resolution imagery (meter-scale) but with longer revisit times typically exceeding ten days. SAR constellations help improve revisit times to a few days, but require large constellations in low Earth orbits (LEOs) for large-scale coverage.

Medium Earth orbits (MEOs) and geosynchronous orbits (GEOs) offer a compelling alternative to address the spatio-temporal sampling gap for frequent revisit over large geographic regions. SAR missions at these altitudes enable a single spacecraft to deliver global coverage on a multi-daily basis and regional coverage—such as countries, continents, or oceans—on a sub-daily basis. These capabilities make high-altitude SAR platforms good candidates for future scientific missions, including those with interferometric requirements.

This dissertation provides an in-depth quantitative analysis of SAR missions in higher orbits, emphasizing critical trade-offs among mission aspects. These trade-offs reveal new operational opportunities and application domains uniquely enabled by monostatic MEO and GEO configurations. Examples include global 3-D deformation monitoring using a single MEO spacecraft at approximately 6000 km altitude and sub-daily coverage of Europe from around 20 000 km. Contrary to prior assumptions, the analysis demonstrates that current technologies can support such high-altitude missions, delivering critical EO data with (i) continental to global coverage, (ii) frequent temporal revisit, and (iii) moderate spatial resolution on the order of tens of meters.

This dissertation proposes two MEO-SAR mission concepts optimized for multi-daily and sub-daily revisit, along with a novel geosynchronous orbit concept for sub-daily interferometric acquisitions. It also introduces a framework for designing observation scenarios for GEO-SAR missions. Furthermore, it develops a comparative framework for evaluating the relative complexity of high-orbit SAR missions and their equivalent monostatic LEO-SAR constellations, supported by distribution strategies and illustrative mission concepts.

Contents

Acronyms and Symbols

Constants

a_{GEO}	Semi-major axis of a GEO	42 164.1696 km
g_0	Standard gravitational acceleration	9.80665 m/s^2
G	Universal gravitational constant	$6.6743 \cdot 10^{-11}$ m^3/kg/s^2
k_{B}	Boltzmann constant	$1.38064852 \cdot 10^{-23}$ J/K
T_0	Standard temperature	290 K
T_{sidereal}	Earth's sidereal day	86 164.090 530 833 s
J_2	Second zonal harmonic coefficient	$0.108263585 \cdot 10^{-2}$
J_3	Third zonal harmonic coefficient	$-0.253243534 \cdot 10^{-5}$
M_{E}	Earth's mass	$5.9726 \cdot 10^{24}$ kg
R_{E}	Earth's equatorial radius	6 378 137.0 m
R_{P}	Earth's polar radius	6 356 752.314 m
ω_{E}	Earth's angular velocity	$7.292115855 \cdot 10^{-5}$ rad/s
$\dot{\Omega}_{\text{ES}}$	Earth's mean motion around the Sun	$1.991063853 \cdot 10^{-7}$ rad/s
μ_{E}	Earth's standard gravitational parameter	$3.986004418 \cdot 10^{14}$ m^3/s^2
π	Pi, ratio of a circle's circumference to its diameter	3.141592653

Mathematical notations and symbols

$\vec{x}$	vector
j	Imaginary unit
$\arcsin(x)$	Inverse sine function
$\arccos(x)$	Inverse cosine function
$\cos(x)$	Cosine function
$\sin(x)$	Sine function
$\text{sinc}(x)$	Sinus cardinalis function, $\text{sinc}(x) = \sin(\pi \cdot x)/(\pi \cdot x)$
$\exp(x)$	Exponential function, $\exp(x) = \text{e}^x$
$\ln(x)$	natural logarithm function
$\langle x \rangle$	Average or expected value
x^*	Complex conjugate
$\dot{x} = \frac{\text{d}x}{\text{d}t}$	Time derivative

mod	Modulo operator (remainder of integer division)
$\sum$	Sum operator
$\prod$	Product operator
$\lfloor \rfloor$	floor operator

Acronyms

1-D	One-Dimensional
2-D	Two-Dimensional
3-D	Three-Dimensional
AASR	Azimuth Ambiguity-to-Signal Ratio
APS	Atmospheric Phase Screen
BAQ	Block-Adaptive Quantization
DEM	Digital Elevation Model
DLR	Deutsches Zentrum für Luft- und Raumfahrt
D-InSAR	Differential Interferometric Synthetic Aperture Radar
ECEF	Earth-Centered, Earth-fixed
ECI	Earth-Centered Inertial
EM	Electromagnetic
EO	Earth Observation
ESA	European Space Agency
GEO	Geosynchronous Earth Orbit
GNSS	Global Navigation Satellite System
GPS	Global Positioning System
GSO	Geostationary Orbit
IHE	Institute for High Frequency Technology and Electronics
InSAR	Interferometric Synthetic Aperture Radar
ITU	International Telecommunication Union
IWV	Interferometric Water Vapor
KIT	Karlsruher Institute for Technology
LEO	Low Earth Orbit
LiDAR	Light Detection and Ranging
LoS	Line of Sight
MEO	Medium Earth Orbit
MJD	Mean Julian Date
ML	Multilook
MLTAN	Mean Local Time at Ascending Node
NESN	Noise-Equivalent Sigma Nought
RAR	Resolution Aspect Ratio
PRF	Pulse Repetition Frequency
PRI	Pulse Repetition Interval
Radar	Radio Detection and Ranging

RAAN	Right Ascension of the Ascending Node
RASR	Range Ambiguity-to-Signal Ratio
RFI	Radio Frequency Interference
RGT	Repeat-Ground Track
ROI	Region of Interest
Rx	Reception
SAR	Synthetic Aperture Radar
SCNR	Signal-to-Clutter Noise Ratio
SCORE	SCan on REceive
SIR	Shuttle Imaging Radar
SLAR	Side-Looking real-Aperture Radar
SLC	Single-Look Complex
SNR	Signal-to-Noise Ratio
SRTM	Shuttle Radar Topography Mission
SSM	Surface Soil Moisture
SSO	Sun-Synchronous Orbit
SWE	Snow Water Equivalent
TanDEM-X	TerraSAR-X Add-on for Digital Elevation Measurement
TID	Total Ionizing Dose
TOD	True Of Date
TOPS	Terrain Observation by Progressive Scans
TRM	Transmit-Receive Module
Tx	Transmission
2-D	Two-Dimensional
3-D	Three-Dimensional

Latin symbols and variables

A_a	Antenna area	m^2
A_r	Access rate	m^2/s
B_r	Range bandwidth	Hz
B_D	Doppler bandwidth	Hz
B_P	Processed Doppler bandwidth	Hz
C_SAR	SAR System Capacity	sample/s
C_r	Coverage rate	m^2/s
D_r	SAR data rate	bps
F_s	System noise factor	-
G_t	Transmit antenna gain	-
G_r	Receive antenna gain	-
H_a	Antenna height	m
I_sp	Specific impulse	s

L_a	Antenna length	m
L_{SA}	Length of the synthetic aperture	m
M_{prop}	Propellant mass	g
N_B	Number of bursts	-
N_{BAQ}	Number of bits per sample	b/sample
P_{avg}	Average transmit power	W
P_t	Peak transmit power	W
R	Slant range from sensor to target	m
R_F	Slant range from sensor to near edge of swath	m
R_N	Slant range from sensor to far edge of swath	m
T_B	Burst duration	s
T_C	Cycle duration (in burst modes)	s
T_{day}	Nodal period of Greenwich	s
T_{ewl}	Echo window length	s
T_N	Nodal period of an orbit	s
T_{SA}	Illumination time	s
W_a	Swath width extension in azimuth	m
W_g	Swath width extension on ground	m
W_s	Swath width extension in slant range	m
a	Semi-major axis	m
c	Speed of propagation of an EM wave in the medium	m/s
e	Eccentricity	-
f_0	Carrier frequency	Hz
f_p	Pulse repetition frequency (PRF)	Hz
h_s	Satellite's altitude	m
i	Inclination	rad
n_0	Mean motion of a satellite	rad/second
r_{Sun}	Range from Earth to Sun	m
v_e	Effective exhaust velocity	m/s
v_g	Beam ground velocity	m/s
v_s	Satellite's velocity	m/s

Greek symbols and variables

Υ	Vernal equinox	-
δx	Azimuth resolution	m
δr	Slant-range resolution	m
δg	Ground-range resolution	m
δ_{rad}	Radiometric resolution	-
$\delta_{rad,dB}$	Radiometric resolution	dB
ΔV	Change in velocity	m/s

ϵ	Obliquity of the ecliptic	rad
η_{orb}	Orbit duty cycle	-
λ	Wavelength of the signal	m
$\lambda_{\text{ecliptic}}$	Ecliptic solar longitude	rad
λ_{lon}	Geodetic longitude	rad
ν	True anomaly	rad
ω	Argument of perigee	rad
Ω	Longitude of the ascending node	rad
ϕ_{lat}	Geodetic latitude	rad
σ_{φ}	Standard deviation of interferometric phase error	rad
τ_{p}	Pulse length	s
θ_{az}	Antenna beamwidth in azimuth	rad
θ_{el}	Antenna beamwidth in elevation	rad
θ_{i}	Beam incident angle	rad
θ_{l}	Antenna look angle	rad
θ_{p}	Angular spread of the PRF	rad
θ_{SA}	Angular extent of the synthetic aperture	rad
$\Theta(t)$	Right ascension of Greenwich meridian at time t	rad

1 Introduction

1.1 Earth Observation

Earth observation (EO) refers to acquiring, processing, and analyzing data that provide relevant insights into Earth's physical, chemical, and biological systems. It is essential for scientific research and practical applications, supporting fields such as climate and environmental monitoring, geology, cryospheric science, hydrology, forestry and agriculture, oceanography, land use and land cover mapping, disaster response, food security, as well as national defense and security.

EO data are acquired using a variety of sensors, which are broadly classified into passive and active types, each with distinct capabilities and limitations. Passive sensors—such as radiometers and spectrometers—rely on naturally available energy sources, including sunlight or thermal radiation, to make measurements. These sensors are characterized by their low power requirements and are well-suited for monitoring climate, cloud cover, water quality, temperature trends, and vegetation cover. However, they are constrained by environmental factors, such as operating without sunlight or penetrating cloud cover, haze, smoke, or dense vegetation. In contrast, active sensors—such as radar, LiDAR, and sonar—generate their illumination by emitting electromagnetic waves, laser pulses, or acoustic waves and measuring the reflected signals from targets. These sensors operate independently of external illumination sources, ensuring continuous functionality regardless of daylight conditions. Notably, active microwave sensors can penetrate various media, including vegetation, soil, snow, ice, smoke, and clouds, making them especially valuable for all-weather observations.[1] Consequently, active sensors are extensively used in applications such as topographic mapping, disaster assessment, soil moisture monitoring, vegetation and forestry analysis, snow and ice monitoring, and ocean surface studies.

[1] The penetration depth of microwave sensors varies depending on the carrier frequency.

EO sensors are deployed on ground-based, airborne, and spaceborne platforms. The choice of a platform is primarily determined by its temporal sampling and spatial coverage capabilities, alongside operational constraints, including cost and deployment feasibility. Ground-based and airborne platforms offer high temporal sampling and flexibility but are significantly limited in spatial coverage. In contrast, spaceborne platforms provide extensive global coverage, making them indispensable for large-scale monitoring despite their lower temporal sampling. As a result, EO increasingly relies on hybrid approaches, combining spaceborne, airborne, and ground-based measurements [1]. This approach allows for enhanced data fidelity, reduces observation gaps, and supports the validation of techniques for future spaceborne implementation. Large-scale initiatives such as the Copernicus program of the European Union [2] and NASA's Earth Observing System [3] exemplify this hybrid approach, delivering continuous, high-quality global data through a network of satellite, airborne, and ground-based observations.

Most EO applications benefit from high temporal and spatial sampling at a global scale. However, the capabilities of existing sensor-platform configurations involve trade-offs among three key factors: temporal sampling, spatial coverage, and spatial resolution. Spaceborne systems occupy a significant portion of this trade-space, offering diverse capabilities. Their temporal sampling ranges from minutes to years, their coverage extends from local to global scales, and their spatial resolution varies from tens of kilometers to sub-meter levels. Within this landscape, synthetic aperture radar systems have played an increasingly vital role over the past decades, providing valuable data as active microwave sensors capable of wide-area coverage and high spatial resolution.

1.2 Evolution of Spaceborne SAR: A Historical Perspective

Synthetic aperture radar (SAR) is an advanced radar imaging technique first developed by Wiley in 1951 under the term Doppler beam sharpening [4]. Significant advancements refined this technology during the 1950s and 1960s, building upon traditional side-looking radar systems [5–7]. By coherently combining Doppler frequency information from radar echoes, SAR substantially improves along-track spatial resolution compared to conventional real-aperture radars. Its deployment on spaceborne platforms has effectively addressed a critical gap in Earth observation by

enabling high-resolution imaging across extensive geographic regions, albeit with the compromise of reduced temporal revisit frequency.

Over the past five decades, the adoption of spaceborne SAR missions has expanded significantly. Table 1.1 summarizes civilian SAR satellite missions launched up to 2024, based on publicly available data. The first civilian spaceborne SAR mission was NASA's Seasat satellite, launched in 1978. It deployed the first L-band SAR sensor in orbit, laying the foundation for future SAR-based EO missions [8]. Seasat's success prompted NASA to launch a series of shuttle-based SAR missions, collectively known as the Shuttle Imaging Radar (SIR) missions [9–11], concluding with the Shuttle Radar Topography Mission (SRTM) in 2000. SRTM produced the first near-global digital elevation model, covering latitudes between 56°S and 60°N [12].

In Europe, the European Space Agency (ESA) launched its first EO satellite, ERS-1, in 1991, followed by ERS-2 in 1995, initiating two decades of C-band SAR observations [13, 14]. In 2002, ESA launched the Envisat satellite to support the continuity of the ERS missions [15]. Envisat remained operational for ten years.

Meanwhile, Japan's Aerospace Exploration Agency (JAXA) entered the spaceborne SAR domain with the launch of JERS-1 in 1992 [16], followed by the ALOS satellite series beginning in 2007, all equipped with L-band SAR instruments [17–19].

The Canadian Space Agency (CSA) launched RADARSAT-1 in 1995, followed by RADARSAT-2 in 2007 [20, 21]. Their successor, the RADARSAT Constellation Mission (RCM), was launched in 2019 with three C-band satellites in a single orbital plane to enhance revisit frequency [22].

The Italian Space Agency (ASI), which had previously collaborated with NASA and on the SIR-C mission, launched the COSMO-SkyMed (CSK) X-band SAR constellation between 2007 and 2010 [23]. The four-satellite constellation enabled sub-daily revisit capabilities over certain latitudes. Its successor, the COSMO-SkyMed Second Generation (CSG), began deployment with launches in 2019 and 2022 [24, 25], offering enhanced revisit and data continuity.

In 2007, Germany launched TerraSAR-X [26, 27], followed by TanDEM-X in 2010 [28, 29], together forming a spaceborne bistatic SAR satellite formation. This unique configuration enabled single-pass, large-baseline interferometry, which allowed to reach the mission's primary objective in 2016—the generation of the first global digital elevation model (DEM) with sub-2 m vertical accuracy [30, 31]. The mission is a collaboration between DLR and Airbus Defence and Space (ADS).

Table 1.1: Overview of launched civilian spaceborne SAR missions (1978–2024). An asterisk (*) denotes SAR constellations, while (pres) indicates ongoing missions. The information is compiled from publicly available sources and may be subject to revision.

Mission	**Year**	**Altitude** [km]	**Rf-band**	**Institution**
Seasat	1978 – 1978	775	L	NASA
SIR-A, B	1981, 1984	225–352	L	NASA
ERS-1,2	1991 – 2011	785	C	ESA
JERS-1	1992 – 1998	568	L	JAXA
SIR-C/X-SAR	1994 – 1994	225	L, C, X	NASA, DLR, ASI
RADARSAT-1, 2	1995 – pres	798	C	CSA
SRTM	2000 – 2000	233	C, X	NASA
Envisat (ASAR)	2002 – 2012	800	C	ESA
ALOS-1, 2, 4	2006 – pres	692, 628	L	JAXA
CSK*/CSG*	2007 – pres	620	X	ASI
TerraSAR-X	2007 – pres	514	X	DLR, ADS
TanDEM-X	2010 – pres			
RISAT-1	2012 – 2017	536	C	ISRO
HJ-1C	2012 – pres	650	S	CAST, CRESDA
Kompsat-5	2013 – pres	550	X	KARI
Sentinel-1A, B, C	2014 – pres	693	C	ESA
Gaofen-3	2016 – pres	755	C	CNSA
PAZ	2018 – pres	514	X	Hisdesat
NovaSAR-S	2018 – pres	580	S	SSTL, UKSA
SAOCOM-1A, 1B	2018 – pres	620	L	CONAE
ICEYE-X*	2018 – pres	570	X	ICEYE
Capella*	2018 – pres	500	X	Capella Space
RCM*	2019 – pres	600	C	CSA
QPS-SAR*	2019 – pres	500–605	X	iQPS Inc.
StriX*	2020 – pres	500	X	Synspective
HiSea-1/Chaohu-1	2020/2 – pres	500–512	C	Spacety
UmbraSAR*	2021 – pres	560	X	Umbra
LuTan-1	2022 – pres	607	L	CAS
NeuSAR	2022 – pres	570	X	DSO
SuperView Neo-2*	2022 – pres	500	X	China Siwei
Ludi Tance-4 01A	2023 – pres	35800	L	CASC
TeLEOS-2	2023 – pres	574	X	ST Engineering
HongTu (PIESAT)*	2023 – pres	520	X	PIESAT

The Indian Space Research Organisation (ISRO) launched its first X-band SAR satellite, RISAT-1, in 2012 [32]. That same year, the China Academy of Space Technology (CAST), in collaboration with the China Center for Resources Satellite Data and Application (CRESDA), launched HJ-1C—the first civilian satellite to carry an S-band SAR instrument—within the framework of an environmental monitoring constellation [33]. In 2013, the Korea Aerospace Research Institute (KARI) deployed KOMPSAT-5, equipped with an X-band SAR instrument [34].

ESA's Sentinel-1 mission, part of the Copernicus program, began delivering operational C-band SAR data with the launch of Sentinel-1A in 2014 [35], followed by Sentinel-1B in 2016 to improve revisit frequency. Sentinel-1B ceased functioning in late 2021 due to a power failure and was replaced by Sentinel-1C in 2024. The launch of Sentinel-1D is planned for 2025 to succeed Sentinel-1A, ensuring the continuity of the two-satellite constellation and maintaining consistent temporal coverage.

China has continued to expand its SAR capabilities with the launch of the Gaofen-3 in 2016, a C-band mission developed by the China National Space Administration (CNSA) [36]. This was followed by the deployment of HiSea-1 in 2020 [37, 38] and Chaohu-1 in 2022 [39], two compact C-band satellites developed by the private company Spacety. In the same year, the Chinese Academy of Sciences (CAS) launched LuTan-1 [40], an L-band bistatic SAR mission inspired by the TerraSAR-X/TanDEM-X formation. Most recently, in 2023, the China Aerospace Science and Technology Corporation (CASC) launched Ludi Tance-4 01A, the world's first geosynchronous SAR satellite. Equipped with an L-band instrument, it enables near-instantaneous imaging of China and surrounding regions [41].

In 2018, the Spanish company Hisdesat launched PAZ, a high-resolution X-band SAR satellite nearly identical to TerraSAR-X [42]. That same year, the United Kingdom deployed NOVASAR-S, their first S-band SAR satellite, a collaborative effort between Surrey Satellite Technology Limited (SSTL) and the UK Space Agency (UKSA) [43].

In Latin America, CONAE[2] launched SAOCOM-1A and 1B in 2018 and 2020, respectively [44]. The two L-band SAR satellites are part of the SIASGE[3] system, sharing an orbital plane with the CSK and CSG constellations. This collaboration enhances EO capabilities by enabling dual-band (L- and X-band) observations for emergency response and environmental monitoring [45].

[2] CONAE, an acronym for *Comisión Nacional de Actividades Espaciales*, is the National Space Activities Commission of Argentina.

[3] SIASGE, an acronym for *Sistema Italo-Argentino de Satélites para la Gestión de Emergencias*, is the Italian-Argentine Satellite System for Emergency Management.

Singapore entered the SAR domain in 2022 with the launch of NeuSAR, its first high-performance X-band micro satellite [46]. NeuSAR was developed by DSO National Laboratories in collaboration with national and international partners, and is notable for being the first fully polarimetric SAR on a small satellite platform. In 2023, ST Engineering, in partnership with the Defence Science and Technology Agency in Singapore, launched TeLEOS-2 [47]. The satellite is also equipped with an X-band full polarimetric SAR payload.

The commercial SAR landscape transformed in 2018 with the emergence of small-satellite constellations. Finnish startup ICEYE launched its first two small X-band satellites, each weighing less than 100 kg [48]. As of December 2024, ICEYE has deployed 40 SAR satellites and continues to expand its constellation. Capella Space, a U.S.-based company, followed with the launch of its prototype satellite Denali in 2018, and has since grown its constellation with the deployment of its second- and third-generation SAR satellites [49]. The Institute for Q-shu Pioneers of Space (iQPS), a spin off company of Kyushu University in Japan, entered the SAR market in 2019 with the launch of QPS-SAR-1, and plans to deploy a 36-satellite X-band constellation in four orbits to achieve a ten minute repeat cycle globally [50]. Japanese startup Synspective joined the market in 2020 with the launch of StriX-α, aiming to establish a 30-satellite X-band constellation by the late 2020s [51]. Umbra [52], another U.S.-based company, launched its first X-band SAR satellite in 2021 and plans to build a 32-satellite constellation, most of which will operate in bistatic pairs [53]. China Siwei, a subsidiary of CASC, launched the Superview Neo-2 01 and 02 X-band SAR satellites in 2022, operating in a tandem formation, with two additional satellites deployed in 2024 to expand the constellation [54]. PIESAT Information Technology Co. Ltd, based in China, launched the HongTu-1 (also referred to as PIESAT-1) four-satellite constellation in 2023, consisting of one active X-band SAR satellite and three passive bistatic receivers operating in a cartwheel formation to form a single-pass, multibaseline SAR interferometer [55]. The company expanded the system with four additional PIESAT-2 satellites in 2024 and plans further deployments to grow the constellation.

In April 2025, ESA launched Biomass, the first civilian spaceborne SAR mission operating in P-band [56, 57]. Several missions are scheduled for launch in the near future. Among them is NISAR, a joint NASA–ISRO mission featuring a dual L- and S-band SAR system [58]. Upcoming continuity missions include CSG-3, SAOCOM-2A/2B, KOMPSAT-6. ESA is also preparing ROSE-L, an L-band Copernicus SAR mission scheduled for launch in 2028 [59], and Harmony, a mission comprising two receive-only SAR satellites flying as companions to Sentinel-1D, scheduled for launch

in 2029 [60]. Meanwhile, the commercial sector continues to grow, with numerous small SAR satellites expected to launch annually. Even planned missions that were ultimately discontinued, such as Tandem-L [61], have advanced SAR technology through their contributions to novel imaging concepts and mission architectures.

The evolution of spaceborne SAR reveals two converging trends. The first is the deployment of constellations to overcome the temporal limitations of single-satellite systems. The second is the advancement of instrument electronics, operational concepts, imaging modes, and processing techniques to extend spatial coverage and enhance resolution. These developments reflect the growing global demand for EO data with increased temporal frequency and finer spatial resolution.

1.3 Motivation of the Work

The scientific understanding of Earth systems has advanced rapidly in recent years, primarily driven by the increasing availability of data from EO satellite missions. Despite this progress, substantial observational and knowledge gaps remain, while the impacts of climate change and anthropogenic pressures continue to intensify [1, 62].

Spaceborne SAR missions play a key role in addressing these gaps by providing global coverage with wide swath imaging—typically spanning few hundred kilometers—while maintaining metric to decametric spatial resolutions, enabled by advanced imaging modes. Current SAR constellations in low Earth orbit (LEO) enable short revisit times on the order of a few days. Complementary to SAR, active radar scatterometers (e.g., the C-band ASCAT instruments on MetOp-B/C, and Ku-band sensors on HY-2B/2C/2D) and passive microwave radiometers (e.g., L-band sensors on SMOS and SMAP, and higher-frequency sensors on AMSR2, MetOp-B/C, and JPSS-1), provide frequent temporal coverage, with revisit intervals ranging from 1 to 3 days. However, their spatial resolution (typically 5 to 50 km) limits their suitability for applications requiring finer spatial detail.

A critical gap persists for EO applications that require both frequent temporal sampling—lower than a few days—and moderate spatial resolution at continental to global scales. These requirements are essential for capturing transient, rapidly evolving, or diurnally varying processes across key Earth system domains, including the atmosphere, cryosphere, land surface, oceans, and solid Earth. Table 1.2 presents a selection of EO applications that would benefit from such observational capabilities. The spatial

Table 1.2: Overview of EO applications that can benefit from high-temporal and moderate-spatial resolution data [63–68].

Application	Revisit (goal) [h]	Resolution (goal) [km]	Coverage
Snow status (wet/dry)	1	0.1	Global land
Integrated water vapor	1	0.5	Global
Vegetation water content	6	0.1	Global land
Permafrost	6	0.1	Global land
River discharge estimation	6	0.1	Regional
Ocean/sea salinity (atmosphere)	6	1	Global ocean
Flood monitoring & mapping	12	0.1	Global land
Canopy state (wet/dry)	12	0.1	Global land
Ocean surface currents	12	1	Global ocean
Landslides & Earthquake mapping	24	0.05	Global land
Volcanic activity & deformation	24	0.05	Regional land
Snow cover mapping	24	0.1	Global land
Snow water equivalent	24	0.1	Global land
Surface soil moisture (agriculture)	24	0.1	Global land
Ocean dynamic topography	24	0.1	Global ocean
Sea ice thickness	24	0.5	Global coastal
Glacier flow	24	0.5	Global land
Surface soil moisture (climate)	24	1	Global land
Sea ice cover, type, extent & drift	24	1	Global coastal
Ocean/sea salinity (climate)	24	5	Global ocean
Ocean temperature	24	10	Global ocean
Vessel & fish farming cages tracking	72	1	Global ocean

and temporal requirements for each application are compiled from multiple sources [63–68], and are expected to evolve as user needs and scientific priorities continue to advance.

While existing and upcoming LEO-SAR missions focus on system-level design approaches—typically optimizing for wide-swath, high-resolution imaging—this thesis takes a mission perspective. Specifically, it explores how orbital design and mission architecture can be strategically employed to address spatio-temporal sampling gaps. Consequently, the central objective of this thesis is to investigate the potential of high-orbit SAR systems

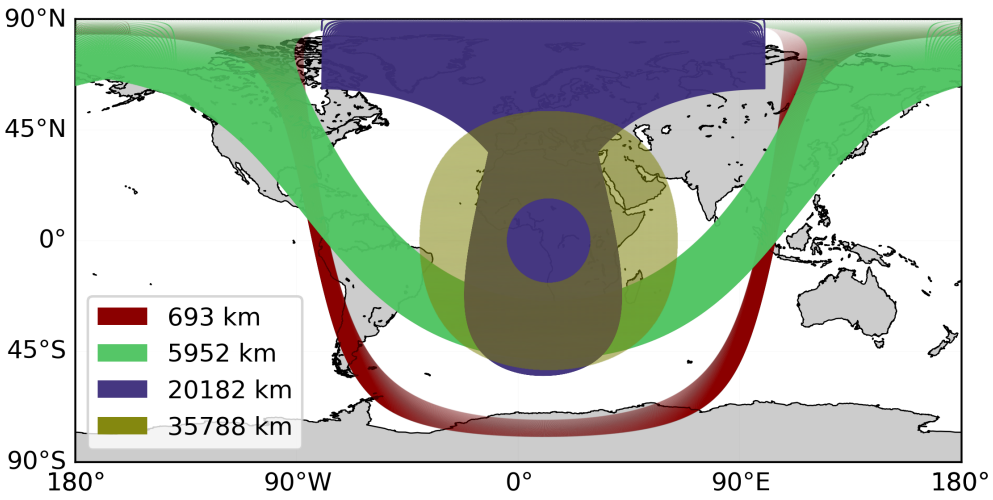

Figure 1.1: Increase in surface access area with orbital altitude, illustrated for four representative orbits after a single orbital revolution. The configurations include a low Earth orbit (LEO) at 693 km, medium Earth orbits (MEO) at 5952 km and 20182 km, and a geosynchronous Earth orbit (GEO) at 35788 km. Access regions are traced assuming a fixed incident-angle range of 20° to 60° over the ellipsoid.

to address the gap in EO data for high-temporal, large-scale dynamic Earth processes. In contrast to LEO systems, high-orbit systems are characterized by increased observational accessibility.[4] Figure 1.1 illustrates this concept, comparing the surface access area of a representative LEO system at 693 km to that of selected high-altitude configurations at 5952 km, 20182 km, and 35788 km, for identical observation geometries. By focusing on orbital geometry and mission design rather than solely on SAR instrument specifications, this research aims to demonstrate how high-orbit SAR platforms can contribute to a more responsive and scalable EO infrastructure. This is supported by the design of exemplary MEO- and GEO-SAR missions and benchmarked against large-scale LEO-SAR constellations with comparable EO data objectives.

Figure 1.2 visualizes the current spatio-temporal observational space of state-of-the-art spaceborne microwave imaging systems, emphasizing the potential of high-orbit SAR systems in MEO and GEO to address the persistent gap in delivering data with high temporal sampling and moderate spatial resolution.

[4] In this context, *accessibility* refers to the portion of the Earth's surface that falls within the viewing geometry of the sensor, constrained by incident angles suitable for acquiring useful measurements.

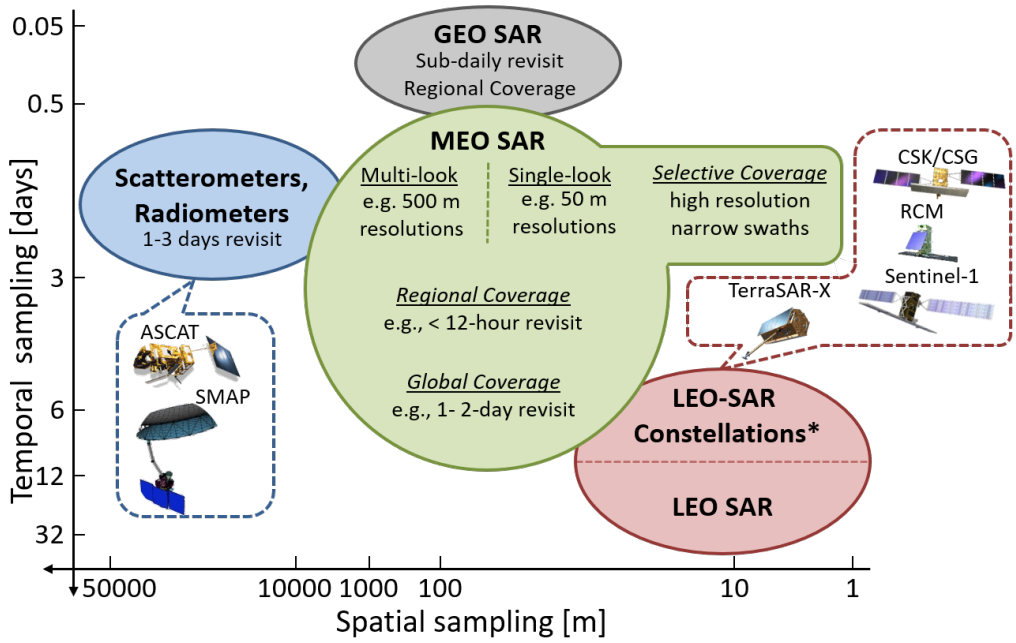

Figure 1.2: Spatio-temporal sampling characteristics of state-of-the-art spaceborne microwave imaging sensors, illustrating the trade-off between spatial resolution and temporal revisit frequency. The investigated MEO- and GEO-SAR systems are highlighted as potential solutions to bridge the existing spatio-temporal observation gap in Earth observation data. The asterisk (*) next to "LEO-SAR Constellations" denotes systems with global coverage capabilities.

Related Work

This thesis builds upon previous research on high-altitude SAR systems. High-orbit SAR has been studied for several decades, primarily in the United States, Europe, and China. However, it was first realized by China in 2023 with the launch of the first inclined GEO-SAR mission, Ludi Tance-4 01A [41].

The earliest discussions on GEO-SAR emerged as early as 1978, when Tomiyasu and Pacelli proposed the use of inclined geosynchronous orbits to provide SAR coverage over North and South America [69, 70]. In the early 2000s, extensive studies were conducted at the Jet Propulsion Laboratory (JPL) [71–75], which analyzed performance trends as a function of orbital altitude. These investigations proposed conceptual designs for MEO and GEO L-band interferometric SAR missions aimed at applications such as continuous seismic monitoring, disaster response, vegetation analysis, and soil moisture observation.

Subsequent research efforts have contributed significantly to the development of novel GEO-SAR mission concepts [76–83] by developing SAR focusing and processing techniques tailored to the unique challenges of

GEO-SAR [84, 85], and addressing key issues such as the estimation and compensation of decorrelation sources associated with long integration times, including atmospheric effects [86–88, 88–94], ground clutter [95], and radio-frequency interference [96, 97]. These efforts were complemented by dedicated measurement campaigns designed to characterize the spatio-temporal behavior of surface backscatter under GEO-SAR-like conditions [98, 99]. Outcomes from these investigations triggered the development of candidate mission proposals for ESA's Earth Explorer (EE) program, namely Hydroterra for EE10 [100–103], and Hydroterra+ for EE12 [104].

In China, numerous studies have addressed challenges specific to high-orbit SAR, such as adapting focusing algorithms for curved satellite trajectories [105–109], analyzing atmospheric decorrelation effects [110], and designing inclined systems tailored to optimize coverage of the Chinese mainland [111, 112].

1.4 Thesis Structure

This thesis is structured as follows. Chapter 2 establishes the foundation for orbit and mission design, focusing on key parameters such as revisit time, coverage, energy constraints, radiation exposure, orbit insertion, and maneuver strategies. Chapter 3 introduces the principles of monostatic SAR, discussing geometric, systematic, and performance aspects with focus on interferometric techniques. Building on these fundamentals, Chapter 4 presents a quantitative analysis of high-altitude SAR missions, examining challenges and opportunities. This chapter explores critical trade-offs in mission design, considering SAR payload, orbit, and platform aspects. The discussion then shifts to medium Earth orbits (MEOs) in Chapter 5, where key advantages of MEO for SAR missions are explored through two exemplary mission concepts: one enabling multi-daily global coverage and the other designed for sub-daily observations over Europe. The focus then moves to geosynchronous orbits (GEOs) in Chapter 6, where a novel orbit concept for sub-daily interferometric SAR acquisitions is introduced. This chapter also outlines a methodology for developing acquisition plans that capitalize on the large instantaneous spatial accessibility of GEO-SAR missions. In Chapter 7, the equivalence between monostatic LEO-SAR constellations and high-orbit monostatic SAR systems is analyzed, offering a generalized framework for assessing mission complexity and informing strategic mission planning. Finally, Chapter 8 concludes the thesis with a discussion of key findings and an outlook on future research directions.

1.5 Main Contributions

In the course of this study, significant contributions have been made to the field of spaceborne SAR and mission analysis, with a particular focus on systems operating in high Earth orbits. The pivotal contributions can be delineated as follows:

1. Quantitative evaluation of high-orbit SAR missions: an in-depth quantitative analysis of SAR missions in higher orbits was carried out, addressing the knowledge gap in system complexity, operating venues, and target products. The study introduces new performance models and emphasizes critical trade-offs involving sensitivity, coverage, launch constraints, and environmental limitations unique to high orbital altitudes.
2. Identification of new applications and novel MEO-SAR mission concepts: this investigation revealed novel opportunities and applications for single SAR systems operating in MEOs. Key findings include the potential for true[5] 3-D global deformation monitoring, sub-daily continental-scale imaging, and hourly interferometric revisit at lower latitudes. These insights substantially expand the operational scope of contemporary Earth observation systems. Two mission architectures specifically optimized for MEO were proposed. The MEO-SAR concepts enable capabilities such as global true 3-D slow deformation monitoring and large-scale sub-daily coverage.
3. Development of a novel orbit concept and novel imaging algorithm for GEO-SAR missions: A novel geosynchronous orbit concept is proposed to enable sub-daily interferometric observations. Furthermore, a novel imaging mode is introduced to optimize mission resource utilization and facilitate the design of effective observation scenarios for GEO-SAR operations.
4. Development of a novel framework for comparing high-orbit SAR with LEO-SAR constellations: a novel framework was established to compare the relative complexity of SAR systems in high Earth orbits with their equivalent monostatic constellations in low Earth orbits. This framework, supported by optimized distribution concepts for constellation design, was applied to the three proposed mission concepts. It enabled a structured evaluation of system performance, architectural complexity, and implementation trade-offs.

[5] In this context, the term *true* refers to the ability to adequately resolve all three displacement components: east-west, north-south, and up-down.

2 Fundamentals of Orbits and Operational Constraints

The choice of a remote sensing satellite's orbit is a critical aspect of mission design, as it directly affects payload performance, such as that of synthetic aperture radar (SAR) systems. Orbital parameters define key mission attributes such as coverage, revisit frequency, and sensitivity, thereby influencing overall system performance and complexity. Additionally, the chosen orbit may impact spacecraft design factors, including component specifications, mission lifespan, and overall cost.

This chapter analyzes Earth's orbits relevant to remote-sensing missions. Section 2.1 begins with an overview of orbital mechanics and the primary perturbation forces acting on satellites. Section 2.2 explores orbit types suitable for SAR missions, particularly repeat-ground track and sun-synchronous orbits, emphasizing their specific advantages. Section 2.3 details the methodology for calculating satellite eclipse durations, a critical parameter in energy budget planning for solar-powered satellites. Section 2.4 examines the space radiation environment near Earth, with a focus on advanced models characterizing the Van Allen radiation belts and their implications for satellites in high-altitude orbits. Finally, Section 2.5 discusses key launch considerations, linking launch vehicle capabilities such as fairing size and performance to the target orbit of a SAR mission.

For additional insights into spacecraft astrodynamics, refer to the textbooks by Vallado [113], Wertz and Larson [114], Montenbruck and Gill [115], Chobotov [116], and Wiesel [117].

Altitude Classification

Earth orbits may be classified according to their altitude into the following categories:

- low Earth orbit (LEO): altitudes between approximately 160 km to 2000 km above Earth's surface;
- medium Earth orbit (MEO): altitudes between approximately 2000 km to 35 786 km above the Earth's surface; and

- geosynchronous Earth orbit (GEO): altitudes of approximately 35 786 km and an orbital period equal to one sidereal day.[1]

A GEO is synchronized with Earth's rotation but is not necessarily equatorial. A special case of GEO is the geostationary orbit (GSO), which is a circular, equatorial GEO at precisely 35 786 km altitude. Satellites in GSO appear stationary relative to Earth's surface, making them of limited interest for SAR, which relies on relative motion to enhance spatial resolution.

2.1 Orbital Mechanics

A satellite orbit is the trajectory a satellite follows in space under the influence of gravitational forces. The study of orbital mechanics, or astrodynamics, dates back to Kepler's empirical laws of planetary motion and Newton's law of universal gravitation [118]. Since the formulation of these foundational models, numerous models have been developed to compute the precise motion of planets and satellites, with a varying degree of accuracy and computational complexity.

2.1.1 Keplerian Orbits

According to Kepler's first law, the orbit of a satellite around a planet—such as Earth—is an ellipse, with the planetary body situated at one focus. Figure 2.1 depicts the principal parameters of an elliptical orbit around a primary body (e.g., Earth). The reference frame for these elements is established by the Earth's equatorial plane and the vernal equinox (Υ).[2] The six Keplerian elements required to fully characterize the satellite's state at a given instant, i.e., position and velocity vectors, as well as its trajectory are:

- Semi-major axis (a): represents half the longest diameter of the elliptical orbit.
- Eccentricity (e): describes the shape of the ellipse, ranging from 0 for circular orbits to values approaching 1 for highly elliptical orbits.
- Inclination (i): the angle between the orbital plane and Earth's equatorial plane.

[1] A *sidereal day* (T_{sidereal}) is the time required for Earth to complete one full rotation relative to distant stars, approximately 86 164.1 s. This is slightly shorter than a solar day, which lasts 86 400 s.

[2] The *vernal equinox* refers to the direction of the Sun as seen from Earth at the beginning of spring in the Northern Hemisphere [115].

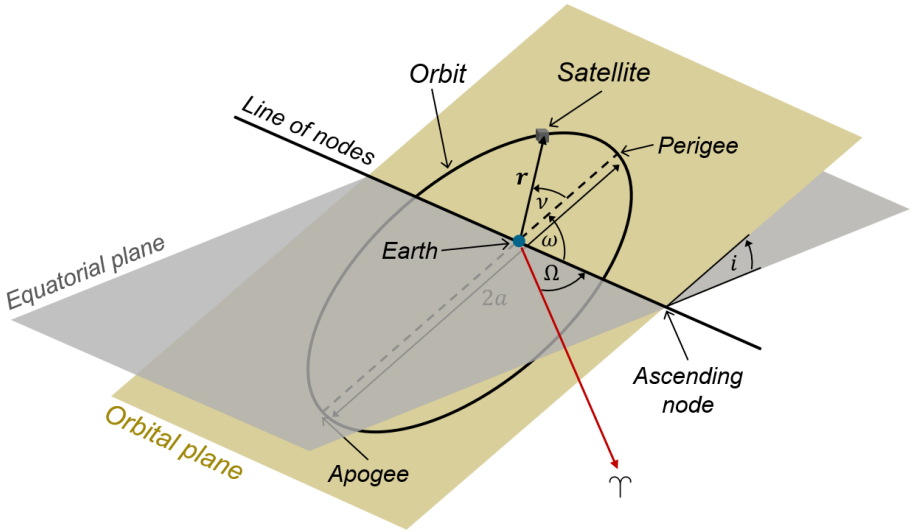

Figure 2.1: Visualization of the primary orbital elements of a satellite orbiting Earth, including major axis ($2a$), inclination (i), longitude of the ascending node (Ω), argument of perigee (ω), and true anomaly (ν). The Earth and the vernal equinox (Υ) establish the reference frame for the elements.

- Longitude of the ascending node (Ω): also known as the right ascension of the ascending node (RAAN), it is the angle from the vernal equinox Υ to the ascending node, where the satellite crosses the equator from south to north.
- Argument of perigee (ω): the angle from the ascending node to the perigee, the point in the orbit closest to Earth.
- True anomaly (ν): the angle from the perigee to the satellite's current position in its orbit, in the direction of motion. Alternatively, the mean anomaly (M) is often used for simplicity. It represents the average angular position of the satellite from the perigee, assuming uniform motion. The mean anomaly can be determined using the equation

$$M = M_0 + n_0 \cdot (t - t_0), \tag{2.1}$$

  where M_0 is the mean anomaly at a reference epoch (t_0), and the mean motion of the satellite (n_0) is defined as

$$n_0 = \sqrt{\frac{\mu_E}{a^3}}, \tag{2.2}$$

  where μ_E is the Earth's standard gravitational constant.

For satellites orbiting Earth, the primary force shaping the satellite's trajectory is the gravitational pull of Earth's mass. This dominant force allows for

an approximation of satellite orbits through the restricted two-body problem model. By applying Newton's second law in conjunction with his law of universal gravitation, the relative motion of a satellite position vector $\vec{r}$ is described as

$$\frac{\mathrm{d}^2\vec{r}}{\mathrm{d}t^2} + \frac{\mu_\mathrm{E}}{r^3} \cdot \vec{r} = 0. \tag{2.3}$$

This is commonly known as the two-body equation of motion and is derived under the following assumptions: (i) the Earth and the satellite are the only two bodies in the system, (ii) the satellite's mass is negligible compared to Earth, (iii) the Earth's mass distribution is spherically symmetric, and (iv) the only force acting on the bodies is their mutual gravitational attraction [113, 114].

2.1.2 Orbit Perturbations

The Keplerian model provides a robust initial prediction of satellite orbits. However, real-world orbits are subject to various perturbative forces that cause deviations from the idealized two-body solution. Despite these perturbations, the central gravitational force remains dominant, and Keplerian motion continues to serve as a useful baseline. For Earth-orbiting satellites, the primary sources of perturbations include:

- Non-uniformity of the central body: Earth's mass distribution is not spherically symmetric,[3] leading to a non-uniform gravitational field that varies with longitude and latitude. The irregular field causes periodic and secular variations in all of the orbital elements, with the most significant being the secular variations in Ω, ω, and ν due to Earth's oblateness.
- Third-body perturbations: the gravitational forces exerted by the Sun and the Moon induce periodic variations in all orbital elements and cause secular variations in Ω and ω. These perturbations are particularly relevant for high-altitude orbits and long-duration missions.
- Atmospheric drag: the resistive force exerted on a spacecraft by the Earth's atmosphere, causing continuous deceleration and eventual orbit decay—especially in LEO if not actively compensated. The magnitude of this effect depends on factors such as orbital altitude, atmospheric density (which changes with altitude and solar activity), and

[3] The Earth is not spherically symmetric and has an uneven mass distribution within the crust and mantle. The Earth resembles an oblate spheroid due to the equatorial bulge and flattened poles resulting from the centrifugal force caused by its rotation.

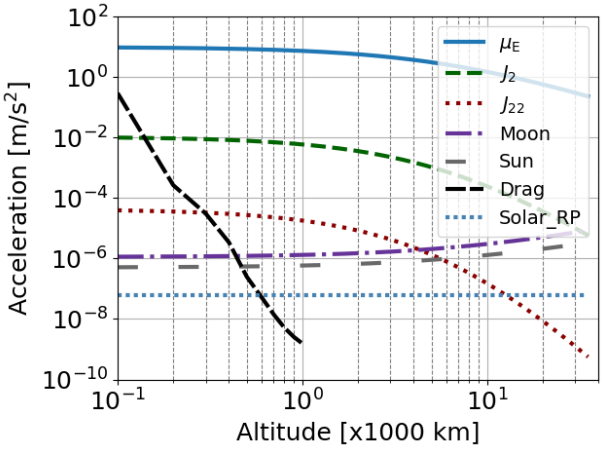

Figure 2.2: Approximate accelerations acting on satellites from various perturbation sources as a function of orbital altitude.

the satellite's physical characteristics, including mass, cross-sectional area, and drag coefficient.

- Solar radiation pressure: the pressure exerted by photons from the Sun generates periodic variations in all orbital elements, particularly for satellites with high area-to-mass ratio and reflectivity.

These perturbations result in secular (long-term), short-period, and long-period variations in orbital parameters. Secular variations, such as those in the longitude of the ascending node and the argument of perigee, are commonly utilized in mission design to achieve specific precession rates—an approach used for sun-synchronous orbit design, discussed in the subsequent section. By carefully optimizing initial orbital parameters, certain secular perturbations can be exploited. Nevertheless, residual perturbations generally necessitate periodic corrective maneuvers to preserve the intended orbit. The frequency and magnitude of such maneuvers depend on mission-specific requirements, including orbital tube constraints, regulatory compliance—such as the International Telecommunication Union (ITU) regulations [119]—and fuel-efficiency considerations.

Figure 2.2 illustrates the variation in the magnitudes of the perturbative accelerations acting on Earth-orbiting satellites at different altitudes caused by major disturbance sources. The accelerations were estimated based on the following assumptions: (i) geopotential perturbations due to the second zonal coefficient (J_2), quantifying the influence of Earth's equatorial bulge on its gravitational field, and the first sectorial coefficient (J_{22}), accounting for longitude-dependent gravitational variations due to Earth's

non-uniform mass distribution, were computed using the results from Milani et al. [120]; (ii) atmospheric drag was modeled using a drag coefficient of 2.3 and an area-to-mass ratio of $0.01\,\mathrm{m}^2/\mathrm{kg}$, with atmospheric density values interpolated from the *U.S. Standard Atmosphere 1976* model [121]; and (iii) solar radiation pressure (RP) was estimated using a radiation pressure coefficient of 1.3, combined with the same area-to-mass ratio of $0.01\,\mathrm{m}^2/\mathrm{kg}$, consistent with values typical for small SAR satellites such as ICEYE.

The results indicate that J_2 remains the dominant perturbation source up to GEO altitudes. In low-altitude LEO, significant perturbations arise from atmospheric drag, J_2, and J_{22}. At MEO, gravitational perturbations from the Sun and Moon become increasingly significant, eventually surpassing the influence of J_2 at GEO altitudes.

A set of Keplerian elements can be computed at any given instant from a satellite's position and velocity vectors. These elements fully characterize the orbital state and provide an approximate prediction of the satellite's trajectory. Because they change continuously due to perturbations, they are referred to as osculating elements.

2.2 Remote Sensing Orbits

Several key considerations drive the design of orbits for Earth observation remote-sensing missions:

- Accessibility: the orbit must provide access to regions of interest, either locally or globally, depending on the mission's objectives.
- Frequent revisit: some missions prioritize high revisit frequency over broad spatial accessibility. For example, sub-daily revisit on a continental scale can be achieved by a single spacecraft operating in high-altitude orbits (typically above 20 000 km) or highly elliptical orbits. For missions targeting low-latitude regions, equatorial orbits may provide efficient and rapid revisit capabilities.
- Interferometric revisit: many remote-sensing applications rely on interferometry, such as interferometric SAR (InSAR), which coherently combines multiple SAR acquisitions with near-identical SAR imaging geometry to detect changes with millimeter-level accuracy. This requires precisely repeating ground tracks to maintain geometrical coherence between acquisitions.

- Efficient payload design: orbital altitude and stability are critical to payload design. For global coverage missions, significant altitude variations may negatively impact power management, antenna efficiency, and fuel budget. This can be mitigated by using near-circular orbits, which help maintain consistent operational parameters.
- Energy efficiency: active remote sensing instruments, such as SAR, have relatively high power demands, making available energy considerations crucial. The average eclipse duration for solar-powered satellites should be minimized to optimize energy availability. Sun-synchronous orbits are advantageous, ensuring consistent solar illumination throughout the mission and reducing reliance on onboard energy storage systems.

2.2.1 Repeat-Ground Track Orbits

Repeat-ground track (RGT) orbits are specialized orbits designed to repeat their ground track after a fixed number of orbits and days. These orbits are essential for Earth observation missions, particularly those employing interferometric techniques for monitoring slow dynamic processes over time, such as surface deformation, glacier movement, and land subsidence. RGT orbits facilitate systematic and repeatable measurement scheduling, which is essential for consistent long-term data collection.

In this work, the irreducible ratio[4] $N_{\text{day}}/N_{\text{rev}}$ is used to represent different repeat orbits, where N_{day} represents the integer number of orbital days (T_{day}) it takes the orbit to repeat itself, and N_{rev} denotes the integer number of orbital revolutions completed in N_{day} days. A solution for such orbits can be obtained by adjusting the semi-major axis a to satisfy the condition

$$N_{\text{rev}} \cdot T_{\text{N}} = N_{\text{day}} \cdot T_{\text{day}}, \tag{2.4}$$

where T_{N} is the nodal period of the orbit. This period varies with a and accounts for secular changes in the mean anomaly (M) and the argument of perigee (ω), and is given by [113]

$$T_{\text{N}} = \frac{2 \cdot \pi}{n_0 + \dot{M} + \dot{\omega}}, \tag{2.5}$$

where $\dot{x}$ denotes the time derivative of x.

[4] An *irreducible ratio* is a fraction expressed in its simplest form, where the greatest common divisor of the numerator and denominator is 1.

All terms in the denominator of (2.5) are expressed in rad/s. The orbital day, commonly referred to as the nodal period of Greenwich, is defined as the period of Earth's rotation with respect to the orbit's ascending node. This period can be calculated in seconds as [113]

$$T_{\text{day}} = \frac{2 \cdot \pi}{\omega_{\text{E}} - \dot{\Omega}}, \tag{2.6}$$

where ω_{E} is the Earth's angular velocity and $\dot{\Omega}$ is the orbit's nodal regression, both measured in rad/s.

The rates of change $\dot{\Omega}$, $\dot{\omega}$, and $\dot{M}$ are primarily dominated by secular variations resulting from the gravitational effects of Earth's equatorial bulge, represented by the second zonal coefficient J_2. The first-order approximation for these rates, due to the second secular zonal harmonic, can be expressed in rad/s as [113]

$$\dot{\Omega} = \frac{-3 \cdot n_0 \cdot J_2 \cdot R_{\text{E}}^2}{2 \cdot a^2 \cdot (1 - e^2)^2} \cdot \cos i, \tag{2.7}$$

$$\dot{\omega} = \frac{3 \cdot n_0 \cdot J_2 \cdot R_{\text{E}}^2}{4 \cdot a^2 \cdot (1 - e^2)^2} \cdot \left(4 - 5 \cdot \sin^2 i\right), \tag{2.8}$$

and

$$\dot{M} = \frac{3 \cdot n_0 \cdot J_2 \cdot R_{\text{E}}^2}{4 \cdot a^2 \cdot (1 - e^2)^{3/2}} \cdot \left(2 - 3 \cdot \sin^2 i\right). \tag{2.9}$$

R_{E} denotes the Earth's equatorial radius.

2.2.2 Sun-Synchronous Orbits

Sun-synchronous orbits (SSO) are another class of specialized orbits, mainly characterized by their capability to provide near-continuous solar illumination and maintain consistent viewing conditions for Earth observation [122].

These orbits are designed by aligning the nodal regression of the orbit ($\dot{\Omega}$) with the average secular motion of the Earth around the Sun ($\dot{\Omega}_{\text{ES}}$), which is 360° per year (365.2421897 days). For a given semi-major axis and eccentricity, the inclination required to achieve sun-synchronicity can be derived using the first-order approximation from (2.7), as

$$i = \arccos\left(\frac{-2 \cdot a^2 \cdot (1 - e^2)^2}{3 \cdot n_0 \cdot J_2 \cdot R_{\text{E}}^2} \cdot \dot{\Omega}_{\text{ES}}\right). \tag{2.10}$$

A design following this equation ensures the orbit's nodal regression rate matches $\dot{\Omega}_{\mathrm{ES}}$, thereby maintaining the sun-synchronous condition. If the objective is to maximize the solar illumination, the initial position of the line of nodes, defined by Ω (see Figure 2.1), should be selected to keep the solar panels perpendicular to the Sun. This is typically achieved by setting Ω to achieve a mean local time at ascending node (MLTAN) of 06:00 or 18:00, which aligns the orbital plane's normal vector with the Sun's position vector ($\vec{s}$).

2.2.3 Frozen Orbits

Frozen orbits are specifically designed to minimize global variations in altitude by reducing the long-term (secular) changes in both the eccentricity (e) and the argument of perigee (ω). The secular rates of e and ω, considering the J_2 and J_3 zonal harmonics, can be analytically represented by the formulations provided by Vallado in [113] as

$$\dot{e} = \frac{-3 \cdot n_0 \cdot J_3 \cdot R_{\mathrm{E}}^3}{2 \cdot a^3 \cdot (1-e^2)^2} \cdot \sin i \cdot \left(1 - \frac{5}{4} \cdot \sin^2 i\right) \cdot \cos\omega, \tag{2.11}$$

$$\begin{aligned}\dot{\omega} = {} & \frac{3 \cdot n_0 \cdot J_2 \cdot R_{\mathrm{E}}^2}{4 \cdot a^2 \cdot (1-e^2)^2} \cdot \left(4 - 5 \cdot \sin^2 i\right) + \\ & \frac{3 \cdot n_0 \cdot J_3 \cdot R_{\mathrm{E}}^3}{8 \cdot e \cdot a^3 \cdot (1-e^2)^3} \cdot \sin\omega \cdot \left[\left(4 - 5 \cdot \sin^2 i\right) \cdot \left(\frac{\sin^2 i - e^2 \cdot \cos^2 i}{e \cdot \sin i}\right) + \right. \\ & \left. 2 \cdot e^2 \cdot \sin i \cdot \left(15 \cdot \sin^2 i - 13\right)\right].\end{aligned} \tag{2.12}$$

To achieve a frozen eccentricity, i or ω must satisfy specific conditions. According to (2.11), the secular rate of eccentricity vanishes at a critical i_ω, or when $i = 0°$, or $\omega_0 = 90°$ or $270°$. When additional constraints—such as the requirement to maintain a SSO—restrict the inclination, it is still possible to freeze the eccentricity by setting $\omega_0 = 90°$ or $270°$. Similarly, according to (2.12), a frozen argument of perigee can be achieved either by setting $i = i_\omega$, or by selecting specific values i, e, and ω that result in $\dot{\omega} = 0$.

McClain's analysis in [123] shows that for $\omega_0 = 90°$ and a desired inclination, frozen orbits can be achieved by setting the initial eccentricity

$$e_0 \approx -0.5 \cdot \frac{J_3}{J_2} \cdot \frac{R_{\mathrm{E}}}{a} \cdot \sin i. \tag{2.13}$$

In practical scenarios, where higher-order harmonics are significant, these initial estimates of ω_0 and e_0 serve as starting points. They can be iteratively refined using numerical propagation methods to achieve a more accurate frozen orbit configuration.

2.2.4 Frozen RGT SSO

A widely used and highly desirable orbit configuration for Earth-observing satellites combines features of three specialized orbit classes: repeat ground track (RGT), sun-synchronous orbit (SSO), and frozen orbits. This hybrid class leverages the benefits of each type to create a stable, efficient platform for continuous Earth observation. The initial Keplerian elements for such orbits are determined through the following steps:

1. Determine the initial semi-major axis (a_0) to achieve the desired ground track repeatability with the ratio $N_{\text{day}}/N_{\text{rev}}$.
2. Calculate the initial inclination (i_0) to ensure sun-synchronicity.
3. Set the initial eccentricity (e_0) and argument of perigee (ω_0) to create a frozen orbit, minimizing long-term variations in altitude (ω_0 is typically set to 90° or 270°).
4. Choose the initial longitude of the ascending node (Ω_0) to achieve the desired MLTAN, such as 06:00 or 18:00, aligning the orbit with specific observation needs.

2.3 Eclipses

Earth-orbiting satellites routinely encounter partial or total eclipses while passing the night side of Earth. The duration of these eclipses is a critical factor in the design of solar-powered satellite missions with active payloads, such as SAR, as it directly influences the availability of solar energy. This, in turn, affects the maximum operational time of the payload and determines the required size of the solar panels and onboard battery. Eclipses by the moon are less frequent and result in marginal changes to the energy budget.

Figure 2.3 shows a simplified representation of Earth's shadow geometry, highlighting the umbral and penumbral regions, which correspond to areas of total and partial shadow during an eclipse, respectively. It is important to note that the geometry in this figure is exaggerated for clarity; in practice, the time a satellite spends in the umbra region is significantly longer

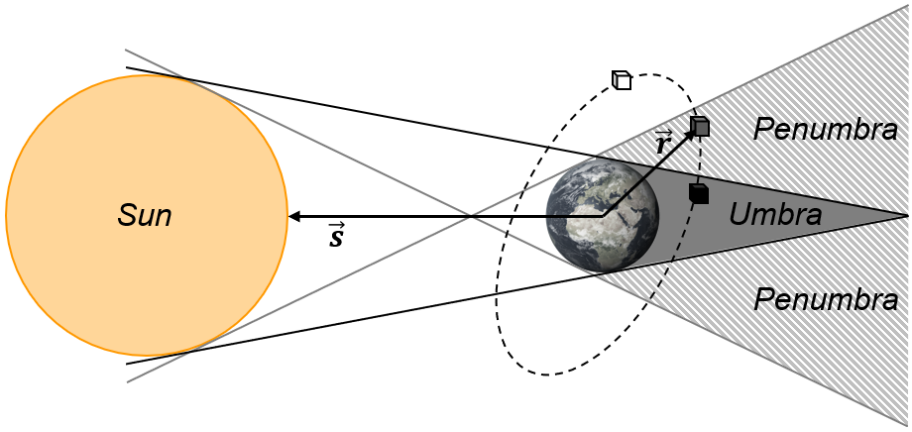

Figure 2.3: Simplified geometry of Earth's shadow, illustrating the distinct umbral and penumbral regions, representing areas of total and partial shadow during an eclipse, respectively.

than in the penumbral region. The eclipse duration is governed by the spacecraft's orbit and Earth's position relative to the Sun. The satellite's orbit can be described using its position vector ($\vec{r}$), which is propagated from the initial Keplerian elements while accounting for various perturbations. The Sun's position relative to Earth, represented by the Sun position vector ($\vec{s}$), is another key factor influencing eclipse duration [115, 124]. The Sun's position vector is time-dependent and can be obtained from precise ephemerides or approximated by [113]

$$\vec{s} \approx \begin{bmatrix} r_{\text{Sun}} \cdot \cos\lambda_{\text{ecliptic}} \\ r_{\text{Sun}} \cdot \sin\lambda_{\text{ecliptic}} \cdot \cos\epsilon \\ r_{\text{Sun}} \cdot \sin\lambda_{\text{ecliptic}} \cdot \sin\epsilon \end{bmatrix}, \tag{2.14}$$

where $\lambda_{\text{ecliptic}}$ is the ecliptic longitude, defined as the angular position of the Sun measured along the ecliptic plane[5] from the vernal equinox; ϵ is the obliquity of the ecliptic, defined as the angle between Earth's equatorial plane and the ecliptic plane; and r_{Sun} is the Sun-Earth distance [113]. Figure 2.4 illustrates the short eclipse duration (less than 8%) experienced by low-altitude dawn-dusk frozen SSO with an MLTAN of 18:00. This short duration allows LEO systems in SSO to use smaller solar panels and batteries, while providing flexibility to conduct acquisitions nearly independent of the satellite's position in orbit.

[5] The *ecliptic plane* is the plane of Earth's orbit around the Sun and serves as a reference for celestial coordinates.

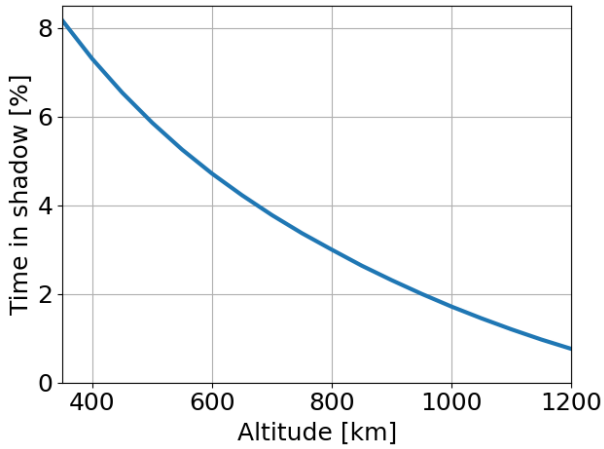

Figure 2.4: Mean eclipse duration (time spent in Earth's shadow) as a function of altitude for frozen sun-synchronous low Earth orbits. The data reflect the average over one year (2040), assuming an initial MLTAN of 18:00.

2.4 Space Radiation Environment

Space radiation—particularly ionizing radiation—poses significant risks to radar payload electronics and spacecraft subsystems. At altitudes up to 40 000 km, the main sources of this radiation are charged particles, primarily electrons and protons, trapped by Earth's magnetic field within the inner and outer Van Allen belts. Figure 2.5 provides a graphical representation of these belts, along with the two NASA Van Allen probes in their highly elliptical orbits. These probes, operated from 2012 to 2019, focused on investigating the structure, dynamics, and variability of the radiation belts and particle acceleration mechanisms within them.

The design and planning of a space mission traversing or operating within the radiation belts must account for radiation effects for the planned duration of the mission. Those include the total radiation dose, displacement damage, electrostatic discharge, and single event upsets. These effects can be mitigated by properly selecting radiation-hardened electronics [126] and shield thickness for protecting sensitive components [114] and reducing the absorbed radiation dose for the mission duration. The total dose rate can be estimated for a given shield geometry and thickness using particle flux data generated by radiation models [127, 128]. As of 2024, the most up-to-date models—AE9/AP9/SPM V1.58—process flux maps derived from 45 satellite-based data sets, including measurements from the Van Allen probes [129]. These models characterize the flux of energetic electrons, energetic protons, and plasma, respectively. They provide flux data for electrons with energies ranging from 0.04 to 10 MeV and protons with energies

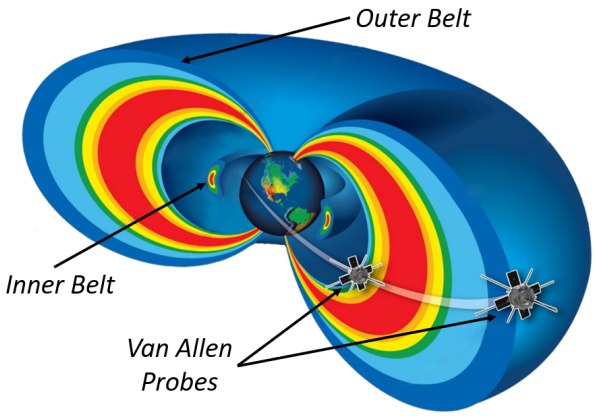

Figure 2.5: A representation of Earth's inner and outer Van Allen radiation belts, with the Van Allen Probes shown traversing these regions to study their dynamics and composition. The radiation intensity of trapped particles peaks at approximately 3500 km in the inner belt and 16 000 km in the outer belt. (Image credit: NASA [125]).

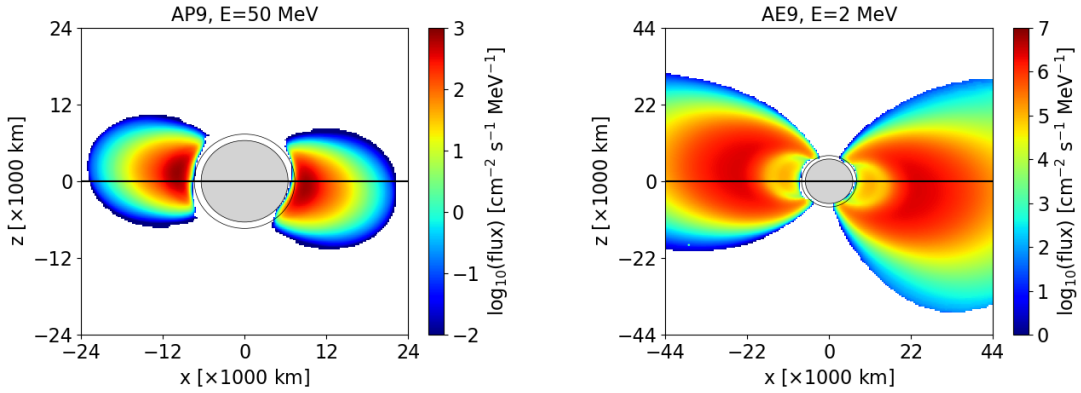

(a) (b)

Figure 2.6: Estimated omnidirectional differential particle fluxes for (a) 50 MeV protons and (b) 2 MeV electrons, based on the AP9 and AE9 models [129]. The flux maps are plotted on a meridional cut in Earth-centered inertial (ECI) coordinates, representing model conditions for January 1, 2024.

from 0.1 to 2000 MeV. Figure 2.6 presents an example of the modeled omnidirectional differential flux[6] for 50 MeV protons and 2 MeV electrons, based on the AP9 and AE9 models.

These maps indicate that radiation in the inner Van Allen belt is primarily dominated by high-energy protons, with intensity peaking at approximately 3500 km. In contrast, the outer belt is dominated by high-energy

[6] In the context of space radiation, *omnidirectional differential flux* refers to the number of charged particles passing through a square centimeter per second, from all directions, at a specific energy.

Table 2.1: List of some active launch sites, organized by their latitude from south to north.

Launch Site	Country	Latitude
Guiana Space Centre	French Guiana (Kourou)	5.24 °N
Satish Dhawan Space Centre	India (Sriharikota)	13.73 °N
SpaceX Starbase	USA (Texas)	26 °N
Xichang Satellite Launch Center	China (Sichuan)	28.25 °N
Cape Canaveral	USA (Florida)	28.56 °N
Kennedy Space Center	USA (Florida)	28.57 °N
Tanegashima Space Center	Japan (Kagoshima)	30.2 °N
Vandenberg Space Force Base	USA (California)	34.63 °N
Rocket Lab Launch Complex	New Zealand (Mahia)	39.26 °N
Jiuquan Satellite Launch Center	China (Gansu border)	40.96 °N
Baikonur Cosmodrome	Kazakhstan (Baikonur)	45.97 °N
Plesetsk Cosmodrome	Russia (Arkhangelsk Oblast)	62.93 °N

electrons, with intensity peaking at approximately 16 000 km. Example calculations of the required shielding thickness for different orbital environments are presented in Chapter 4.

2.5 Orbit Insertion and Maneuvers

2.5.1 Mass and Volume Capabilities of Launch Vehicles

The payload capacity of a launch vehicle is a critical factor in determining mission feasibility and launch costs. This capacity is influenced by several key factors, including the altitude and inclination of the target orbit and the geographical latitude of the launch site. For direct launches to orbits with inclinations below the latitude of the launch pad, a plane change is required, involving non-coplanar maneuvers. These maneuvers increase fuel consumption, reducing the launch vehicle's effective payload capacity. Table 2.1 lists some active orbital launch sites organized by latitude. The location of these sites significantly impacts the energy needed to reach specific orbits. As of 2024, around 35 launch sites are operational globally, highlighting the international nature of space access.

The volume capacity of a launch vehicle is equally important and is determined by the dimensions of its payload fairing. This becomes particularly relevant when deploying large or complex satellites, such as single SAR

satellites or constellations. Launch vehicles such as Vega-C [130], Ariane 5 and 6 [131, 132], Falcon 9 and Heavy [133], and Soyuz 2 [134, 135] provide a variety of payload faring sizes and launch adapters which can be well-suited for these types of missions. In a typical launch configuration, the available volume within the payload fairing must accommodate the spacecraft, launch adapter, and supporting structures—such as clamps and securing mechanisms—especially in ride-share missions. To fully utilize the mass and volume capacity of the fairing, payload design often incorporates foldable components, such as antennas and solar panels.

2.5.2 Orbital Maneuvers

Orbital maneuvers are fundamental to satellite deployment, orbit transfers, and ongoing maintenance operations. They enable precise adjustments to orbital parameters and are broadly categorized into two types: coplanar transfers and non-coplanar transfers.

Coplanar orbit transfers allow for adjustments to the semi-major axis (a), eccentricity (e), and argument of perigee (ω) while keeping the orbital plane unchanged. The Hohmann transfer is a commonly used method for coplanar transfers. It involves two tangential burns: the first at the perigee of the initial orbit and the second at the apogee of the transfer orbit. The Hohmann transfer is highly efficient in minimizing the total velocity change, but requires a minimum transfer time equal to half the orbital period of the transfer orbit [113]. For circular orbits, the required velocity change to adjust the semi-major axis from an initial value a_i to a final value a_f is [136]

$$\Delta V_{a,\mathrm{circ}} = \sqrt{\frac{\mu_\mathrm{E}}{a_\mathrm{i}}} \cdot \left(\sqrt{\frac{2 \cdot a_\mathrm{f}}{a_\mathrm{i} + a_\mathrm{f}}} - 1 \right) + \sqrt{\frac{\mu_\mathrm{E}}{a_\mathrm{f}}} \cdot \left(1 - \sqrt{\frac{2 \cdot a_\mathrm{i}}{a_\mathrm{i} + a_\mathrm{f}}} \right). \tag{2.15}$$

Non-coplanar orbit transfers enable adjustments to the inclination (i) and the longitude of the ascending node (Ω). A pure inclination change of Δi, assuming a circular orbit and an impulsive (instantaneous) maneuver at a nodal crossing, requires a velocity increment

$$\Delta V_{i,\mathrm{circ}} \approx 2 \cdot \sqrt{\frac{\mu_\mathrm{E}}{a}} \cdot \sin\left(\frac{\Delta i}{2} \right). \tag{2.16}$$

Similarly, a change in the longitude of the ascending node by $\Delta\Omega$ requires

$$\Delta V_{\Omega,\text{circ}} \approx 2 \cdot \sqrt{\frac{\mu_\text{E}}{a}} \cdot \sin\left(\frac{\arccos\left(\cos^2 i + \sin^2 i \cdot \cos\Delta\Omega\right)}{2}\right). \tag{2.17}$$

When both i and Ω need to be changed, a simultaneous adjustment can be performed by applying a velocity increment

$$\Delta V_{i\&\Omega,\text{circ}} \approx 2 \cdot \sqrt{\frac{\mu_\text{E}}{a}} \cdot \sin\left(\frac{\sqrt{\Delta\Omega^2 \cdot \sin^2 i + \Delta i^2}}{2}\right) \tag{2.18}$$

at a point of crossing between the initial and final orbit [113]. In real scenarios, combined maneuvers—such as simultaneous adjustments to the semi-major axis and inclination—are often preferred, as careful optimization can result in a slight reduction in total ΔV and transfer time.

The total ΔV budget is the sum of all the increments applied for different maneuvers. These can include orbit raising, plane adjustments, and orbit maintenance. The mass of propellant (M_prop) required for generating the total ΔV can be calculated using Tsiolkovsky's rocket equation

$$\Delta V = v_\text{e} \cdot \ln\left(\frac{M_\text{i}}{M_\text{i} - M_\text{prop}}\right) = g_0 \cdot I_\text{sp} \cdot \ln\left(\frac{M_\text{i}}{M_\text{i} - M_\text{prop}}\right), \tag{2.19}$$

where M_i is the initial mass of the spacecraft, and v_e is the effective exhaust velocity—typically expressed as the product of the specific impulse (I_sp) and the standard gravitational acceleration (g_0).

2.5.3 Propulsion Systems

Two primary propulsion system types are commonly employed for Earth-orbiting spacecraft: chemical propulsion and electric propulsion. Chemical propulsion systems are known for their high thrust, enabling rapid acceleration and enhanced maneuverability. However, their efficiency is limited by a relatively low exhaust velocity—typically not exceeding 4.5 km/s for most systems—which results in lower fuel efficiency compared to alternative propulsion methods. In contrast, electric propulsion systems—such as ion and Hall effect thrusters—use electric energy to offer significantly higher fuel efficiency and achieve much greater exhaust velocities. These systems allow fine control over thrust levels, providing precise maneuverability. However, they are generally more complex, require an on-board

electrical power source, and produce lower thrust, resulting in slower acceleration compared to chemical propulsion systems [137].

3 Synthetic Aperture Radar Remote Sensing

Synthetic Aperture Radar (SAR) is an advanced microwave remote sensing system that uses electromagnetic (EM) waves to capture high-resolution two-dimensional (2-D) images of planetary surfaces. SAR synthesizes an extremely long virtual antenna aperture by coherently integrating radar echoes along the flight path. This process allows SAR to achieve high-resolution imaging without the need for a physically large antenna. SAR systems provide detailed insights into the physical characteristics of observed targets based on their unique interactions with the transmitted EM waves. This capability makes SAR a versatile tool that is widely utilized for applications in diverse fields such as environmental monitoring, agriculture, forestry, disaster management, urban planning, oceanography, cartography, reconnaissance, and surveillance.

This chapter presents a comprehensive overview of SAR principles. Section 3.1 introduces the acquisition geometry and operation principle of monostatic SAR systems. Section 3.2 outlines classical SAR operation modes pertinent to this thesis. Section 3.3 delves into SAR interferometry, with an emphasis on techniques and tools used for estimating 3-D surface deformation. Section 3.4 presents key performance metrics for evaluating both high-altitude platforms and low-altitude constellations, forming the analytical basis for the following chapters. Section 3.5 examines common antenna architectures employed in spaceborne SAR systems.

3.1 SAR Geometry and Working Principle

In its basic form, a monostatic SAR system operates as a side-looking real-aperture radar (SLAR) that exploits the Doppler history of targets to enhance the along-track resolution, by making it equivalent to that of a longer synthetic aperture [138–140]. Figure 3.1 illustrates a simplified geometry of a SAR system in operation. The following aspects characterize the system:

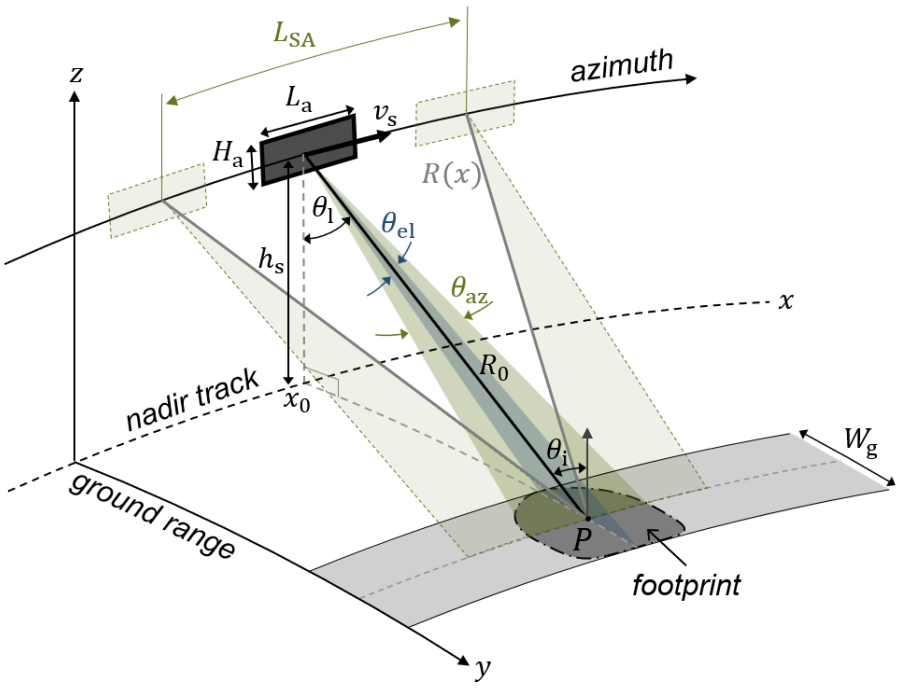

Figure 3.1: Example SAR acquisition geometry.

- **Antenna and Platform:** a SAR antenna (shown here with a rectangular aperture) of length L_a along azimuth and a height H_a along elevation. The antenna is mounted on a spaceborne or an airborne platform traveling at an altitude h_s above its ground track on the planet's surface.
- **Looking Geometry:** the system uses a side-looking geometry, in this example, right-looking relative to the azimuth track. The angle between the nadir vector and the antenna pointing direction is referred to as the look angle (θ_l).
- **Footprint:** the footprint represents the projection of the antenna's beam onto the ground, where θ_{az} and θ_{el} are the azimuth and elevation beamwidths, respectively. In the absence of beamforming, they correspond to the antenna's natural half-power beamwidth (HPBW). These beamwidths depend on the transmitted wavelength (λ) and the antenna dimensions, where $\theta_{az} \approx \lambda / L_a$ and $\theta_{el} \approx \lambda / H_a$.
- **Swath:** the swath width (W_g) denotes the lateral extent of the ground area imaged by the SAR sensor during a single pass, measured in the ground-range direction.
- **Line-of-Sight (LoS) Vector:** this vector originates from the platform's position at acquisition time and extends to a point on the surface, typically within the footprint. The magnitude of this vector is defined as the slant range (R).

- **Cross-track:** the cross-track direction refers to the direction perpendicular to the sensor's flight path (also known as the along-track or azimuth direction). It is commonly referred to as the range direction and corresponds to the direction to which the SAR antenna faces.

  he cross-track direction refers to the direction perpendicular to the sensor's flight path (also known as the along-track or azimuth direction). It is commonly referred to as the range direction and corresponds to the direction in which the SAR antenna is pointed.

- **Incident angle:** the incident angle (θ_i) is the angle between the LoS vector and the normal (perpendicular) to the surface at that intersection point.

- **Illumination time:** the illumination time (T_SA) is the duration for which a target remains in the main beam of the antenna and relates to the synthetic aperture length (L_SA) by $T_\mathrm{SA} = L_\mathrm{SA}/v_\mathrm{s}$, where v_s is the relative speed of the platform with respect to the surface.[1]

During operation, the SAR system typically transmits a sequence of frequency-modulated pulsed waveforms, each with a duration τ_p, at a specified pulse repetition frequency (PRF, f_p), while moving in the along-track (azimuth) direction with velocity v_s. Following each transmitted pulse, the radar switches to receive mode to collect echoes scattered back from the ground and store the received signals onboard. In pulsed systems, the time allocated for receiving these echoes, referred to as the echo window length (T_ewl), is constrained by

$$T_\mathrm{ewl} < \frac{1}{f_\mathrm{p}} - \tau_\mathrm{p}. \tag{3.1}$$

The stored signals form a 2-D raw data matrix, commonly indexed by fast time (range direction) and slow time (azimuth direction).

The formation of a SAR-focused image from 2-D raw data involves several processing steps, including range compression and azimuth compression, where the raw data are matched filtered with reference functions. Various focusing algorithms have been developed, each differing in computational complexity, accuracy, and suitability for different applications. Notable algorithms for spaceborne data include the range-Doppler algorithm, the chirp scaling algorithm, and the Omega-K algorithm [141–143].

[1] The relative speed (v_s) corresponds to the magnitude of the instantaneous velocity vector $\vec{v}_\mathrm{s}$ expressed in the Earth-Centered Earth-Fixed (ECEF) frame, accounting for both the satellite's orbital motion and the Earth's rotation.

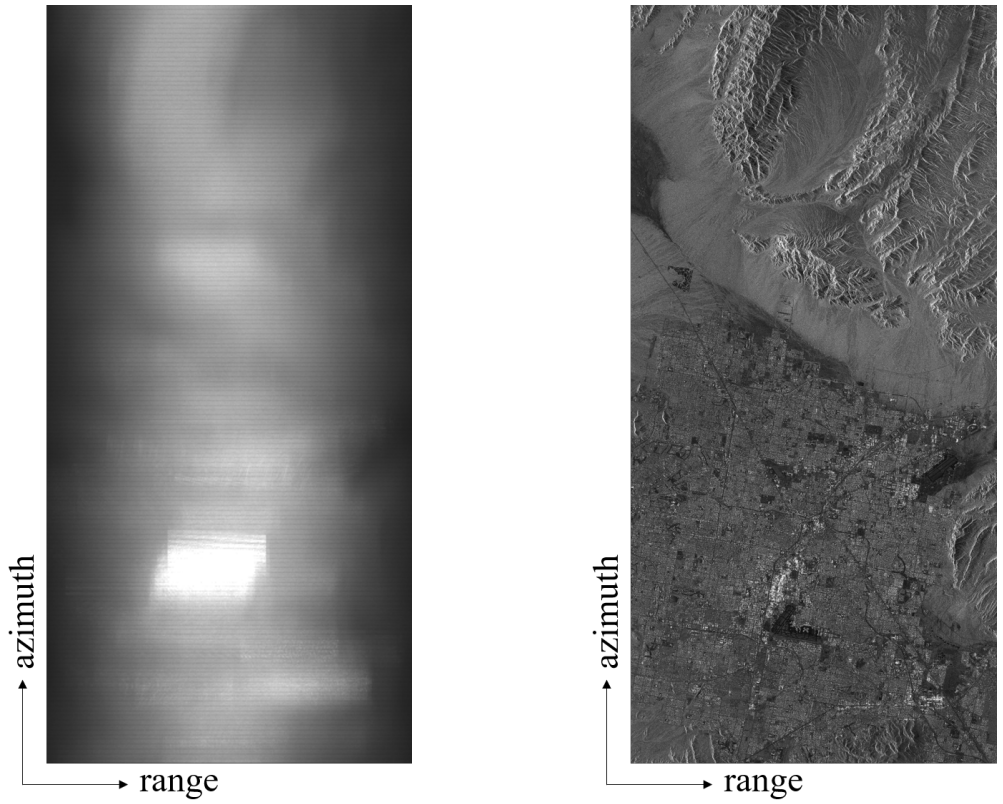

(a) (b)

Figure 3.2: (a) SAR raw data and (b) the corresponding focused image of Las Vegas, acquired by TanDEM-X. The scene was captured in stripmap mode with a swath width of 30 km, using right-looking geometry during an ascending pass on August 13, 2020.

Figure 3.2 presents an example 2-D raw-data matrix and the corresponding SAR-focused image amplitude of Las Vegas, acquired by TanDEM-X on August 13, 2020.

3.1.1 Azimuth Resolution

The azimuth resolution of a focused SAR image is the minimum distance at which two points on the ground can be resolved in the azimuth direction. For conventional SLAR, this resolution is constrained by the azimuth extension of the antenna footprint on the ground

$$\delta x \approx R \cdot \theta_{\mathrm{az}} \approx R \cdot \frac{\lambda}{L_{\mathrm{a}}}, \tag{3.2}$$

which degrades linearly with increasing range. As proposed by Wiley [4], SAR enhances azimuth resolution by utilizing the unique Doppler signature

$$f_{\mathrm{D}} = \frac{2 \cdot v_{\mathrm{s}}}{\lambda} \cdot \sin\theta_x \approx \frac{2 \cdot v_{\mathrm{s}}}{\lambda \cdot R} \cdot x \tag{3.3}$$

of targets at different azimuth angles (θ_x), where x is the azimuth coordinate of the target. Consequently, the azimuth resolution can be expressed as

$$\delta x \approx \left(\frac{\lambda \cdot R}{2 \cdot v_{\mathrm{s}}}\right) \cdot \delta f_{\mathrm{D}}, \tag{3.4}$$

where δf_{D} is the Doppler resolution and is expressed as the inverse of the illumination time, given by

$$\delta f_{\mathrm{D}} = \frac{1}{T_{\mathrm{SA}}} \approx \frac{v_{\mathrm{s}}}{L_{\mathrm{SA}}} \approx \frac{v_{\mathrm{s}}}{R \cdot \theta_{\mathrm{SA}}}, \tag{3.5}$$

with θ_{SA} representing the azimuth angular extent of the synthetic aperture. For low platform altitudes, θ_{SA} is often approximated by θ_{az}; however, this approximation can introduce significant discrepancies at higher orbits due to the natural curvature of the platform's trajectory in Earth orbits (more details in Chapter 4). By combining (3.4) and (3.5), a more general form for azimuth resolution is obtained:

$$\delta x \approx \frac{\lambda \cdot R}{2 \cdot v_{\mathrm{s}} \cdot T_{\mathrm{SA}}} \approx \frac{\lambda}{2 \cdot \theta_{\mathrm{SA}}}. \tag{3.6}$$

In practice, the azimuth resolution is derived from the focused SAR image after processing and is defined as the half-power beam width of the focused impulse response. An alternative definition is

$$\delta x = v_{\mathrm{g}} \cdot \delta t_{\mathrm{IR}} = k_{\mathrm{w}} \cdot \frac{v_{\mathrm{g}}}{B_{\mathrm{p}}}, \tag{3.7}$$

where δt_{IR} is the time resolution of the impulse response and is inversely proportional to the processed Doppler bandwidth (B_{p}), v_{g} is the ground velocity of the beam, and k_{w} is a factor representing any losses in resolution due to windowing (e.g., Hamming). The ratio $\theta_{\mathrm{az}}/\theta_{\mathrm{SA}}$ caused by the curvature of orbits is equivalent to the ratio $v_{\mathrm{g}}/v_{\mathrm{s}}$. Equations (3.6) and (3.7) yield the same value if the selected processed bandwidth B_{p} corresponds to the full extent of the synthetic aperture, i.e., the full Doppler bandwidth (B_{D}). The Doppler bandwidth is in turn related to the Doppler rate ($\dot{f}_{\mathrm{D}}$) by

$$B_{\mathrm{D}} = |\dot{f}_{\mathrm{D}}| \cdot T_{\mathrm{SA}}, \tag{3.8}$$

where the Doppler rate can be approximated by

$$\dot{f}_{\mathrm{D}} = \frac{\mathrm{d}f(t)}{\mathrm{d}t} \approx -\frac{2 \cdot v_{\mathrm{eff}}^2}{\lambda \cdot R}. \tag{3.9}$$

The PRF (f_{p}) is not directly tied to the azimuth resolution; however, it must satisfy

$$f_{\mathrm{p}} \geq B_{\mathrm{D}} \tag{3.10}$$

to prevent aliasing of the Doppler spectrum.

3.1.2 Range Resolution

Analogously, slant-range resolution of a SAR system is the minimum distance at which two points can be resolved in slant range and is defined by

$$\delta r = \frac{c}{2 \cdot B_{\mathrm{r}}}, \tag{3.11}$$

where c is the speed of the EM wave in the medium, and B_{r} is the bandwidth of the transmitted signal.

Similarly, the ground-range resolution describes the ability to discriminate targets on the ground. It can be approximated on a flat-Earth surface (ignoring local slopes) as follows

$$\delta g = \frac{c}{2 \cdot B_{\mathrm{r}} \cdot \sin\theta_{\mathrm{i}}}. \tag{3.12}$$

3.1.3 Data Rate

The data rate of a SAR system quantifies the volume of data generated per second during radar imaging. This metric is crucial for mission design, as it directly influences the requirements for onboard storage, processing capacity, downlink capacity, and the feasible orbit duty cycle. It is given by

$$D_{\mathrm{r}} = \sum_{i=1}^{N_{\mathrm{B}}} \left(2 \cdot N_{\mathrm{bps}}\right) \cdot N_{\mathrm{pol}} \cdot f_{\mathrm{r},i} \cdot T_{\mathrm{ewl},i} \cdot f_{\mathrm{p},i}, \tag{3.13}$$

where N_{bps} is the number of bits per sample, the factor 2 is for the separate quantization of the in-phase and quadrature components, N_{pol} is the total number of polarizations, f_{r} is the range sampling frequency, f_{p} is the pulse

repetition frequency (PRF), and T_{ewl} is the echo window length, defined as

$$T_{\text{ewl},i} = \frac{2 \cdot |R_{\text{F},i} - R_{\text{N},i}|}{c} + \tau_{\text{p}}, \tag{3.14}$$

where R_{F} and R_{N} are the far and near slant ranges to the edges of the imaged swath, respectively. The summation over the number of subswaths (N_{B}) accounts for burst operation modes, such as ScanSAR.

3.2 SAR Imaging Modes

SAR systems can be designed to operate in various modes, each with distinct implications on hardware complexity and system efficiency. These modes allow the manipulation of the nominal resolution-swath relation.[2] This section provides an overview of the basic operation modes, as illustrated in Figure 3.3, relevant to the high-altitude systems and low-altitude constellations characterized in this thesis.

3.2.1 Stripmap

Stripmap is the fundamental SAR imaging mode, widely used for its simplicity and high-efficiency in continuous area imaging. It is based on a side-looking imaging geometry with a fixed antenna look angle and no beam steering [138]. Deviations from this mode are either caused by the need to achieve better resolution, cover wider swaths, or avoid degraded resolutions over blind ranges.[3]

3.2.2 Spotlight

Spotlight mode, nominally refers to staring spotlight, is a high-resolution imaging mode in which the radar beam is continuously steered to keep the antenna's main beam always pointing at a fixed point on ground. The beam steering can extend the observation time beyond the natural illumination time of the antenna in a stripmap mode, thereby increasing the Doppler

[2] The resolution-swath relation refers to the fundamental trade-off in SAR systems, where enhancing spatial resolution typically results in a reduced swath width, and vice versa [140].

[3] *Blind ranges* are areas where the reception of the full echo of the transmitted pulse is interrupted by different transmit events or nadir returns.

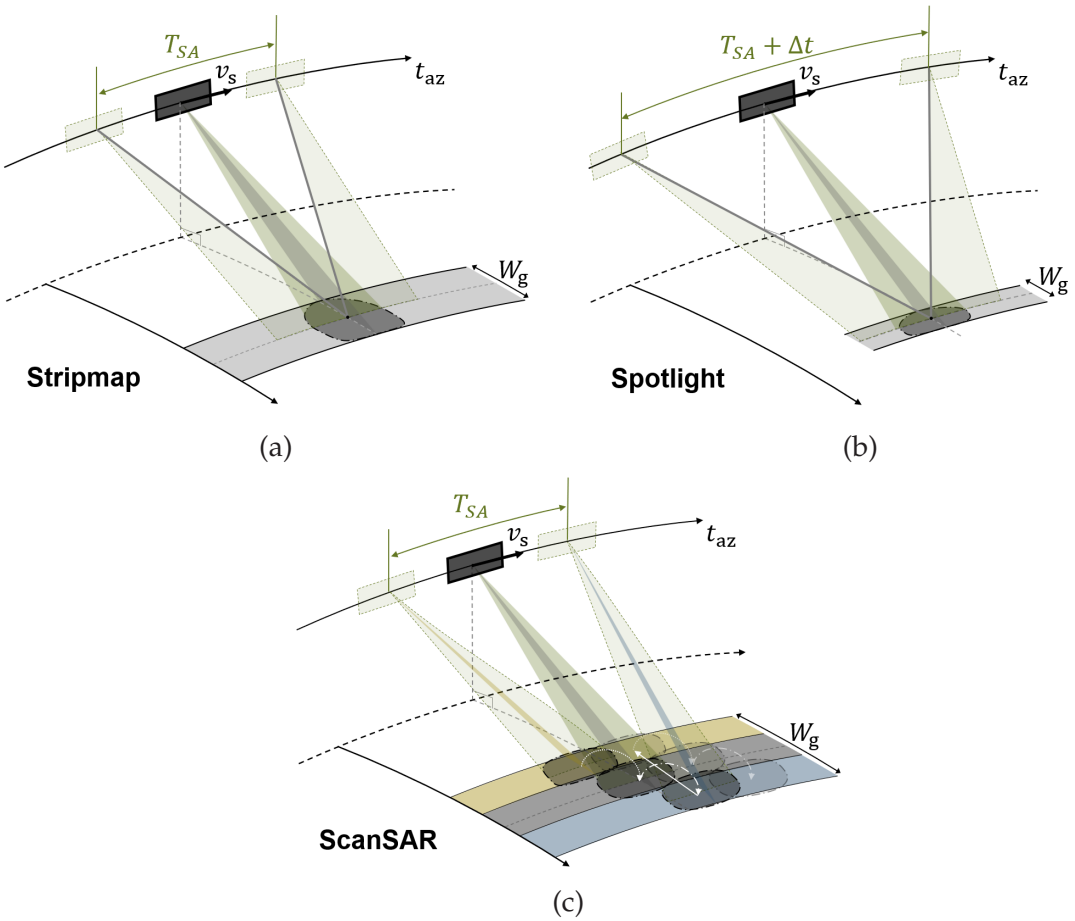

Figure 3.3: Illustration of classical SAR imaging modes used in spaceborne SAR systems: (a) Stripmap mode, with a fixed illumination time (T_{SA}); (b) Spotlight mode, utilizing extended illumination through mechanical or electronic beam steering in azimuth; and (c) ScanSAR mode, featuring cyclic illumination of subswaths within T_{SA} using electronic beam steering in elevation.

bandwidth and enhancing azimuth resolution [138]. The trade-off, however, is a reduced swath extension in range and azimuth directions and the need for more sophisticated signal processing algorithms [144].

Sliding spotlight mode provides a compromise between staring spotlight and stripmap modes. In this configuration, the antenna beam is steered dynamically but not fixed to a single point on ground nor strictly following a zero-Doppler pointing. The controlled steering enables a flexible trade-off between azimuth resolution and scene extent [145, 146].

3.2.3 ScanSAR

ScanSAR is a burst operation mode designed to achieve a broader swath coverage at the expense of degraded azimuth resolution [147]. This is

achieved by periodically switching the radar beam between multiple sub-swaths in elevation, resulting in a combined swath width (W_g) that exceeds the natural elevation beamwidth of the used antenna. The timing of the ScanSAR cycle (T_C), defined as the sum of the individual burst durations ($T_B[i]$), must be carefully designed to ensure sufficient overlap in azimuth illumination between consecutive cycles, such that

$$T_{SA} \geq \max(T_B) + T_C = \max(T_B) + \sum_{i=1}^{N_B} T_B[i] \approx (N_B + 1) \cdot \max(T_B), \quad (3.15)$$

where N_B is the total number of sub-swaths or bursts per ScanSAR cycle. Under this approximation, the available Doppler bandwidth per burst is limited to

$$B_B \leq \frac{B_D}{N_B + 1}, \quad (3.16)$$

which translates to an approximate degradation of azimuth resolution by a factor of $(N_B + 1)$ compared to the nominal resolution of the full Doppler bandwidth (B_D) supported by the antenna length in azimuth. In addition to the reduced resolution, this mode introduces scalloping,[4] a consequence of different targets being observed by different portions of the azimuth antenna pattern (i.e., with squint).

Terrain Observation with Progressive Scan (TOPS) is a burst operation mode similar to ScanSAR, designed to broaden the swath width at the expense of a degraded azimuth resolution. However, it employs azimuth beam steering to homogenize the radiometric loss at the edges of the bursts and reduce scalloping. While the timeline derivation follows a similar conceptual approach to (3.15), the equations differ, as detailed in [148, 149].

3.3 SAR Interferometry

SAR interferometry (InSAR) is a differential imaging capable of measuring surface topography, ground deformation, and other temporal changes with sub-wavelength accuracy. This is achieved by analyzing the phase difference between complex SAR images, which can be acquired from different positions (spatial baselines) and/or at different times (temporal baselines). The outcome of this technique is the creation of interferograms, which are 2-D images obtained by multiplying a reference SAR image with the complex conjugate of a second SAR image. Each pixel in the interferogram

[4] *Scalloping* refers to the system-induced periodic modulation of the amplitude in a focused SAR image.

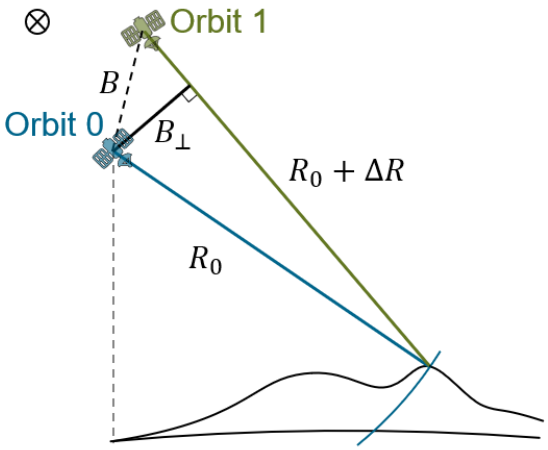

Figure 3.4: Schematic of cross-track SAR interferometry. Two SAR acquisitions are made from sensor positions separated by a baseline B. The effective perpendicular baseline ($B_\perp$) lies in a plane perpendicular to the sensor flight paths (indicated as into the page).

contains phase information that represents range changes, with accuracy on the order of a fraction of the radar wavelength. For a comprehensive review of InSAR techniques and their applications, refer to [140, 150–156].

The following subsections provide a brief introduction to cross-track interferometry and differential interferometry.

3.3.1 Cross-track Interferometry

Cross-track interferometry is a variant of InSAR that employs a large spatial baseline in a plane perpendicular to the flight direction to enhance sensitivity to elevation changes, making it particularly effective for topographic mapping. Figure 3.4 illustrates a typical cross-track interferometric configuration, where two SAR acquisitions are obtained from different positions, separated by a baseline B. The range difference (ΔR) to a common target results in an interferometric phase

$$\Delta\varphi = \varphi_1 - \varphi_0 = -\frac{4 \cdot \pi \cdot \Delta R}{\lambda}. \tag{3.17}$$

Using geometric triangulation, $\Delta\varphi$ can be related to the corresponding topographic height (h) relative to a reference body by

$$h = -\frac{\lambda \cdot R_0 \cdot \sin\theta_\mathrm{i}}{4 \cdot \pi \cdot B_\perp} \cdot \Delta\varphi, \tag{3.18}$$

where $B_\perp$ is the perpendicular cross-track baseline [151, 156]. A key parameter in interferometry is the height of ambiguity (h_{amb}), which represents the height difference corresponding to a full 2π phase cycle [140, 157]. Substituting $\Delta\varphi = 2 \cdot \pi$ into (3.18) yields

$$h_{\text{amb}} = \frac{\lambda \cdot R_0 \cdot \sin\theta_{\text{i}}}{2 \cdot B_\perp}. \tag{3.19}$$

This interferometric phase is ambiguous, wrapped to integer multiples of 2π. To recover the true, unambiguous phase variation, a process known as phase unwrapping must be applied [158].

3.3.2 Differential Interferometry

Differential interferometric SAR (D-InSAR) is an advanced remote sensing technique that enables high-precision measurement of ground deformation projected on the LoS. These measurements are important for monitoring and tracking surface displacements caused by natural or anthropogenic hazards.

In D-InSAR, two SAR images are acquired over the same area with a temporal baseline and ideally zero spatial baselines to isolate LoS displacements from topographic signatures. However, a certain (non-zero) spatial baseline is usually present, depending on the satellite orbit control strategy. This baseline introduces an additional phase component related to topography, which can be removed using an external digital elevation model (DEM) or estimated at processing stages. The accuracy of the deformation measurement is limited by the accuracy of the external DEM, the degree of temporal decorrelation, and the variations in the propagation medium [159].

3.3.3 Estimation of 3-D Displacements

The measurement of 3-D displacements extends the capabilities of D-InSAR to provide information on surface deformation in the three dimensions: East-West (E-W), North-South (N-S), and Up-Down (U-D). The process, known as inversion, involves combining LoS deformation measurements from multiple interferograms acquired with different imaging geometries. The measured LoS displacements are then inverted into a local 3-D coordinate system [160–162].

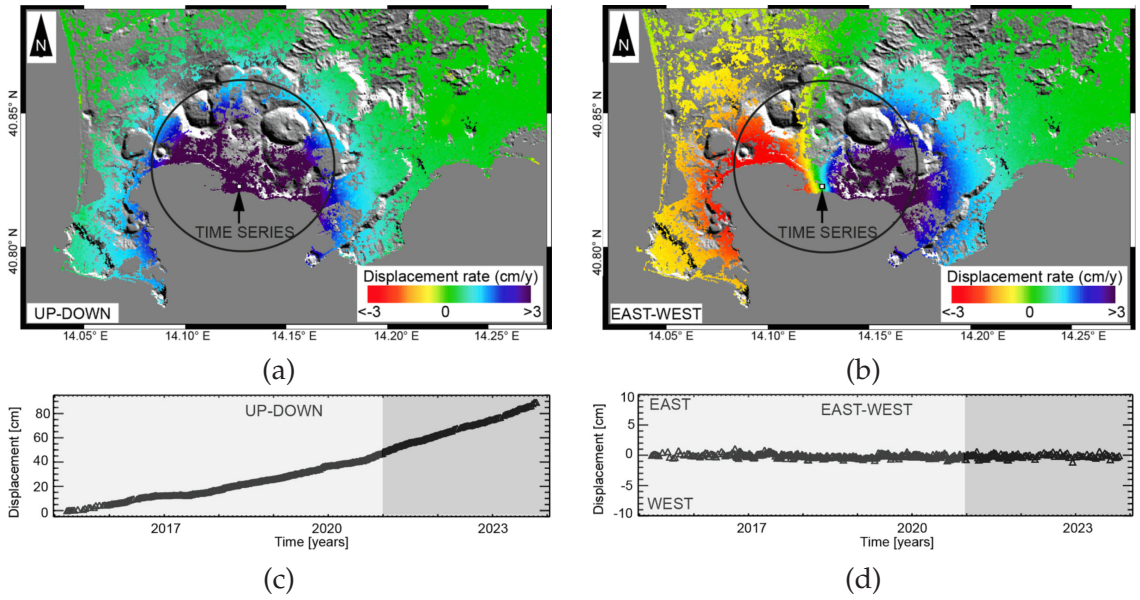

Figure 3.5: Sentinel-1 D-InSAR results for the Campi Flegrei caldera (Italy) during the 2015–2023 period, retrieved from [163]. (a) Up-Down component of deformation. (b) East-West component of deformation. (c) Time series of Up-Down displacement for the pixel corresponding to the area of maximum uplift (indicated by the arrow in panel (a)). (d) Time series of East-West displacement for the same pixel (indicated in panel (b)).

Diverse imaging geometries can be achieved by combining SAR acquisitions from ascending and descending orbital passes, left- and right-looking sensors, or squinted acquisitions. In the absence of sufficient geometric diversity, displacement estimation becomes constrained to a lower-dimensional subspace—typically yielding only two-dimensional results, or in the worst case, deformation measurements limited to the line-of-sight (LoS) direction. Figure 3.5 demonstrates the application of this method for the Campi Flegrei caldera in Italy, a region experiencing significant deformation. The analysis, based on Sentinel-1 data from ascending and descending passes, was presented in [163]. Panels (a) and (b) show the annual displacement rates for the U-D and E-W components, respectively, while panels (c) and (d) present the displacement time series over the period 2015 to 2023, showing a cumulative displacement of approximately 90 cm. The N–S component is not included due to the limited sensitivity of Sentinel-1 in that direction—a limitation resulting from its near-polar orbital configuration, which lacks sufficient geometric diversity to resolve displacements along the N–S axis.

The 3-D displacement vector in the local frame of the pixel can be expressed as

$$\vec{d} = [d_{\mathrm{E}}, d_{\mathrm{N}}, d_{\mathrm{U}}]^T .$$

Each observed LoS displacement is related to the 3-D motion through

$$d_{\mathrm{LoS},i} = \vec{u}_i \cdot \vec{d},$$

where $\vec{u}_i$ is the unit vector in the LoS direction for the i-th observation. By stacking N such observations, the system can be written as

$$\vec{R} = P \cdot \vec{d},$$

where $\vec{R}$ contains the observed LoS displacements, and

$$P = [\vec{u}_1, \vec{u}_2, \ldots, \vec{u}_N]^T$$

consists of the corresponding unit vectors. Assuming that the observation errors are characterized by a known covariance matrix Q_y, the weighted least-squares estimate of the 3-D displacement vector is

$$\vec{d} = \left(P^T \cdot Q_y^{-1} \cdot P\right)^{-1} \cdot P^T \cdot Q_y^{-1} \cdot \vec{R}. \tag{3.20}$$

The precision of InSAR-derived LoS displacement measurement can be approximated using the Cramér–Rao lower bound [159, 161], leading to the estimated variance

$$\sigma^2_{\mathrm{LoS}} = \frac{1-\gamma^2}{2 \cdot N \cdot \gamma^2} \cdot \left(\frac{\lambda}{4 \cdot \pi}\right)^2 + \sigma^2_{\mathrm{APS}}, \tag{3.21}$$

where γ denotes the interferometric coherence, N is the number of independent looks or samples used in the phase estimation, and σ^2_{APS} accounts for atmospheric phase screen (APS) noise.

Using this formulation, the estimation covariance matrix for the 3-D displacement vector serves as a statistical measure of precision

$$\left(P^T Q_y^{-1} P\right)^{-1} = \begin{bmatrix} \sigma^2_{\mathrm{E}} & \sigma_{\mathrm{EN}} & \sigma_{\mathrm{EU}} \\ \sigma_{\mathrm{EN}} & \sigma^2_{\mathrm{N}} & \sigma_{\mathrm{NU}} \\ \sigma_{\mathrm{EU}} & \sigma_{\mathrm{NU}} & \sigma^2_{\mathrm{U}} \end{bmatrix}, \tag{3.22}$$

where the diagonal terms represent the variances in the east, north, and up directions, while the off-diagonal terms capture the correlations between motion components. The detailed derivation of the D-InSAR performance estimation across different system configurations can be found in [161, 162, 164].

3.4 Performance Metrics

SAR performance metrics help characterize the system's ability to resolve, detect, and measure target properties accurately under given operational conditions. Generic metrics include the resolution of the single-look complex (SLC) SAR image, system sensitivity to thermal noise, and tolerance to undesired ambiguities. Specific metrics, particularly relevant to interferometric and radiometric SAR products discussed in later chapters, encompass the standard deviation of the interferometric phase error and radiometric resolution. Accurate estimation of these metrics requires careful consideration of decorrelation sources, which lead to variations in the signal propagation path or the characteristics of the observed scene.

3.4.1 Thermal Sensitivity

The sensitivity of a SAR system to thermal noise is characterized by the signal-to-noise ratio (SNR), defined as the ratio of the signal power (P_s) to the thermal noise power (P_n). Assuming a homogeneous scene with a mean backscatter coefficient (σ_0), the SNR after coherent processing of the radar data at a given elevation angle θ_e is given by

$$\mathrm{SNR}(\theta_\mathrm{e}) = \frac{P_\mathrm{t} \cdot \lambda^2 \cdot c \cdot \tau_\mathrm{p} \cdot \phi_{f_\mathrm{p}} \cdot \sigma_0}{2 \cdot (4 \cdot \pi)^3 \cdot R(\theta_\mathrm{e})^3 \cdot \sin\theta_\mathrm{i} \cdot L \cdot P_\mathrm{N} \cdot \phi_{B_\mathrm{p}}} \cdot \int_{\phi_{B_\mathrm{p}}} G_\mathrm{t}(\theta_\mathrm{e}, \phi) \cdot G_\mathrm{r}(\theta_\mathrm{e}, \phi)\, \mathrm{d}\phi, \tag{3.23}$$

where P_t is the peak transmit power, L accounts for all losses along the transmit/receive chain, and G_t and G_r are the antenna patterns including the gain on transmit and receive, respectively. ϕ_{f_p} is the angular spread in azimuth corresponding to the extent of the PRF (f_p), such that

$$\phi_{f_\mathrm{p}} = \frac{\lambda \cdot f_\mathrm{p}}{2 \cdot v_\mathrm{s}} > \phi_{B_\mathrm{p}}, \tag{3.24}$$

where ϕ_{B_p} is the angular spread in azimuth corresponding to the extent of B_p, typically the HPBW of the antenna aperture in azimuth. P_N is the noise power approximated by

$$P_\mathrm{N} \approx F_\mathrm{s} \cdot k_\mathrm{B} \cdot T_0 \cdot B_\mathrm{r}, \tag{3.25}$$

where F_s is the system noise factor, k_B is Boltzmann's constant, and T_0 is the standard temperature.

The Noise-Equivalent Sigma Nought (NESN) is another metric representing the instrument's sensitivity independent of the imaged target. It is defined as the backscatter coefficient that results in a signal power equal to the noise power (i.e., SNR $= 0\,\mathrm{dB}$)

$$\mathrm{NESN} = \frac{\sigma_0}{\mathrm{SNR}}. \tag{3.26}$$

For a given elevation angle θ_e, the thermal NESN can be represented as

$$\mathrm{NESN}_\mathrm{th}(\theta_\mathrm{e}) = \frac{128 \cdot \pi^3 \cdot R(\theta_\mathrm{e})^3 \cdot \sin\theta_\mathrm{i} \cdot L \cdot F_\mathrm{s} \cdot k_\mathrm{B} \cdot T_0 \cdot B_\mathrm{r} \cdot \phi_{B_\mathrm{p}}}{P_\mathrm{t} \cdot \lambda^2 \cdot c \cdot \tau_\mathrm{p} \cdot \phi_{f_\mathrm{p}} \cdot \int_{\phi_{B_\mathrm{p}}} G_\mathrm{t}(\theta_\mathrm{e},\phi) \cdot G_\mathrm{r}(\theta_\mathrm{e},\phi)\,\mathrm{d}\phi}. \tag{3.27}$$

An alternative representation incorporates the average transmit power

$$P_\mathrm{avg} = P_\mathrm{t} \cdot \tau_\mathrm{p} \cdot f_\mathrm{p} = P_\mathrm{t} \cdot dc, \tag{3.28}$$

where dc is the instrument duty cycle, which represents the fraction of time the instrument is actively transmitting—that is, the ratio of the pulse duration (τ_p) to the pulse repetition interval (PRI $= 1/f_\mathrm{p}$). Substituting (3.24) and (3.28) into (3.27) results in the alternative expression

$$\mathrm{NESN}_\mathrm{th}(\theta_\mathrm{e}) = \frac{256 \cdot \pi^3 \cdot R(\theta_\mathrm{e})^3 \cdot v_\mathrm{s} \cdot \sin\theta_\mathrm{i} \cdot L \cdot F_\mathrm{s} \cdot k_\mathrm{B} \cdot T_0 \cdot B_\mathrm{r} \cdot \phi_{B_\mathrm{p}}}{P_\mathrm{avg} \cdot \lambda^3 \cdot c \cdot \int_{\phi_{B_\mathrm{p}}} G_\mathrm{t}(\theta_\mathrm{e},\phi) \cdot G_\mathrm{r}(\theta_\mathrm{e},\phi)\,\mathrm{d}\phi}. \tag{3.29}$$

3.4.2 Azimuth Ambiguity-to-Signal Ratio

The azimuth ambiguity-to-signal ratio (AASR) quantifies the system's robustness against undesired ambiguities in the azimuth direction, which arise due to undersampling of the Doppler spectrum. The spectrum is weighted by the azimuth antenna pattern and is constrained by the processed Doppler bandwidth (B_p). The AASR is then defined as the ratio of the power of the azimuth ambiguities (i.e., the aliased part of the Doppler spectrum) to the power of the signal (i.e., the Doppler spectrum within the processed bandwidth). Assuming separable transmit and receive patterns, it can be estimated as

$$\mathrm{AASR} \approx \frac{\sum_{\substack{k=-N_\mathrm{A} \\ k\neq 0}}^{N_\mathrm{A}} \int_{B_\mathrm{p}} G_\mathrm{t}(f + k \cdot f_\mathrm{p}) \cdot G_\mathrm{r}(f + k \cdot f_\mathrm{p}))\,\mathrm{d}f}{\int_{B_\mathrm{p}} G_\mathrm{t}(f) \cdot G_\mathrm{r}(f)\,\mathrm{d}f}, \tag{3.30}$$

where f denotes the Doppler frequency, and N_A is the number of aliased ambiguities considered on each side of the spectrum.

3.4.3 Range Ambiguity-to-Signal Ratio

The range ambiguities in a pulsed radar system arise from the simultaneous reception of the returns from different pulses, which repeat every $1/f_\mathrm{p}$. For example, the return of the j-th pulse from a target located at slant range R coincides with the return of the $(j-k)$-th pulse from a target at an ambiguous slant range

$$R_{jk} = R_j + k \cdot \frac{c}{2 \cdot f_\mathrm{p}}, \tag{3.31}$$

where k is the ambiguity order. The range ambiguity-to-signal ratio (RASR) is defined as the ratio of the power of the range ambiguities (S_a) to the power of the desired signal (S). For a given slant range R_j, corresponding to the j-th pulse,

$$\mathrm{RASR} \approx \frac{S_{\mathrm{a},jk}}{S_j}, \tag{3.32}$$

where

$$S_{\mathrm{a},jk} = \sum_{\substack{k=-\frac{N_\mathrm{R}}{2} \\ k\neq 0}}^{\frac{N_\mathrm{R}}{2}} \frac{\sigma_{0,jk}}{R_{jk}^3 \cdot \sin\theta_{\mathrm{i},jk}} \int_{\phi_{B_\mathrm{p}}} G_\mathrm{t}(\theta_{\mathrm{e},jk},\phi) \cdot G_\mathrm{r}(\theta_{\mathrm{e},jk},\phi)\,\mathrm{d}\phi, \tag{3.33}$$

and

$$S_j = \frac{\sigma_{0,jk}}{R_{jk}^3 \cdot \sin\theta_{\mathrm{i},jk}} \int_{\phi_{B_\mathrm{p}}} G_\mathrm{t}(\theta_{\mathrm{e},jk},\phi) \cdot G_\mathrm{r}(\theta_{\mathrm{e},jk},\phi)\,\mathrm{d}\phi, \quad \text{for } k = 0. \tag{3.34}$$

Here, N_R represents the total number of ambiguous pulses considered, constrained by the range to the horizon.

3.4.4 Standard Deviation of the Interferometric Phase Error

The precision of interferometric measurements is influenced by the uncertainty in the phase difference, which is characterized by the standard deviation of the interferometric phase error

$$\sigma_\varphi = \sqrt{\int_{-\pi}^{\pi} (\varphi - \langle\varphi\rangle)^2 \cdot p_\varphi(\varphi)\,\mathrm{d}\varphi}, \tag{3.35}$$

where $p_\varphi(\varphi)$ is the probability density function (pdf) of the phase difference between two interferometric SAR acquisitions, and the term $\langle\varphi\rangle$ represents the expected (mean) value of the phase. The pdf depends on the total coherence (γ_T) and the number of independent looks (N_l) in the interferogram, and can be expressed according to [165] as

$$\begin{aligned} p_\varphi(\varphi) = &\frac{\Gamma\left(N_\mathrm{l} + \frac{1}{2}\right) \cdot \left(1 - \gamma_\mathrm{T}^2\right)^{N_\mathrm{l}} \cdot \gamma_\mathrm{T} \cdot \cos\varphi}{2 \cdot \sqrt{\pi} \cdot \Gamma(N_\mathrm{l}) \cdot \left(1 - \gamma_\mathrm{T}^2 \cdot \cos^2\varphi\right)^{N_\mathrm{l}+\frac{1}{2}}} \\ &+ \frac{\left(1 - \gamma_\mathrm{T}^2\right)^{N_\mathrm{l}}}{2 \cdot \pi} \cdot F\left(N_\mathrm{l}; 1; \frac{1}{2}; \gamma_\mathrm{T}^2 \cdot \cos^2\varphi\right), \end{aligned} \tag{3.36}$$

where Γ is the gamma function, and F is the Gauss hypergeometric function [166].

3.4.5 Interferometric Coherence

Coherence refers to the magnitude of correlation of two complex SAR images s_1 and s_2, defined as

$$\gamma = \frac{\langle s_1 \cdot s_2^* \rangle}{\sqrt{\langle |s_1|^2 \rangle \cdot \langle |s_2|^2 \rangle}}, \tag{3.37}$$

where * indicates complex conjugation and $\langle\cdot\rangle$ indicates spatial averaging, typically estimated using a moving window across the images. Its magnitude varies across pixels and ranges from 0 (no coherence) to 1 (full coherence).

Assuming statistical independence among the various contributing factors, the total coherence can be expressed as the product of individual coherence terms

$$\gamma_\mathrm{T} = \prod_i \gamma_i. \tag{3.38}$$

The primary sources of coherence loss can be incorporated into

$$\gamma_T = \gamma_{th} \cdot \gamma_{amb} \cdot \gamma_{rg} \cdot \gamma_{az} \cdot \gamma_{vol} \cdot \gamma_{temp} \cdot \gamma_{atm} \cdot \gamma_{clut} \cdot \gamma_{proc}. \tag{3.39}$$

Each of the above terms represents a distinct coherence loss mechanism [29, 167]. These include losses due to thermal noise (γ_{th}), ambiguities (γ_{amb}), shift of the range spectra(γ_{rg}), shift of the Doppler spectra (γ_{az}), volumetric decorrelation (γ_{vol}), temporal decorrelation (γ_{temp}), atmospheric decorrelation (γ_{atm}), clutter decorrelation (γ_{clut}), and processing (γ_{proc}) which combines several decorrelation sources such as co-registration errors or quantization noise. The following subsections provide high-level models for quantifying the most relevant factors in terms of coherence loss or signal-to-noise ratio.

3.4.6 Noise Decorrelation

The interferometric coherence (γ) can be expressed as a function of the signal-to-noise ratios (SNR) of the two SAR images forming the interferogram, where

$$\gamma = \frac{1}{\sqrt{\left(1 + \mathrm{SNR}_1^{-1}\right) \cdot \left(1 + \mathrm{SNR}_2^{-1}\right)}}. \tag{3.40}$$

If both images have a similar SNR, the equivalent coherence simplifies to

$$\gamma = \frac{\mathrm{SNR}}{1 + \mathrm{SNR}}. \tag{3.41}$$

Conversely, if the coherence is known, the equivalent SNR can be estimated as

$$\mathrm{SNR} = \frac{\gamma}{1 - \gamma}. \tag{3.42}$$

3.4.7 Spectral Shifts and Decorrelation

Spectral shifts can occur in both the range and Doppler domains and, if not properly compensated, can lead to a loss of interferometric coherence. To mitigate this, common band filtering is typically applied during processing. While this ensures spectral alignment between image pairs, it reduces the effective number of samples and thereby decreases the efficiency of the acquired data.

In the range direction, spectral shift arises from the spatial separation between sensor positions during the acquisition of interferometric image

pairs. The effective perpendicular baseline ($B_\perp$), measured in the plane perpendicular to the flight path (cross-track), induces a shift in the range frequency spectrum

$$\Delta f_\mathrm{r} = \frac{c \cdot B_\perp}{R \cdot \lambda \cdot \tan(\theta_\mathrm{i} - \zeta)}, \tag{3.43}$$

where ζ is the slope of the terrain [151, 153, 168]. The critical baseline ($B_{\perp,\mathrm{crit}}$) is defined as the baseline at which the spectral shift equals the system's range bandwidth (i.e., $\Delta f_\mathrm{r} = B_\mathrm{r}$). It is given by

$$B_{\perp,\mathrm{crit}} = \frac{\lambda \cdot B_\mathrm{r} \cdot R \cdot \tan(\theta_\mathrm{i} - \zeta)}{c}. \tag{3.44}$$

In the azimuth (Doppler) domain, spectral shifts may occur due to geometric discrepancies such as across-track separation, orbit errors, or variations in squint angle. These lead to differences in Doppler centroid frequency (f_DC) between interferometric acquisitions.

If no spectral filtering is applied, the range spectral coherence resulting from a residual range spectral shift Δf_r can be approximated by:

$$\gamma_\mathrm{rg} = \frac{B_\mathrm{r} - \Delta f_\mathrm{r}}{B_\mathrm{r}}, \quad \text{for } \Delta f_\mathrm{r} < B_\mathrm{r}. \tag{3.45}$$

Similarly, the Doppler spectral coherence resulting from a residual Doppler centroid shift Δf_DC can be approximated by

$$\gamma_\mathrm{az} \approx \frac{B_\mathrm{p} - |\Delta f_\mathrm{DC}|}{B_\mathrm{p}}, \quad \text{for } |\Delta f_\mathrm{DC}| < B_\mathrm{p}. \tag{3.46}$$

While common band filtering can restore full spectral coherence by aligning the usable portions of the spectra, it does so at the expense of reduced bandwidth. This reduction leads to fewer independent looks in multilook processing, thereby slightly degrading the quality of the final interferometric product.

3.4.8 Volumetric Decorrelation

Volume decorrelation occurs when radar signals scatter from distributed targets located within a vertical structure, such as forest canopies, vegetation layers, or snow layers [169]. It introduces additional randomness due to signal penetration and interaction at different depths within the medium.

As described by Treuhaft in [170], the volume coherence can be modeled as an integral over the vertical coordinate

$$\gamma_{\text{vol}} = \exp\left[j\phi_0(z_0)\right] \cdot \frac{\int_0^{h_\text{v}} \exp\left(jk_\text{z} \cdot z\right) g_\text{v}(z)\,\text{d}z}{\int_0^{h_\text{v}} \cdot g_\text{v}(z)\,\text{d}z}, \tag{3.47}$$

where $g_v(z)$ is the vertical distribution of scattering within the volume, h_v is the height of the volume, and $\phi_0(z_0)$ is the reference phase at some height z_0. The vertical wavenumber k_z is related to the height of ambiguity h_amb, defined in (3.19), by

$$k_\text{z} = \frac{2 \cdot \pi}{h_\text{amb}}. \tag{3.48}$$

Assuming a uniform distribution of scatterers within the volume and negligible ground contribution, the volume coherence can be approximated using the simplified sinc model from [171] as

$$\gamma_{\text{vol}} = \text{sinc}\left(\frac{h_\text{v} \cdot \cos\theta_\text{i}}{h_\text{amb}}\right), \tag{3.49}$$

where $\text{sinc}(x) = \sin(\pi \cdot x)/(\pi \cdot x)$.

3.4.9 Temporal Decorrelation

Temporal decorrelation is caused by changes in the scene's structure and dielectric properties during the time interval between the two acquisitions that form an interferogram. The time-dependent decorrelation model, as described in [172], is given by

$$\gamma_{\text{temp}}(t) = (1 - \gamma_\infty)\exp\left(-\frac{t}{\tau}\right) + \gamma_\infty, \tag{3.50}$$

where γ_∞ denotes the persistent (long-term) coherence and τ is the decorrelation time constant. The values of these parameters depend on the radar frequency and the physical characteristics of the observed scene. The experiments in [172] demonstrated that higher radar frequencies tend to exhibit shorter decorrelation times (τ) and lower persistent coherence.

3.4.10 Impact of Atmospheric Perturbations on Coherence

Atmospheric decorrelation results from phase deviations introduced by variations in signal propagation delays and phases as radar waves traverse the atmosphere. For short integration times—typically up to a few seconds as in LEO-SAR missions—the atmospheric perturbations can often be considered frozen in time [173, 174]. However, in high MEO- and GEO-SAR missions, integration times range from several tens of seconds to minutes and even hours. under such conditions, the atmosphere is both time- and space-varying, potential leading to co-registration errors, image defocusing, and phase distortions that degrade image quality and interferometric performance.

To address this, Ruiz Rodon et al. [89] proposed an autofocusing technique to estimate the time- and space-varying atmospheric phase screen (APS) using lower-resolution intermediate products, specifically sub-aperture images. The method exploits persistent targets (i.e., targets with sufficient SNR) within the APS resolution cell, and its performance can be influenced by speckle noise within those cells. In a related study, Monti Guarnieri et al. [92] introduced an interferometric autofocusing technique that also uses sub-aperture images, but instead leverages the reflectivity of the entire scene. The quality of the APS estimate, which is typically be degraded by decorrelation due to thermal noise, temporal changes, and atmospheric variability, can be improved by averaging across a number of range bins in which the APS is assumed to remain stationary.

Assuming a separable time–space model for tropospheric delays, Monti Guarnieri et al. further proposed a simplified expression for estimating the coherence loss due to the APS [92]

$$\gamma_{\text{atm}} \approx \frac{4 \cdot \tau_0^2}{T_{\text{opt}}^2} \cdot \left(1 - \exp\left(-\frac{T_{\text{opt}}}{2\tau_0}\right)\right)^2, \tag{3.51}$$

where T_{opt} is the optimal sub-aperture time, defined as

$$T_{\text{opt}} = \sqrt{\frac{\lambda \cdot R \cdot t_0}{2 \cdot v_s \cdot y_0}}, \tag{3.52}$$

with t_0 and y_0 denoting atmospheric temporal and spatial decorrelation constants, respectively. Typical values are $t_0 \approx 10\,\text{h}$ and $y_0 \approx 10\,\text{km}$, extrapolated from measurements from global navigation satellite systems

(GNSS), LEO-SAR, ground-based SAR, and meteorological models. The APS-limited integration time constant (τ_0) is expressed as

$$\tau_0 = \frac{\lambda^2 \cdot t_0}{(4\pi)^2 \cdot \sigma^2_{\text{atm}}}, \tag{3.53}$$

where σ^2_{atm} is the variance (sill value) of atmospheric delay fluctuations, typically ranging from 100 to 1000 mm^2 depending on atmospheric conditions—from calm to turbulent—as observed through GPS, ground-based SAR, and meteorological data [175–178].

3.4.11 Clutter Decorrelation

Clutter decorrelation is an additional source of interferometric noise arising from non-stationary scatterers, such as windblown trees or moving vegetation, during the synthetic aperture time. Its impact becomes more pronounced with longer integration times and is typically quantified using the signal-to-clutter noise ratio (SCNR), or the equivalent coherence γ_{clut}.

A well-established model for characterizing decorrelation in windblown ground clutter under homogeneous conditions is the intrinsic clutter model (ICM). First proposed by Billingsley [179, 180], the ICM was derived from experimental observations of windblown trees at near-grazing incident angles and short integration times (typically less than one minute). In [95], Recchia et al. demonstrated the applicability of the model to longer integration times—such as those encountered in geosynchronous SAR—with only minor adjustments to the model parameters. Under this model the SCNR can approximated by

$$\text{SCNR} \approx \frac{r}{1 - \exp\left(-\frac{v_s \cdot \beta \cdot \lambda}{2 \cdot L_a}\right)}, \tag{3.54}$$

where r is the DC/AC ratio,[5] β is the spectral slope, v_s is the relative speed of the platform, and L_a is the length of the antenna along azimuth. Based on extensive measurement campaigns, Billingsley proposed the empirically derived analytic expression [179]

$$r = 140.7 \cdot w^{-1.55} \cdot \left(f_0 \cdot 10^{-9}\right)^{-1.21}, \tag{3.55}$$

[5] The DC/AC ratio quantifies the relative strength of the DC or zero-Doppler term to the AC or varying component in the power spectrum of the returned signal.

which captures the dependence of r on the wind speed w (in m/s) and the carrier frequency f_0 (in Hz). Although this exponential model was originally derived for windblown trees, Billingsley demonstrated that it generalizes well to other types of windblown vegetation—such as scrub desert, rangeland, and cropland—by appropriately adjusting its DC/AC term. Furthermore, Recchia et al. [95] extended the ICM framework to account not only for longer integration times, but also for spatially and temporally heterogeneous scenes. Additionally, Monti Guarnieri et al. [181] proposed a generalized clutter decorrelation model based on a sum of exponentials, capable of more accurately capturing complex temporal decorrelation behaviors over extended integration periods.

3.4.12 Radiometric Resolution

The radiometric resolution characterizes the minimum detectable variation in backscatter intensity within a SAR image that the SAR system can reliably measure. According to [138], it is given by

$$\delta_{\text{rad}} = 1 + \frac{1 + \text{SNR}_{\text{T}}^{-1}}{\sqrt{N_{\text{l}}}}, \tag{3.56}$$

where N_{l} is the number of independent processed looks, and SNR_{T} is the total signal-to-noise ratio. The radiometric resolution is typically represented in dB as

$$\delta_{\text{rad,dB}} = 10 \cdot \log_{10}(\delta_{\text{rad}}). \tag{3.57}$$

Under the assumption of randomness and statistical independence, the total SNR can be determined by combining the individual noise contributions—namely thermal noise, ambiguity noise, atmospheric noise, and clutter noise—accumulated over the integration time as

$$\frac{1}{\text{SNR}_{\text{T}}} = \sum_i \frac{1}{\text{SNR}_i}. \tag{3.58}$$

3.5 Antenna Aspects

The design of an antenna for a SAR system is driven by performance requirements and platform constraints. From a performance perspective, the antenna plays a critical role in defining resolution, sensitivity, ambiguity suppression, and coverage. It also enables advanced functionalities like beam steering and beamforming during transmission and reception. On

the other hand, platform-related considerations, such as the mass, volume, and power budgets, strongly influence the choice of antenna technology and aperture dimensions. For instance, large apertures may require deployable or foldable structures, which introduce mechanical complexity and require additional support mechanisms. Similarly, systems with digital beamforming capabilities require transmit/receive modules (TRMs) for each channel, significantly impacting the system's overall mass, volume, and power requirements.

3.5.1 Performance Metrics

The key antenna parameters influencing SAR performance include antenna gain, beamwidth, and peak-to-sidelobe ratio. The maximum achievable gain for a physical aperture of area A_a is given by

$$G = \eta_\mathrm{ant} \cdot \frac{4 \cdot \pi \cdot A_\mathrm{a}}{\lambda^2}, \tag{3.59}$$

where η_ant represents the antenna efficiency, accounting for spill-over, illumination, and phase distortion in the case of a reflector design. The half-power beamwidth, which defines the angular resolution of the antenna, is determined by the aperture length L along a given direction

$$\theta_\mathrm{3dB} = k_\mathrm{a} \cdot \frac{\lambda}{L}, \tag{3.60}$$

where k_a is a factor that depends on the geometrical shape of the aperture. For a planar antenna, $k_\mathrm{a} \approx 0.89$, while for a parabolic reflector, $k_\mathrm{a} \approx 1.22$.

3.5.2 Typical Antenna Technologies

Planar Antennas

Planar antennas are flat radiating surfaces confined in a plane. These antennas are compact and exhibit high-density characteristics. In multimodal SAR systems, active phased array antennas are commonly employed. These antennas can use phase shifters and time delay units to control the radiating elements, enabling electronic beam steering. State-of-the-art SAR systems utilize variants of the planar antenna technology, such as microstrip arrays and slotted waveguides. Examples of such systems include TerraSAR-X/TanDEM-X [26, 182], SARah-1 [183], COSMO-SkyMed [184], and RADARSAT-2 [185].

Reflector Antennas

Reflector antennas use a curved reflective surface to focus EM waves onto a radiating feed antenna. These systems are known for their low density, high gain, and high directivity, making them well-suited for systems requiring large apertures. Typical configurations include offset, Cassegrain, Gregorian, and center-fed designs, each differing in design complexity and blockage effects. Examples of current and upcoming SAR missions utilizing this technology include Capella [49], SARah-2/3 [186], Biomass [57, 187], and NISAR [58, 188].

4 Quantitative Analysis of High-Orbit SAR

The block diagram in Figure 4.1 illustrates some core components of a SAR mission design, starting with the definition of user objectives (scientific and/or operational), desired SAR products, and frequency. These objec-

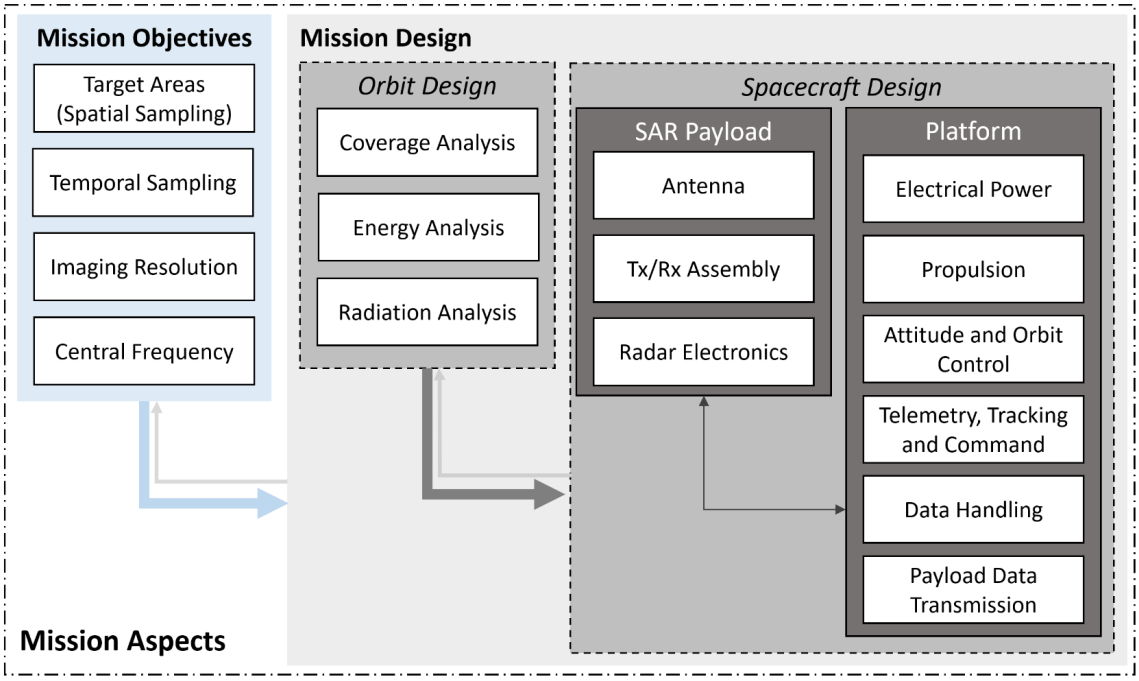

Figure 4.1: Key design components of a SAR mission for Earth observation.

tives guide the orbit design process, primarily focusing on coverage and temporal revisit requirements while analyzing the varying space environment. These, in turn, influence SAR payload specifications (e.g., antenna size, power, electronics) and the spacecraft platform (e.g., energy, radiation resilience, propulsion, data handling). Given the interdependencies among the design elements, this process is iterative, balancing mission objectives with constraints such as the overall mission budget.

This chapter presents a quantitative analysis of SAR missions in high Earth orbits, addressing a critical gap in the available literature. It systematically explores key trade-offs among sensitivity, spatial coverage, launch constraints, and radiation challenges associated with higher altitudes. Through this analysis, the chapter advances the understanding of SAR system complexity and performance in high Earth orbits, offering novel insights into mission architecture, imaging capabilities, and the identification of optimal operational venues tailored to diverse mission objectives.

Section 4.1 examines key aspects of orbit and platform design for high-altitude SAR missions, emphasizing their enhanced global and local coverage capabilities. The analysis highlights the implications for solar energy availability, noting that while sun-synchronous frozen orbits are not feasible beyond 5500 km, shorter eclipse durations ease power constraints for solar-powered platforms. The section also characterizes the space radiation environment, showing that with adequate shielding and careful orbit selection, radiation exposure can be kept at LEO-comparable levels. Finally, it addresses launch constraints, identifying electric propulsion as a cost-effective alternative to direct high-altitude insertion, albeit with extended transfer durations.

Section 4.2 investigates the sensitivity degradation of SAR systems at high altitudes and its implications for achievable SAR imaging performance and payload design. It analyzes how extended illumination times affect stripmap imaging and revisits the classical azimuth resolution-to-antenna length relationship under high-altitude geometries. The section proposes two operation concepts: (A) achieving LEO-like resolution and swath width with frequent global or large-scale access, and (B) extended swath coverage at moderate resolution. The section details the corresponding payload requirements necessary to realize each concept.

The findings in this chapter represent a core contribution of the thesis and provide the analytical basis for the MEO and GEO conceptual designs presented in Chapter 5 and Chapter 6. Part of this work has been published in [189, 190].

4.1 Orbit and Platform Design

SAR systems in higher orbits offer an expanded instantaneous field of view and have the potential to enhance the coverage; however, they suffer from a more challenging operation environment and higher launch costs.

4.1.1 Access and Coverage Rates

To better understand the enhanced coverage capabilities of high-altitude systems, this section introduces two key metrics: access and coverage rates. Both metrics provide insights on the potential area that can be acquired by a SAR instrument over time, typically measured in m^2/s. By analyzing these metrics, optimal operational altitudes can be identified to maximize coverage efficiency and support frequent global or regional revisit.

The access rate (A_r) quantifies the rate at which a swath is accessible, though not necessarily imaged. The accessible swath width (W_{acc}) is typically constrained by the desirable range of incident angles for the specific SAR application under consideration. It can be defined as

$$A_r = v_g \cdot W_{acc}, \tag{4.1}$$

where v_g is the velocity of the radar beam on the ground. Alternatively, the coverage rate (C_r) quantifies the rate at which a swath can be imaged. The covered swath width (W_g) is constrained by the instantaneous imaging capabilities of the SAR instrument, including factors such as sensitivity, ambiguity suppression, and beamforming capabilities. It can be defined as

$$C_r = v_g \cdot W_g. \tag{4.2}$$

The natural beam velocity on the ground depends on the orbital geometry, including the semi-major axis (a), inclination (i), and eccentricity (e); the SAR geometry, such as the incident angle (θ_i) and look angle (θ_l); and the scene location, for example, the latitude of the imaged scene (ϕ_{lat}), assuming an ellipsoidal Earth model. For near-circular orbits,

$$v_g \approx \sqrt{\frac{\mu_E}{a^3}} \cdot R_E \cdot \cos(\theta_l - \theta_i) - \omega_E \cdot R_E \cdot |\cos\phi_{lat}| \cdot \cos i, \tag{4.3}$$

where μ_E, R_E, and ω_E are Earth's standard gravitational parameter, equatorial radius, and angular velocity, respectively. This approximation holds with an error below 0.5 dB for moderate altitudes (e.g., up to approximately 10 000 km), making it suitable for characterizing systems designed for near-global access. In high-resolution imaging modes such as sliding spotlight, the effective beam velocity can be intentionally reduced through electronic or mechanical beam steering. This reduction improves the azimuth resolution but comes at the cost of decreased coverage rates.

Figure 4.2 provides a graphical representation of the difference between the two swath definitions. The accessible swath, W_{acc}, is bounded by the near

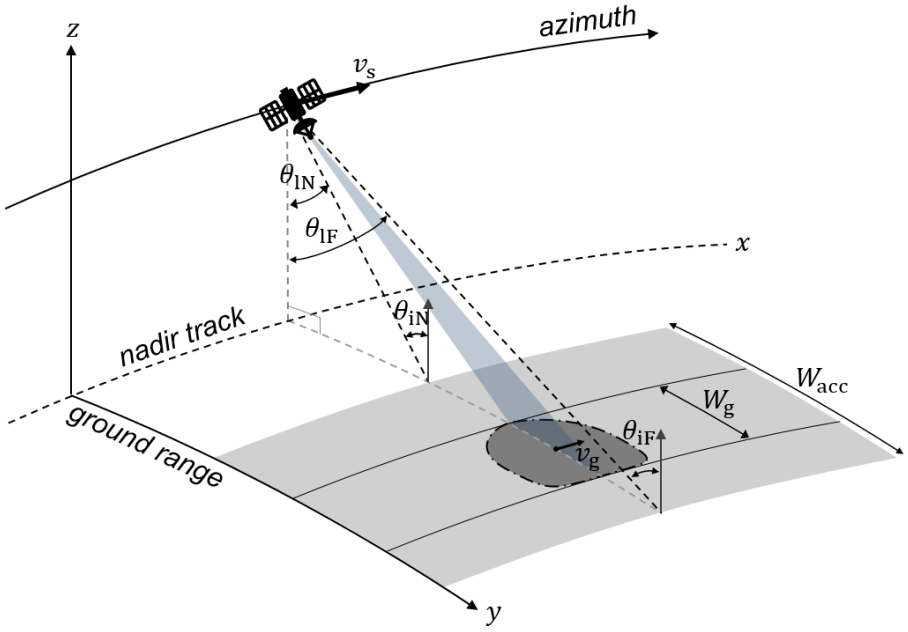

Figure 4.2: Example SAR acquisition geometry showcasing the difference between the accessible swath width (W_{acc}), constrained by a range of incident angles, and the covered swath width (W_g), determined by the instantaneous extension of the antenna beamwidth on the ground in the range direction.

and far incident angles, θ_{iN} and θ_{iF}, respectively. On the other hand, W_g corresponds to the extension of the antenna beamwidth (θ_{el}) on the ground along the range direction, which can be approximated using the arc length formula by

$$W_g \approx \frac{R_M \cdot \theta_{el}}{\cos \theta_{iM}}, \tag{4.4}$$

where θ_{iM} and R_M are the incident angle and slant range to the center of the scene, respectively. In practice, the radar beam can be sharpened to cover narrower areas or broadened or steered to cover larger portions of the access area.

Figure 4.3 shows the variation in the access and coverage rates with altitude, assuming nominal beam steering conditions (e.g., zero Doppler). The analysis is conducted across a range of orbital inclinations and scene latitudes, and results are compared against a reference LEO case at an altitude of 400 km. The results indicate a strong dependency of both access and coverage rates on altitude and inclination, with a minor sensitivity to scene latitudes for near-circular orbits. Significant degradation in both rates is observed for low-inclination orbits (e.g., $i = 30^\circ$), primarily due to the larger

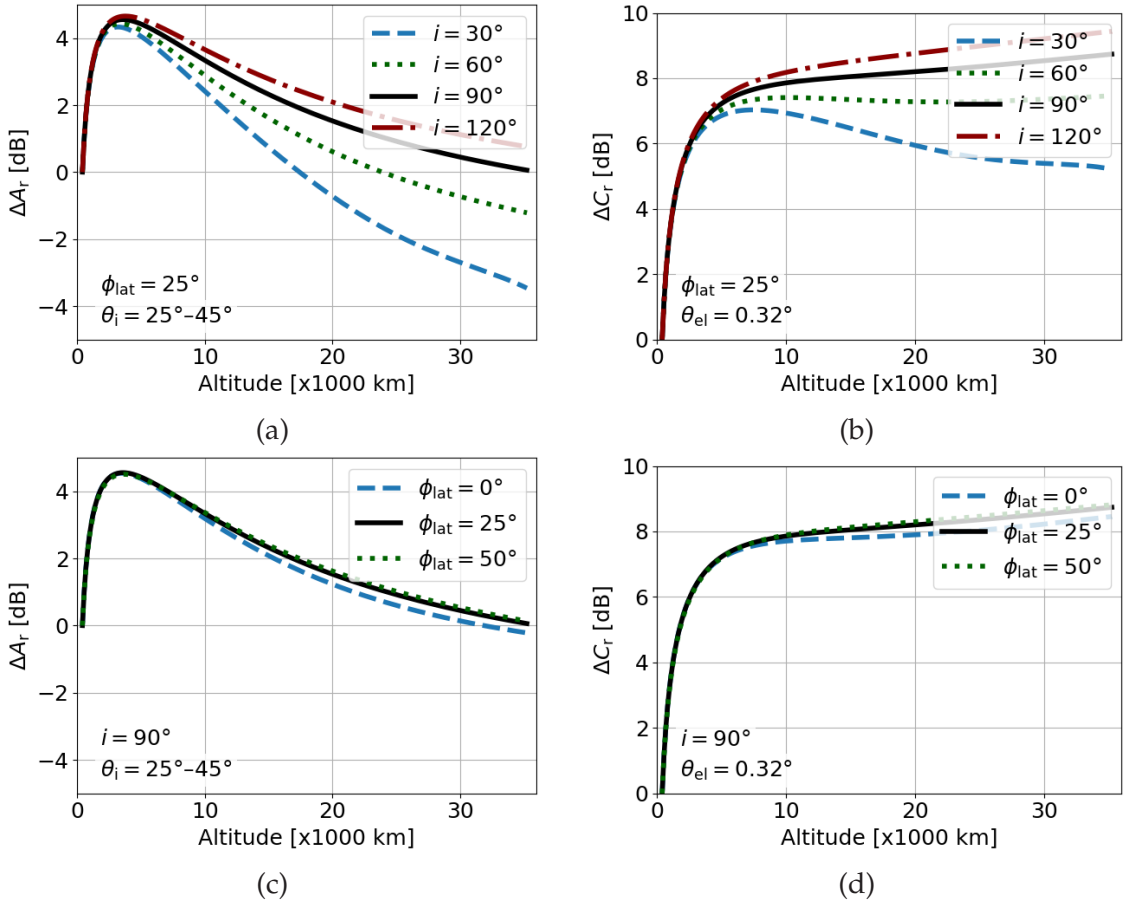

Figure 4.3: Variation in the access rate (A_r, left) and coverage rate (C_r, right) with altitude for near-circular orbits under different: (a and b) orbital inclinations i, and (c and d) scene latitudes ϕ_{lat}. An elevation beamwidth (θ_{el}) of 0.32° is assumed for estimating C_r. The variations are expressed in dB, referenced to an altitude of 400 km. These values represent changes in coverage and access rates only, and do not account for SAR-specific imaging capabilities such as resolution.

reduction in relative velocity for prograde orbits.[1] Variations in the elevation beamwidth (θ_{el}) introduce only marginal changes in ΔC_r. For systems without beamforming capability, an example elevation of θ_{el} =0.32° corresponds to planar antenna heights of approximately 5, 9, and 38 m for X-, C-, and L-band systems, respectively.

The results also reveal a distinct advantage in coverage and access rates within the low-MEO altitude range of 3000 km to 10 000 km. Access rates peak at around 3500 km, while coverage rates reach saturation near 8000 km. At higher MEO altitudes, up to GEO, the marginal gains—or, in the case of low inclination, reductions—in access rates render these orbits

[1] *Prograde orbits* have inclinations between 0° and 90°. In prograde orbits, objects move in the same direction as the rotation of the primary body (in this case, the Earth), whereas in retrograde orbits, they move in the opposite direction.

less efficient for broad coverage. Nonetheless, their low relative motion with respect to Earth makes them particularly suitable for SAR missions focused on persistent or frequent (e.g., sub-daily) monitoring of specific regions, countries, or continents with a minimal number of satellites. At GEO, despite the significant degradation in sensitivity, performance can be recovered by extending the synthetic aperture time using imaging modes such as sliding or staring spotlight. This, however, comes at the expense of substantially reduced coverage rates compared to those illustrated in the plots.

Potential coverage rates for low-MEO SAR systems, assuming a 100 % orbit duty cycle and a moderate incident-angle range, can range from 200 to 500 Mkm^2/d ("M" denotes million and "d" denotes day). In contrast, GEO-SAR systems may achieve rates below 100 Mkm^2/d, with coverage limited to specific regions. State-of-the-art wide-swath LEO-SAR systems could provide coverage rates of around 150 to 250 Mkm^2/d. For context, the Earth's total surface area is approximately 510 Mkm^2, with land area accounting for about 149 Mkm^2. In practice, the orbit duty cycle is constrained by several factors, including energy availability, thermal limitations, data downlink capacity, and acquisition priorities. The orbit duty cycle for power-demanding SAR systems is typically restricted to values below 30 %.

4.1.2 Latitude Access

Latitude reach is a crucial factor in orbit design and is often specified in mission objectives as requirements such as near-global coverage or polar access capabilities. The latitude reach represents the maximum or minimum latitude observable by a SAR instrument within a specified range of incident angles suitable for SAR acquisitions, typically between 15° and 60°. Figure 4.4 shows that higher altitudes facilitate access to polar latitudes, even at lower inclinations. For instance, polar access is achievable at altitudes above 4500 km with inclinations exceeding 60°, while inclinations over 45° enable polar access at altitudes above 14 000 km.

Equatorial orbits present another opportunity, offering optimal interferometric revisit efficiency but typically constrained in latitude reach, including restricted access to the equator itself due to SAR geometry constraints. Increasing orbital altitude broadens the accessible latitude range, as illustrated in Figure 4.5. SAR systems capable of both left and right-looking can leverage the expanded latitude reach to perform observations across both Earth hemispheres.

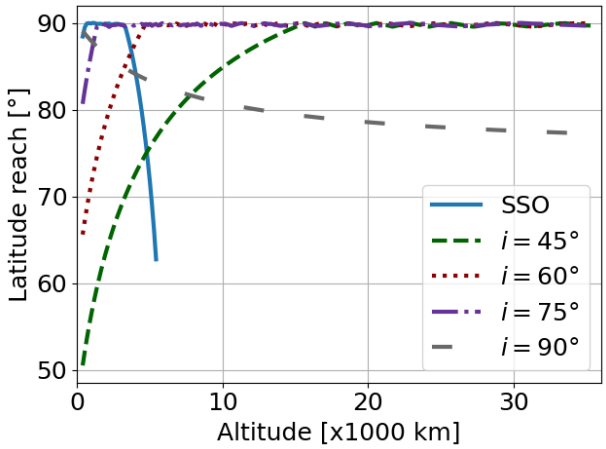

Figure 4.4: Latitude reach as a function of altitude and inclination for frozen near-circular Earth orbits, with a valid incident-angle range of 15° to 60°.

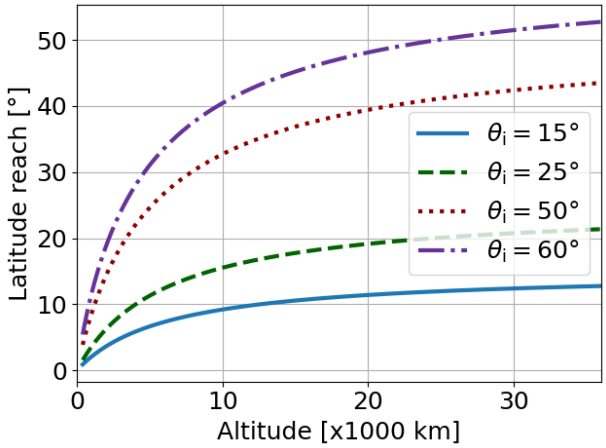

Figure 4.5: Latitude reach as a function of altitude for near-circular equatorial Earth orbits.

4.1.3 Availability of Solar Energy

SAR satellites typically require high transmit power, and increasing orbital altitude does not alleviate this demand. As discussed in Section 4.2, maintaining sufficient sensitivity at higher altitudes may necessitate a reduction in resolution or a larger antenna to avoid significantly increasing the transmit power. To ensure near-continuous solar illumination, most high-performance, solar-powered LEO-SAR systems employ sun-synchronous orbits (SSO), as outlined in Section 2.2.

By applying (2.10), the main orbit parameters for potential SSO at higher altitudes can be calculated. Figure 4.6 illustrates the corresponding inclinations for frozen and more eccentric SSOs. The maximum achievable semi-

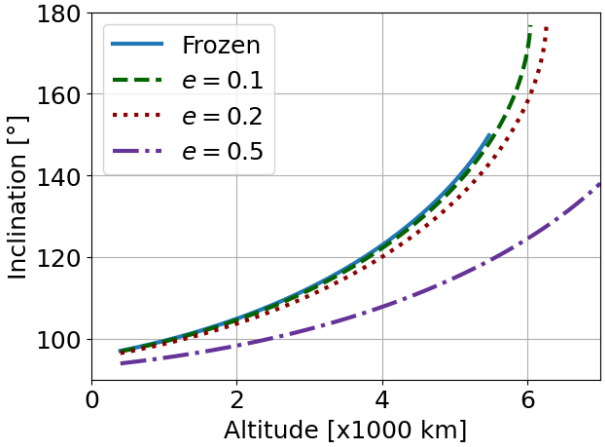

Figure 4.6: Variation of orbital inclination with altitude for maintaining sun-synchronous conditions.

major axis is given by

$$a \leq \sqrt[7]{\frac{9 \cdot \mu_{\mathrm{E}} \cdot J_2^2 \cdot R_{\mathrm{E}}^4}{4 \cdot (1-e^2)^4 \cdot \dot{\Omega}_{\mathrm{ES}}^2}}, \tag{4.5}$$

which results in a maximum altitude of approximately 5500 km for frozen orbits.

The relatively close proximity of LEO-SAR systems to Earth can lead to extended eclipse durations if the orbits are not properly designed. SSOs offer an optimal solution for mitigating the issue, reducing eclipse times to less than 8%, as illustrated in Figure 2.4. Additionally, the nodal regression requirement for frozen SSO results in near-polar inclinations at LEO altitudes, enabling access to polar latitudes. Although SSOs are also feasible at lower MEO altitudes, as shown in Figure 4.6, they are highly inclined retrograde orbits, which restrict access to the entire globe—a key requirement for SAR missions aiming for global coverage.

Figure 4.7 shows the annual variation in mean eclipse duration for Earth-orbiting satellites. The analysis considers frozen near-circular orbits at various inclinations—including sun-synchronous orbits, where both inclination and eccentricity were adjusted according to altitude. Solar ephemerides were computed assuming an initial mean local time at ascending node (MLTAN) of 18:00 for all cases. The results show that satellites in high-altitude non-sun-synchronous orbits experience significantly shorter eclipse durations compared to those in LEO. For instance, inclined orbits with $i > 45°$ exhibit eclipse durations of less than 7.25% at altitudes

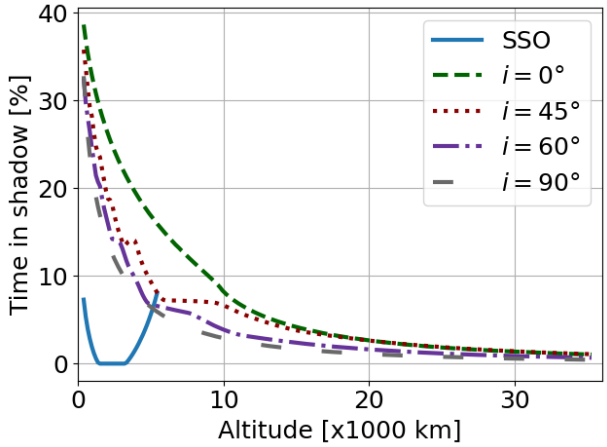

Figure 4.7: Mean eclipse duration (time spent in Earth's shadow) as a function of altitude and inclination for frozen near-circular Earth orbits, assuming an initial MLTAN of 18:00.

above 6000 km, while near-equatorial orbits maintain eclipse durations under 15% above this same altitude. These findings indicate that solar energy can be effectively harnessed for SAR missions in high Earth orbits. In lower MEO, at altitudes between 2000 km and 3500 km, near-zero eclipse durations are achievable in SSO. However, solar panels operating at these altitudes are subject to material degradation and efficiency loss due to elevated radiation exposure in the inner Van Allen belt.

4.1.4 Space Radiation Exposure

Radiation levels increase significantly with altitude, introducing additional challenges in spacecraft design. This necessitates enhanced shielding and the integration of radiation-hardened electronics to ensure mission reliability. The analysis below quantifies the impact of elevated radiation exposure by evaluating the additional shielding required to maintain the total ionizing dose[2] (TID) below a specified threshold. For reference, a nominal annual TID of 5 krad/y is assumed, representative of the radiation environment experienced by spacecraft operating in low Earth SSO with aluminum shielding in the range of 1 mm to 2 mm.

[2] The *total ionizing dose* (TID) refers to the cumulative amount of ionizing radiation energy absorbed per unit mass of a material over time, typically measured in units of rad. Specifically, $1\,\text{rad} = 0.01\,\text{J/kg} = 6.242 \times 10^{10}\,\text{MeV/kg}$. TID is often calculated over an extended exposure period, such as over the course of a year, or during the entire duration of a mission, to assess the effects on materials or components.

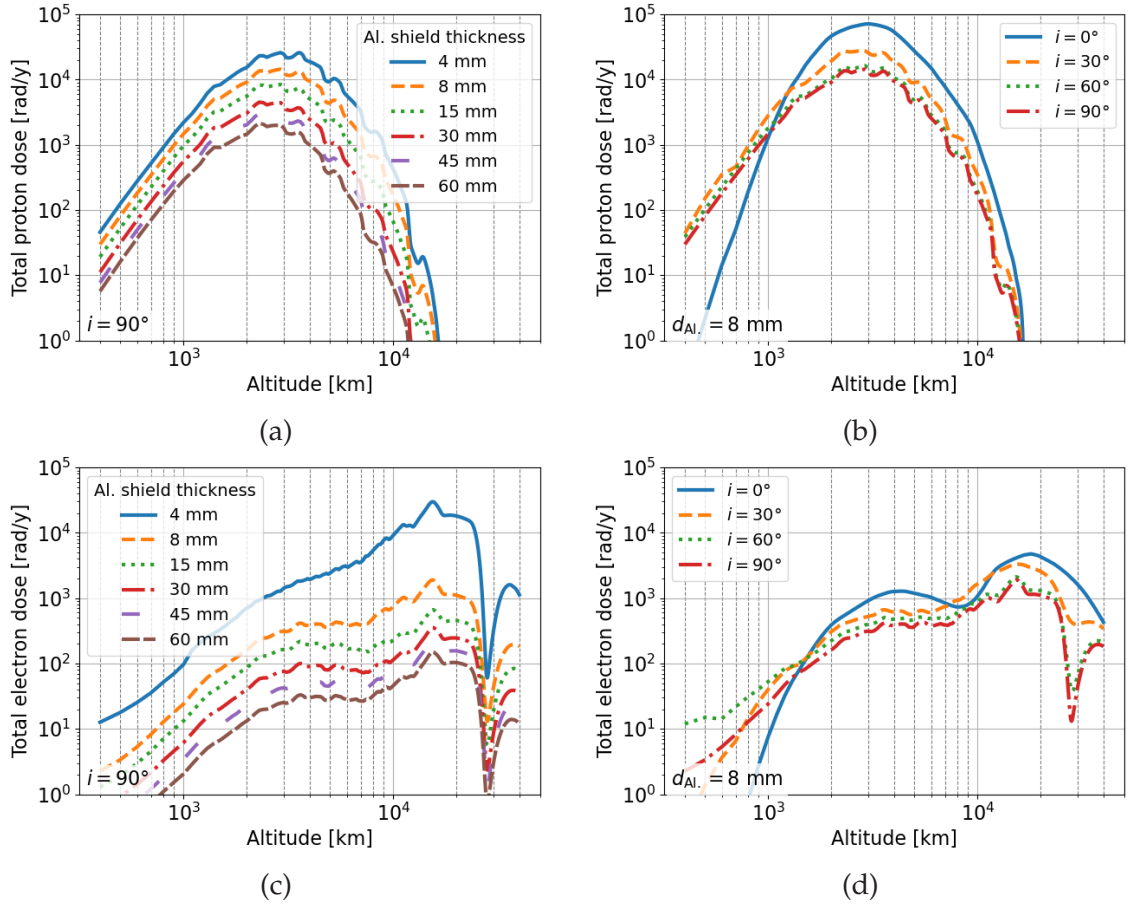

Figure 4.8: Projected total annual dose as a function of altitude, calculated using the AE9/AP9/SPM V1.58 model for near-circular orbits. Panels (a) and (b) show proton doses (with energies ranging from 0.1 to 2000 MeV) for varying shield thicknesses at 90° inclination, or a fixed 8 mm shield with varying inclinations, respectively. Panels (c) and (d) show electron doses (with energies ranging from 0.04 to 10 MeV) for varying shield thicknesses at 90° inclination, or a fixed 8 mm shield with varying inclinations, respectively.

Figure 4.8 illustrates the primary contributors to TID at higher altitudes. It shows the estimated annual dose rates from trapped protons and electrons across a range of shield thicknesses, based on simulations using the AE9/AP9/SPM v1.58 radiation models [129]. The curves show a peak at the inner Van Allen belt, centered around 3500 km, and indicate that high-energy protons are more challenging to attenuate with aluminum shielding than high-energy electrons (or lower-energy protons) [127]. At higher altitudes, where the outer Van Allen belt dominates, radiation primarily consists of high-energy electrons and ions.

As shown in Figure 4.8(a), for a polar orbit (90° inclination), increasing the aluminum shielding thickness to 8 mm reduces the proton dose to below 4.7 krad/y and the electron dose to below 0.42 krad/y at altitudes above

5500 km, with further reductions to below 3 krad/y and 0.39 krad/y, respectively, at altitudes above 5900 km. Figures 4.8(b) and (d) reveal similar altitude-dependent dose trends across various orbital inclinations for a fixed aluminum shield thickness of 8 mm. Notably, while equatorial LEO experiences relatively low radiation levels, equatorial MEO is exposed to significantly higher doses due to greater interaction with the Van Allen belts.

To quantify the mass impact of increased shielding thickness, an aluminum shield with a density of 2.7 g/cm^3 is considered for a satellite bus with dimensions 50 cm × 50 cm × 50 cm. For an 8 mm thick enclosure, the resulting shield mass is 32.4 kg. When the bus is extended to 100 cm × 50 cm × 50 cm, the shield mass increases to 54 kg. Compared to a 2 mm thick shield, this corresponds to a mass increase of 24.3 kg and 40.5 kg, respectively.

4.1.5 Launch Constraints

Reaching high Earth orbits typically involves a two-step process. Initially, the spacecraft or the upper stage of the launch vehicle is inserted into a low Earth parking orbit. Subsequently, an orbital transfer maneuver is executed to transition to the desired final orbit.

The orbital transfer requires a velocity change (ΔV) as detailed in Section 2.5. The associated ΔV requirement translates into an additional propellant mass, reducing the net payload capacity of the launch vehicle. The corresponding payload mass loss can be derived from Tsiolkovsky's equation (2.5.2) as

$$\Delta M = \frac{M_\mathrm{f}}{M_\mathrm{i}} = \exp\left(-\frac{\Delta V}{v_\mathrm{e}}\right) = \exp\left(-\frac{\Delta V}{g_0 \cdot I_\mathrm{sp}}\right), \tag{4.6}$$

where M_f is the remaining mass after the maneuver, and $M_\mathrm{i} - M_\mathrm{f} = M_\mathrm{prop}$ represents the propellant mass consumed during the transfer. The effective exhaust velocity (v_e) is expressed as the product of the specific impulse (I_sp) and the standard gravitational acceleration (g_0).

Figure 4.9 illustrates the increase in ΔV and reduction in payload capacity with altitude. Panel (a) depicts the ΔV required for coplanar transfers, specifically to adjust the semi-major axis from a reference value at an altitude of 400 km to various higher orbit altitudes. Panel (b) shows the associated reduction in mass-to-orbit capacity for different propulsion systems, characterized by their specific impulse (I_sp). The analysis includes propulsion systems with representative specific impulse values: 300 s for solid-fuel engines such as the Zefiro-9 [191], 350 s for liquid-fuel engines

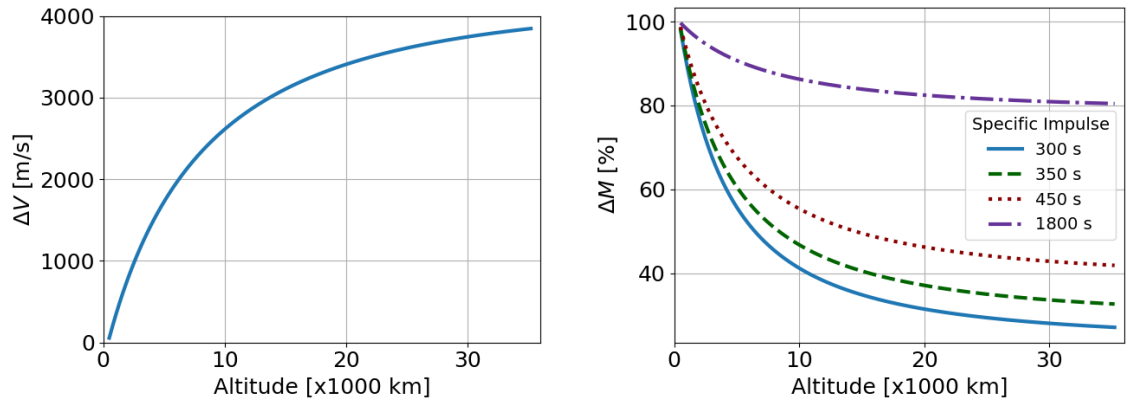

(a) (b)

Figure 4.9: (a) Required ΔV for transferring from an initial LEO at 400 km to higher orbits, and (b) corresponding reductions in mass-to-orbit capacity for various vacuum engine technologies with different I_{sp}.

like the Merlin Vacuum [133], 450 s for high-efficiency cryogenic engines such as the Vinci [192], and 1800 s for electric propulsion systems exemplified by the PPS-5000 Hall effect thrusters [193] employed in missions like OneWeb. These values span a range of technologies from conventional chemical propulsion to advanced electric propulsion engines, providing a comprehensive perspective. It is important to note that the results shown in Figure 4.9 are based on idealized conditions and do not account for secondary effects such as the added mass of propellant tanks, thrusters, or spacecraft structural reinforcements. These effects are generally mission specific and are not expected to substantially affect the conclusions.

The analysis indicates a significant reduction in payload capacity for insertions into high-altitude orbits. Specifically, transfers to MEO altitudes between 5500 km and 10 000 km, suitable for global-coverage missions, result in payload capacity losses ranging from 40% to 60% when using chemical propulsion systems with an I_{sp} of 350 s, compared to LEO insertions. In contrast, employing electric propulsion systems with an I_{sp} of 1800 s significantly mitigates these losses to approximately 10% to 14%. Additional reductions in payload capacity should be anticipated if orbital inclination adjustments are required.

While electric propulsion systems, such as ion thrusters and Hall effect thrusters, offer improved efficiency, their low thrust output results in extended transfer durations to achieve the required ΔV. Prolonged transit through Earth's radiation belts can degrade critical spacecraft components, including solar panels, necessitating design margins to mitigate the effects.

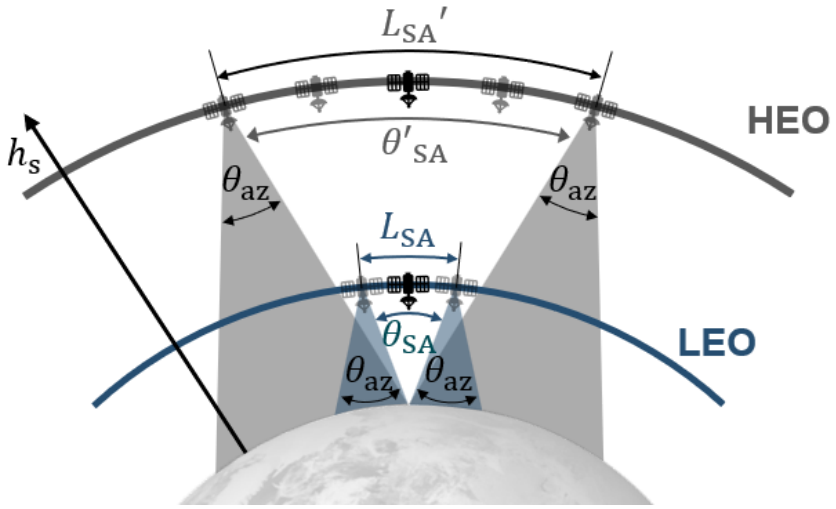

Figure 4.10: Qualitative representation of the increase in the angular extent (θ_{SA}) and corresponding length (L_{SA}) of the synthetic aperture with altitude (h_s) for a fixed antenna beamwidth (θ_{az}).

A possible approach to mitigate extended transfer duration is the integration of multiple propulsion engines, including hybrid approaches combining chemical and electric thrusters.

4.2 Emerging Aspects in SAR System Design

Increasing the orbital altitude expands the field of view, enabling increased coverage of the Earth's surface. However, this also extends the propagation path of the SAR signal, resulting in a significant reduction in system sensitivity. Nevertheless, the curved nature of Earth orbits allows for a partial recovery of the lost signal energy by exploiting the increased angular extent of the synthetic aperture, thereby significantly extending the illumination time.

4.2.1 Enhanced Azimuth Resolution

Figure 4.10 qualitatively illustrates the impact of high orbital altitudes on the angular extent of the synthetic aperture θ_{SA}. The increase in angular extent is a result of the satellite's curved orbital path, in conjunction with the typical attitude control strategies used by SAR satellites to reduce the Doppler centroid to zero, e.g, via yaw and pitch steering [194]. The figure shows that for a constant azimuth antenna beamwidth θ_{az} (corresponding

to a fixed physical antenna length L_a), θ_{SA} increases with altitude. As discussed in (3.6), this results in enhanced azimuth resolution.

The enhancement factor F_a is introduced to link the generic azimuth resolution definition in (3.6) to the widely used half-length linear-geometry approximation [195], such that

$$\delta x = \frac{\lambda}{2 \cdot \theta_{SA}} = \frac{\lambda}{2 \cdot \theta_{az}} \cdot F_a \approx \frac{L_a}{2} \cdot F_a, \tag{4.7}$$

and

$$F_a = \frac{\theta_{az}}{\theta_{SA}(a,i,e,\theta_i,\phi_{lat})} = \frac{v_g(a,i,e,\theta_i,\phi_{lat})}{v_s(a,i,e,\theta_i,\phi_{lat})}. \tag{4.8}$$

The equation shows that F_a is related to the ratio of the beam velocity to the relative satellite velocity, which under nominal attitude control, depends on the orbit geometry, SAR geometry, and the scene location (e.g., ϕ_{lat}). The relative satellite velocity (v_s) decreases with increased altitude and experiences larger variations between its minimum and maximum. The exact value of v_s depends on the suitable acquisition interval, which is influenced by θ_i and ϕ_{lat}, particularly for low-inclined orbits.

Figure 4.11 shows the variation of the factor ΔF_a (in dB) with altitude for different incident angles, orbital inclinations, and target latitudes. These results are presented relative to a reference LEO altitude of 400 km, assuming zero-Doppler steering. In the benchmark case (i =90°, θ_i =40°, ϕ_{lat} =25°), depicted by solid black lines, F_a decreases from 0.94 at 400 km to below 0.5 at MEO altitudes starting around 6000 km. As illustrated in panel (d), altitude is the predominant factor affecting F_a up to high MEO, whereas the impact of incident angle, inclination and target latitude remains relatively low. However, for prograde orbits where the target latitude approaches the orbital inclinations (e.g., $\phi_{lat} = 25°$, $\theta_i = 30°$), increased deceleration of v_s relative to v_g during the acquisition interval leads to the convex trend observed in panel (b). The influence of incident angle and target latitude on F_a, as illustrated in panels (a) and (c), becomes more pronounced at higher MEO altitudes, particularly above 15000 km. For a fixed Doppler bandwidth, this can induce variations in azimuth resolution along the SAR acquisition track.

Overall, the enhancement factor decreases significantly with increasing altitude. As indicated by (4.7), this reduction can be leveraged in two ways: (i) to improve azimuth resolution for a fixed antenna length, or (ii) to increase the antenna length while maintaining a fixed azimuth resolution. The latter approach is particularly beneficial for recovering sensitivity, as larger apertures provide higher antenna gain.

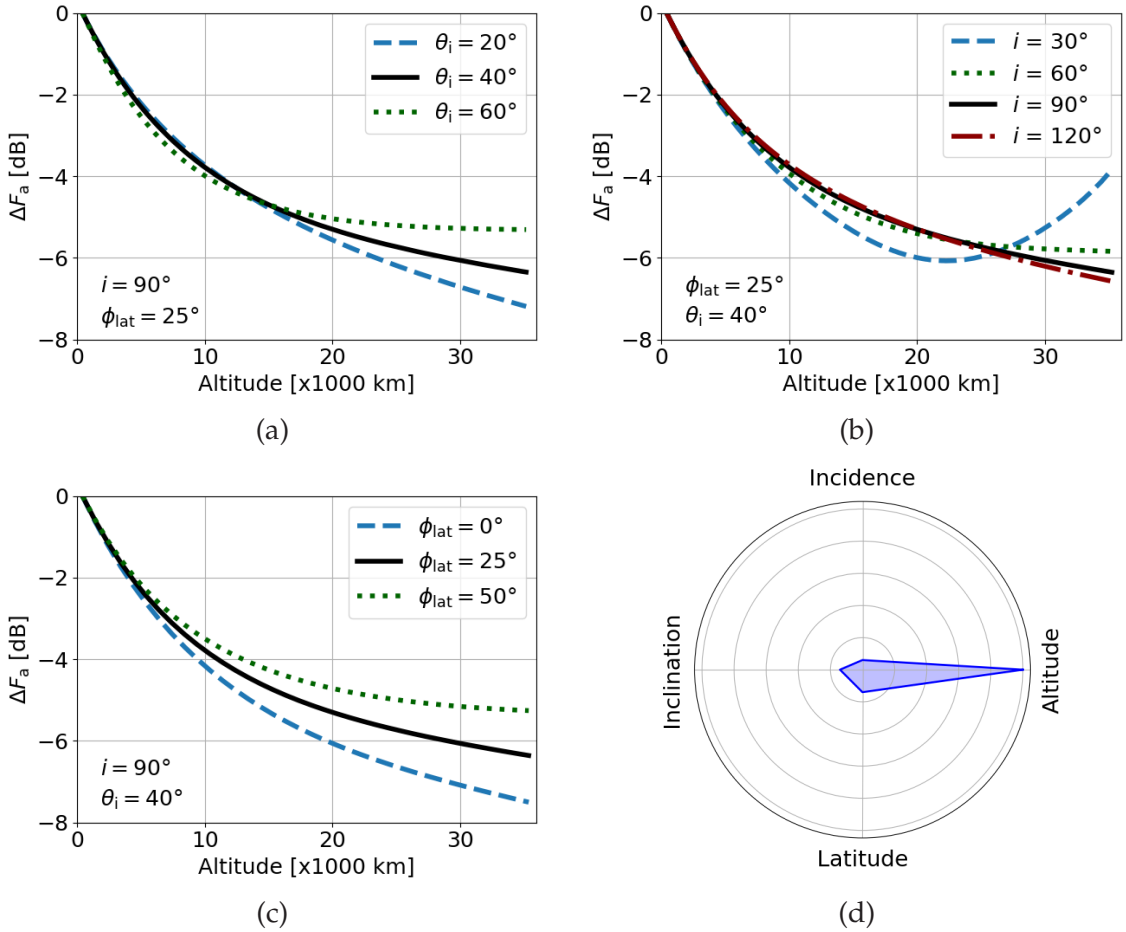

Figure 4.11: Variation of the enhancement factor (ΔF_a, in dB) with altitude for SAR in near-circular orbits under zero-Doppler steering, relative to a reference altitude of 400 km. Panels (a), (b), and (c) show the sensitivity of the enhancement factor to changes in incident angle (θ_i), orbital inclination (i), and latitude (ϕ_{lat}), respectively. Solid black lines represent a benchmark case with $i = 90°$, $\theta_i = 40°$, and $\phi_{lat} = 25°$. Panel (d) presents a radar chart (Kiviat diagram) illustrating the relative influence of altitude, incident angle, inclination, and target latitude on F_a across the combined scenarios in (a)–(c).

4.2.2 Extended Illumination Time

In terms of illumination time, (3.5) can be rewritten as

$$T_{SA} = \frac{R \cdot \theta_{SA}}{v_s} = \frac{R \cdot \theta_{az}}{v_s} \cdot \frac{1}{F_a} = \frac{R \cdot \theta_{az}}{v_g} \approx \frac{R \cdot \lambda}{L_a \cdot v_g}. \tag{4.9}$$

Figure 4.12 illustrates the variation in nominal illumination time—i.e., for zero-Doppler steering—with altitude and carrier frequency, based on the benchmark case ($i = 90°$, $\theta_i = 40°$, $\phi_{lat} = 25°$) and assuming a fixed antenna length. The ratio of T_{SA} across the three frequencies corresponds to the in-

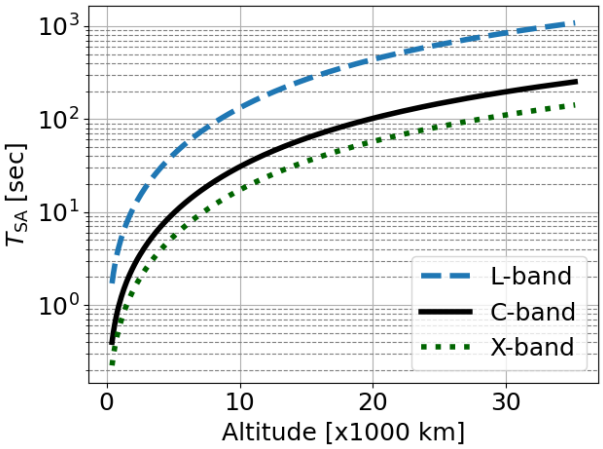

Figure 4.12: Variation in illumination time with altitude for a fixed antenna length of 10 m across different carrier frequencies. The results are based on the benchmark case illustrated in Figure 4.11 (i =90°, θ_i =40°, ϕ_{lat} =25°).

verse ratio of the frequencies. Illumination time can range from fractions of a second at LEO altitudes to several minutes, or even hours, as the orbit approaches geosynchronous altitudes. For GEO-SAR systems with continuous access to the imaged scene, illumination time can be further extended by reducing v_g through sliding or starring spotlight operation. This extension allows the recovery of imaging performance, as will be discussed in Chapter 6.

4.2.3 Antenna Constraints

The SAR antenna is a core component of the payload, significantly influencing imaging performance in terms of ambiguity suppression, resolution, sensitivity, and swath width. As outlined in Section 3.5, the antenna is also often a major contributor to spacecraft mass, volume, and overall system complexity.

A key driver of antenna size is ambiguity suppression, commonly quantified by the performance metrics AASR in (3.30) and RASR in (3.32). In basic SAR architectures, such as stripmap operation with simple antenna front-ends and no beamforming, the minimum antenna area required to achieve acceptable ambiguity levels is primarily governed by the sensor's altitude and carrier frequency.

The derivation of this minimum area begins with the requirement to adequately sample the Doppler bandwidth (B_D) using the PRF (f_p). According

to the Nyquist sampling criterion and using the Doppler bandwidth associated with the nominal azimuth resolution from (3.7) and (4.7), the PRF must satisfy

$$f_{\mathrm{p}} \geq B_{\mathrm{D}} \approx \frac{2 \cdot v_{\mathrm{s}}}{L_{\mathrm{a}}}. \tag{4.10}$$

To avoid range ambiguities, the maximum slant-range extension of the unambiguous swath within two transmitted pulses is limited by

$$W_{\mathrm{s}} \leq \frac{c}{2} \cdot \left(\frac{1}{f_{\mathrm{p}}} - 2 \cdot \tau_{\mathrm{p}} \right), \tag{4.11}$$

where τ_{p} is the pulse duration. The swath width can be approximated geometrically using the arc length formula

$$W_{\mathrm{s}} \approx W_{\mathrm{g}} \cdot \sin\theta_{\mathrm{i}} \approx R_{\mathrm{M}} \cdot \tan\theta_{\mathrm{i}} \cdot k_{\mathrm{s}} \cdot \frac{\lambda}{H_{\mathrm{a}}}, \tag{4.12}$$

where R_{M} is the slant range to the scene center, H_{a} is the antenna height, and k_{s} is a correction factor accounting for the difference between the actual antenna aperture and its approximation λ / H_{a}. By substituting (4.11) and (4.12) into (4.10), assuming a small transmit duty cycle and rearranging terms, the following expression is obtained

$$L_{\mathrm{a}} \cdot H_{\mathrm{a}} \geq \frac{4 \cdot v_{\mathrm{s}} \cdot R_{\mathrm{m}} \cdot k_{\mathrm{s}} \cdot \lambda \cdot \tan\theta_{\mathrm{i}}}{c}, \tag{4.13}$$

commonly referred to as the minimum antenna area constraint for SAR [138, 139, 196].

Figure 4.13 illustrates the relationship between the minimum antenna area, orbital altitude, and incident angle for C-band and L-band systems. The results indicate that SAR missions at higher altitudes require larger antenna apertures to maintain effective ambiguity suppression. While antenna areas exceeding $50\,\mathrm{m}^2$ may be challenging for current planar-array technologies, such apertures are achievable using reflector antennas. For instance, a 15 m-diameter parabolic reflector provides an effective area of approximately $176\,\mathrm{m}^2$, which is within the capabilities of modern deployable reflector antenna structures. However, in reflector-based architectures, uniformly illuminating large apertures often requires beamforming through the use of a feed array.

From a sensitivity perspective, requirements for higher antenna gain or extended swath coverage inherently demand larger antenna apertures. In

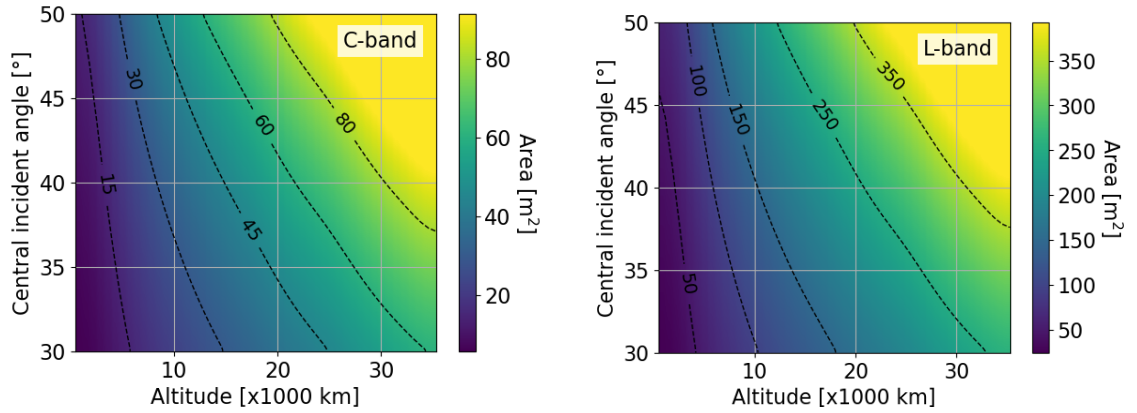

(a) (b)

Figure 4.13: Minimum antenna area, expressed in m^2, as a function of orbital altitude and incident angle for (a) C-band and (b) L-band SAR. Calculations are based on (4.13), assuming $k_s = 1$.

scenarios where broader swath widths are desired, burst imaging modes—such as ScanSAR or TOPS—can be employed to increase coverage while preserving acceptable levels of ambiguity suppression.

Nevertheless, the deployment of spaceborne antennas with diameters or lengths exceeding 25 m remains technologically challenging in the near future. Key limitations include increased mass, mechanical stability, deployment complexity, and constraints imposed by the dimensions of launch vehicle fairings [197].

4.2.4 Sensitivity and Operation Solutions

The variation in the Noise Equivalent Sigma Naught (NESN) with altitude, for a constant frequency, system bandwidth (range resolution), noise power density, and backscatter geometry (similar angles of incidence), can be derived from (3.29). The relationship is expressed in decibels (dB) as

$$\Delta\mathrm{NESN} \approx 3 \cdot \Delta R + \Delta v_s - \Delta P_{avg} - \Delta G_t - \Delta G_r. \tag{4.14}$$

In this equation, ΔR and Δv_s represent the changes in slant range and satellite velocity with altitude, respectively. The terms ΔP_{avg}, ΔG_t and ΔG_r account for any desired changes in average transmit power, transmit gain, and receive gain, respectively. All factors in (4.14) are given in dB relative to a reference orbital altitude (e.g., LEO).

To express (4.14) in purely geometrical terms, it is assumed that for a monostatic system—where the same antenna is used for both transmission and

reception, without employing digital beamforming—the change in gain is proportional to the change in antenna area, as indicated in (3.59). Therefore,

$$\Delta G_\mathrm{t} = \Delta G_\mathrm{r} \approx \Delta L_\mathrm{a} + \Delta H_\mathrm{a}, \tag{4.15}$$

where ΔL_a and ΔH_a denote the change in antenna length and height, respectively. The change in antenna height (ΔH_a) can be linked to the change in swath width (ΔW_g) in terms of the required change in elevation beamwidth ($\Delta\theta_\mathrm{el}$) from (4.4) by

$$\Delta H_\mathrm{a} = \Delta R + \Delta\theta_\mathrm{el} \approx \Delta R - \Delta W_\mathrm{g}. \tag{4.16}$$

To maintain a constant azimuth resolution ($\Delta\delta x = 0\,\mathrm{dB}$) at higher altitudes, longer antennas can be used according to (4.7), resulting in an increase in antenna gain. Hence, ΔL_a can be substituted with $-\Delta F_\mathrm{a}$. However, at higher altitudes, the potential for growth in antenna size may be limited by technological constraints.

Assuming constant resolution, and considering the increase in antenna surface according to (4.7) and (4.16), (4.14) translates to

$$\Delta\mathrm{NESN} \approx \Delta R + \Delta v_\mathrm{s} + 2\cdot\Delta F_\mathrm{a} + 2\cdot\Delta W_\mathrm{g} - \Delta P_\mathrm{avg}. \tag{4.17}$$

The factors Δv_s and $2\cdot\Delta F_\mathrm{a}$, both negative, partially compensate for the worsening in the NESN caused by ΔR and $2\cdot\Delta W_\mathrm{g}$ at higher orbital altitudes. Following the discussion above, two possible concepts emerge for operating high-orbit SAR systems:

A. a LEO-like swath width (i.e., $\Delta W_\mathrm{g} = 0\,\mathrm{dB}$) and LEO-like resolution with a broader accessible swath and an increase in average transmit power when needed; and

B. an extended swath width (i.e., $\Delta W_\mathrm{g} > 0\,\mathrm{dB}$) with moderate resolution, potentially covering the entire accessible swath. The reduced resolution helps bring sensitivity to acceptable values.

The benefits of the second operation concept are more substantial than those of the first when compared to both current and future LEO-SAR counterparts. Furthermore, if the system designed for the second concept incorporates beamforming in elevation, it can be readily adapted to cover narrower swaths within the access area with higher resolution as in concept (A). This adaptation allows to regain sensitivity by focusing the available energy on a smaller area.

In scenarios where extended access to the imaged scene is available—such is the case for SAR systems in low-inclination geosynchronous orbits—an

alternative approach can be employed to recover performance at the expense of a reduced coverage rate. This approach involves extending the illumination time beyond that achievable with nominal zero-Doppler steering. The additional samples acquired during the extended illumination period enable the averaging of statistically independent looks during processing, which can improve imaging performance. For example, it can enhance radiometric quality by effectively reducing speckle noise, and improve interferometric phase accuracy by reducing decorrelation noise in interferograms. Such an extension in illumination time can be implemented using sliding or starring spotlight modes, in which the beam's ground velocity is deliberately reduced to accommodate the required increase in illumination duration. This approach is examined in more detail in Chapter 6.

The implications of concepts (A) and (B) for the SAR instrument are elaborated below.

Concept A: Small Swaths, Great Access

In this concept, the swath width is fixed to LEO-like values (i.e., $\Delta W_g = 0\,\mathrm{dB}$), while benefiting from the broad access area and more frequent revisit enabled by higher altitudes for a fixed range of incident angles. This mode is particularly well suited for event-triggered applications, such as monitoring natural or anthropogenic disasters, or supporting reconnaissance operations.

Figure 4.14 illustrates the variation in NESN with altitude, evaluated for a constant average transmit power (i.e., $\Delta P_{\mathrm{avg}} = 0\,\mathrm{dB}$) and an incident angle of 40°, for different orbital inclinations and target latitudes, in comparison to a reference LEO at 400 km. A quick analysis of the results indicates that maintaining a LEO-like swath width results in a moderate degradation in sensitivity, which can be compensated by increasing the transmit power. Furthermore, the results show that operating at orbital altitudes beyond 4000 km allows the natural reduction in relative spacecraft velocity and the possible use of larger antennas (for $\Delta\delta x = 0\,\mathrm{dB}$) to counteract the additional increase in free-space loss.

The corresponding increase in antenna length is inversely proportional to the enhancement factor shown in Figure 4.11. For example, achieving an azimuth resolution of 5 m from an altitude of 400 km allows for the efficient use of a 10-m long antenna. However, the same resolution at altitudes beyond 15 000 km would require spaceborne antennas longer than 25 m, assuming optimal imaging efficiency and gain utilization. This poses significant challenges with current technology.

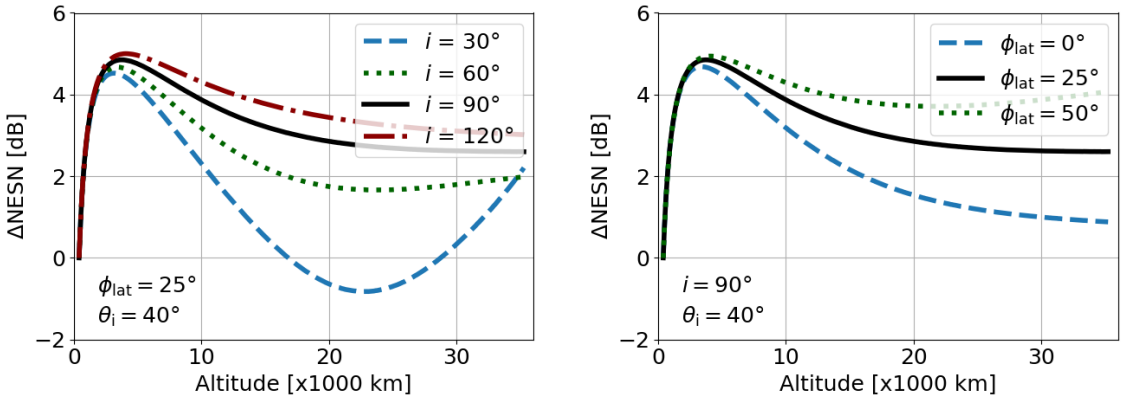

Figure 4.14: Variation in the NESN with altitude for a fixed swath width (ΔW_g =0 dB) and average transmit power (ΔP_{avg} =0 dB), considering an inherent increase in antenna length ($\Delta L_a = -\Delta F_a$) and height, relative to a reference altitude of 400 km. Panel (a) shows the variation for different orbital inclinations, while Panel (b) depicts the variation for different target latitudes. Both panels assume an incident angle of 40°. The solid black lines represent the reference case with i =90°, θ_i =40°, and ϕ_{lat} =25°.

If practical constraints limit antenna growth—i.e., if the antenna length is not scaled proportionally with the enhancement factor ΔF_a—then the term $2 \cdot \Delta F_a$ in (4.17) must be substituted by $-2 \cdot \Delta L_a$, resulting in an additional sensitivity loss. It is important to note, however, that this loss is accompanied by an improvement in azimuth resolution, offering a potential trade-off depending on mission objectives.

Concept B: Larger Swaths, Moderate Resolutions

In this concept, the swath width increases with altitude (i.e., $\Delta W_g > 0$ dB), potentially enabling coverage of the entire accessible swath with moderate spatial resolution. This approach offers significant advantages for a wide range of scientific applications that benefit from increased coverage rates and frequent recurring acquisitions, thereby supporting the generation of SAR data capable of addressing the spatio-temporal Earth observation gap that motivates this thesis.

Figure 4.15 illustrates the variation in NESN with altitude, expressed relative to a reference LEO configuration at 400 km altitude. The analysis is conducted under two different assumptions: constant average transmit power (panels a and b) and constant surface irradiance[3] (panels c and d). The evaluation considers increasing swath widths corresponding to a fixed

[3] *Irradiance* refers to the electromagnetic power received per unit surface area, expressed in W/m^2.

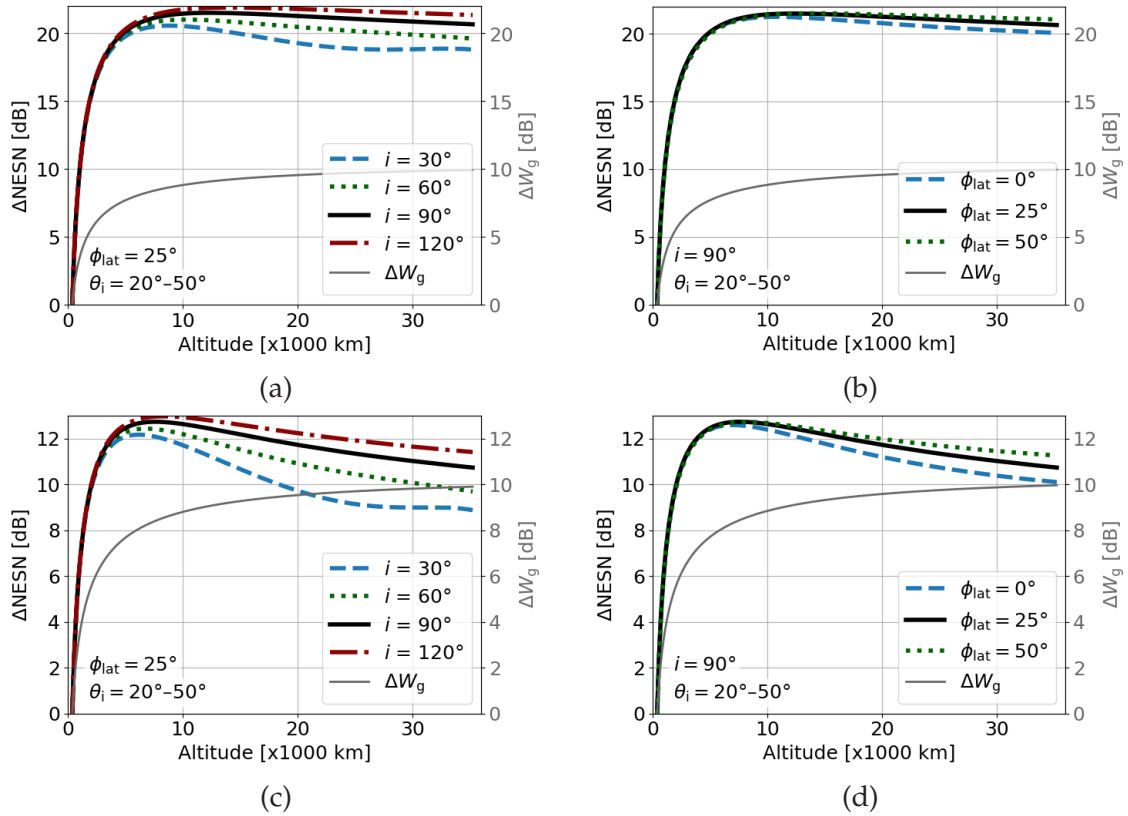

Figure 4.15: Variation in the NESN with altitude for a fixed incident-angle range and increasing swath, relative to a reference altitude of 400 km. Panels (a) and (b) present results assuming constant average transmit power, evaluated across different orbital inclinations and target latitudes, respectively. Panels (c) and (d) show the corresponding results under the assumption of constant surface irradiance. The gray curve (referenced to the right vertical axis) indicates the increase in swath width (ΔW_g) with altitude, corresponding to a fixed incident-angle range of 20° to 50°.

incident-angle range of 20° to 50°, and includes variations in orbital inclination and target latitude.

For example, the swath width increases from approximately 420 km at an altitude of 600 km to 1880 km at a MEO altitude of 6000 km, corresponding to an increase of about 6.5 dB. This increase in swath width leads to a sensitivity loss of approximately 16 dB, if the average transmit power is maintained constant.

To provide a fair comparison between wide-swath, high-altitude systems and narrow-swath LEO systems, panels (c) and (d) in Figure 4.15 illustrate the corresponding NESN variation under the assumption of constant surface irradiance—i.e., constant average transmit power per resolution cell.

This assumption reduces the sensitivity loss by a factor of $-\Delta W_g$ to approximately 9.5 dB for the same example. Additionally, since the PRF varies with altitude according to

$$\Delta f_p = \Delta v_s - \Delta L_a, \tag{4.18}$$

maintaining constant peak transmit power under the constant average transmit power assumption requires a corresponding adjustment to the chirp duration.

4.2.5 Design Trade-off Summary

The analysis presented in the previous section highlights that high-altitude SAR systems offer an expanded access area but experience a significant sensitivity loss.

For a high-orbit-SAR system to operate with high resolution over swaths comparable to those of LEO systems (concept A)—a valuable feature for applications such as disaster monitoring—the sensitivity loss is relatively minor at low MEO altitudes (below 15 000 km) and can be effectively mitigated by increasing the transmit power. However, beyond this altitude, any changes in sensitivity are generally associated with a growth in antenna length, which is likely constrained by available technology (e.g., reflector antennas around 25 m in diameter).

Alternatively, if a high-orbit-SAR system is designed to cover at full resolution a wide swath close to its access area (concept B), it will experience a more pronounced sensitivity loss. This can be compensated for by increasing transmitted power or reducing resolution. Typical average transmit power values are in the order of a few kilowatts. Notably, range resolution is somewhat coupled to azimuth resolution from a design perspective; a reduction in range resolution by a factor of two generally results in a sensitivity improvement of around 3 dB. However, gains in azimuth resolution are limited by antenna lengths, which remains constrained by existing technology.

Further possibilities to enhance the power budget include using higher antennas to illuminate different portions of the swath during transmission or reception. Techniques that implement this concept include burst operation modes such as ScanSAR and TOPS, or multi-beam antenna technologies (e.g, [148, 149, 198]). Receive-side approaches include systems with SCan-On-REceive (SCORE) or SweepSAR capabilities (e.g., [61, 199–201]).

4.3 Chapter Remarks

This chapter presented the key design considerations for SAR missions at higher altitudes, addressing a critical gap in the available literature. It examined fundamental trade-offs in mission design across SAR payload, platform, orbital configuration, radiation environment, and launch approach, highlighting both challenges and opportunities.

Section 4.1 demonstrated that high Earth orbits offer superior coverage capabilities, enabling single-satellite systems to achieve short global revisits from moderate MEO altitudes (3000 km to 10 000 km), and more frequent or even persistent coverage over large regions from higher MEO up to GEO. The analysis showed that transitioning from near-polar LEOs to less-inclined, higher-altitude orbits can maintain coverage advantages due to reduced Earth proximity. The radiation environment assessment indicated that operations above 5500 km are feasible with moderate shielding, e.g., 8 mm of aluminum, and radiation hardened electronics. Additionally, the section quantified payload mass penalties associated with direct high-altitude insertions and identified electric propulsion as a viable means to mitigate increased launch costs.

Section 4.2 investigated the consequences of increased coverage on SAR payload performance, revealing that sensitivity reduction can be partially compensated by leveraging the larger angular extent of the synthetic aperture at higher altitudes. Achieving full performance, however, requires enhancements such as larger antennas, higher transmit power, beamforming-capable hardware, or reduced resolution. Two operational concepts for high-altitude SAR systems were proposed: (A) a LEO-like swath width and resolution with frequent global or large-area access, or (B) extended swath coverage—potentially spanning the entire accessible area—at moderate resolution. The section also detailed the corresponding payload requirements for each concept, including antenna size, transmit power, and onboard beamforming capabilities needed to meet mission objectives. A distinct operational concept emerges for GEO-SAR systems, where continuous access to the imaged scene is possible. In such cases, reduced sensitivity can be accommodated by extending the illumination time through the use of sliding or starring spotlight modes. This approach enhances image quality through noise averaging, albeit at the expense of reduced coverage rates.

Overall, the findings indicate that although high-altitude SAR systems present challenges—such as reduced launch vehicle payload capacity and increased spacecraft mass due to larger antennas, enhanced radiation

shielding, and possibly augmented power systems to support higher transmit power—these factors are unlikely to pose fundamental limitations. Continued advancements in launch technologies, particularly in reusability, along with the growing maturity of electric propulsion systems, further support the feasibility of such missions in the future.

The enhanced latitude reach of inclined orbits, as discussed in Section 4.1.2, unlocks the potential for single-satellite systems to provide global true 3-D deformation mapping with frequent revisit. This unique capability, along with other MEO-specific opportunities, will be further explored in Chapter 5. Additionally, design trade-offs for SAR systems operating at low-MEO, high-MEO, and GEO altitudes will be illustrated through example mission concepts in Chapters 5 and 6.

5 MEO SAR: Mission Design

Medium Earth Orbits (MEOs) occupy the region between LEOs and GEOs, spanning altitudes from approximately 2000 km to 35786 km above Earth's surface. These orbits offer an effective balance between coverage capability and signal sensitivity, which led to their increased adoption during the 1970s and 1980s, particularly for navigation systems such as the Global Positioning System (GPS).

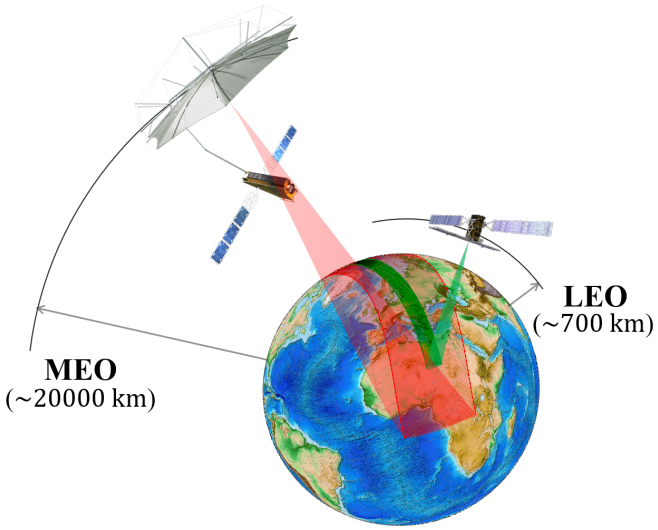

Figure 5.1: Visualization of the extended field of view of a MEO-SAR system at 20000 km compared to a LEO-SAR system at 700 km. The green and red access areas correspond to a fixed incident-angle range of 20° to 60°.

This chapter explores the strategic advantages of MEO for SAR missions, exploiting their expanded spatial accessibility compared to LEO, as depicted in Figure 5.1. It builds upon the foundational investigations in Chapter 4 to identify new MEO-enabled applications and develop exemplary mission concepts for selected use cases.

Section 5.1 introduces novel opportunities uniquely enabled by MEO, including high-frequency revisit capabilities, improved access from lower-inclination orbits, and distinctive acquisition geometries that enable true

3-D ground deformation monitoring using single SAR systems. These opportunities are further substantiated through two representative mission concepts in Section 5.2. The first concept aims at providing global coverage and 3-D deformation mapping capabilities from an altitude of 5952 km, achieving a 1.5-day revisit interval. The second focuses on continental-scale observation from 20 181 km, enabling sub-daily revisit intervals across extensive regions of Europe.

The new opportunities and mission concepts outlined in this chapter constitute a key contribution of this thesis. The two mission concepts are further analyzed in Chapter 7, where their complexity is assessed by comparing them to equivalent LEO-SAR constellations. Portions of the material presented here have been published in [189, 202].

5.1 New Opportunities

This section delves into the details of the key products enabled by MEO, as identified in Chapter 4, and introduces new opportunities enabled by single MEO-SAR systems. These include the capability of true 3-D displacement measurement on a global scale, frequent global accessibility, and the potential for sub-daily local or continental coverage.

5.1.1 Large-Scale True 3-D Deformation Measurement

Accurate 3-D deformation measurements are essential for monitoring natural hazards, including surface displacement caused by active tectonics, volcanic activity, landslides, and the movement of glaciers and ice sheets. SAR systems facilitate these measurements on a large scale using D-InSAR techniques, achieving displacement precision at the centimeter to millimeter level, as discussed in Section 3.3.

Current state-of-the-art LEO-SAR systems, including TanDEM-X [28, 29], TerraSAR-X [27], Sentinel-1 [203], and CosmoSkymed [25], provide data suitable for high-precision line-of-sight (LoS) displacement measurements. However, their near-polar orbits, designed for global coverage and sun-synchronous operation, limit their sensitivity to the North-South component of displacement, posing a significant challenge for obtaining true 3-D deformation measurements. Addressing this limitation requires additional geometric diversity in the LoS vectors. One approach is deploying satellites in less inclined orbits, which improves North-South sensitivity but restricts accessibility to higher latitudes (e.g., above 50°). This trade-off is a notable

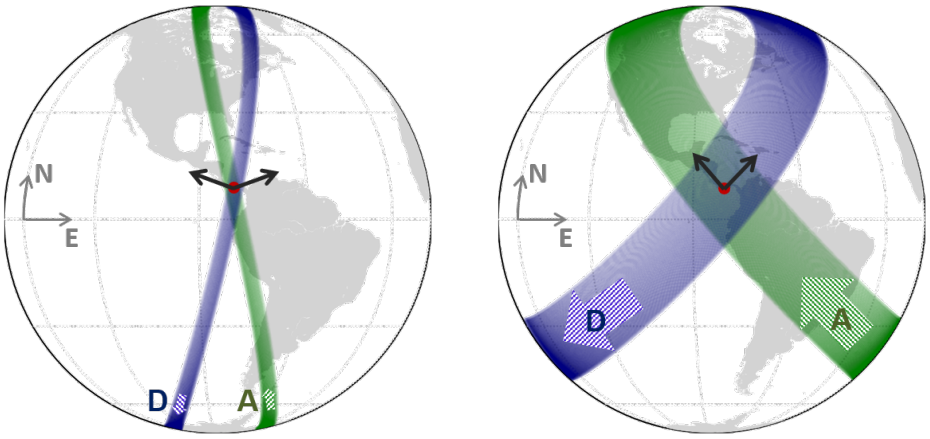

(a) (b)

Figure 5.2: Ground-projected LoS vectors, shown as black arrows, for acquisitions from two orbital configurations: (a) a sun-synchronous near-polar LEO at approximately 700 km, and (b) a moderately inclined repeat MEO at approximately 6000 km. The green (labeled A) and blue (labeled D) swaths correspond to the ascending and descending right-looking satellite passes, respectively.

drawback for single-satellite LEO-SAR missions. Alternatively, deploying additional satellites with complementary viewing geometries—for example, as proposed in the Earth Explorer 10 Harmony mission, which plans to add two companion satellites to Sentinel-1D [60]—can help overcome these challenges while maintaining global access.

Medium Earth orbits enable a flexible trade-off among LoS diversity, ground accessibility, and energy efficiency through careful design of orbital inclination. For instance, a MEO-SAR system operating in 60° inclined orbits can achieve near-global accessibility at altitudes above 6000 km, as shown in Figure 4.4. These orbits also offer favorable conditions for power generation, with eclipse durations remaining below 7%, as illustrated in Figure 4.7. Figure 5.2 demonstrates how increased orbital inclination can be utilized to provide distinct observation geometries between ascending and descending satellite passes. The figure compares the ground-projected LoS vectors for acquisitions from two orbit configurations: (a) a sun-synchronous near-polar LEO at 700 km, and (b) a moderately inclined MEO at around 6000 km. In the LEO case, the LoS vectors are predominantly along the East-West direction, resulting in limited sensitivity to North-South displacements. In contrast, the MEO case provides a more balanced observation geometry, with LoS projections exhibiting comparable sensitivity for the North-South and East-West components. This improved symmetry enhances the capability for accurate 3-D ground displacement measurements.

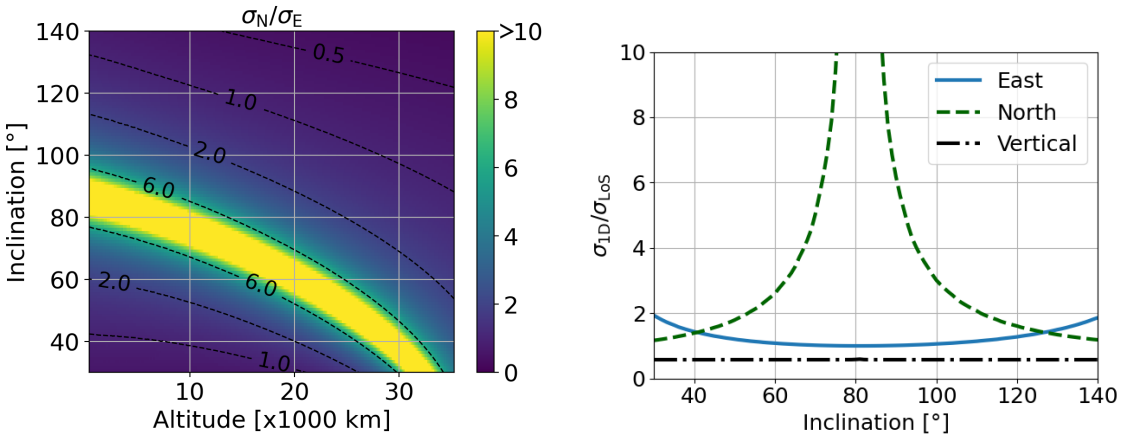

(a) (b)

Figure 5.3: Variation in 3-D displacement accuracy with altitude and inclination. (a) Ratio of North-to-East accuracy (σ_N/σ_E) for different altitudes and inclinations, showing near-equal accuracy at moderate prograde and retrograde inclinations. (b) Distribution of absolute accuracy for the East, North, and Vertical displacement components of a MEO-SAR system at 6000 km, presented as the ratio of displacement accuracy along each of the three components (σ_{1D}) to that of the LoS (σ_{LoS}). Results were derived using (3.20) for equatorial targets observed at 30° incidence, incorporating four distinct acquisition geometries corresponding to ascending and descending satellite passes in both left- and right-looking geometries.

The impact of altitude and inclination on displacement accuracy is further analyzed in Figure 5.3. Panel (a) shows the accuracy ratio in Northward to Eastward displacement as a function of orbital altitude and inclination. The results indicate that MEO altitudes combined with moderate inclinations yield near-unity ratios, signifying balanced deformation accuracy in both directions. Panel (b) shows the individual accuracy of the three displacement components (East, North, and Vertical) for a MEO-SAR system at 6000 km. The plot highlights convergence regions around inclinations of 41° and 126°, where all three components achieve comparable accuracy. In contrast, reduced Northward accuracy is observed in regions where the ground-projected LoS vectors are predominantly aligned along longitudinal (East-West) directions. These results were derived using (3.20) for equatorial targets observed at 30° incidence, incorporating four distinct acquisition geometries corresponding to ascending and descending satellite passes in both left- and right-looking geometries.

5.1.2 Frequent Global Access

The enhanced coverage capabilities of high-altitude systems, as discussed in Chapter 4, indicate that moderate MEO altitudes outperform LEO in

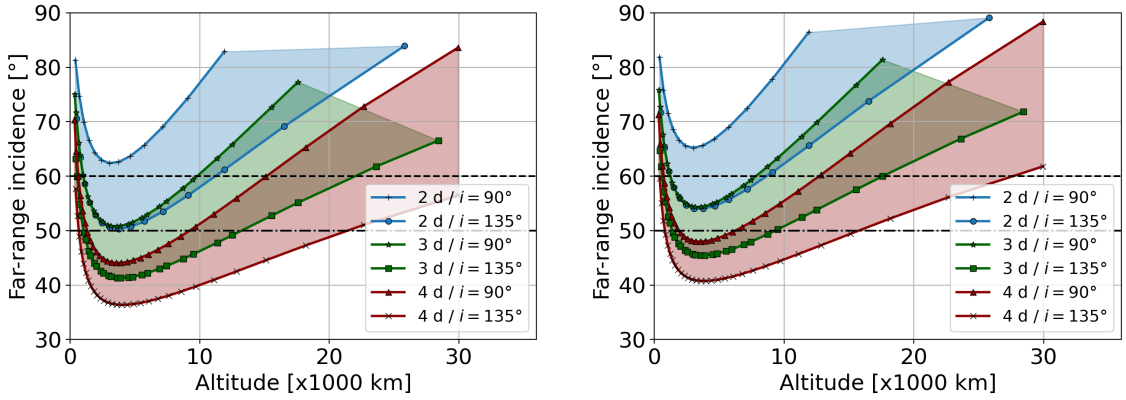

(a) (b)

Figure 5.4: Required far-range incident angles for gap-free equatorial coverage in single-pass geometry, assuming (a) a near-range incident angle of 20° and (b) 25°, for various orbital altitudes and inclinations. The dashed horizontal lines corresponds to far-range incident angles of 50° and 60°.

terms of access and coverage rates. This suggests that global accessibility and coverage can be achieved with shorter revisit times from MEO.

To assess potential revisit frequencies, repeat-ground-track (RGT) orbits with revisit periods of a few days are considered. The analysis calculates the optimal incident-angle range necessary to achieve complete equatorial coverage in a single-pass geometry (i.e., ascending or descending passes) across various orbital altitudes and inclinations. Figure 5.4 illustrates the far-range incident angle required for gap-free equatorial coverage from RGT orbits with 2-, 3-, and 4-day repeat cycles, assuming a near-range incident angle of (a) 20° and (b) 25°. The plotted symbols represent all possible RGT orbits, while the shaded regions correspond to orbital inclinations between 90° and 135°.

The results indicate that achieving gap-free equatorial coverage at a maximum far-range incident angle of 50° requires RGT MEOs with a repeat cycle of at least three days. A near-incident angle of 20° enables inclined orbits with favorable LoS geometries—up to 135°—to maintain gap-free coverage. However, increasing the near-incident angle to 25° restricts gap-free coverage to near-polar MEO configurations. If the SAR application permits a shallower far-range incident angle of 55°, two-day RGT MEOs can achieve gap-free equatorial coverage.

The average revisit time at the equator is half the repeat cycle, as both ascending and descending passes contribute to coverage. At higher latitudes, increased overlap between satellite passes further enhances revisit frequency. However, for InSAR measurements, maintaining an identical

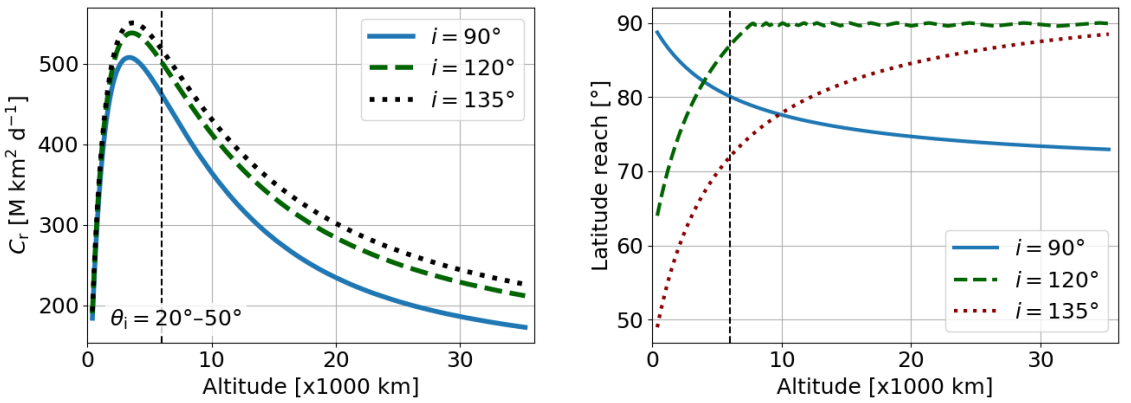

Figure 5.5: (a) Daily coverage rates in Mkm^2/d ("M" denotes million and "d" denotes day) for a swath covering the incident-angle range of 20° to 50°, and (b) latitude reach, shown across various orbital altitudes and inclinations. The values in (a) are based on a 100% orbit duty cycle and can be scaled proportionally. The vertical dashed lines mark an altitude of 6000 km.

observation geometry is essential; thus, the effective interferometric revisit cycle for a single SAR system is limited to the repeat cycle.

These results are based on retrograde orbits ($90° < i < 135°$) to benefit from Earth's rotation. While prograde orbits offer lower launch costs, they result in lower relative velocities, which negatively impact coverage rate and revisit frequency. The analysis also assumes single-satellite systems; however, as in LEO, MEO constellations can be employed to further reduce revisit times—potentially enabling global daily or sub-daily coverage.

In terms of coverage, Figure 5.5 illustrates the variation in daily coverage rate as a function of altitude and inclination, assuming 100% orbit duty cycle and a swath covering the incident-angle range of 20° to 50°. Higher retrograde inclinations slightly enhance the coverage rate due to increased ground velocity. However, moderate incident-angle ranges of interest for SAR missions (e.g., 20° to 50°) can limit access to polar latitudes at such inclinations. Extending latitude reach may require shallower far-range incident angles, particularly for high-inclination retrograde orbits. The vertical dashed line represents a mean altitude of interest for global MEO-SAR missions. This altitude minimizes radiation exposure, as discussed in Section 4.1.4, provides superior coverage rates, and achieves sufficient latitude reach for inclinations relevant to InSAR missions capable of true 3-D displacement measurement on a near-global scale. While increasing the altitude—for example, to 10 000 km—enhances polar reach, it introduces trade-offs, including more significant sensitivity loss and a reduction in coverage rate by a factor of 0.8.

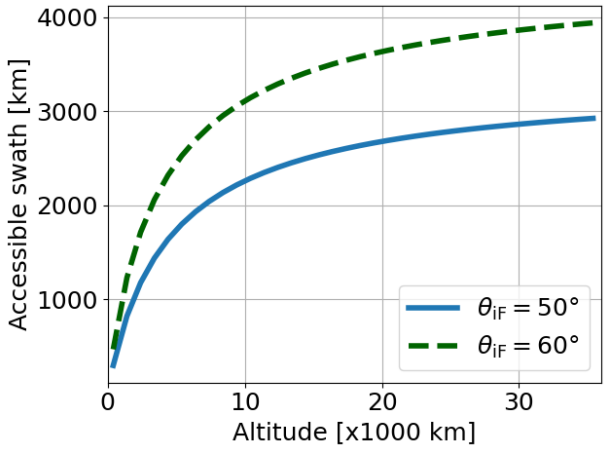

Figure 5.6: Increase in the instantaneous accessible swath with altitude for a fixed near-range incident angle of 20° and far-range incident angles of 50° and 60°.

5.1.3 Large-Scale Sub-Daily Revisit

Sub-daily revisit capabilities are essential for monitoring diurnal cycles. They require frequent overlapping passes of SAR sensors over the regions of interest. These capabilities can be achieved by leveraging orbital mechanics, such as the overlap of ascending and descending passes or the natural orbit convergence at higher latitudes for near-polar inclinations. Alternatively, deploying a satellite constellation enhances revisit frequency by increasing spatial and temporal coverage.

Single LEO-SAR systems, with their limited instantaneous accessibility (on the order of a few hundred kilometers for state-of-the-art and next-generation systems), are constrained in their interferometric revisit capability. However, they can achieve opportunistic non-interferometric frequent revisits within narrow latitude bands. These bands depend on the selected orbital inclination, which strongly influences the spatial distribution and overlap of orbital tracks. Extending frequent revisit capabilities to larger regions, such as countries or continents, typically requires a constellation of LEO satellites to overcome the limitations of single-satellite overlap. Similarly, increasing interferometric revisit frequency generally requires a constellation of LEO satellites distributed within the same orbital plane, with offsets in the longitude of the ascending node and the mean anomaly, as demonstrated by Sentinel-1A and Sentinel-1C.

Albeit their relatively lower daily coverage rates, high-altitude MEOs provide significantly wider instantaneous access, making them suitable for SAR missions targeting frequent revisits over extended regions. Figure 5.6 depicts the increase in instantaneous accessible swath width with altitude for two ranges of incident angles: [20° to 50°] and [20° to 60°].

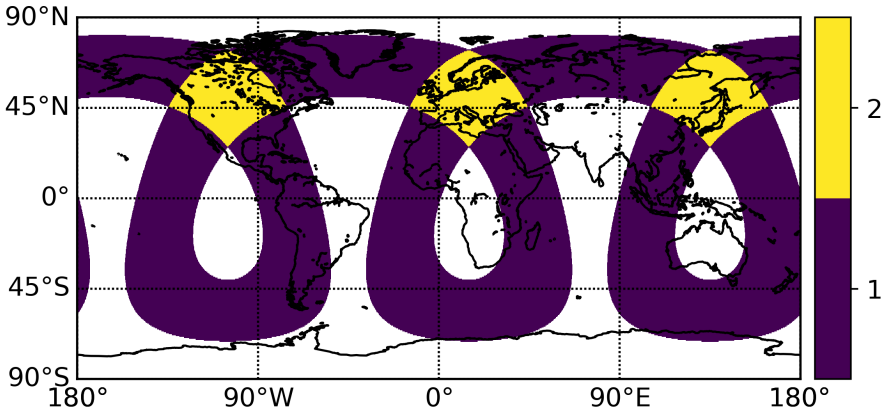

Figure 5.7: Potential daily coverage frequency map for a 1/3 RGT MEO satellite at 13 890 km altitude and 85° inclination. The swath spans an incident-angle range of 20° to 60° and is captured with a left-looking imaging geometry.

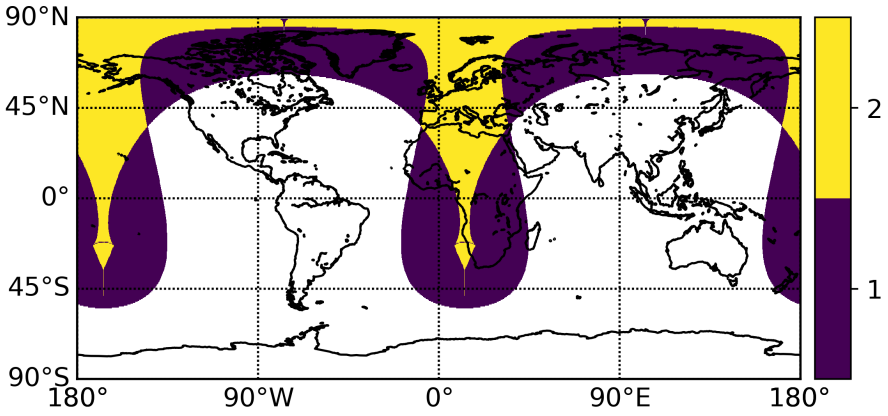

Figure 5.8: Potential daily coverage frequency map for a 1/2 RGT MEO satellite at 20 181 km altitude and 70° inclination. The swath spans an incident-angle range of 20° to 60° and is captured with a left-looking imaging geometry.

The wide-area coverage capabilities of MEO-SAR systems enable daily interferometric measurements over large regions. With optimized coverage strategies—including careful selection of orbital inclination, longitude of the ascending node, and incident angles—sub-daily non-interferometric monitoring of large areas can also be achieved. Figures 5.7 and 5.8 present coverage maps for two MEO configurations employing circular RGT orbits with 1-day repeat cycles.

The potential to revisit significant portions of Europe twice daily is demonstrated, utilizing both ascending and descending orbital passes within an incident-angle range of 20° to 60°. If the satellite is capable of alternating between left- and right-looking imaging geometries, the 1/3 RGT MEO satellite, as shown in Figure 5.7, can provide an additional acquisition over Europe, increasing the revisit frequency to three times per day.

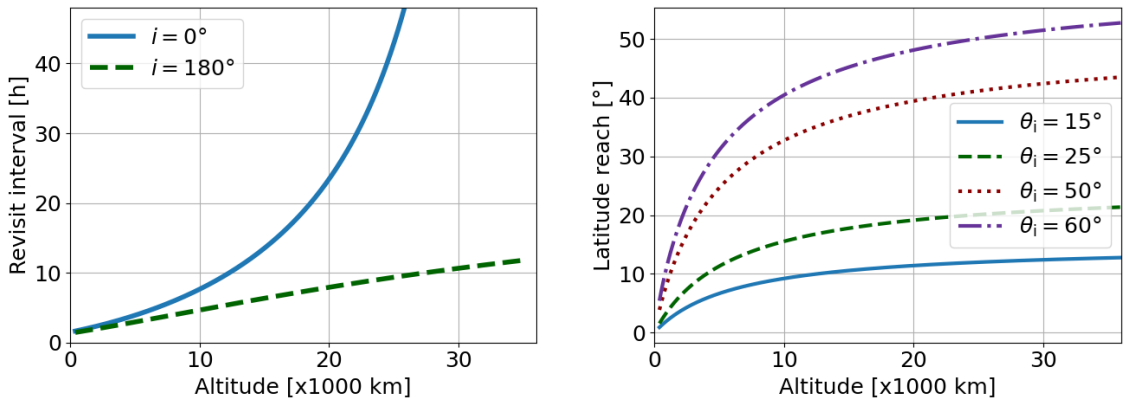

(a) (b)

Figure 5.9: (a) Revisit intervals achievable with circular equatorial Earth orbits at varying altitudes, illustrating prograde motion (i =0°) and retrograde motion (i =1800°), and (b) latitude reach as a function of altitude for various incident angles from Figure 4.5.

5.1.4 Sub-daily Interferometry from Equatorial MEO

The potential of equatorial orbits for frequent interferometric revisit was briefly introduced in Section 4.1.2. Figure 4.5, reproduced as Figure 5.9(b), illustrates the enhanced latitude reach enabled by equatorial MEOs. These orbits support coverage of higher latitudes, for example, up to approximately ±30° to 50° at an incident angle of 60°.

The interferometric revisit frequency in hours can be expressed as

$$f_{\text{rev}} = \frac{\omega_{\text{E}}}{n_0 \mp \omega_{\text{E}}} \cdot \frac{T_{\text{sidereal}}}{3600}, \tag{5.1}$$

where ω_{E} is the Earth's angular velocity, n_0 is the satellite's mean motion as defined in (2.2), and T_{sidereal} is the duration of a sidereal day in s. The sign in the denominator accounts for the motion type: $(-)$ corresponds to prograde motion (i =0°), while addition $(+)$ corresponds to a retrograde motion (i =180°). Figure 5.9(a) illustrates the achievable interferometric revisit intervals for equatorial orbits at varying altitudes. While retrograde orbits offer significantly shorter revisit intervals due to the increased relative velocity of the satellite, they incur considerably higher launch costs. Selecting an optimal altitude for an equatorial MEO-SAR mission involves a trade-off between minimizing revisit intervals and maximizing latitude coverage. Figure 5.10 shows the possible coverage of an equatorial orbit at 8035 km altitude, using left- and right-looking geometries. The resulting

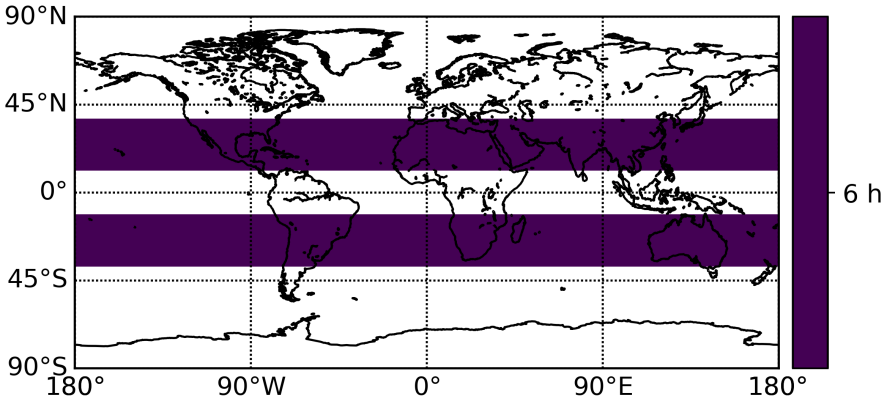

Figure 5.10: Potential coverage frequency map—or average revisit time, in hours—for a prograde equatorial MEO satellite at 8035 km. The swath spans an incident-angle range of 20° to 60° and is shown for left-looking (northern hemisphere) and right-looking (southern hemisphere) imaging geometries.

coverage areas are shown over the northern and southern hemispheres, respectively. The achievable interferometric revisit time for any target along the covered stripes is 6 hours.

5.2 Exemplary MEO-SAR Missions

This section presents two exemplary MEO-SAR missions using the information presented in the previous sections. These mission concepts provide realistic estimates of achievable SAR products while assessing the complexity of spacecraft design, with a focus on the SAR payload (antenna and electronics) and specific platform components.

Although a dedicated SAR mission design would typically employ a systematic approach—encompassing mission objectives, user requirements, available technology, and budget constraints—the examples presented here illustrate both the potential capabilities and the inherent challenges of MEO-SAR systems.

5.2.1 Global MEO-SAR Mission

This global MEO-SAR mission concept aims to deliver products comparable to those provided by state-of-the-art LEO-SAR constellations, but using a single monostatic SAR satellite. For comparison, ESA'S Sentinel-1 constellation—comprising two satellites—is selected as a benchmark [35].

Parameter	Mode A	Mode B	Mode C	Mode D
Frequency [GHz]	5.405			
Resolution ($\delta x \times \delta g$) [m^2]	$< 5 \times 5$	$< 20 \times 5$	$< 40 \times 20$	-
Swath width [km]	> 80	> 250	> 410	-
Orbit repeat frequency [d]	< 6			
Incident-angle range [°]	-	-	-	20 – 47
NESN [dB]	< -22			
AASR [dB]	< -25			
RASR [dB]	< -25			

Table 5.1: Basic mission and system requirements for the global MEO-SAR mission example (aligned with Sentinel-1) in different imaging modes. A dash (–) indicates that no strict requirement is defined for the corresponding parameter in that mode.

At the same time, the proposed SAR mission leverages the unique advantages of MEO, including increased revisit frequency and enhanced geometrical diversity.

Mission Requirements

The mission objectives align with the Earth observation goals of Sentinel-1, adopting similar requirements for observation geometry and SAR level-1 products. Table 5.1 summarizes the key characteristics of the system, including swath, resolution, sensitivity, and ambiguity rejection. Modes A, B, and C roughly correspond in terms of resolution and sensitivity to Sentinel's stripmap (SM), Interferometric Wide swath (IW), and Extended Wide swath (EW) modes. Mode D, however, is a MEO-specific configuration to be optimized for high-frequency revisits. It shall provide coverage across an accessible area defined by incident angle limits comparable to Sentinel-1 (here defined as 20° to 47°), with relaxed resolution requirements compared to Mode C to accommodate the loss in sensitivity outlined in Section 4.2.

Orbit Design

As discussed in Chapter 4, designing an optimal orbit for a MEO-SAR mission requires careful consideration of several key factors, including coverage, radiation shielding, payload capacity, and instrument sensitivity. In

particular, the radiation environment is critical in determining mission lifetime, with regions of lower radiation—such as altitudes above 5500 km—being more favorable for prolonged operations.

The orbit design is primarily driven by observation requirements, which for this mission include near-global coverage and an incident-angle range of 20° to 47°. To ensure gap-free equatorial coverage, retrograde RGT orbits with a minimum 3-day repeat cycle are required at altitudes below 12 000 km, as shown in Figure 5.4(a). This configuration enables a revisit frequency of 1.5 days at the equator by utilizing both ascending and descending passes, or 3 days for InSAR products.

Given the mission's global coverage objective, the semi-major axis of the 3-day repeat orbit is selected to optimize the coverage rate within the radiation gap zone. Lower altitudes in this range offer advantages in instrument sensitivity (due to reduced free-space path loss) and improved launch efficiency.

Inclination selection involves a trade-off between maximizing spatial coverage and enhancing geometrical diversity. It enables a balance between overall Earth surface (or land) coverage and the ability to accurately measure 3-D deformation, as illustrated in Figure 5.3.

The gap-free coverage[1] percentage, calculated as the ratio of continuous coverage over a latitudinal band to the total Earth surface area, is shown in Figure 5.11. The optimal orbit for the mission, identified as a 3/19 RGT orbit at an altitude of 5952 km, offers the highest coverage and instrument sensitivity within lower-radiation zones above 5500 km. This orbit achieves peak gap-free coverage of 86% over land and ocean at an inclination of 122°. For land-only coverage, the percentage increases to 90.5%. Table 5.2 summarizes the key parameters of the selected orbit.

Despite the non-sun-synchronous nature of the designed RGT orbit, its higher altitude limits average eclipse durations to less than 8%. The chosen inclination provides good sensitivity to the three directions of motion. Increasing the inclination can further enhance the sensitivity to the North-South deformation component, though at the cost of a slight reduction in coverage percentage and launch efficiency. Conversely, decreasing the inclination below 122° would introduce coverage gaps over lower latitudes, compromising the mission's global observation goals.

Figure 5.12 illustrates the revisit frequency for descending passes over a 3-day repeat cycle, assuming a right-looking imaging geometry and an incident-angle range of 20° to 47°. Figure 5.13 presents the average revisit

[1] In this context, *gap-free coverage* refers to the complete coverage of a geographic block on Earth's surface without spatial gaps.

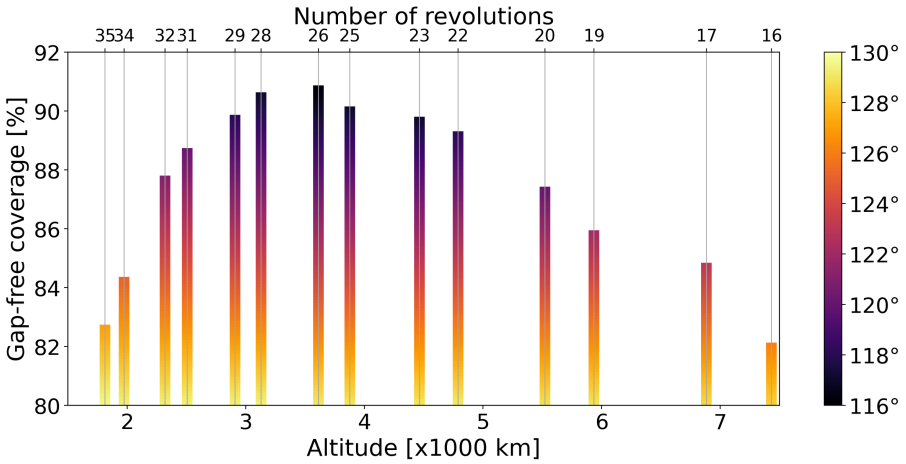

Figure 5.11: Distribution of 3-day RGT orbits capable of achieving over 80% gap-free coverage of the Earth's surface (including both land and oceans), presented as a function of orbital altitude and inclination. The swath is assumed to cover an incident-angle range of 20° to 47° and is captured using a right-looking imaging geometry.

Parameter	Value
Repeat cycle (N_{day}) [d]	3
Revolutions per cycle (N_{rev})	19
Semi-major axis (a) [km]	12329.9
Eccentricity (e)	0
Inclination (i) [°]	122
Altitude at equator [km]	5952
Average eclipse duration [%]	< 8

Table 5.2: Key parameters of the RGT MEO designed for the global MEO-SAR mission.

Parameter	Mode A	Mode B	Mode C	Mode D
Swath width [km]	> 80	> 250	> 410	1667
Orbit repeat frequency [d]		3		

Table 5.3: Updated swath width and orbit repeat frequency for the various imaging modes of the MEO-SAR mission example.

time, in hours, accounting for both ascending and descending passes. The figure highlights sub-daily revisit intervals at higher latitudes. Polar accessibility would be achievable with an incident angle of 58°. The updated values for swath width and orbit repeat frequency, based on the designed orbit, are detailed in Table 5.3.

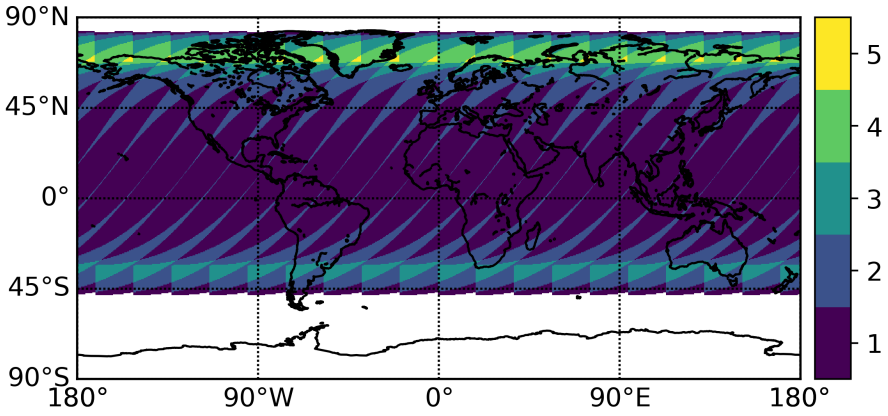

Figure 5.12: Potential coverage frequency per 3-day cycle for the 3/19 RGT MEO satellite at an altitude of 5952 km and an inclination of 122°, considering only descending passes. The satellite can access 86% of the Earth's surface for an incident-angle range of 20° to 47° under a right-looking imaging geometry. Polar accessibility would require an incident angle of 58°.

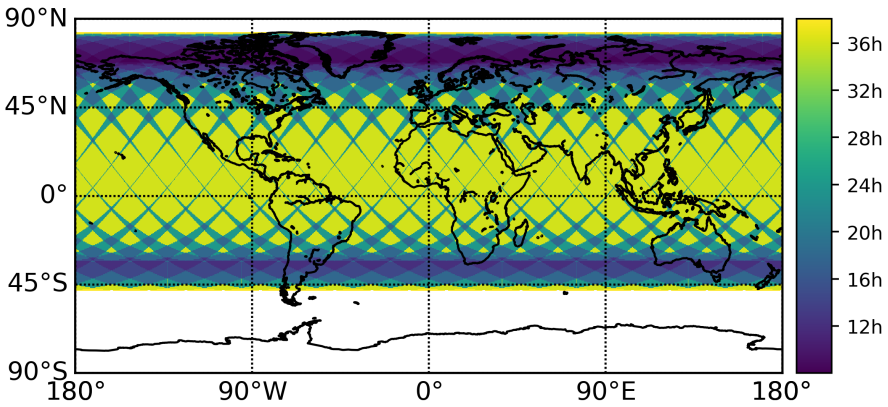

Figure 5.13: Potential coverage frequency map—or average revisit time, in hours—for the 3/19 RGT MEO satellite, based on total (ascending and descending) passes. The swath spans an incident-angle range of 20° to 47° and is captured with a right-looking imaging geometry.

Instrument and Antenna Design

The design of the instrument and imaging modes is driven by the key performance requirements outlined in Table 5.1 and Table 5.3 and is guided by the system-level considerations discussed in Section 4.2.

Based on (4.7), achieving the highest azimuth resolution requirement of 5 m necessitates an antenna length of 22 m for a C-band system operating at an altitude of 5952 km. In terms of sensitivity, imaging Mode D—which provides coverage of the entire access range (a 1667 km swath)—faces a sensitivity deficit of approximately 15 dB compared to a Sentinel-1 system

operating at 693 km. This calculation, based on the ΔNESN estimation in (4.17), assumes no change in transmit power. To partially mitigate this sensitivity loss, the system incorporates a 22-m reflector antenna equipped with SCORE capabilities. As outlined in Section 4.2, the remaining loss can be compensated by i) increasing the transmit power, ii) reducing the imaging resolution, or iii) narrowing the 1667-km swath width. For context, Sentinel-1 operates with an average transmit power of approximately 370 W for the SM and IW modes and 200 W for the EW mode.

To accommodate the full incident-angle range of 20° to 47°, the 22-m reflector antenna must incorporate digital beam steering capabilities in elevation over an angular span of approximately 12°. The single-element beamwidth is approximately 0.176°, necessitating precise element spacing to control the scalloping effect in elevation. For example, element spacing of 1.15λ and 0.66λ yield scalloping levels below 3 dB and 1 dB, respectively. The design adopts the tighter spacing of 0.66λ, resulting in 120 elements in elevation and providing redundancy to accommodate potential element failures.

The feed array incorporates two azimuth elements into a single channel to reduce the cross-talk between polarizations [187, 204]. If needed, additional azimuth elements can be used to collect the energy spread at the edges of the array, thereby improving the gain of the edge channels [205]. The feed array can be deployed on a 5 m × 1 m plate, which is expected to cause negligible blockage considering the size of the reflector.

Table 5.4 presents the parameters for the proposed antenna design, while Figure 5.14 shows the radiation patterns for the center and edge channels, highlighting the defocusing effects on gain and beamwidth when moving away from the focal point. The different SCORE beams are formed along the elevation span by applying complex weighting to a set of neighboring channels. The complex weights are designed to refocus the beam towards a specific location. This enhances the sensitivity by providing an additional 6 dB to 10 dB gain from the edges to the center of the swath by leveraging the entire surface of the 22-m reflector antenna [199, 200].

Mode Design and SAR Performance

The design of the operational modes for the global MEO-SAR mission is guided by the requirements for resolution, sensitivity (NESN), and ambiguity suppression (AASR and RASR) presented in Table 5.1, along with the updated swath width specifications detailed in Table 5.3. To achieve

Parameter	Value
Antenna type	parabolic reflector
Antenna diameter [m]	22
Focal length [m]	19.8
Offset (elevation) [m]	0
Frequency [GHz]	5.405
Feeding elements (azimuth × elevation)	2×120
Digital channels (azimuth × elevation)	1×120
Element spacing	0.66λ
Feed array size [m^2]	4.33×0.07
Feed array mount [m^2]	5×1

Table 5.4: Key parameters of the 22-m reflector antenna design and feeding network proposed for the global MEO-SAR mission.

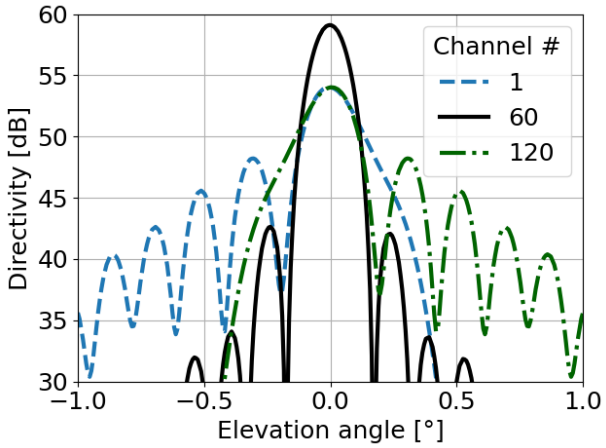

Figure 5.14: Simulated radiation patterns for the central and edge channels of the 22-m reflector antenna designed for the global MEO-SAR mission. The patterns, generated using the GRASP software [206], are superimposed to illustrate the defocusing effects on gain and beamwidth.

a resolution of 5 m in Mode A, a stripmap imaging mode is chosen. Multiple design options are feasible for modes B, C, and D, including multi-beam stripmap or burst-mode techniques [207–209]. As the mission aims to demonstrate the feasibility of MEO-SAR for frequent global monitoring, a ScanSAR imaging mode is adopted for these three modes to ensure simplicity.

The smaller look-angle range required to cover the wide swaths from an altitude of 5952 km leads to relaxed timing constraints. Figure 5.15 presents the timing diagrams, which include candidate sub-swath selections for

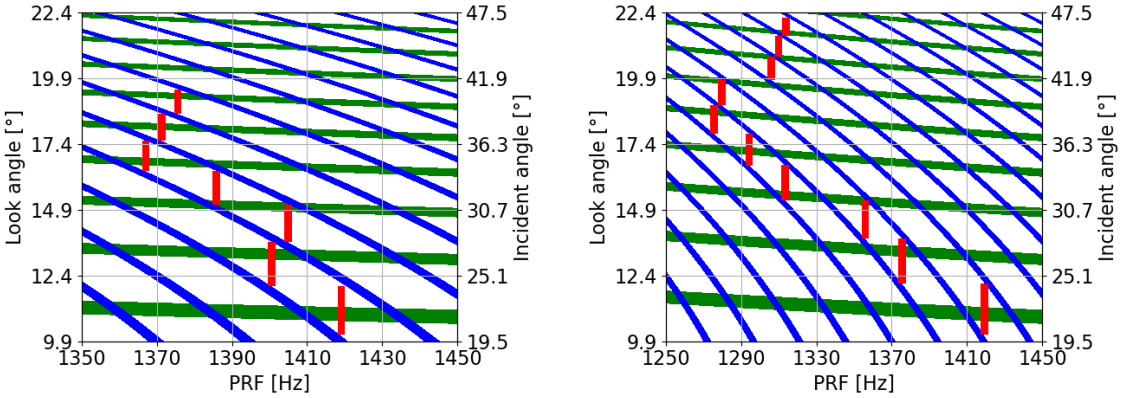

Figure 5.15: Timing diagrams illustrating the distribution of candidate sub-swaths based on look or incident angles and the corresponding PRF for (a) Mode C and (b) Mode D. The quasi-horizontal green stripes represent nadir echoes, the oblique blue stripes indicate transmission events, and the vertical red bars correspond to the selected swaths. The duty cycle is 8%.

modes C and D. The diagrams illustrate the distribution of transmit events (oblique blue stripe) with an 8% duty cycle, as well as nadir echoes (quasi-horizontal green stripe), for a range of pulse repetition frequencies (PRFs) across the geometry of interest (incident-angle range and corresponding look angles).

For Mode C, seven ScanSAR bursts (represented by vertical red bars in Figure 5.15) are extended to fully utilize the gaps between transmit events. This configuration achieves the required azimuth resolution of 40 m while covering a total swath width of 1211 km. The definition of the sub-swaths assumes perfect nadir echo suppression—a reasonable assumption given the size of the reflector and the system's digital beamforming capabilities. If needed, nadir echoes can also be effectively mitigated at no additional cost using the dual-focusing suppression technique, which employs waveform diversity on transmit [210].

The PRF optimization for the seven bursts followed an iterative process to meet the required AASR and RASR of -25 dB. An average transmit power of 350 W is needed to achieve a ground-range resolution of 20 m with a NESN of -22 dB.

For Mode D, ten ScanSAR bursts are employed to cover the full access area, resulting in an azimuth resolution of 57 m. With an average transmit power of 350 W, the system satisfies the NESN requirements, achieving a ground-range resolution of 20 m.

Mode B is a subset of Mode C, where the three central bursts are used to cover a 500 km swath with an azimuth resolution of 20 m. An average

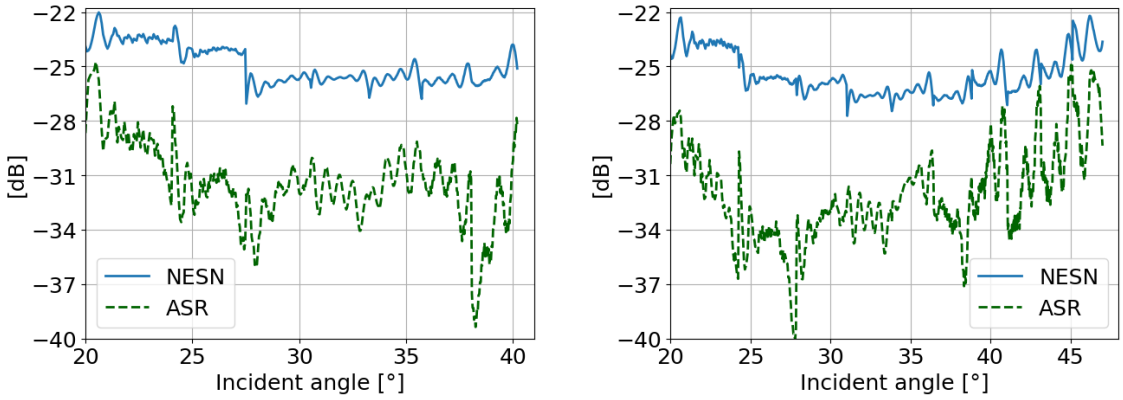

(a) (b)

Figure 5.16: Variation of NESN and ASR with incident angle for the swath extensions designed for (a) Mode C and (b) Mode D.

transmit power of 400 W is needed to achieve a ground-range resolution of 5 m while meeting the NESN requirement of −22 dB.

For Mode A, each single stripmap swath is a subset of the various bursts in Mode D. The swath widths range from 115 km to 206 km, depending on their positions in the timing diagram. A total average transmit power of 300 W is sufficient for the central swaths; however, the edge swaths require an additional power increase of approximately 2.8 dB to compensate for the defocusing of the patterns.

The transmit beams associated with the designed bursts are synthesized using uniform excitation of groups of neighboring channels, following a switched subarray approach. Alternatively, more advanced beamforming techniques could be applied to better shape the beam patterns, reducing sidelobes and thereby enhancing ambiguity suppression. However, these methods typically result in reduced gain across the swath and may be considered for detailed system optimization if required.

Figure 5.16 illustrates the variation of NESN and total ambiguity-to-signal ratio (ASR)[2] across the full swath for modes C and D. The resulting performance metrics for all modes are summarized in Table 5.5.

[2] In this thesis, ASR denotes the *linear* sum of the azimuth ambiguity-to-signal ratio (AASR) and the range ambiguity-to-signal ratio (RASR), i.e., ASR = AASR + RASR (in linear power units).

Parameter	Mode A	Mode B	Mode C	Mode D
Imaging mode	stripmap	ScanSAR	ScanSAR	ScanSAR
Resolution ($\delta x \times \delta g$) [m^2]	$< 5 \times 5$	$< 20 \times 5$	$< 40 \times 20$	$< 57 \times 20$
Swath width [km]	115 – 206	500	1211	1667
Incident-angle range [°]	20 – 47	27.3 – 35.6	20 – 40.3	20 – 47
Average transmit power [W]	300 – 575	400	350	350
PRF range [Hz]	1290 – 1418	1366 – 1404	1365 – 1419	1290 – 1418
System bandwidth [MHz]	43 – 87	55 – 66	12 – 22	11 – 22
Total losses [dB]	4			
Noise figure [dB]	3			
Duty cycle [%]	8			
Backscatter law	Ulaby (Short Vegetation) [211]			
NESN [dB]	< -22	< -22	< -22	< -22
AASR [dB]	< -26	< -30	< -25	< -25
RASR [dB]	< -30	< -30	< -30	< -30

Table 5.5: Performance metrics for the global MEO-SAR mission example across different operational modes.

Deformation Retrieval Performance

The MEO-SAR system, with its 122° orbital inclination, enables true 3-D large-scale deformation mapping by leveraging acquisitions with substantial geometrical diversity. This diversity arises from oblique ascending and descending passes in both right- and left-looking geometries over extensive portions of the globe. As a consequence, the system allows for ground-deformation measurements with comparable accuracy in all three motion directions—East-West, North-South, and Up-Down, as discussed in Section 5.1.1. Figure 5.17 illustrates the obliqueness of swaths from ascending and descending passes in right-looking geometries, expressed in terms of northing angles.[3] The central portion of the passes (e.g., latitudes between 0° and 45°) exhibits a mean northing angle of approximately $\pm$ 132°, corresponding to a southing angle of $\pm$ 42°.

The expected performance of deformation retrieval for the mission is assessed through a mission simulation. In this simulation, each ground point is assigned a time series of acquisitions with corresponding geometries spanning the a predefined duration. The differential SAR interferometry (D-InSAR) performance is then evaluated using the hybrid Cramér-Rao

[3] *Northing angle* refers to the angle between the ground projection of the line of sight (LoS) vector and the local north direction.

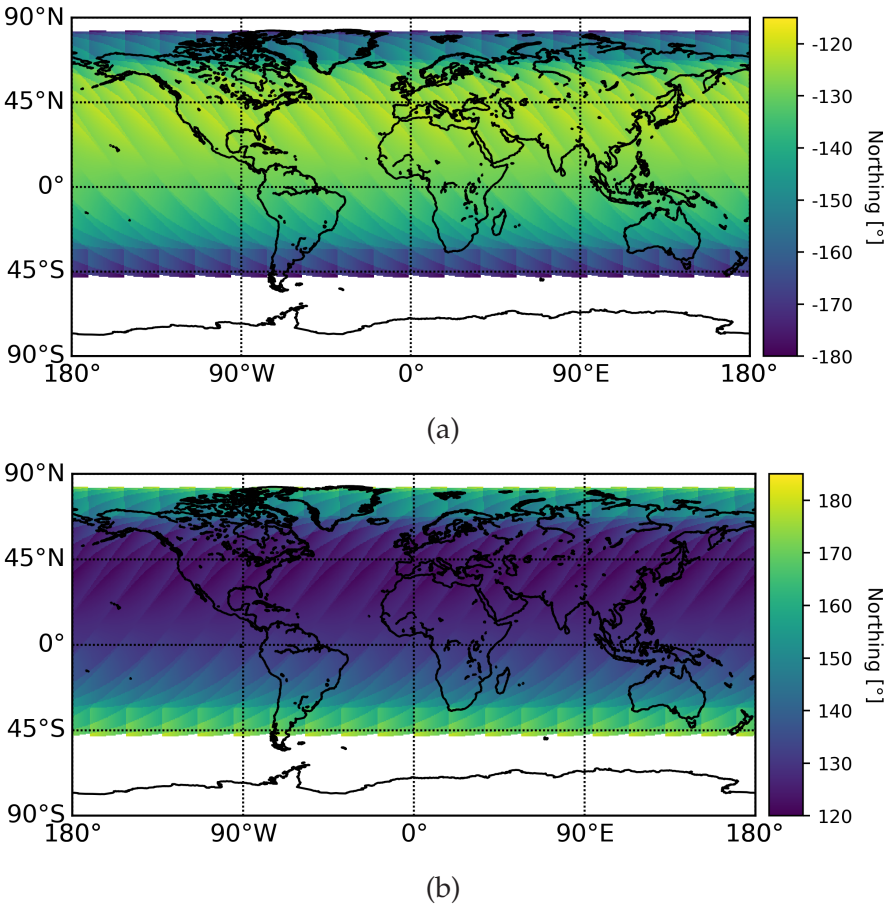

Figure 5.17: Northing angles of the (a) ascending and (b) descending passes in right-looking geometries, showing the angle between the LoS projection on ground and the local north.

bound (HCRB), as detailed in Section 3.3. An exponential model is assumed for temporal decorrelation, where τ represents the decorrelation time constant, and γ_∞ corresponds to the persistent coherence term [172]. Additionally, decorrelation due to the signal-to-noise ratio (SNR) is computed based on the system's NESN and the backscatter values, which can be modeled or retrieved from global backscatter maps such as those derived from Sentinel-1 data [212, 213].

Table 5.6 summarizes the key mission and environmental parameters used in combination with the Mode D parameters from Table 5.5 to assess the system's deformation retrieval performance. The mission follows a nominal acquisition sequence (LRRL): one year of left-looking acquisitions, followed by two years of right-looking acquisitions, and concluding with a final year of left-looking acquisitions. The analysis assumes a product resolution of 500 m $\times$ 500 m, with standard deviations of 2 cm and 1 cm for tropospheric (σ_{trop}) and ionospheric (σ_{iono}) delays, respectively.

Parameter	Value
Mission duration [y]	4
Look directions	left & right
Temporal decorrelation constant (τ) [d]	40
Persistent coherence term (γ_∞)	0.05
Tropospheric delay std. (σ_{trop}) [cm]	2
Ionospheric delay std. (σ_{iono}) [cm]	1
Product resolution [m^2]	500×500
Backscatter map	Sentinel-1

Table 5.6: Mission and environmental parameters for the deformation retrieval performance assessment of the C-band global MEO-SAR mission example. A mission duration of four years is assumed for the accuracy analysis, though it does not constitute a strict constraint on the actual mission lifetime.

Parameter	LRRL
E-W accuracy (mean | 3-sigma) [mm/y]	0.75 | 3.6
N-S accuracy (mean | 3-sigma) [mm/y]	1.10 | 2.91
U-D accuracy (mean | 3-sigma) [mm/y]	1.18 | 4.15

Table 5.7: Deformation accuracy statistics (mean and 3-sigma[4]) for the C-band example MEO-SAR mission after four years of acquisitions. The acquisition sequence (LRRL) consists of one year of left-looking, followed by two years of right-looking, and concluding with one year of left-looking. The mean and 3-sigma values are computed based on the distribution of all points within the high seismic hazard zones shown in Figure 5.18.

Figure 5.18 presents 2-D deformation accuracy maps (in mm/year) for regions classified as high seismic hazard zones. The corresponding statistical results are summarized in Table 5.7. The mean deformation accuracy, evaluated across all three displacement directions, is 0.77 mm/y in the East-West direction, 1.1 mm/y in the North-South direction, and 1.18 mm/y in the Up-Down direction. At latitudes between $\pm$ 47°, the overlap between left- and right-looking acquisitions improves the LoS geometry, reducing the maximum uncertainty to below 2.5 mm/y in all directions. At higher latitudes, however, where only single-direction acquisitions overlap with varying observation geometries, the accuracy declines.

The combination of high sensitivity to all displacement directions and a short revisit duration makes this MEO-SAR mission example particularly well-suited for hazard monitoring applications.

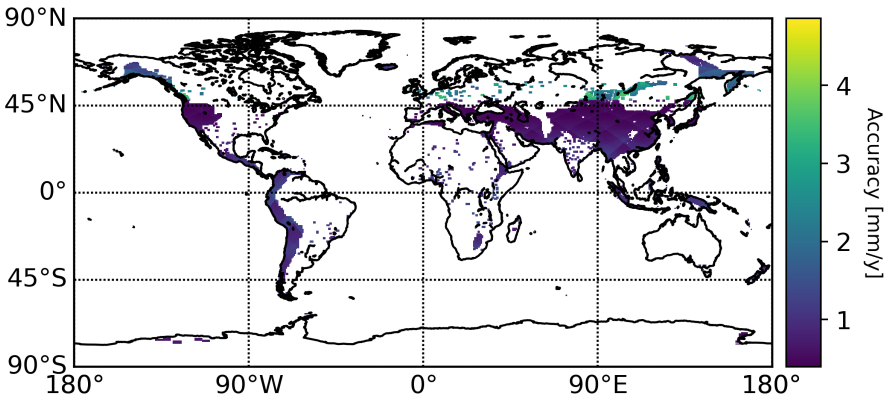

(a)

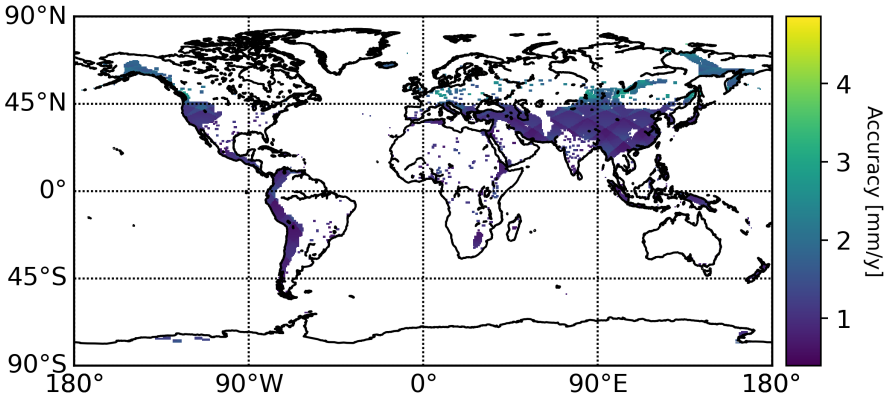

(b)

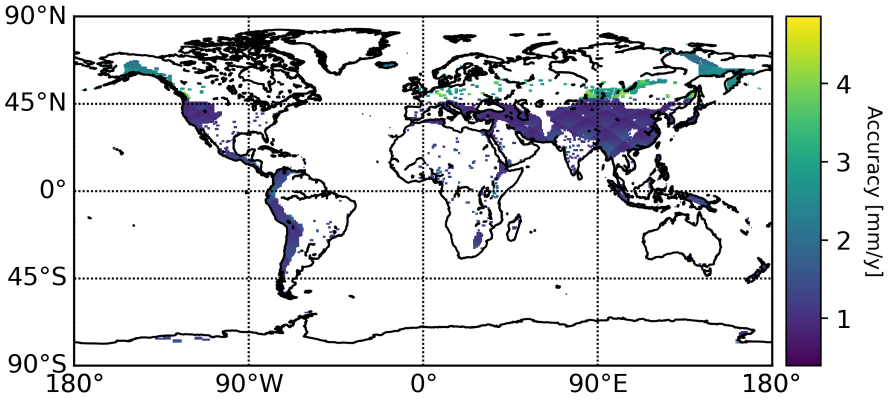

(c)

Figure 5.18: Deformation accuracy maps (in mm/y) for the C-band global MEO-SAR mission example in high seismic hazard zones, shown for (a) East-West, (b) North-South and (c) Up-Down directions.

Comparison with Sentinel-1

A preliminary analysis indicates that a MEO system with moderate resolution—for instance, Mode D with $\delta x \times \delta g = 57\,\text{m} \times 20\,\text{m}$—and moderate power is potentially better suited for moderate-resolution applications, such as soil moisture estimation or deformation monitoring, than contemporary LEO missions.

Compared to Sentinel-1, the proposed MEO-SAR system example offers several advantages, including a 1.5 to 3-fold increase in imaged swath, a significantly shorter interferometric revisit interval of three days with a single satellite (compared to six days with two satellites), and sensitivity to the Northing component of deformation due to the selected orbital inclination. These benefits come with a modest increase of 1 dB to 2 dB in average transmit power, the use of a large reflector antenna with SCORE capabilities, the need for radiation hardened electronics and shielding, and a reduced launch efficiency.

Furthermore, reducing the interferometric revisit interval, for example to six days, allows for system simplification by halving the covered swath width, without compromising three-day accessibility for event-triggered acquisitions.

An L-band System Alternative

An alternative mission example using L-band, operating in the same orbit, leverages the enhanced penetration capabilities of longer wavelengths through vegetation cover. This can result in more accurate soil moisture estimates and improved coherence, which is essential for reliably measuring slow surface deformations.

Table 5.8 summarizes the key mission, instrument, and atmospheric parameters specific to the L-band mission example. Other parameters are assumed to be identical to those of the C-band mission example. Given the longer wavelength, the SAR antenna employs a feed array of 35 elevation channels to digitally steer the beam over the required incident-angle range. Each channel is formed by a combination of 6 azimuth elements to improve beam focus, compensating for the increased defocusing due to the offset-fed parabolic reflector design.

The corresponding performance metrics are summarized in Table 5.9. For demonstration purposes, a single operational mode is evaluated, covering the 1667 km swath necessary for near-global coverage using 10 ScanSAR bursts. The system achieves a SLC resolution of $57\,\text{m} \times 100\,\text{m}$ and a NESN

Parameter	Value
Frequency GHz	1.2575 GHz
Antenna type	parabolic reflector
Antenna diameter [m]	22
Focal length [m]	19.8
Offset (elevation) [m]	10
Feeding elements (azimuth $\times$ elevation)	6×35
Digital channels (azimuth $\times$ elevation)	1×35
Element spacing	0.6λ
Feed array size [m^2]	4.95×0.81
Temporal decorrelation constant (τ) [d]	60
Persistent coherence term (γ_∞)	0.2
Backscatter map	ALOS PALSAR

Table 5.8: Main mission, instrument, and environmental parameters for the L-band global MEO-SAR mission example.

Parameter	Value
Imaging mode	ScanSAR
Resolution ($\delta x \times \delta g$) [m^2]	$< 57 \times 100$
Swath width [km]	1667
Incident-angle range [°]	20 – 47
Average transmit power [W]	120
PRF range [Hz]	1240 – 1445
System bandwidth [MHz]	2 – 4.5
NESN [dB]	< -25
ASR (2-sigma) [dB]	-22
E-W accuracy (mean | 3-sigma) [mm/y]	1.18 | 4.50
N-S accuracy (mean | 3-sigma) [mm/y]	1.73 | 3.74
U-D accuracy (mean | 3-sigma) [mm/y]	1.57 | 4.88

Table 5.9: Main performance metrics for the L-band mission alternative in full-swath mode.

better than -25 dB, with an average transmitted power of approximately 120 W. Although the improved coherence enhances performance, the deformation accuracy is slightly reduced due to a lower number of available range looks (reduced by a factor of 5) for a comparable product resolution. In mid-latitudes (between $\pm$ 47°), accuracy remains better than 3.23 mm/y

Parameter	Value
Frequency [GHz]	1.2575
Resolution ($\delta x \times \delta g$) [m^2]	$< 1000 \times 1000$
Coverage	Europe
Revisit interval [h]	< 24
NESN [dB]	< -25
AASR [dB]	< -28
RASR [dB]	< -28

Table 5.10: Basic mission and system requirements for the sub-daily continental MEO-SAR mission example.

in all directions. Additionally, the offset-fed design reduces ambiguity suppression capabilities, particularly in far-range swaths. To mitigate this performance degradation, the system may incorporate ambiguity suppression techniques [214] or employ a larger reflector surface. These enhancements can enable the attainment of an ASR of $-22\,\mathrm{dB}$ or better over 3-sigma of the swath, compared to the estimated 2-sigma without such measures.

5.2.2 Sub-daily Continental MEO-SAR Mission

The sub-daily continental MEO-SAR mission is designed to address a critical observational gap by providing sub-daily, kilometer-scale measurements of the ecosystem water status across Europe [63, 66, 67]. This mission concept utilizes the orbital configurations identified in Section 5.1.3 to enable twice-daily revisits over substantial portions of the European continent.

Mission Requirements

The primary objective of the mission is the sub-daily monitoring of surface soil moisture across extensive regions of Europe. To achieve this, the mission adopts an L-band carrier frequency, selected for its strong vegetation penetration, enabling reliable observations even in densely vegetated regions. Table 5.10 outlines the key system parameters, including revisit frequency, coverage, spatial resolution, sensitivity, and ambiguity rejection.

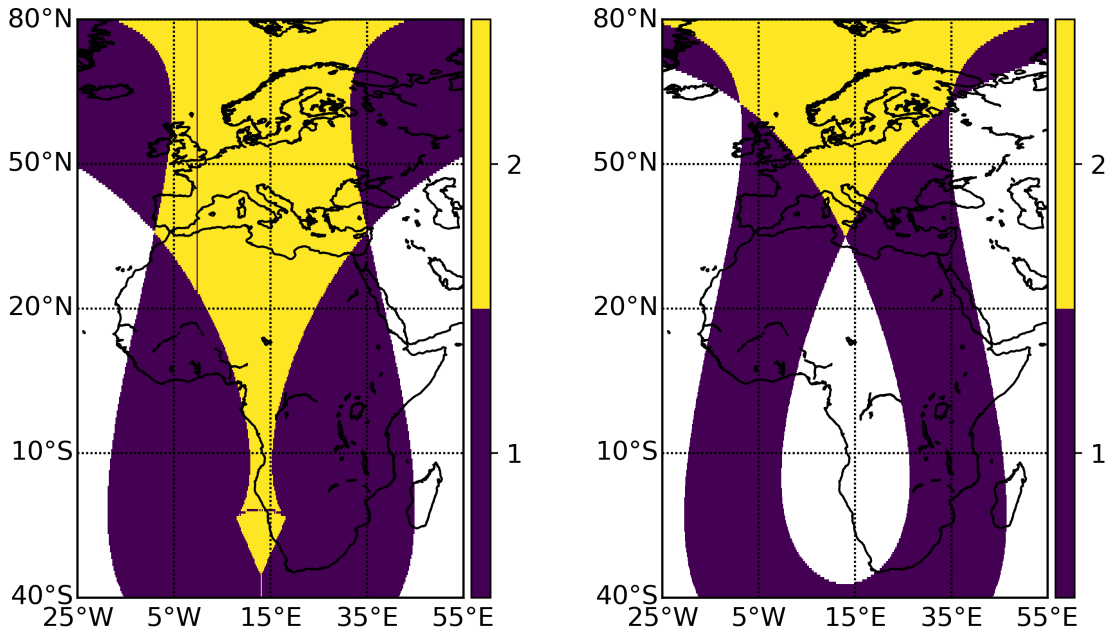

Figure 5.19: Daily coverage frequency map for a 1/2 RGT MEO satellite at an altitude of 20181 km and an inclination of 70°. Panel (a) shows the swath spanning an incident-angle range of 20° to 60°, while panel (b) covers the narrower range of 18° to 42°, both captured using a left-looking imaging geometry.

Orbit Design

The chosen orbit design for this mission is a 1/2 RGT MEO at an altitude of 20181 km. This orbit provides coverage with sub-daily revisit over most of the European continent for an incident-angle range of 20° to 60°, as well as at least daily revisit across western Europe for a narrower incident-angle range of 18° to 42°. These characteristics enable potential simplifications to the SAR payload, attributed to the reduction in swath width from 3640 km to 2116 km. Figure 5.19 illustrates the corresponding daily coverage frequency map for the two incident-angle ranges.

While a 1/3 RGT MEO at 13890 km also offers sufficient coverage over Europe within the 20° to 60° incident-angle range, with the added advantages of reduced sensitivity loss and lower launch costs, the higher altitude design provides valuable insights into the complexity and potential benefits of operating at higher orbital altitudes. This comparison is particularly relevant when considered alongside the lower-altitude example discussed in the previous section.

Parameter	Value
Repeat cycle (N_{day}) [d]	1
Revolutions per cycle (N_{rev})	2
Semi-major axis (a) [km]	26559.7
Eccentricity (e)	0
Inclination (i) [°]	70
Altitude at equator [km]	20181
Average eclipse duration [%]	< 1.5

Table 5.11: Key parameters of the RGT MEO designed for the sub-daily continental MEO-SAR mission.

Parameter	Value
Antenna type	parabolic reflector
Antenna diameter [m]	25
Focal length [m]	22.5
Offset (elevation) [m]	15
Frequency [GHz]	1.2575
Feeding elements (azimuth × elevation)	6 × 17
Digital channels (azimuth × elevation)	1 × 17
Element spacing	0.6λ
Feed array size [m^2]	2.38 × 0.8

Table 5.12: Key parameters of the 25-m reflector antenna design and feeding network proposed for the sub-daily continental MEO-SAR mission.

Table 5.11 outlines the key parameters of the selected orbit. Notably, the reduced proximity to Earth results in average eclipse durations of less than 1.5%.

Instrument and Antenna Design

Following the analysis in Section 4.2, a significant sensitivity loss is expected for a SAR sensor at an altitude of 20181 km. To partially recover the sensitivity, the design adopts a large deployable offset reflector with a diameter of 25 m. To keep the complexity of the SAR payload at an acceptable level, the narrower incident-angle range of 18° to 42° is adopted. Table 5.12 presents the parameters of the proposed offset-fed parabolic reflector antenna design. The system incorporates 17 elevation channels to digitally

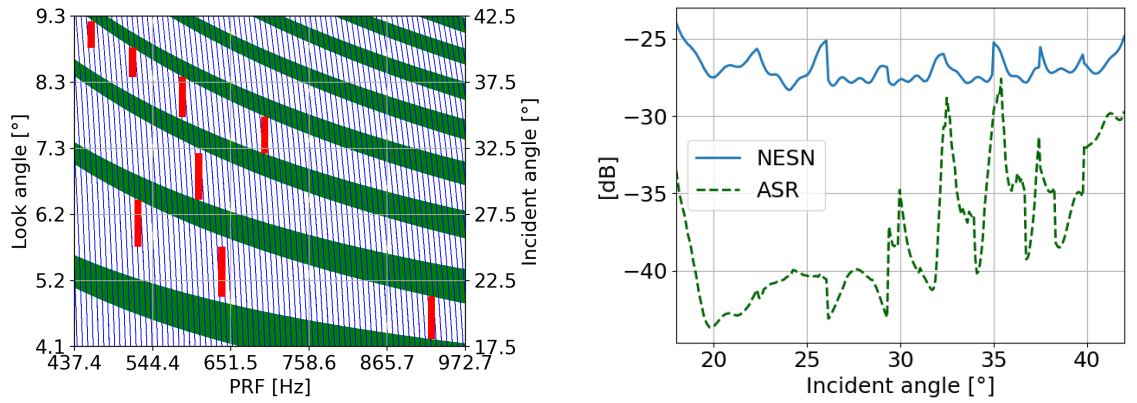

(a) (b)

Figure 5.20: (a) Timing diagrams illustrating the distribution of candidate sub-swaths based on look or incident angles and the corresponding PRF. (b) Variation of NESN and ASR with incident angle for Mode A.

steer the beam over the 2116 km swath. Each channel is formed from an analogue combination of 6 feed elements along azimuth. Hence, the complete feed array incorporates 6×17 feed elements occupying a space of $2.38\,\text{m} \times 0.8\,\text{m}$.

Mode Design and Performance

A primary wide-swath mode (Mode A) has been designed for this mission example, covering the incident-angle range of 18° to 42°. This mode employs 8 ScanSAR beams to achieve full coverage of the access area, allowing for an azimuth resolution of 25 m. With an average transmitted power of 100 W, the system attains a NESN better than −25 dB for a ground resolution of 500 m.

In addition, a secondary mode (Mode B) has been designed to provide narrower swaths with higher resolution. Each swath in Mode B is acquired in stripmap mode, utilizing a PRF that is a subset of the bursts used in Mode A. The swath widths vary between 200 km and 305 km, depending on their position in the timing diagram. Figure 5.20 (a) illustrates the timing diagram, including candidate sub-swath selections that avoid transmission events and nadir returns. The corresponding NESN and ASR for Mode A are shown in Figure 5.20 (b).

Table 5.13 summarizes the key SAR performance metrics and system parameters for both modes. Improved ground-range resolution in the SLC product is feasible but comes at the cost of increased power demand or reduced NESN. For instance, achieving a 160 m ground-range resolution in Mode A would degrade the NESN to −20 dB. Additional modes can be

Parameter	Mode A	Mode B
Imaging mode	ScanSAR	Stripmap
Resolution ($\delta x \times \delta g$) [m^2]	$< 25 \times 500$	$< 6.7 \times 300$
Swath width [km]	2115	200 – 305
System bandwidth [MHz]	0.47 – 1	1 – 2.1
Average transmit power [W]	100	
Incident-angle range [°]	18 – 42	
PRF range [Hz]	460 – 930	
Total losses [dB]	4	
Noise figure [dB]	3	
Duty cycle [%]	8	
NESN [dB]	< -25	
AASR [dB]	< -28	
RASR [dB]	< -28	

Table 5.13: Performance metrics for the global MEO-SAR mission example across different operational modes.

developed, though any extension of the incident-angle range would necessitate a more complex feed network. Alternatively, mechanical steering of the satellite could be employed to extend coverage to larger incident angles at different mission phases, seasons, or satellite passes.

5.3 Chapter Remarks

This chapter identified four new opportunities unique to single-satellite MEO-SAR systems, as outlined in Section 5.1: (1) true 3-D deformation mapping on a global scale, (2) frequent global access with three-day interferometric revisit and one- to two-day non-interferometric revisit, (3) subcontinental coverage with daily interferometric revisit and sub-daily non-interferometric revisit, and (4) high-latitude accessibility from equatorial orbits, with sub-daily revisit intervals of just a few hours.

Section 5.2 then detailed the derivation of two exemplary mission concepts. The first mission leverages unique acquisition geometries to enable 3-D deformation mapping while maintaining global coverage with one- to two-day revisit, utilizing a C-band reflector-based system in a 3/19 RGT MEO at 5952 km. The second mission focuses on large-scale sub-daily revisit,

providing coverage over the European continent and addressing observational gaps in ecosystem water status monitoring. This mission employs an L-band reflector-based system in a 1/2 RGT MEO at 20181 km.

The different MEO-SAR concepts offer moderate resolution and unprecedented accessibility, but they involve a higher degree of system complexity. This complexity, however, appears to be manageable, especially when compared to the design challenges of with current flagship missions such as NISAR and ROSE-L. A comparative analysis of system complexity for the two MEO-SAR concepts introduced in Section 5.2 will be presented in Chapter 7, where they are evaluated relative to their equivalent LEO-SAR constellations.

6 GEO SAR: Mission Design

Geosynchronous orbits (GEO) are gaining increasing interest for SAR remote sensing missions due to their potential to offer very high temporal resolutions, potentially on the order of hours, with a single spacecraft. However, this advantage is accompanied by several trade-offs, including increased propagation losses, limited global access, and higher fuel requirements for station-keeping due to perturbations from the Sun and Moon. Furthermore, GEO satellites are more susceptible to atmospheric variations and radio frequency interference (RFI) [76, 107, 114].

GEO-SAR missions benefit from near-continuous accessibility to extensive regions of the Earth, enabling increased operational flexibility. In particular, longer integration times in a spotlight-like acquisition mode can be employed to accommodate sensitivity losses associated with increased propagation losses and various sources of decorrelation. Furthermore, low-inclination, low-eccentricity GEO-SAR configurations enable sub-daily interferometric acquisitions—a capability otherwise achievable only through SAR satellite constellations, or through equatorial MEO-SAR systems over lower latitudes, as discussed in Chapter 5.

The design of a sub-daily interferometric GEO-SAR mission involves trade-offs among spatial resolution, scene size, and revisit frequency. Enhancing system performance can help to relax the trade-space; however, it is challenged by various decorrelation sources, resulting from the instrument, the acquisition geometry, and other environmental factors, as discussed in Chapter 3. In particular, baseline decorrelation between sub-daily acquisitions is a critical factor that strongly depends on the specific orbital design of the GEO-SAR system.

This chapter presents an overview of GEO SAR, offering insights into orbit design by examining the impact of the Keplerian elements on orbital tracks in Section 6.1. Section 6.2 introduces a novel GEO concept optimized for sub-daily interferometric revisits, aiming to minimize baseline decorrelation—an approach that holds significant potential for future GEO-SAR missions. Section 6.3 then develops a novel imaging mode for the efficient utilization of mission resources in such orbital regimes. This imaging mode is used to derive the observation scenarios[1] for Hydroterra,

[1] In this context, an *observation scenario* refers to a specific configuration of imaging parameters, such as scene size, spatial resolution, revisit frequency, and operation mode,

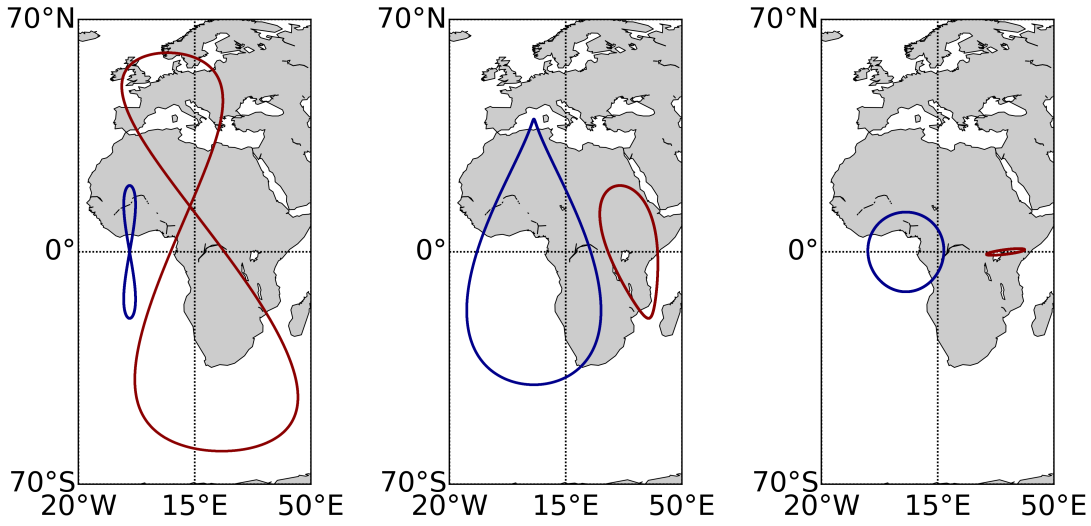

Figure 6.1: Illustration of three distinct geosynchronous satellite ground track patterns: (a) analemmas, (b) teardrop shapes, and (c) ovals, with circular as a special case of the oval category.

a previously proposed GEO-SAR mission concept under ESA's Earth Explorer 10 program, and a candidate for ESA's Earth Explorer 12 as Hydroterra+.

6.1 Geosynchronous Orbit Properties

Geosynchronous orbits are characterized by an orbital period equal to a sidereal day. Various ground track configurations can be realized by manipulating key orbital parameters, specifically eccentricity, inclination, and argument of perigee. These patterns can extend satellite coverage to higher latitudes, modify longitudinal span, adjust dwell times over specific regions, or, in some cases, establish geometries suitable for interferometry-compatible acquisitions.

Figure 6.1 presents three distinct ground track patterns: (a) analemmas (commonly referred to as "figure-8" patterns), (b) teardrop shapes, and (c) ovals. For each pattern, two examples are presented: longitudinal sym-

designed to fulfill particular mission objectives or user requirements in SAR data acquisition.

Table 6.1: Orbital parameters corresponding to the ground track patterns presented in Figure 6.1, with a reference epoch of 2040-03-21T12:00:00.000Z UTC. All elements are specified in the TOD reference frame.

Pattern	a [km]	e	i [°]	Ω [°]	ω [°]	M_0 [°]
Analemma (blue)	42167.47	0	20	355	90	270
Analemma (red)	42164.22	0.1	60	240	225	270
Teardrop (blue)	42166.01	0.15	40	185	270	270
Teardrop (red)	42167.50	0.075	20	5	120	270
Circular (blue)	42167.90	0.1	11.45	5	90	270
Oval (red)	42168.08	0.05	1	80	45	270

metry (blue) and asymmetry (red). These examples highlight the flexibility achieved by adjusting geosynchronous orbital parameters. The corresponding orbital parameters, defined in the true of date (TOD) frame, [2] are listed in Table 6.1 with a reference epoch of 2040-03-21T12:00:00.000Z UTC.

The design and optimization of a GEO can be systematically guided by leveraging the direct parametric relationships between orbital elements and the resulting ground track characteristics. For instance, the central longitude of the ground track ($\lambda_{\text{lon},0}$) is related to the longitude of the ascending node (Ω), the argument of perigee (ω), and the mean anomaly at a reference epoch (M_0) through the expression

$$\lambda_{\text{lon},0} \approx \Omega + \omega + M_0 - \Theta(t_0), \tag{6.1}$$

where $\Theta(t_0)$ denotes the right ascension of the Greenwich meridian at the epoch t_0, expressed in radians [115]. In addition, the longitude extent ($\Delta\lambda_{\text{lon}}$) depends on both inclination and eccentricity [114]. For a circular GEO ($e = 0$), the longitude extent in radians is given by

$$\Delta\lambda_{\text{lon}} \approx 2 \cdot \arctan\left(\frac{\sqrt{1/\cos i} - \sqrt{\cos i}}{2}\right). \tag{6.2}$$

For non-zero eccentricity and near-zero inclination (e.g., oval ground-track patterns), the longitude extent in radians becomes

$$\Delta\lambda_{\text{lon}} \approx 4 \cdot e. \tag{6.3}$$

[2] *True of date* (TOD) frame refers to a coordinate frame where the orientation of the Earth's equator and equinox is taken as of the specified epoch, accounting for precession and nutation effects up to that date.

Similarly, the latitude extent of a ground track ($\Delta\phi_{\text{lat}}$) is primarily determined by the orbital inclination, with the relationship

$$\Delta\phi_{\text{lat}} \approx 2 \cdot i. \tag{6.4}$$

GEO satellites are subject to regulatory constraints imposed by the International Telecommunication Union (ITU), which limits the allowable longitude span for a satellite crossing the equatorial plane to a slot of $\pm 0.1^\circ$, approximately equivalent to 150 km [119]. This restriction is particularly critical for GEO satellites with near-zero inclination and eccentricity, which are often prioritized for single-spacecraft, sub-daily interferometric SAR missions. While ITU regulations permit the allocation of up to five orbital slots for scientific missions, the increasing global demand for GEO positions, coupled with the finite number of available slots, poses a growing challenge for securing multiple consecutive slots for future SAR systems.

6.2 Specialized Sub-daily Interferometric GEO

This section introduces a novel design for geosynchronous orbits optimized for sub-sidereal interferometric acquisitions targeting a region of interest (ROI) on Earth's surface. The proposed concept minimizes baseline decorrelation between sub-daily InSAR acquisitions, thereby improving system performance and relaxing orbit maintenance requirements.

Figure 6.2 illustrates the geometric approach for minimizing the cross-track perpendicular baseline ($B_\perp$) in a sub-daily interferometric acquisition pair over a ROI. The approach derives orbital parameters that ensure near-zero $B_\perp$ for interferometric acquisition pairs centered at the perigee and apogee, thereby minimizing the residual $B_\perp$ across different acquisition centers. The design assumes low-inclination, low-eccentricity orbits with elliptical ground-track patterns, facilitating multiple sub-daily interferometric acquisitions over extensive areas [83, 100, 101, 215].

The derivation of the orbital parameters follows a five-stage process, as illustrated in the flowchart in Figure 6.3:

1. Eccentricity determination: the eccentricity (e) is determined based on the desired longitudinal extent of the ground track ($\Delta\lambda_{\text{lon}}$) using (6.3). This extent is constrained to a few ITU slots, often just one.
2. Inclination derivation: the inclination (i) is derived for a nominal geostationary orbit, assuming a default semi-major axis ($a = a_{\text{GSO}}$) and an argument of perigee ($\omega = 90^\circ$), independent of the relative longitude

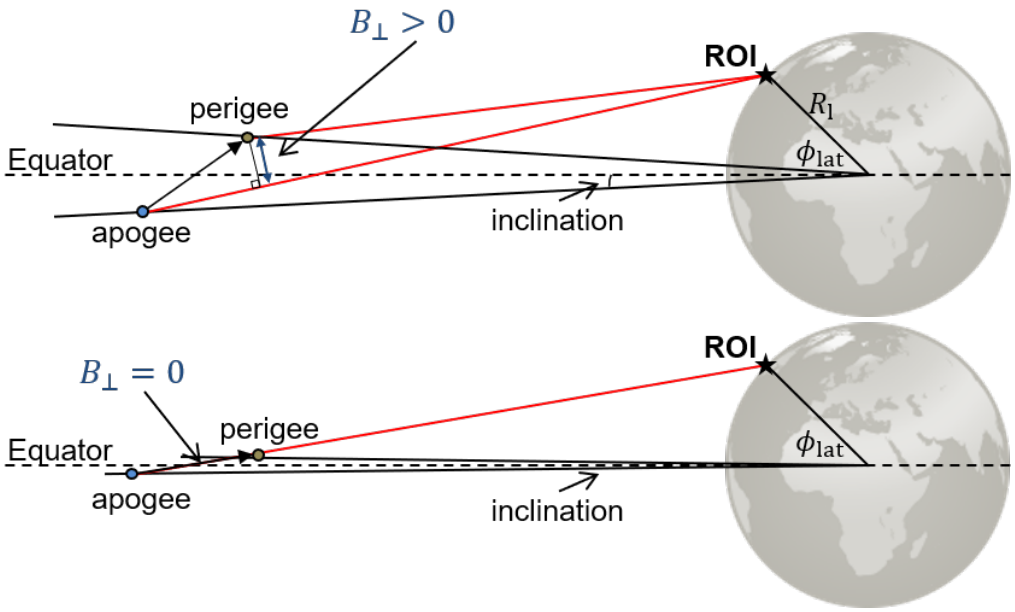

Figure 6.2: (Top) Orbital configuration with a non-zero cross-track perpendicular baseline ($B_\perp$). (Bottom) Orbital configuration with a zero $B_\perp$, optimized for sub-sidereal interferometry. The approach minimizes the baseline for an interferometric acquisition pair of a region of interest (ROI) on Earth's surface, taken from the perigee and apogee positions.

shift between the orbit and the target. This formulation allows i to be solved in the novel trigonometric equation derived in Appendix A

$$x_t \cdot \sin i + e \cdot z_t \cdot \cos i - a \cdot \left(1 - e^2\right) \cdot \sin i \cdot \cos i = 0, \tag{6.5}$$

where (x_t, y_t, z_t) are the Cartesian coordinates of a specific point within the ROI and can be related to its geodetic coordinates (ϕ_{lat}, λ_{lon}, h) using (A.15) in Appendix A.

3. Semi-major axis optimization: once e and i are determined, the semi-major axis (a) is numerically optimized to improve repeat-ground track characteristics while accounting for secular perturbations, as discussed in Section 2.2.

4. Argument of perigee optimization: in this stage, ω is derived for the actual orbit parameters and a specific target position (x_t,y_t,z_t) using an iterative approach to minimize the perpendicular baseline ($B_\perp$). This step is particularly crucial when the central longitude of the ground track ($\lambda_{\text{lon},0}$) is misaligned with the longitude of the ROI.

5. RAAN calculation: the longitude of the ascending node (Ω) is calculated for a specified epoch, sometimes expressed as a mean Julian date (MJD), under the assumption that the mean anomaly at epoch is zero

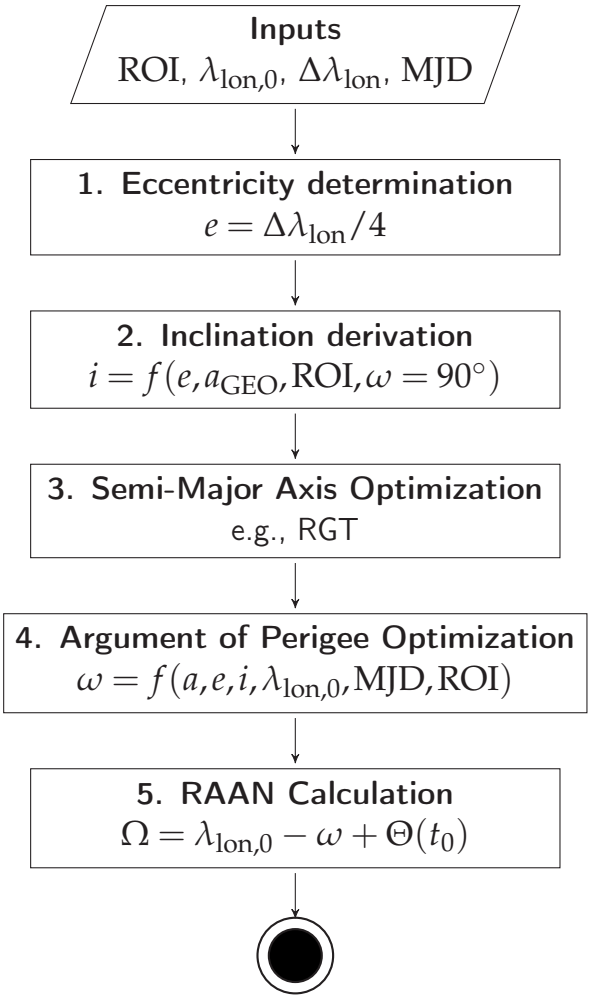

Figure 6.3: Flowchart illustrating the novel approach to derive orbit parameters for an interferometric GEO mission with a minimum zero-perpendicular baseline.

($M_0 = 0$), which corresponds to the satellite being at perigee. Using (6.1), this simplifies to

$$\Omega = \lambda_{\text{lon},0} - \omega + \Theta(t_0) \tag{6.6}$$

Figure 6.4(a) illustrates the relative orbital positions of sub-daily interferometric acquisition pairs in a GEO-SAR mission with an oval ground-track pattern. Figure 6.4(b) presents the corresponding $B_\perp$ for a sample design, calculated for a target in the Alps using an orbit spanning multiple ITU slots ($\Delta\lambda_{\text{lon}} = 0.9°$) and centered at a shifted longitude ($\lambda_{\text{lon},0} = 19°$). The baselines are estimated for acquisition centers in the first half of the orbit (-6 h to 6 h relative to perigee) and their interferometric counterparts, selected to match Doppler characteristics, in the second half of the orbit (6 h to 18 h). Nominal $B_\perp$ values remain below 8 m for various sub-daily pairs.

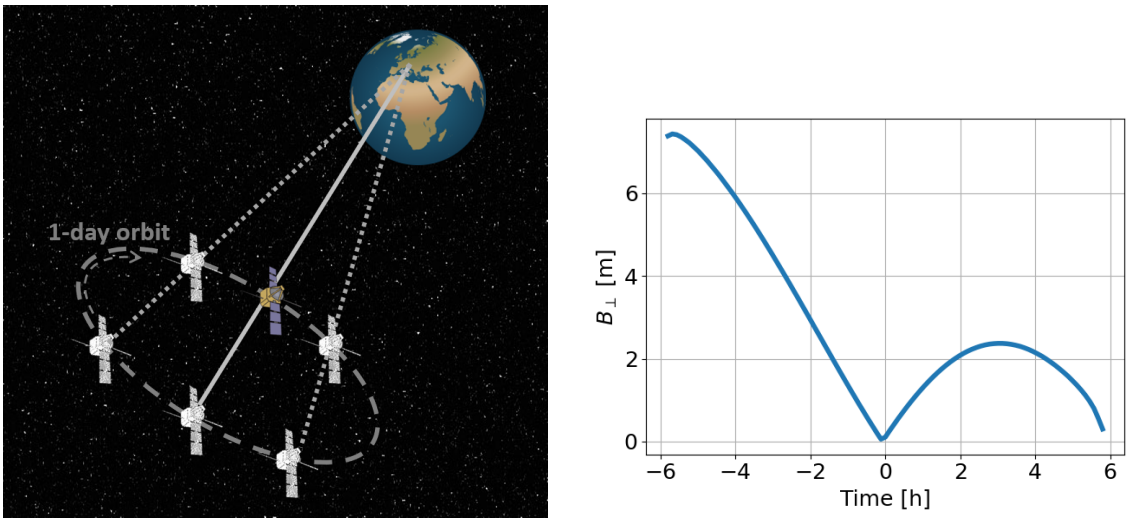

(a) (b)

Figure 6.4: (a) Artistic representation of GEO-SAR sub-daily interferometric acquisition pairs from different orbital positions. (b) Corresponding perpendicular cross-track baselines ($B_\perp$) calculated for an example GEO configuration using the proposed interferometric design approach over a region in the Alps.

6.3 Sub-daily Interferometric GEO-SAR Mission Example

This section presents an example of a GEO-SAR mission optimized for sub-daily interferometric acquisitions. The mission concept is based on Hydroterra, a former candidate from ESA's Earth Explorer 10 program, which proposed a monostatic SAR system in geosynchronous orbit to monitor key diurnal water cycle processes over Europe and Africa [100, 102]. The evolution of the Hydroterra mission concept was informed by the developments described in this section.

The section addresses several critical components essential to the design of observation scenarios in sub-daily interferometric GEO-SAR missions. These include: (1) orbit design, demonstrating the methodology outlined in Section 6.2; (2) the development of an imaging mode for generating acquisition plans that comply with temporal revisit constraints; and (3) the derivation and analysis of potential observation scenarios aligned with the mission's scientific objectives. Some elements of this work have been explored within the Phase-0 Science Study for Hydroterra [215].

Parameter	Value
Antenna type	parabolic reflector
Antenna diameter [m]	7
Frequency [GHz]	5.405
Average transmit power [W]	350
Noise figure [dB]	4
Two-way losses [dB]	3
System bandwidth [MHz]	< 20

Table 6.2: Assumed SAR instrument parameters for assessing observation scenarios in the example sub-daily interferometric GEO-SAR mission.

6.3.1 Requirements and Assumptions

The design of observation scenarios involves balancing user requirements with mission resource constraints. Below is an outline of the key assumptions regarding the available resources of the selected SAR payload, user requirements, and defined products. Additionally, it includes considerations of measurement conditions influenced by environmental and scene-specific factors.

SAR Payload Assumptions

The SAR instrument plays a critical role in determining the overall mission performance. For the analysis and design of observation scenarios, the parameters listed in Table 6.2 are assumed. The example concept features a 7-meter parabolic reflector antenna illuminated by a feed doublet per polarization. This configuration achieves a peak gain of 48 dB and provides a 3-dB footprint with ground extent in the range of 350 km to 600 km from a low-inclined geosynchronous orbit. The design, inherited from Hydroterra, is primarily constrained by platform limitations to ensure compatibility with a potential launch to GEO using a Vega-C launcher [100]. Minor modifications within these constraints, such as adjustments to antenna diameter or transmit power, are discussed at the end of this section.

Product name	Req. (T/G)	Revisit [h]	ML resolution (1-side) [m]	Performance metric (1-σ)
IWV	T	1	5000	$\sigma_\varphi = 0.5$ rad
	G	1	1000	$\sigma_\varphi = 0.5$ rad
SWE	T	6	200	$\sigma_\varphi = 0.5$ rad
	G	3	100	$\sigma_\varphi = 0.5$ rad
Glacier flow	T	6	100	$\sigma_\varphi = 0.5$ rad
	G	6	50	$\sigma_\varphi = 0.5$ rad
Landslides	T	6	100	$\sigma_\varphi = 0.5$ rad
	G	6	50	$\sigma_\varphi = 0.5$ rad
SSM (meteorology)	T	1	5000	$\delta_{\mathrm{rad,dB}} = 0.5\,\mathrm{dB}$
	G	1	1000	$\delta_{\mathrm{rad,dB}} = 0.5\,\mathrm{dB}$
SSM (flood prediction)	T	6	500	$\delta_{\mathrm{rad,dB}} = 0.5\,\mathrm{dB}$
	G	6	200	$\delta_{\mathrm{rad,dB}} = 0.5\,\mathrm{dB}$
SSM (agriculture)	T	3	500	$\delta_{\mathrm{rad,dB}} = 0.5\,\mathrm{dB}$
	G	3	200	$\delta_{\mathrm{rad,dB}} = 0.5\,\mathrm{dB}$
Snowmelt	T	6	200	$\delta_{\mathrm{rad,dB}} = 1.0\,\mathrm{dB}$
	G	6	200	$\delta_{\mathrm{rad,dB}} = 0.5\,\mathrm{dB}$
Flood extent	T	6	200	$\delta_{\mathrm{rad,dB}} = 1.0\,\mathrm{dB}$
	G	6	100	$\delta_{\mathrm{rad,dB}} = 1.0\,\mathrm{dB}$

Table 6.3: Threshold (T) and goal (G) measurement requirements for Hydroterra's interferometric (white rows) and radiometric (grey rows) multilook (ML) products. "1-side" refers to a single side of a squared two-dimensional resolution cell.

User Requirements

The Hydroterra mission example was proposed to support hydrometeorology, hydrology, and land cryosphere studies. The corresponding user requirements can be summarized as a suite of products addressing both primary and secondary mission objectives, along with performance requirements and associated geographical regions of interest for each product.

The Hydroterra products fall into two categories: interferometric products for measuring integrated water vapor (IWV), snow water equivalent (SWE), glacier flow, and landslides; and radiometric products for assessing surface soil moisture (SSM), snowmelt, and flood extent. Table 6.3 lists the corresponding threshold (T) and goal (G) requirements for each product. Revisit time is defined as the interval between independent acquisitions of

the same product over the same region, rather than the interferometric lag. The multilook (ML) resolution is expressed as the side length of a square cell. The key 1-sigma (1-σ) performance metrics include the standard deviation of the interferometric phase error (σ_φ) and the radiometric resolution ($\delta_{\text{rad,dB}}$), as introduced in Chapter 3.

The mission's primary geographical regions of interest have been identified, with time-exclusive operations assigned based on seasonal priorities and emergency response needs. The selected regions and their corresponding observation products are:

- Western Mediterranean: IWV and SSM (for meteorology);
- Western Sahel: IWV and SSM (for meteorology);
- Alpine region: SWE, glacier flow, snowmelt, landslides, flood extent, IWV, and SSM (for meteorology and flood prediction); and
- South Africa: SSM (for agriculture and meteorology), and IWV.

Measurement Conditions Assumptions

The performance of interferometric and radiometric products is influenced by various decorrelation factors, as introduced in Chapter 3. In addition to stable decorrelation sources related to the instrument and imaging geometry, environmental and scene-dependent factors can introduce variability.

Table 6.4 summarizes the assumed values for these factors under best- and worst-case conditions for the different products. These assumptions enable the design of imaging scenarios that account for a range of environmental conditions, ensuring robust performance assessments. The strength of the atmospheric delay fluctuations is characterized by the sill value (σ^2_{atm}), which is used to estimate the atmosphere-induced clutter coherence (γ_{atm}) using the model in (3.51). Radio-frequency interference (RFI) is modeled as an equivalent noise temperature (T_{RFI}) uniformly distributed across the system bandwidth. The impact of RFI with varying characteristics on Hydroterra-like imaging, along with potential mitigation strategies, has been analyzed in [98].

For interferometric products that rely on acquisitions at different time instants and geometries, temporal coherence (γ_{temp}) and volumetric coherence (γ_{vol}) play a significant role. The volumetric coherence depends on the volume height and cross-track perpendicular baseline ($B_\perp$) and can be estimated over forested areas using the model in (3.49).

Product name	**Case (B/W)**	σ^2_{atm} [m^2]	**Temporal coherence**	**Wind speed** [m/s]	**Volume height** [m]	T_{RFI} [K]
IWV	B	0.1e-3	0.95	N/A	5 – 15	-
	W	1e-3	0.7	N/A	5 – 15	2400
SWE	B	5e-6	0.95	N/A	5	-
	W	0.1e-3	0.7	N/A	5	2400
Glacier flow	B	5e-6	0.95	N/A	5	-
	W	0.1e-3	0.7	N/A	5	2400
Landslides	B	5e-6	0.95	N/A	50	-
	W	0.1e-3	0.7	N/A	50	2400
SSM (meteorology)	B	0.1e-3	N/A	0	N/A	-
	W	1e-3	N/A	3	N/A	2400
SSM (flood prediction)	B	5e-6	N/A	0	N/A	-
	W	0.1e-3	N/A	3	N/A	2400
SSM (agriculture)	B	5e-6	N/A	0	N/A	-
	W	0.1e-3	N/A	3	N/A	2400
Snowmelt	B	5e-6	N/A	N/A	N/A	-
	W	0.1e-3	N/A	N/A	N/A	2400
Flood extent	B	5e-6	N/A	0	N/A	-
	W	0.1e-3	N/A	3	N/A	2400

Table 6.4: Best-case (B) and worst-case (W) measurement conditions for Hydroterra's interferometric (white rows) and radiometric (grey rows) products. N/A indicates conditions not applicable to a given product. σ^2_{atm} denotes the variance (sill value) of atmospheric delay fluctuations, and T_{RFI} represents the equivalent noise temperature of radio-frequency interference (RFI).

For radiometric products, decorrelation due to moving clutter within the integration time—induced by the wind—can be quantified using the signal-to-clutter noise ratio (SCNR) from (3.54).

The cross-track perpendicular baselines are determined by the specific design of the reference orbit but are subject to deviations caused by orbital perturbations and station-keeping strategies. These deviations are not considered in the design of observation scenarios and can be addressed separately by evaluating the trade-off between the complexity and cost of orbital maneuvers and the potential loss of observation opportunities due to degraded interferometric performance.

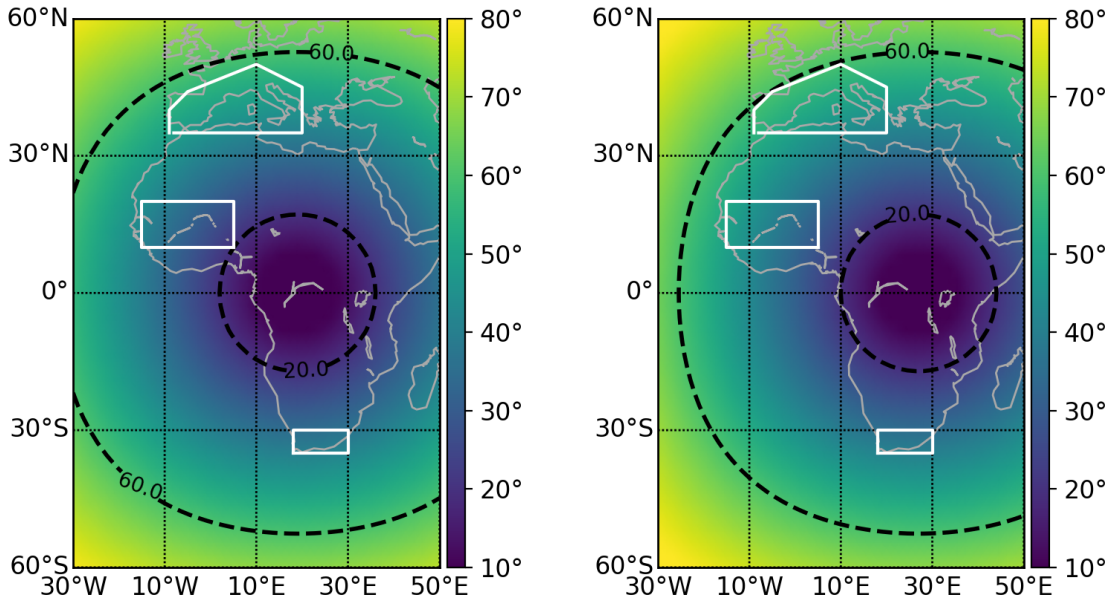

(a) (b)

Figure 6.5: Incident angles for different regions of interest in Europe and Africa, demonstrating the valid range of central longitudes ($\lambda_{\text{lon},0}$) for observation. The regions remain within the specified incident-angle range of 20° to 60° for a nominal central longitude of (a) 19° and (b) 27°.

6.3.2 Design of Sub-daily Interferometric GEO

The orbit design for the sub-daily interferometric mission example follows the five-stage approach outlined in Section 6.2, with minor adjustments to the mission's boundary conditions. These include:

- ensuring geographical accessibility to Europe (specifically the Alpine region and Western Mediterranean) and Africa (specifically Western Sahel and South Africa), with an incident-angle range of 20° to 60°;
- limiting the longitudinal span to a maximum of five ITU slots, including margins; and
- minimizing the cross-track perpendicular baseline ($B_\perp$) for sub-daily interferometric pairs over the Alpine region.

The first condition constrains the range of valid central longitudes ($\lambda_{\text{lon},0}$) for the orbit. As shown in Figure 6.5, all target regions are observable within the specified incident-angle range of 20° to 60°, provided that $19° < \lambda_{\text{lon},0} < 27°$.

The second condition imposes a constraint on the eccentricity. Assuming five available ITU slots at the relevant longitudes, based on Hydroterra

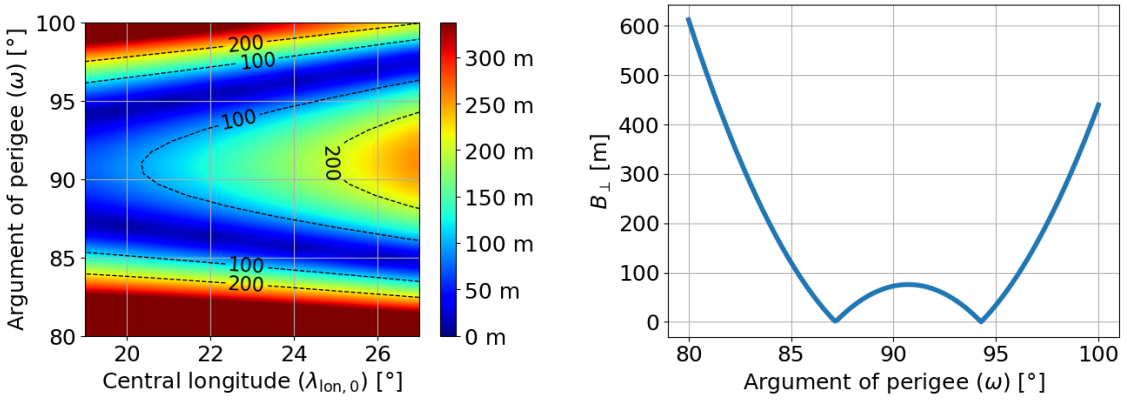

(a) (b)

Figure 6.6: (a) Variation of the cross-track perpendicular baseline ($B_\perp$) as a function of the argument of perigee and the central longitude. (b) Vertical cross-section for $\lambda_{\text{lon},0} = 19°$. The values are computed based on the derived orbital parameters (a, e, and i) and assume a single target, Mont Blanc.

boundary conditions, and incorporating a $0.1°$ margin (ξ), the eccentricity can be computed from (6.3) as

$$e = \frac{\Delta\lambda_{\text{lon}} - \xi}{4} = \frac{5 \cdot 0.2 - 0.1}{4} \cdot \frac{\pi}{180} = 0.003927, \tag{6.7}$$

where the factor $\pi/180$ converts degrees to radians.

The third condition allows for the derivation of the inclination required to satisfy the zero-$B_\perp$ condition, using (6.5). For a reference target in the Alpine region, such as Mont Blanc (geodetic coordinates: 6.87°E, 45.83°N, 4810 m), the inclination required to achieve a zero $B_\perp$ between apogee and perigee acquisitions is $0.02716°$.

The semi-major axis (a) can be numerically determined to satisfy the equality in (2.4), ensuring that the nodal period equals one orbital day. Considering secular variations due to the second zonal harmonic, this results in $a = 42166.2585\,\text{km}$.

The optimization of the argument of perigee, in this case, is a two-dimensional problem that depends on the desired central longitude ($\lambda_{\text{lon},0}$) and $B_\perp$. Figure 6.6(a) illustrates the variation of $B_\perp$ with $\lambda_{\text{lon},0}$ and ω, highlighting regions where $B_\perp$ approaches zero, particularly around $\omega = 90°$. This demonstrates the flexibility in selecting an appropriate central longitude while maintaining the ability to achieve $B_\perp \approx 0$, which facilitates the optimization of the angle of incidence to regions of interest and relaxes constraints on available ITU slots. In this example mission scenario, a central longitude of $\lambda_{\text{lon},0} = 19°$ is chosen to enhance signal returns due to steeper incident angles over Europe compared to higher central longitudes,

Parameter	Value
Semi-major axis (a) [km]	42166.2585
Eccentricity (e)	0.003927
Inclination (i) [°]	0.02716
RAAN (Ω) [°]	284.34913
Argument of perigee (ω) [°]	94.27136
Mean anomaly at epoch (M_0) [°]	0

Table 6.5: Optimized orbital parameters for a GEO-SAR system, constrained to five ITU slots and designed for sub-sidereal interferometry. The reference epoch is 2040-03-21T12:00:00.000Z UTC, with all parameters expressed in the TOD frame.

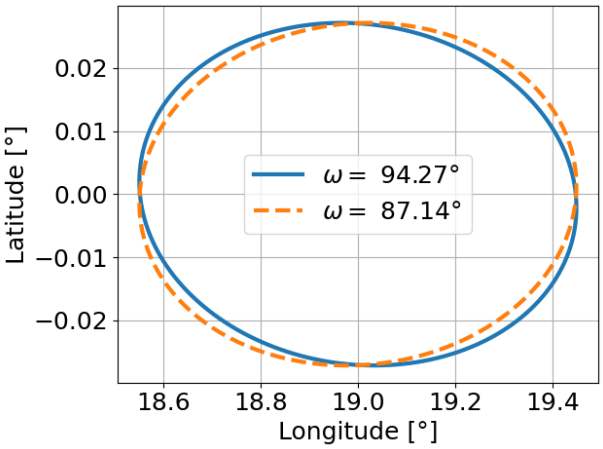

Figure 6.7: Projection of the designed orbit, shown alongside the alternative $\omega = 87.13568°$ solution.

as shown in Figure 6.5. Figure 6.6(b) further indicates that for $\lambda_{\text{lon},0} = 19°$, two values of ω yield near-zero $B_\perp$: $\omega = 87.13568°$ and $\omega = 94.27136°$.

Finally, the longitude of the ascending node is determined from (6.1), resulting in $\Omega = 284.34913°$ for a mean anomaly of $M_0 = 0°$ at the reference epoch of 2040-03-21T12:00:00.000Z UTC. The derived orbital parameters are expressed in the TOD frame and are summarized in Table 6.5. The presented values are the outcome of an initial iteration and can be further optimized to reduce the ΔV budget required for orbit maintenance. The projected trajectory of the designed orbit, along with the alternative ω solution, is shown in Figure 6.7. The resulting latitude variation is constrained to 0.05°, corresponding to a spatial span of 40 km. The longitude span is aligned with the intended 0.9°, centered at $\lambda_{\text{lon},0} = 19°$, and corresponds to a spatial span of approximately 636 km.

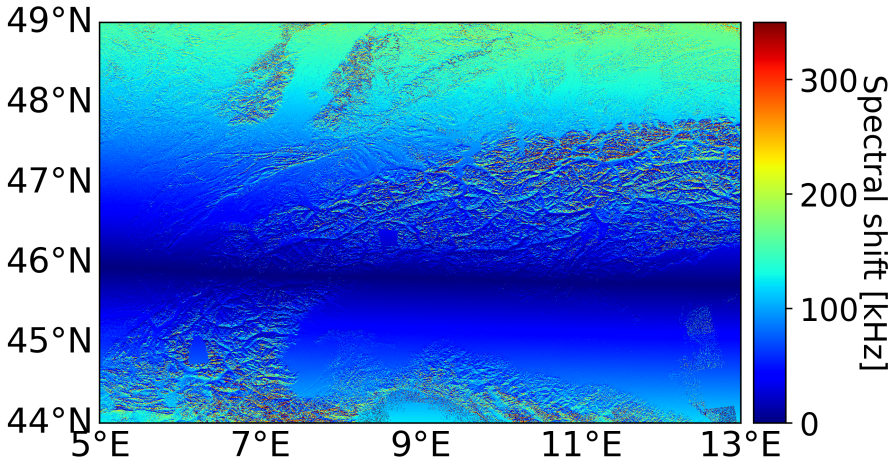

Figure 6.8: Spectral shifts induced by $B_\perp$ in an Alpine region targeted for landslide monitoring. The smallest shifts occur for targets at latitudes similar to Mont Blanc, approximately 45.83°N. Local slopes were estimated using the TanDEM-X 90-m Digital Elevation Model [31].

Figure 6.8 illustrates the spectral shift of the optimized interferometric orbit over an Alpine region for an acquisition pair separated by twelve hours. The shifts, computed using (3.43), result from residual $B_\perp$ and are further amplified by the region's topography. Notably, areas at latitudes comparable to the reference target used for optimization (Mont Blanc, 45.83°N) exhibit near-zero spectral shifts. The terrain slope (ζ) in these calculations is derived from the TanDEM-X 90-m Digital Elevation Model along the South-North direction. This approximation is justified by the predominantly East-West relative motion of the GEO-SAR, as shown in Figure 6.7.

The residual spectral shift over imaged regions results in a reduction of the common bandwidth of the interferogram, thereby decreasing the number of range looks after applying a common band filter.

6.3.3 Design of Observation Scenarios

Unlike low-altitude SAR missions, geosynchronous orbits with low inclination and low eccentricity offer continuous accessibility to a fixed region of the globe. This flexibility necessitates careful analysis of mission objectives and system resources to fully leverage the capabilities of a GEO-SAR mission.

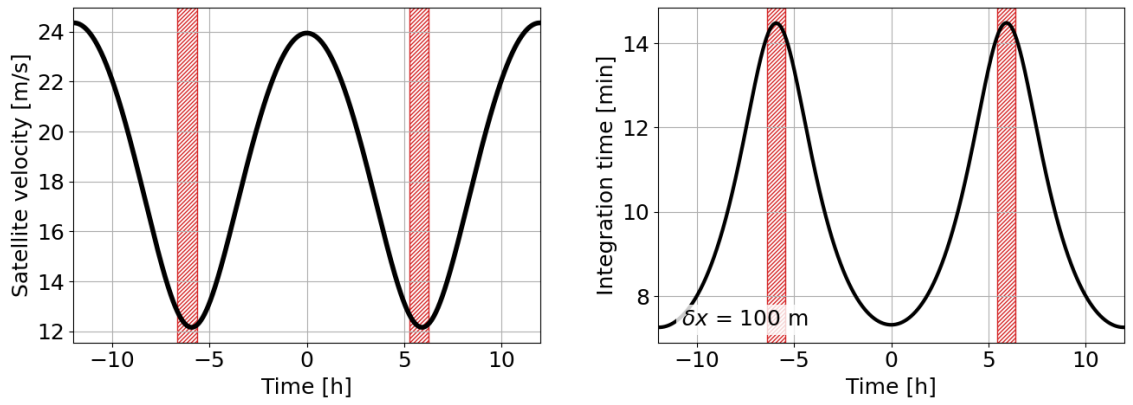

(a) (b)

Figure 6.9: Temporal variation over one orbital period of (a) the satellite's velocity and (b) the required integration time to achieve an azimuth resolution of $\delta x = 100\,\mathrm{m}$. The integration time corresponds to an observation over Mont Blanc from the designed zero $B_\perp$ orbit. Red-patterned vertical bands indicate 1-hour dead zones centered at locations where the Doppler rate approaches zero.

Designing observation scenarios requires balancing user requirements with mission resource constraints while considering expected measurement conditions. These constraints can be broadly categorized into operational constraints, imaging limitations, and SAR payload limitations.

Operational Constraints

Operational constraints primarily determine the duration available for SAR payload operation, which is influenced by electrical energy availability, required downtime, and orbit geometry. Energy availability depends on solar panel generation and, when needed, stored reserves (e.g., batteries) during surplus periods. Downtime encompasses intervals for data downlink, orbital maintenance maneuvers, and energy conservation to replenish storage reserves.

Regarding orbit geometry, Figure 6.9 illustrates the temporal variation of (a) the satellite velocity and (b) the corresponding integration time over Mont Blanc for an azimuth resolution of 100 m over one orbital period. The red-patterned vertical bands indicate dead zones of duration $t_{\mathrm{off}} = 1\,\mathrm{h}$, centered at locations where the Doppler rate approaches zero (approximately at $-6\,\mathrm{h}$ and $6\,\mathrm{h}$ relative to the apsides.[3] The exact duration of these dead zones is a design parameter, as SAR imaging efficiency is significantly reduced in these regions. Consequently, this time can be repurposed for other

[3] The *apsides* refer collectively to the two extreme points in an orbit around a central body, specifically the perigee (closest point) and the apogee (farthest point).

operations or energy conservation. The integration time depends on the orbit's longitudinal extent ($\Delta\lambda_{\text{lon}}$). For instance, reducing this extent from 0.9° to 0.2°, equivalent to a single ITU slot, proportionally increases the required integration time near the apsides from approximately 7.25 minutes to 32.5 minutes.

Given the interferometric nature of the mission, the available time for sub-daily interferometric acquisitions in the proposed orbit geometry can be expressed as

$$t_{\text{av}} = \frac{T_{\text{N}}}{2} - t_{\text{off}}, \tag{6.8}$$

where the nodal period (T_{N}) for GEO is approximately one sidereal day. This available time can be allocated to acquire N_{int} interferometric pairs, such that

$$\left(t_{\text{acq}}(t) + t_{\text{buff}}\right) \cdot N_{\text{int}} \leq \frac{T_{\text{N}}}{2} - t_{\text{off}}, \tag{6.9}$$

where t_{buff} is a time buffer to account for interruptions due to mechanical beam steering within the acquisition, if necessary.

Although the mission is primarily interferometric, imposing a radiometric revisit interval (T_{rev}) leads to a more stringent constraint on scene acquisition time

$$t_{\text{acq}}(t) \leq T_{\text{rev}} - t_{\text{buff}}. \tag{6.10}$$

This constraint ensures a uniform distribution of single acquisition windows along the orbit and limits the maximum number of achievable sub-daily interferometric acquisition pairs to

$$N_{\text{int}} \leq \left\lfloor \frac{T_{\text{N}} - 2 \cdot t_{\text{off}}}{2 \cdot T_{\text{rev}}} \right\rfloor + 1, \tag{6.11}$$

where $\lfloor\rfloor$ is the floor operator. Furthermore, the radiometric revisit requirement imposes stricter constraints on acquisitions away from the apsides, where slower orbital velocities can reduce the scene extent for a fixed azimuth resolution.

Figure (6.10) illustrates the potential distribution of acquisition centers for interferometric acquisitions with one-, three-, and six-hour revisit intervals. In this example, reference acquisitions are evenly distributed around the perigee ($t = 0\,\text{h}$) in the upper part of the orbit projection, where latitudes are positive. The corresponding sub-daily acquisition pairs, selected based on matching Doppler frequencies for a target over the Alps, are located in the lower part of the orbit projection, where latitudes are negative. This distribution enables up to 11 one-hour (dark blue), 4 three-hour (green), or 2 six-hour (red) sub-daily interferometric acquisitions. If the dead zones

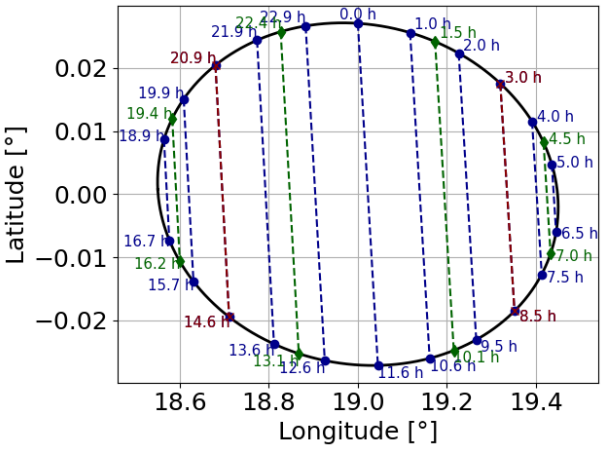

Figure 6.10: Example of sub-daily interferometric pairs obtained from the designed GEO, showing acquisitions with one-, three-, and six-hour revisit intervals over a region in the Alps. Time is referenced to the orbit's perigee.

are extended to two hours each, the number of available one-hour interferometric acquisitions decreases to 9.

SAR Imaging Limitations

SAR imaging from GEO must overcome significant signal losses due to the long propagation path and other decorrelation effects to achieve the desired performance metrics, such as the interferometric phase error (σ_φ) or the radiometric resolution (δ_{rad}). One effective approach is multilooking, which involves averaging multiple statistically independent observations of the same area during processing. Range multilooking requires increasing the chirp bandwidth beyond that required for the desired range resolution cell such that

$$B_{\text{r}} = N_{\text{l,r}} \cdot \frac{c}{2 \cdot \delta g \cdot \sin\theta_{\text{i}}}, \tag{6.12}$$

where $N_{\text{l,r}}$ denotes the number of required range looks. Similarly, azimuth multilooking requires extending the Doppler bandwidth relative to the desired multilook (ML) azimuth resolution cell. This is facilitated using staring or sliding spotlight imaging modes, where the observation time (T_{obs}) is extended beyond the nominal illumination time (T_{SA}), given by

$$T_{\text{obs}}(t) = N_{\text{l,a}} \cdot T_{\text{SA}}(t) = N_{\text{l,a}} \cdot \frac{\lambda \cdot R(t)}{2 \cdot v_{\text{s}}(t) \cdot \delta x}, \tag{6.13}$$

where $N_{\text{l,a}}$ represents the number of required azimuth looks.

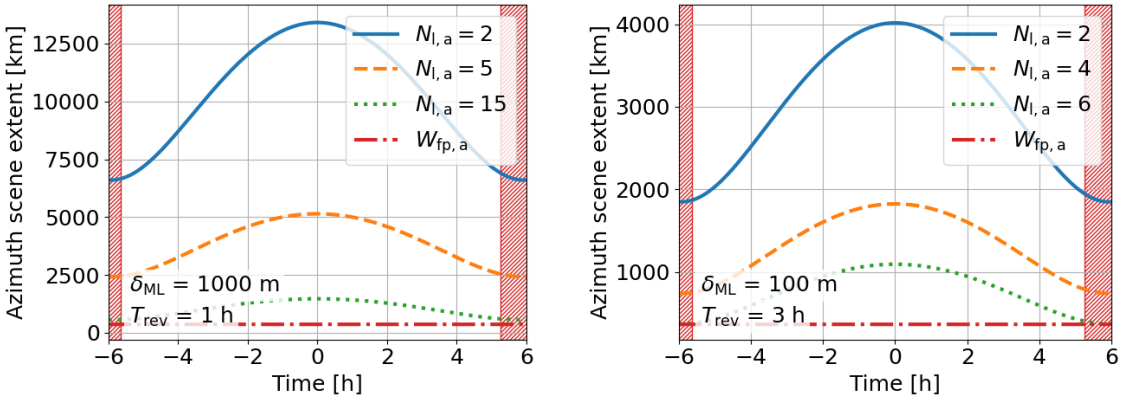

Figure 6.11: Azimuth scene extent as a function of the number of looks at different acquisition centers for two example products over an Alpine region: (a) a revisit time of one hour with an azimuth resolution of 1000 m, and (b) a revisit time of three hours with an azimuth resolution of 100 m. The lower bound is constrained by the azimuth extent of the footprint ($W_{fp,a}$), approximately 367 km for a 7-m-diameter reflector antenna pointed towards Mont Blanc.

In staring spotlight mode, the antenna's main beam remains fixed on the center of the scene throughout the observation, thereby imaging an area approximately equal to the footprint of the antenna beam on the ground. In contrast, during sliding spotlight mode, the beam is continuously steered across a scene with an equivalent beam ground velocity

$$v_g(t) \approx \frac{W_{fp,a}}{T_{obs}(t)} = \frac{W_{fp,a}}{N_{l,a} \cdot T_{SA}(t)}, \tag{6.14}$$

where $W_{fp,a}$ represents the azimuth footprint of the antenna beam on the ground over a certain region of interest. Consequently, for an acquisition duration $t_{acq}(t)$, the azimuth extent of the scene is

$$W_a(t) \approx \left(t_{acq}(t) - T_{obs}(t)\right) \cdot v_g(t) = W_{fp,a} \cdot \left(\frac{t_{acq}(t)}{N_{l,a} \cdot T_{SA}(t)} - 1\right). \tag{6.15}$$

This indicates that if the available acquisition time is shorter than twice the observation time (i.e., $t_{acq}(t) < 2 \cdot N_{l,a} \cdot T_{SA}(t)$), staring spotlight can provide comparable scene coverage more efficiently in terms of time.

Figure 6.11 illustrates the potential azimuth scene extent for varying numbers of azimuth looks at different acquisition centers for two example products over an Alpine region: (a) a revisit time of one hour with an azimuth resolution of 1000 m, and (b) a revisit time of three hours with an azimuth resolution of 100 m. The lower bound, determined by the azimuth extent of the footprint ($W_{fp,a}$), is approximately 367 km for a 7 m-diameter reflector

antenna pointed toward Mont Blanc. If a high number of looks is required to maintain imaging performance over a single footprint, the number of possible acquisitions (N_{int}) may be reduced, or the revisit interval (T_{rev}) may need to be relaxed.

For a fixed scene extent and product resolution, as required in differential interferometry, the shorter acquisition times near the apsides can be leveraged to enhance performance (via increased $N_{\text{l,a}}$), reduce energy consumption or allocate resources to other operations.

SAR Payload Limitations

The SAR payload resources impose performance constraints, determining whether the available operational resources derived above can be fully or partially utilized. The power budget, accounting for transmit power, antenna gain, range bandwidth, losses, and noise characteristics, directly affects the instrument's sensitivity under different measurement conditions. Lower sensitivity necessitates a larger number of looks to compensate for noise from decorrelation sources, reducing the achievable scene extent, as illustrated in Figure 6.11. The SAR instrument parameters for the example Hydroterra concept are listed in Table 6.2.

From Individual Products to Observation Scenarios

Deriving observation scenarios requires a careful evaluation of mission resources for each product and its corresponding user requirements. A comprehensive analysis of a group of products linked by their geographical region of interest—for the Hydroterra example, Western Mediterranean, Western Sahel, Alpine region, and South Africa—enables a trade-off among scene extent (W_{a}), revisit interval (T_{rev}), and the number of products that satisfy the user requirements outlined in Table 6.3.

The trade-off informs the design of candidate observation scenarios exclusive in time and geographical coverage. While the design of non-exclusive scenarios is also feasible, it requires a further redistribution of mission resources, leading to reduced coverage or revisit capability compared to the exclusive case.

Given available resources, the trade-space is populated by estimating the maximum possible azimuth swath extent for each product and revisit time. This is achieved by solving for the minimum number of looks needed to meet the performance requirements on σ_{φ} or δ_{rad}. Priority is given to reducing azimuth looks rather than range looks, as broader scene extents are

achieved through fewer azimuth looks, as indicated by (6.15). The upper bound for azimuth looks is determined from (6.13) and (6.10), by setting the maximum observation time ($T_{\text{obs}}^{\max}(t)$) to the maximum acquisition duration (t_{acq}), which is constrained by the required revisit. This results in

$$N_{\text{l,a}} \leq \frac{T_{\text{obs}}^{\max}(t)}{T_{\text{SA}}(t)} = \frac{T_{\text{rev}} - t_{\text{buff}}}{T_{\text{SA}}(t)}. \tag{6.16}$$

Similarly, the upper bound for range looks is constrained by the maximum available system bandwidth (B_{r}) and is determined using (6.12) as

$$N_{\text{l,r}} \leq (B_{\text{r}} - \Delta f_{\text{r}}) \cdot \frac{2 \cdot \delta g \cdot \sin\theta_{\text{i}}}{c}, \tag{6.17}$$

where Δf_{r} represents the spectral shift caused by $B_{\perp}$ between an interferometric acquisition pair, calculated using (3.43). Δf_{r} is irrelevant for radiometric products and set to zero.

Figure 6.12 illustrates the trade-space by showing variation in maximum azimuth scene extent as a function of revisit interval for the four regions of interest. The results correspond to threshold requirements (T) and were generated using worst-case decorrelation parameters from Table 6.4. To improve readability, meteorology-related products (IWV and SSM Meteo) are omitted from panels (c) and (d), as their relaxed resolution requirements allow for significantly larger scene extents, as shown in panels (a) and (b). Similar plots can be generated for best-case conditions or by excluding specific decorrelation sources, such as RFI, to better understand their impact on performance and, consequently, scene extent.

Certain products impose stricter requirements than others in each of the four regions shown in Figure 6.12. This leads to two possible design approaches: (i) constrain the scene extent and revisit interval to meet the demands of the most restrictive product, ensuring that a single scenario provides valid data for a broader range of products, or (ii) group products with similar requirements into separate scenarios, allowing for larger swath extents and shorter revisit intervals, but with data tailored to a more specific subset of products.

The following analysis explores candidate observation scenarios for each of the four regions. The suggested scenarios satisfy threshold requirements to meet mission objectives under varying conditions. While goal requirements are more demanding and offer enhanced capabilities if achieved, they remain optional; thus, they are assessed but do not necessarily dictate the sizing of the observation scenarios.

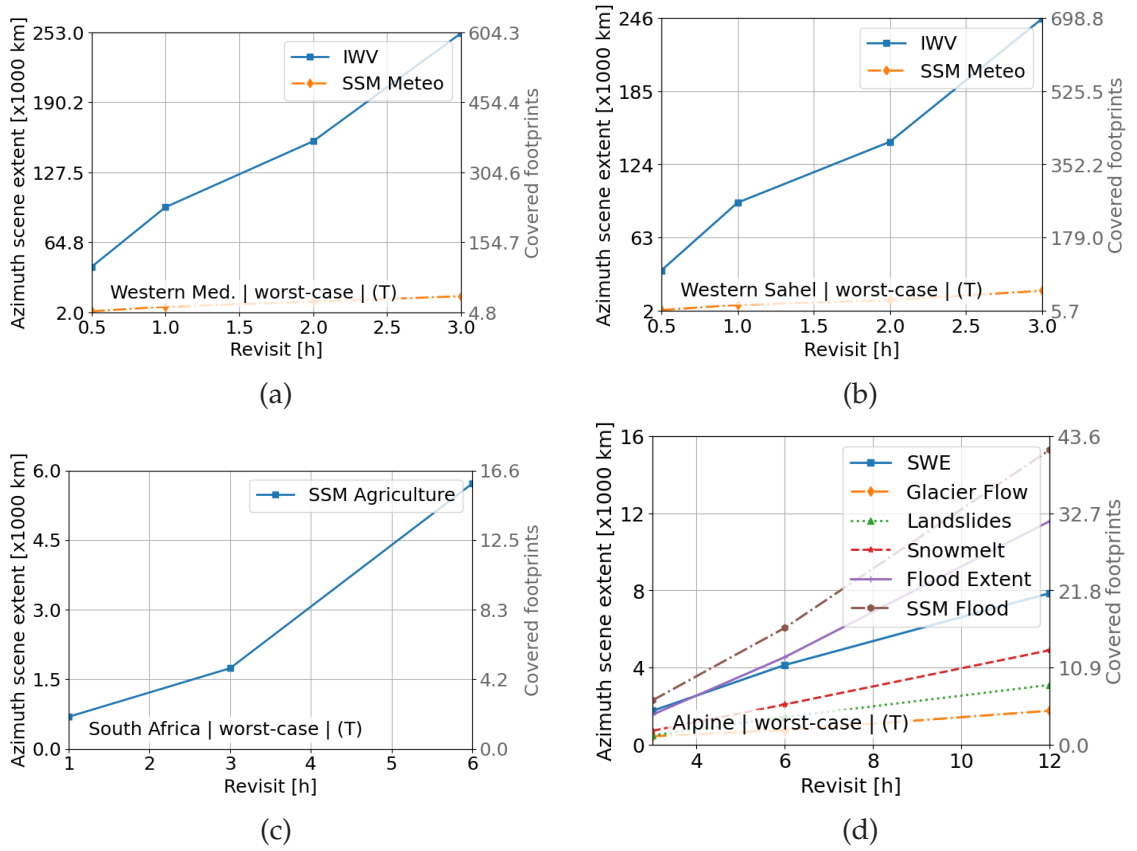

Figure 6.12: Maximum azimuth scene extent as a function of revisit interval for the four geographical regions of interest: (a) Western Mediterranean, (b) Western Sahel, (c) South Africa, and (d) the Alpine region. The results correspond to threshold requirements (T) and are generated using worst-case decorrelation parameters from Table 6.4. Meteorology-related products (IWV and SSM Meteo) are excluded from panels (c) and (d) for improved readability.

The Western Mediterranean region, as defined by the polygon in Figure 6.5, spans approximately 4 Mkm^2 ("M" denotes million). Assuming a reflector antenna with a diameter of 7 m and an elevation footprint of about 525 km over the region, full coverage of the outlined area would require an azimuth extent of approximately 8000 km.

In this region, SSM Meteo is the most demanding product. Under threshold requirements, a one-hour revisit interval enables an azimuth swath extent of approximately 7000 km, potentially covering a substantial portion of the target area. For IWV, the additional resources allow for an enhanced resolution of 1 km^2, meeting the goal requirements, compared to the threshold resolution of $(5\,\text{km})^2$ used in Figure 6.12(a). Under goal requirements for SSM Meteo, a resolution of 1 km^2 restricts the swath extent to 1500 km, covering only about 15% of the designated region.

Scenario	Coverage [Mkm^2]	Revisit [h]	Product name	ML resolution (1-side) [m]
Western Med. (WM)	1.8	1	IWV	500
			SSM Meteo	2500

Table 6.6: Potential observation scenario for Hydroterra over the Western Mediterranean region. "1-side" refers to one side of the multilook (ML) squared two-dimensional resolution cell.

Scenario	Coverage [Mkm^2]	Revisit [h]	Product name	ML resolution (1-side) [m]
Western Sahel (WS)	1	1	IWV	500
			SSM Meteo	2500

Table 6.7: Potential observation scenario for Hydroterra over the Western Sahel region. "1-side" refers to one side of the multilook (ML) squared two-dimensional resolution cell.

Table 6.6 summarizes the candidate scenario and achievable product resolutions, considering worst-case conditions and the example SAR instrument from Table 6.2. The proposed scenario balances threshold and goal SSM Meteo requirements, enabling a $(2.5\,\mathrm{km})^2$ resolution with the assumed instrument and conditions. This configuration covers approximately half of the designated area, which is sufficient to meet the mission's scientific objectives.

The Western Sahel region, as defined by the polygon in Figure 6.5, spans approximately 2.5 Mkm^2. Assuming a 7-m-diameter antenna with an elevation footprint over the region of about 360 km, full coverage of the outlined area would require an azimuth extent of approximately 7000 km.

As in the Western Mediterranean region, SSM Meteo is the most demanding product. Under threshold requirements, an azimuth extent of approximately 6700 km can be covered, closely matching the extent of the defined polygon. For IWV, additional resources allow for an increased resolution of 1 km^2, meeting the goal requirement. Under goal requirements for SSM Meteo, achieving a 1 km^2 resolution limits the swath extent to 1000 km, covering only 15% of the designated polygon area.

Table 6.7 summarizes the candidate scenario and achievable product resolutions under worst-case conditions. The proposed scenario balances threshold and goal SSM Meteo requirements, enabling spatial resolutions

Scenario	Coverage [Mkm^2]	Revisit [h]	Product name	ML resolution (1-side) [m]
South Africa (SA)	0.6	3	SSM Agriculture	500
			SSM Meteo	700
			IWV	250
South Africa 2 (SA2)	0.167	3	SSM Agriculture	200
		1	SSM Meteo	500
		1	IWV	250

Table 6.8: Potential observation scenarios for Hydroterra over South Africa. South Africa 2 (SA2) is covered with a staring spotlight mode to achieve the required resolution for SSM agriculture. "1-side" refers to one side of the multilook (ML) squared two-dimensional resolution cell.

similar to the Western Mediterranean scenario. This configuration allows to cover a span of 1 Mkm^2, corresponding to 40% of the outlined area.

The South African region, as defined by the polygon in Figure 6.5, spans approximately 0.8 Mkm^2. Assuming a 7-m-diameter antenna with an elevation footprint over the region of about 460 km, full coverage of the region would require an azimuth extent of approximately 1800 km.

The primary product in this region is SSM for agriculture. Under threshold requirements, 75% of the outlined region can be covered with a three-hour revisit interval. Enhancing the spatial resolution to meet the goal requirement of $(200\,\mathrm{m})^2$ reduces the covered area to a single footprint of approximately 167 000 km^2. This can be achieved by operating the SAR in staring spotlight mode, enabling the generation of diverse revisit products by exploiting the temporal diversity of a continuous acquisition interval (e.g., up to eleven hours), and trading longer illumination times (or higher resolution) for more frequent revisits during processing.

Based on these considerations, two candidate observation scenarios are proposed to accommodate both threshold and goal requirements, as summarized in Table 6.8. The listed resolutions represent achievable values under worst-case conditions.

The Alpine Region spans 1200 km, extending from France to Slovenia, closely aligning with the satellite's azimuth direction.

For a six-hour revisit interval, all threshold requirements can be met for a maximum azimuth extent of 528 km. This coverage can be extended to 800 km by reducing the glacier flow spatial resolution to $(120\,\mathrm{m})^2$. The full 1200 km stretch could be covered in the absence of strong RFI or through

Scenario	Coverage [Mkm^2]	Revisit [h]	Product name	ML resolution (1-side) [m]
Alps North (AN)	0.45	6	Glacier flow	110
			Landslides	100
			Snowmelt	200
			SWE	150
			Flood extent	100
			SSM Flood	200
			IWV	150
			SSM Meteo	150
Alps Center (AC)	0.257	12	Glacier flow	50
		12	Landslides	50
		3	Snowmelt	200
		3	SWE	100
		3	Flood extent	100
		3	SSM Flood	200
		1	IWV	200
		1	SSM Meteo	250

Table 6.9: Potential observation scenarios for Hydroterra over the Alpine region. Alps North employs sliding spotlight mode, whereas Alps Center employs starring spotlight mode over a single footprint. "1-side" refers to one side of the multi-look (ML) squared two-dimensional resolution cell.

effective RFI mitigation [98]. Alternatively, increasing the revisit interval to twelve hours allows for the required coverage.

The goal requirements, particularly the need for higher spatial resolution in glacier flow and landslide monitoring, as well as the shorter revisit interval for SWE, restrict the possible coverage to a single footprint. By employing a staring spotlight mode, a range of products and revisit intervals can be achieved over a fixed footprint. Based on these considerations, two candidate observation scenarios are proposed for this region, as summarized in Table 6.9. Scenario Alps North (AN) covers a swath extent of approximately 800 km, fulfilling the goal requirements for flood extent and SSM flood monitoring. In contrast, the Alps Center (AC) scenario covers a single footprint of approximately 257 000 km^2, enabling continuous monitoring while maintaining flexibility to accommodate various products with different revisit intervals. The values in Table 6.9 illustrate a possible configuration that aligns with user requirements.

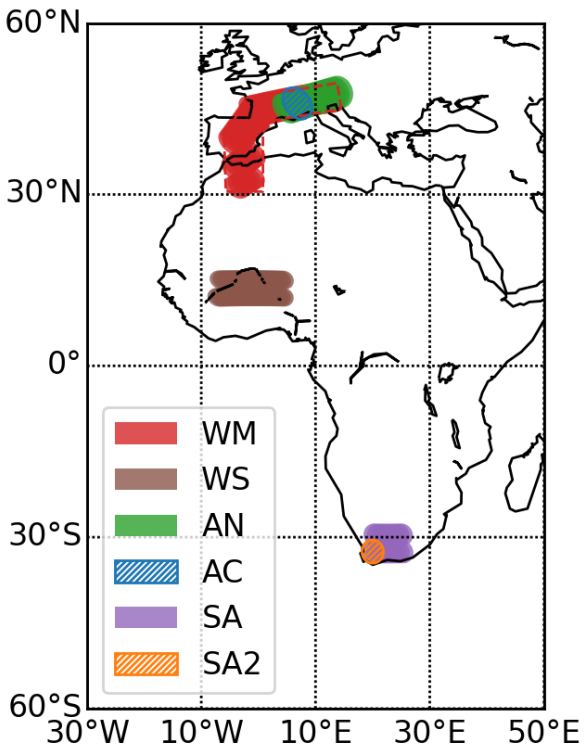

Figure 6.13: Candidate observation scenarios for the Hydroterra Mission over Europe and Africa, optimized through a trade-off between user requirements and mission resources. The following abbreviations correspond to the scenarios: WM – Western Mediterranean; WS – Western Sahel; AN – Alps North; AC – Alps Center; SA – South Africa; SA2 – South Africa 2.

Figure 6.13 illustrates the geographical span of the six derived candidate observation scenarios, closely resembling the one proposed for the Hydroterra concept in the Phase-0 study. Note that interrupted sliding spotlight swaths, such as those used in the WM, WS, or SA scenarios, result in a minor loss of swath extent

$$W_{\mathrm{a,loss}} \approx v_{\mathrm{g}} \cdot \left(T_{\mathrm{SA}} \cdot N_{\mathrm{l,a}} + t'_{\mathrm{buff}} \right), \tag{6.18}$$

which corresponds to the portion of the acquisition time that does not yield the required resolution, assuming a constant beam velocity (v_{g}), along with a short buffer time (t'_{buff}) needed for mechanical steering to the adjacent stripe.

6.3.4 Distribution of Interferometric Lags

The hybrid nature of the mission products imposes a constraint on the maximum number of interferometric acquisition pairs (N_{int}), which is limited

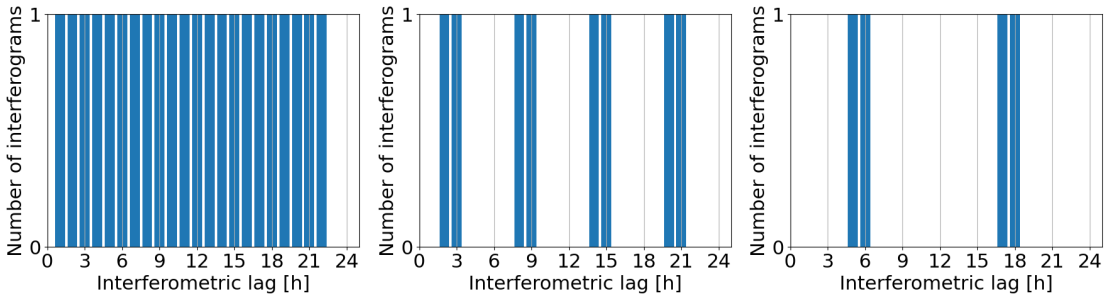

Figure 6.14: Possible distribution of sub-daily interferometric lags for Hydroterra complying with the radiometric revisit intervals of (a) one hour, (b) three hours, and (c) six hours.

by the revisit interval (T_{rev}) used for radiometric products, as defined in (6.11). These acquisitions potentially enable the formation of L_{sub} sub-daily interferometric lags, given by

$$L_{\text{sub}} = 2 \cdot N_{\text{int}} \leq 2 \cdot \left(\left\lfloor \frac{T_{\text{N}} - 2 \cdot t_{\text{off}}}{2 \cdot T_{\text{rev}}} \right\rfloor + 1 \right). \tag{6.19}$$

The factor of 2 accounts for lags from interferograms formed by (i) the acquisition pairs at t_{ref} and $t_{\text{ref}} + \Delta t_{\text{lag}}$, and ii) the acquisition pairs at $t_{\text{ref}} + \Delta t_{\text{lag}}$ and $t_{\text{ref}} \pm T_{\text{N}}$. Figure 6.14 illustrates the distribution of sub-daily interferometric lags for the Hydroterra mission, considering radiometric revisit intervals of (a) one hour, (b) three hours, and (c) six hours. For a one-hour revisit interval, the mission can generate up to 22 sub-daily interferograms for low-resolution products. This includes four acquisitions near the dead zones, corresponding to the acquisition pairs (5 h, 6.5 h) and (16.7 h, 18.9 h) in Figure 6.10. If performance is constrained near the edges or adjustments to the dead zone window are required, the number of available sub-daily lags may decrease to 20 or 18. For longer revisit intervals, the mission can provide 8 and 4 sub-daily interferometric lags for the three-hour and six-hour revisit products, respectively.

6.3.5 Implications of System and Orbit Design Alterations

System Design

Reducing the average transmit power (e.g., from 350 W to 175 W) or antenna diameter (e.g., from 7 m to 5 m) simplifies the SAR payload and decreases the overall volume and mass of the spacecraft. However, these

modifications also impact SAR performance and, consequently, the achievable mission products.

A reduction in average transmit power primarily affects high-resolution products, such as those targeting the Alpine region, where thermal noise-induced decorrelation becomes comparable to other decorrelation sources. This degradation can be mitigated by lowering the resolution or reducing scene extent. Notably, the 2-D resolution cell size reduction would scale proportionally with power only if thermal noise remains the dominant decorrelation source.

Similarly, a decrease in antenna diameter leads to reduced gain and increased susceptibility to RFI due to a larger footprint. As with power reductions, this impacts the power budget and negatively affects high-resolution products where thermal noise and RFI are dominant decorrelation factors. For example, achieving 50-m resolution for monitoring landslides and glacier flow in the Alpine region becomes unfeasible, even with a 12-hour revisit time over a single footprint, necessitating a resolution reduction. Nonetheless, lower-resolution products for the same region remain viable at the expense of reduced revisit frequency or resolution. However, an increased antenna footprint offers advantages in scenarios where thermal decorrelation is less significant, such as in the Western Mediterranean and Western Sahel. The larger footprint enables broader scene coverage with minimal impact on low-resolution products in these scenarios.

Orbit Design

In orbit design, reducing the longitudinal extent to minimize the number of required ITU slots affects the achievable system performance. Specifically, a reduction factor k_{red}, defined relative to a reference number of ITU slots ($N_{\text{ITU,ref}}$), leads to a proportional decrease in eccentricity and relative satellite velocity, which necessitates an inversely proportional increase in illumination time for a fixed azimuth resolution. This relationship is expressed as

$$k_{\text{red}} = \frac{N_{\text{ITU,ref}}}{N_{\text{ITU}}} = \frac{\Delta\lambda_{\text{lon,ref}}}{\Delta\lambda_{\text{lon}}} \approx \frac{e_{\text{ref}}}{e} \approx \frac{v_{\text{s,ref}}}{v_{\text{s}}} \approx \frac{T_{\text{SA}}}{T_{\text{SA,ref}}}, \tag{6.20}$$

where subscript "$_{\text{ref}}$" denotes reference design parameters.

According to (6.15), increasing the illumination time extends the observation time (T_{obs}) for a fixed number of azimuth looks. This assumption disregards potential adjustments in azimuth looks required to maintain product

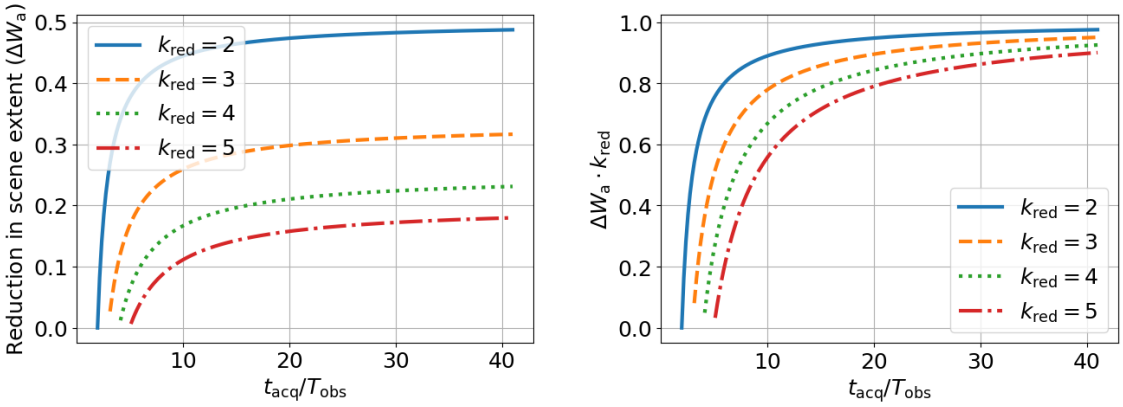

(a) (b)

Figure 6.15: Impact of reduction in ITU slots in a low-inclination, low-eccentricity GEO-SAR on scene extent. a) Variation of scene extent reduction (ΔW_a) as a function of the acquisition-to-observation time ratio (t_{acq}/T_{obs}) for different longitude or slot reduction factors (k_{red}). (b) Scene extent reduction normalized by k_{red} to better understand proportionality.

performance due to increased atmospheric or clutter decorrelation. Under this assumption, the reduction in azimuth scene extent is given by

$$\Delta W_a = \frac{W_{a,ref}(t)}{W_a(t)} \approx \frac{t_{acq}(t) - T_{obs}(t)}{t_{acq}(t) - k_{red} \cdot T_{obs}(t)}, \tag{6.21}$$

where the acquisition window (t_{acq}) is constrained by the revisit interval of the radiometric products, as defined in (6.10).

Figure 6.15(a) illustrates the exponential decline in azimuth scene extent as the acquisition-to-observation time ratio decreases for different reduction factors (k_{red}). The results indicate that in the best-case scenario, where the acquisition-to-observation time ratio is relatively high, the scene extent reduction (ΔW_a) is approximately proportional to k_{red}, as shown in Figure 6.15(b). However, the reduction becomes significantly more pronounced for smaller ratios, leading to a substantial decrease in coverage.

Furthermore, longer integration times increase signal decorrelation in the atmosphere, potentially requiring additional looks, which may further constrain the usable scene extent. As with previous cases, this reduction can be partially mitigated by decreasing resolution and adjusting the revisit frequency to achieve performance requirements.

For instance, in the case of a single ITU slot, corresponding to $k_{red} = 0.45$ compared to a reference $\Delta\lambda_{lon} = 0.9°$, the scene extent for the Western Mediterranean and Western Sahel scenarios would be reduced to approximately 400 km for a one-hour revisit. This extent could be increased to

800 km by extending the revisit interval to three hours or degrading the resolution by 3 dB. For scenarios with higher-resolution products, such as Alps North and South Africa, different products can be accommodated within a single footprint, though some may require additional reduction in revisit time or resolution.

6.4 Chapter Remarks

This chapter examined the potential of geosynchronous Earth orbits for interferometric SAR missions with frequent revisits. It developed a specialized orbit concept for sub-daily interferometric acquisitions, aiming to minimize cross-track perpendicular baselines. Additionally, it proposed a novel framework for the efficient allocation of mission resources and outlined key design considerations for interferometric GEO-SAR missions. The developments presented herein laid the groundwork for designing the observation scenarios for Hydroterra, a former candidate for ESA's Earth Explorer 10 program.

Section 6.2 presented the derivation of the specialized GEO concept, introducing a novel trigonometric equation for estimating orbital inclination, with a complete derivation provided in Appendix A. Section 6.3 demonstrated the application of this orbital concept in a concrete mission example based on Hydroterra. Furthermore, this section proposed a systematic approach for generating observation scenarios in GEO-SAR missions, capitalizing on their continuous accessibility to a fixed portion of the globe. The approach was supported by the derivation of design metrics to characterize operational and imaging constraints.

The complexity of this mission concept, introduced in Section 6.3, will be further evaluated in Chapter 7, where it is compared to an equivalent LEO-SAR constellation.

7 Equivalent LEO-SAR Constellations to Higher Orbit Systems

Satellite constellations[1] play a crucial role in enhancing the capabilities of SAR systems, especially in LEO. They enable frequent revisits, expanded coverage, improved resolution, single-pass interferometry or tomography, and distinct imaging geometries. These features support numerous applications, including digital elevation model (DEM) generation, 2-D/3-D motion estimation, and target detection and tracking. State-of-the art SAR constellations include TerraSAR-X/TanDEM-X [28], Sentinel-1A/B/C [35], SAOCOM-1A/B [216], RADARSAT [185], ICEYE [48], Capella [49], COSMO-SkyMed [25], and Umbra [52], among others.

In SAR mission design, a constellation-based approach enables the distribution of a single SAR satellite's capabilities across multiple smaller satellites. This approach reduces the complexity of individual spacecraft, particularly in terms of SAR payload and corresponding platform requirements, by replacing a single, highly complex satellite with multiple less-complex satellites. This trade-off offers advantages, including improved payload efficiency, enhanced agility, increased redundancy, and cost benefits per unit due to economies of scale. However, it also introduces challenges, such as formation flying, constellation management, data downlink constraints, and launch configuration complexities.

The systems required for the high-altitude missions in Chapters 5 and 6 are intricate and complex, driven by the increased free-space propagation loss and launch costs. As outlined in previous chapters, these challenges can be mitigated using larger antenna structures, digital beamforming, and possibly electric propulsion for progressive orbit raising from low-Earth parking orbits. This situation introduces an opportunity for competitive low-altitude constellations composed of simpler, lighter satellites.

This chapter explores LEO-SAR constellations designed to function as alternatives to higher-altitude SAR systems. It introduces a novel comparison framework illustrated by three realistic mission concepts analogous to the example designs presented in Chapters 5 and 6. The primary focus is distributing the unique coverage and temporal revisit capabilities of

[1] In this thesis, the term *constellation* is used to also encompass close formations, such as TanDEM-X and TerraSAR-X.

high-orbit systems across a constellation of simple monostatic SAR satellites. Figure 7.1 shows a realization of a LEO-SAR constellation designed to match the performance of a high-altitude, wide-swath MEO-SAR system. The individual satellites of the constellation can cover narrower swaths, which collectively match the wide-swath capabilities of higher-altitude systems. Acquisitions can be simultaneous, non-simultaneous, or squinted to achieve equivalent performance.

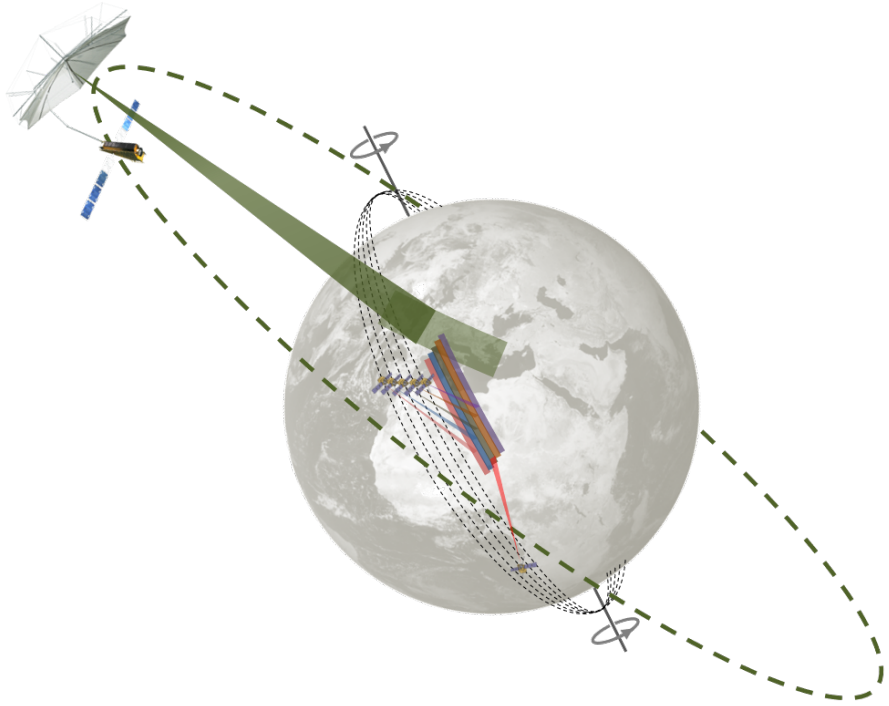

Figure 7.1: A realization of a LEO constellation of simple SAR satellites equivalent to a high-altitude MEO-SAR system.

Section 7.1 presents the theoretical framework for system equivalence and introduces system capacity as a metric for assessing equivalence. Section 7.2 outlines the methodology for distributing the system capacity in space and time, providing a new design concept for efficient constellations capable of distributing both swath and interferometric revisit. Section 7.3 presents the equivalent constellations for the three high-orbit mission concepts introduced earlier, offering realistic figures for instrument design and constellation sizes.

Parts of this material have been previously published in [217–219].

7.1 Equivalence Framework

The equivalence of SAR missions can be defined by their ability to deliver comparable end products that align with consistent mission objectives. Key factors include:

- operational frequency,
- 2-D resolution, including single-look complex (SLC) or multilook (ML) products,
- geometry (swath or incident-angle range),
- revisit frequency,
- geographical coverage,
- polarimetric channels, and
- interferometric or tomographic capabilities.

Besides, the products must maintain comparable quality (or performance) metrics, such as ambiguity rejection and NESN. Additional metrics such as radiometric resolution, thermal phase noise threshold, and accuracy in 3-D deformation measurements may also be relevant depending on the specific mission requirements.

Beyond this generic equivalence definition, SAR missions acquire an average number of independent samples per second, referred to in this thesis as system capacity (C_{SAR}). System capacity can be increased by increasing system complexity—to allow expanding swath width, improving resolution, or extending orbit duty cycle—or by deploying additional satellites. A thorough understanding of these contributing factors enables an optimized distribution of system complexity and, ultimately, a fair determination of an equivalent constellation size that achieves the same capacity.

7.1.1 System Capacity

The system capacity is defined as the average rate of acquired samples per second. It can be expressed as

$$C_{\mathrm{SAR}} = \frac{W_{\mathrm{s}}}{\delta r} \cdot \frac{W_{\mathrm{a}}}{\delta x} \cdot \frac{1}{T_{\mathrm{N}}} = \frac{W_{\mathrm{s}}}{\delta r} \cdot \frac{v_{\mathrm{g}}}{\delta x} \cdot \eta_{\mathrm{orb}}, \tag{7.1}$$

where W_{s} is the swath width measured in slant range, and W_{a} is the total azimuth extent (length) of the acquired swath over a single orbit. T_{N}

denotes the nodal period of the orbit, and η_{orb} is the orbit duty cycle, defined as the ratio between the active time per orbit during which the SAR is operational and the nodal period T_{N}. The terms δr and δx represent the resolution in slant range and azimuth, respectively, and v_{g} is the ground velocity of the radar beam.

This metric can be linked to system complexity by a breakdown of the individual terms into their respective SAR payload and spacecraft subsystem metrics. From (4.12) and (3.11), the ratio of slant-range swath width to resolution is expressed as

$$\frac{W_{\text{s}}}{\delta r} \approx \frac{2 \cdot B_{\text{r}} \cdot \lambda \cdot R \cdot \tan\theta_{\text{i}} \cdot k_{\text{s}}}{c \cdot H_{\text{a}}}, \tag{7.2}$$

where B_{r} is the range bandwidth, λ is the wavelength, R is the slant range, θ_{i} is the incident angle, H_{a} is the antenna height, and k_{s} is a correction factor accounting for the difference between the actual antenna aperture and its approximation λ / H_{a}. Similarly, from (4.7) and (4.8), the ratio of beam velocity to azimuth resolution is given by

$$\frac{v_{\text{g}}}{\delta x} = \frac{2 \cdot v_{\text{s}}}{L_{\text{a}} \cdot k_{\text{x}}}, \tag{7.3}$$

where v_{s} is the relative speed of the platform, L_{a} is the antenna length, k_{x} is a constant that accounts for the relationship between the factor λ / L_{a} and the azimuth beamwidth (θ_{az}), as well as any azimuth oversampling. Combining these two ratios results in

$$C_{\text{SAR}} \approx \frac{B_{\text{r}} \cdot \lambda \cdot \eta_{\text{orb}}}{L_{\text{a}} \cdot H_{\text{a}}} \cdot \left(\frac{4 \cdot v_{\text{s}} \cdot R \cdot \tan\theta_{\text{i}} \cdot k_{\text{s}}}{c \cdot k_{\text{x}}} \right) = \frac{B_{\text{r}} \cdot \lambda \cdot \eta_{\text{orb}}}{L_{\text{a}} \cdot H_{\text{a}}} \cdot k_{\text{c}}, \tag{7.4}$$

where k_{c} is a geometric factor representing the term inside the parentheses. The range bandwidth can be further connected to the system's sensitivity and antenna characteristics. By combining the relations from (3.29) and (3.59), it can be described as

$$B_{\text{r}} = \eta_{\text{ant}}^2 \cdot L_{\text{a}}^2 \cdot H_{\text{a}}^2 \cdot P_{\text{avg}} \cdot \text{NESN}_{\text{th}} \cdot \lambda \cdot k_{\text{r}}, \tag{7.5}$$

where η_{ant} is the antenna efficiency, P_{avg} is the average transmit power, and k_{r} is a constant that combines system and geometry factors derived from the NESN expression

$$k_{\text{r}} = \frac{c}{16 \cdot \pi \cdot R^3 \cdot v_{\text{s}} \cdot \sin\theta_{\text{i}} \cdot F_{\text{s}} \cdot k_{\text{B}} \cdot T_0}, \tag{7.6}$$

where F_s is the system noise factor, k_B is Boltzmann's constant, and T_0 is the standard temperature. The average transmitted power can be further linked to the spacecraft's complexity by expressing it as

$$P_{avg} = P_{sat} \cdot \eta_{plat} \cdot \eta_{SAR}, \tag{7.7}$$

where P_{sat} denotes a representative measure of the spacecraft's power consumption (e.g., considering the selected platform, solar panel capacity, and thermal design complexity), η_{plat} describes the power efficiency of the platform excluding the SAR payload, and η_{SAR} is an efficiency term associated with the imaging mode of the SAR instrument, as detailed in Appendix B. Substituting (7.5) and (7.7) into (7.4) yields

$$C_{SAR} = k_M \cdot \eta_{ant}^2 \cdot L_a \cdot H_a \cdot P_{sat} \cdot \eta_{plat} \cdot \eta_{SAR} \cdot \eta_{orb} \cdot \mathrm{NESN}, \tag{7.8}$$

where $k_M = k_c \cdot k_r$ is a parameter that depends on the system's noise characteristics and the observation geometry. This equation quantifies the amount of information the system can measure as a function of parameters directly proportional to system quality and complexity. It shows that the analogous performance of two systems requires

$$\eta_{ant}^2 \cdot L_a \cdot H_a \cdot P_{sat} \cdot \eta_{plat} \cdot \eta_{SAR} \cdot \eta_{orb} \tag{7.9}$$

to be roughly constant. It should be noted that the above equations are asymptotic and assume some implicit factors, such as the effects of antenna pattern shape, the resolution area distribution, and the dependencies of SNR or NESN on the incident angle.

7.1.2 System Simplification Concepts

The complexity of SAR payloads arises from the need to surpass the natural system capacity of a simple instrument. This challenge primarily stems from the conflicting demands of achieving high resolution and wide swath coverage while maintaining the required sensitivity and ambiguity rejection, leading to an inherent trade-off between system capacity and complexity.

The proposed simplification concept distributes the capacity of a complex monostatic SAR satellite across multiple, typically identical, less-complex satellites such that

$$C_{SAR,ref} = \sum_{i=1}^{N_{sat}} C_{SAR,i}, \tag{7.10}$$

where N_{sat} represents the number of satellites in the equivalent constellation, and $C_{SAR,ref}$ denotes the system capacity of the reference. Additionally, a design approach emphasizing low complexity enables a fair comparison of systems by exploiting the key advantage of constellations, namely the use of small, lightweight platforms.

The most efficient distribution, incorporating factors introduced in (7.9), can be achieved by substituting a wide-swath complex system with a constellation of monostatic SAR satellites. Each satellite covers a portion of the swath while maintaining a similar resolution cell area and adhering to the natural swath-resolution relationship. This approach enables a modest reduction in antenna area, close to the minimum area constraint defined in (4.13), and a reduction in power demands. Additionally, it allows maximizing the system capacity of each satellite within the constellation by addressing inefficiencies related to the antenna (e.g., surface utilization during transmission and reception), imaging mode (e.g., stripmap vs. ScanSAR), instrument design (e.g., reducing lossy elements), propagation, and redundant coverage.

Further reductions in antenna size and power consumption can be achieved by replacing each monostatic SAR unit with a set of multistatic SAR units. However, this approach sacrifices data efficiency due to oversampling to enable the use of smaller SAR payloads. The optimized distribution of capacity onto multistatic units falls outside the scope of this thesis.

7.2 Distribution of System Capacity

7.2.1 Distribution of Swath

The complexity of wide-swath systems can be mitigated by employing monostatic constellations, where each satellite covers a portion of the total swath (W_{tot}). Assuming an equal distribution of coverage, the required number of satellites is given by

$$N_{sat} = \left\lceil \frac{W_{tot}(\phi_{lat})}{W_g} \cdot (1 + \alpha(\phi_{lat})) - \alpha(\phi_{lat}) \right\rceil, \tag{7.11}$$

where W_g denotes the swath covered by a single satellite, and α is an overlap factor that controls the degree of overlap between consecutive subswaths at a given latitude (ϕ_{lat}). The overlap factor α ranges between 0

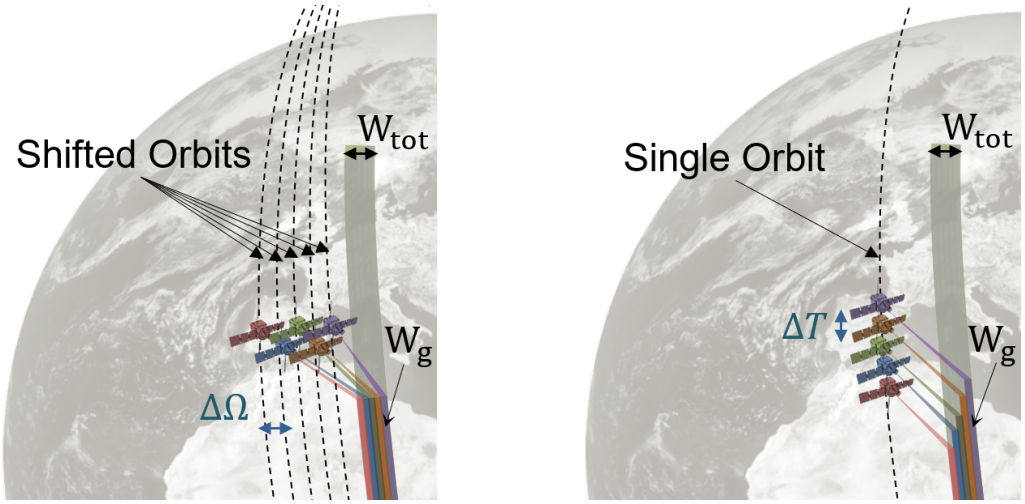

(a) (b)

Figure 7.2: Example orbit formations for monostatic SAR constellations designed for swath distribution. Panel (a) shows platforms arranged in orbits with a shifted longitude of ascending node by $\Delta\Omega$, while panel (b) depicts a configuration within a single orbital plane with a time delay ΔT between consecutive satellites.

and 1, with higher values indicating increased overlap. In the same manner, for a fixed number of satellites, the required swath per satellite can be calculated as

$$W_g = \frac{W_{tot}(\phi_{lat}) \cdot (1 + \alpha(\phi_{lat}))}{N_{sat} + \alpha(\phi_{lat})}. \tag{7.12}$$

Coverage accumulation can be achieved by distributing satellites across multiple orbital planes or by using a single orbital plane and leveraging Earth's rotation to achieve broader coverage over time. The latter approach is often more cost-effective, particularly when only a single orbital insertion is available. However, it may introduce some temporal variations between different swath partitions of a cumulative wide swath, particularly in large constellations where acquisitions are separated by longer temporal baselines (e.g., tens of minutes to hours).

To enable simultaneous imaging of wide swaths, the satellites in the constellation can be placed in adjacent orbital planes with minimal along-track baselines, as shown in Figure 7.2(a). This configuration is achieved by using neighboring orbits whose longitude of the ascending node is shifted by

$$\Delta\Omega(\phi_{lat}) \approx \frac{W_g}{R_E \cdot \cos\phi_{lat} \cdot |\sin\theta_N(\phi_{lat})| \cdot (1 + \alpha(\phi_{lat}))}, \tag{7.13}$$

where θ_N represents the northing angle. $\Delta\Omega$ is estimated at the equator for gap-free global coverage, resulting in increased swath overlap at higher

latitudes. This aspect facilitates individual system management and helps reduce the overall orbit duty cycle if redundant samples are not desired. However, implementing this configuration necessitates signal separation between satellites (e.g., using frequency diversity), and the use of formation flying techniques to prevent collisions.

Alternatively, for semi-simultaneous imaging, the satellites in the constellation can adopt different along-track baselines, corresponding to temporal lags of several tens of seconds for swaths on the order of tens of kilometers, all within the same orbital plane, as illustrated in Figure 7.2(b). The time lag,

$$\Delta T = \frac{\Delta\Omega\left(\phi_{\text{lat}}\right)}{\omega_{\text{E}}}, \tag{7.14}$$

between consecutive platforms is optimized for ϕ_{lat} while leveraging Earth's angular velocity (ω_{E}). This approach creates regions with varying degrees of overlap at different latitudes, which can reduce the overall orbit duty cycle, similar to the previous approach. While other orbital formations are possible, they typically result in non-simultaneous imaging of the total swath.

The entire constellation can be launched with a minimal number of launchers, typically just one, directly into the desired or a lower parking orbit. In the latter case, individual spacecraft are then raised to their final orbits at separate intervals to achieve the required drifts. Existing constellations, such as ICEYE, Capella, and Starlink, employ similar procedures.

A single-satellite failure leads to approximately a $100/N_{\text{sat}}$% loss in total coverage, yet it does not compromise mission continuity. Mitigation measures include adjusting the acquisition plan, performing roll maneuvers, or modifying the formation flight configuration, albeit with a slight reduction in temporal coverage and a potential increase in fuel consumption.

Coverage Efficiency

Coverage efficiency (η_{cov}) is a metric introduced to quantify the improvement in mission performance for global-coverage constellations through optimized system management of swath overlap regions. By leveraging this efficiency, the required orbital duty cycle of the entire constellation can be reduced while maintaining a consistent number of independent samples.

For gap-free coverage at a given latitude ϕ_{lat}, the total swath width required of a single SAR system in a repeat-ground track (RGT) orbit is approximated by

$$W_{\text{tot,req}}(\phi_{\text{lat}}) \approx \frac{2 \cdot \pi \cdot R_{\text{E}} \cdot \cos\phi_{\text{lat}} \cdot |\sin\theta_{\text{N}}(\phi_{\text{lat}})|}{N_{\text{rev}}}, \tag{7.15}$$

where N_{rev} is the integer number of orbital revolutions completed within the orbit's repeat cycle. This formulation assumes a uniform distribution of swath along the longitude to ensure consistent coverage of the entire latitudinal circumference. It further assumes a single-pass orientation—either ascending or descending—which would theoretically enable gap-free coverage of the equator twice within a repeat cycle, albeit with differing acquisition geometries.

For a satellite constellation, the total accumulated swath depends on the latitude and the number of active satellites (N_{act}) and is expressed as

$$W_{\text{tot}}(\phi_{\text{lat}}) = \frac{W_{\text{g}} \cdot (N_{\text{act}} + \alpha(\phi_{\text{lat}}))}{1 + \alpha(\phi_{\text{lat}})}. \tag{7.16}$$

The minimum required number of active satellites to achieve gap-free coverage at ϕ_{lat} can be estimated by

$$N_{\text{act}}(\phi_{\text{lat}}) \geq \left\lceil \frac{W_{\text{tot,req}}(\phi_{\text{lat}}) \cdot (1 + \alpha_{\text{ol}})}{W_{\text{g}}} \right\rceil, \tag{7.17}$$

where α_{ol} denotes the designed overlap ratio, typically evaluated at $\phi_{\text{lat}} = 0$ for global coverage missions.

The coverage efficiency at a given latitude ($\eta_{\text{cov}}(\phi_{\text{lat}})$) can be expressed as the ratio of useful swath samples to the total accumulated swath covered by the active satellites in the constellation

$$\eta_{\text{cov}}(\phi_{\text{lat}}) \approx \min\left(\frac{W_{\text{tot,req}}(\phi_{\text{lat}})}{W_{\text{g}} \cdot N_{\text{act}}(\phi_{\text{lat}})}, 1\right). \tag{7.18}$$

The overall coverage efficiency can then be approximated as a weighted sum over latitude

$$\eta_{\text{cov}} = \frac{\int \eta_{\text{cov}}(\phi_{\text{lat}}) \cdot \cos\phi_{\text{lat}} \, \mathrm{d}\phi_{\text{lat}}}{\int \cos\phi_{\text{lat}} \, \mathrm{d}\phi_{\text{lat}}}. \tag{7.19}$$

This metric offers a general measure of coverage performance for global missions with randomly distributed regions of interest at specific latitudes.

If uniform swath coverage across all latitudes is required—similar to a single reference monostatic system—each satellite in the constellation must operate over a different range of incident angles. Consequently, this necessitates non-identical instrument designs, which can negatively affect cost efficiency by reducing economies of scale and compromising performance uniformity.

Efficient Orbit Design

The design of a LEO for an equivalent constellation differs from that of higher orbits discussed in Chapter 4. While higher Earth orbits are restricted by high radiation intensities and launch inefficiencies, lower orbits are restricted by coverage and energy inefficiencies.

Regarding orbital inclination, achieving near-polar latitude reach—a critical factor for missions targeting global coverage—requires near-polar inclinations (see Figure 4.4). Additionally, for SAR missions in Earth orbits relying on solar energy, deviations from sun-synchronous inclinations can lead to substantial reductions in energy efficiency, with losses of approximately 30% to 40% (see Figure 4.7). Conversely, while sun-synchronous inclinations enhance energy efficiency, they negatively impact true 3-D deformation measurement accuracy. Specifically, measurement accuracy in the North–South direction from single-satellite acquisitions can be degraded by an order of magnitude compared to the Up–Down and East–West directions. To partially mitigate this accuracy degradation, two approaches are proposed:

(i) use D satellites within the constellation for squinted acquisitions, or

(ii) employ D satellites for bistatic acquisitions over areas of interest, at the cost of $< 100 \cdot D / N_{\text{sat}}$% coverage loss.

When considering orbital altitude, lower altitudes offer several advantages, including improved launch efficiency, increased SAR payload efficiency (e.g., smaller antenna sizes and reduced power requirements due to decreased free-space propagation loss), and higher beam velocity. However, these benefits must be balanced against the drawbacks of increased atmospheric drag and higher orbit decay rates [113], which can require more frequent ground operations and orbital maneuvers, potentially offsetting the advantages in spacecraft dimensioning.

The higher beam velocity at lower altitudes (v_{g}) allows to cover narrower swaths while maintaining system capacity, as described in (7.1). For missions aiming for global coverage, an equivalent LEO mission can achieve gap-free coverage with narrower swath widths.

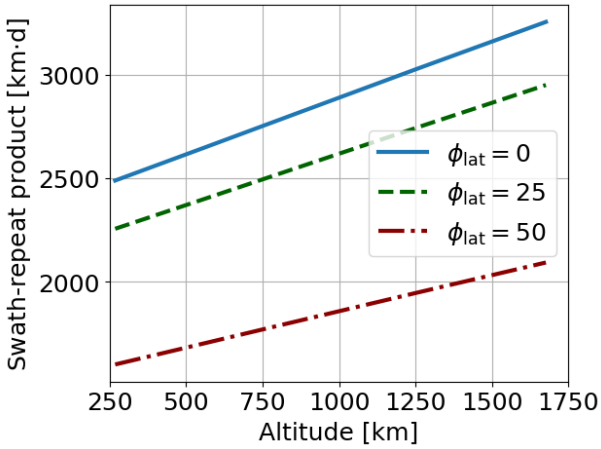

Figure 7.3: Swath-repeat product enabling gap-free coverage across various latitudes using sun-synchronous repeat orbits. The required swath width is determined by dividing the swath-repeat product by the desired orbital repeat cycle (in days).

Figure 7.3 shows the required swath-repeat product to achieve gap-free coverage across different latitudes using sun-synchronous repeat orbits. The required swath width can be determined by dividing the swath-repeat product by the desired orbital repeat cycle (in days). For low-Earth SSO, the exact repeat cycles provide discrete solutions that are sparsely sampled across the altitude range. Alternative repeat cycles can be considered to enhance altitude sampling and allow mission optimization based on other factors, such as the launch approach and acquisition mode. However, shorter cycles compared to the reference would necessitate roll maneuvers, while longer cycles require careful orbital insertion strategies to maintain the desired interferometric revisit, as discussed next in Section 7.2.2.

Efficient Instrument Design

The efficiency of a SAR payload is determined by the combined efficiencies of its various subsystems, including the antenna, deployment mechanism, transmit/receive modules (TRMs), RF distribution network, and back-end components such as switches, control modules, and power conditioning units. Maximizing efficiency involves adopting a streamlined design approach, which includes employing a stripmap operation mode, minimizing onboard processing, utilizing single-phase center (low-density) antennas, and integrating high-efficiency amplifiers.

Given specific mission requirements, including swath width, resolution, and SAR performance, a high-efficiency instrument architecture can be systematically derived. Figure 7.4 illustrates the general methodology used to derive an efficient instrument architecture based on total swath (W_{tot}),

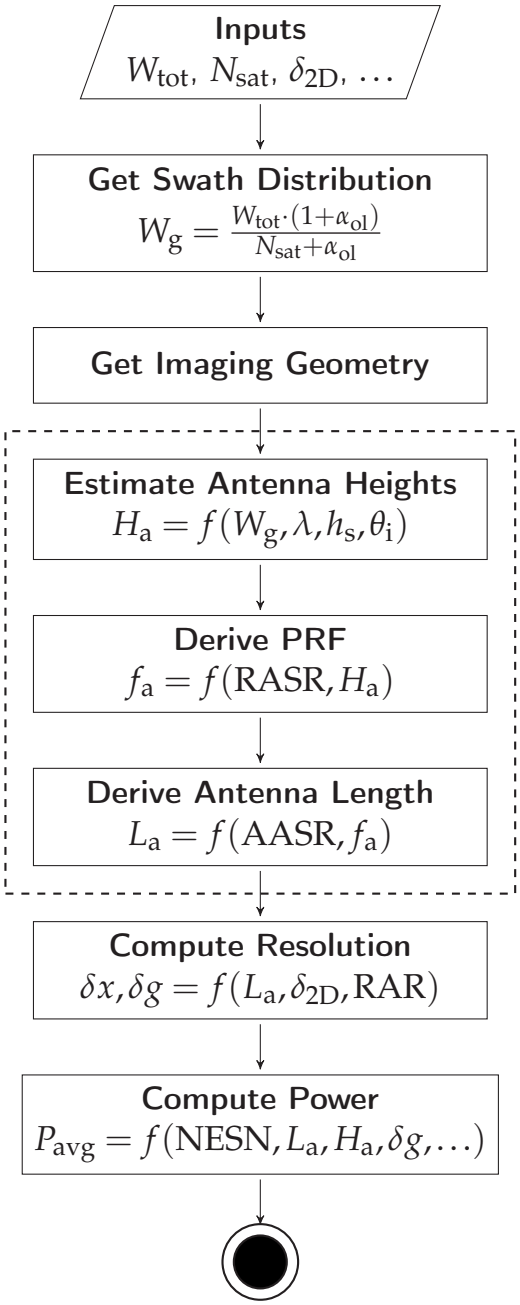

Figure 7.4: Flowchart illustrating the process for deriving instrument architecture, detailing the optimization of antenna size and power requirements for identical SAR payloads within a distributed satellite constellation.

constellation size (N_{sat}), and two-dimensional SLC resolution (δ_{2D}). This approach provides the minimum antenna dimensions required to cover a specified swath portion (W_{g}) while meeting constraints on AASR and RASR, as well as the minimum average transmit power needed to achieve the desired resolution and NESN.

A general trend in this distribution concept is the enhancement of azimuth resolution through the use of stripmap mode and reduction in antenna length. This results in a degradation in ground-range resolution (δg) for a given δ_{2D}. To mitigate large asymmetries, the resolution aspect ratio (RAR) is introduced as a constraint. While this impacts the SNR (and NESN) due to changes in range bandwidth, the increased number of looks, defined as $N_l = \delta_{2D}/(\delta x \cdot \delta g)$, can be exploited. For example, this can reduce the standard deviation of interferometric phase noise, which might otherwise increase due to the degraded SNR, as described in (3.35).

The overall mission efficiency depends on the SAR payload and factors such as the platform, constellation size, and launch constraints. For instance, while a SAR payload with certain antenna dimensions or power consumption might optimize payload efficiency, it could introduce significant challenges in platform integration and launch logistics. In such cases, achieving an optimal design may require careful trade-offs in efficiency between subsystems. For instance, a reduction in antenna length can be achieved by limiting the processed Doppler bandwidth to values below the full bandwidth supported by the antenna—without impacting instrument complexity [196]—though this comes at the cost of reduced azimuth resolution and sensitivity. Similarly, burst-mode operations can be employed to further reduce antenna size or to improve antenna dimensioning, such as optimizing the height-to-length ratio. Since other trade-offs are heavily influenced by available technology, this thesis concentrates on payload efficiency and constellation sizing, focusing on factors that directly affect these parameters.

7.2.2 Distribution of Interferometric Revisit

Interferometric revisits are a key feature of SAR missions, enabling numerous applications related to change detection. These revisits require the spacecraft to repeatedly pass over specific regions of interest under consistent geometrical conditions. In a constellation, this can be achieved by placing spacecraft at orbits offset by the longitude of the ascending node and the mean anomaly. A revisit interval T_{rev} (in seconds) requires a change in the right ascension of the ascending node (in radians) of

$$\Delta\Omega = (\omega_E - \dot{\Omega}) \cdot T_{\text{rev}}, \tag{7.20}$$

and a change in mean anomaly (in radians) of

$$\Delta M = -\frac{2\pi}{T_N} \cdot (T_{\text{rev}} \mod T_N), \tag{7.21}$$

where mod is the modulo operator, and T_N represents the orbit's nodal period, as defined in (2.5).

If only a single orbit insertion opportunity is available, modifying Ω requires changing the orbital plane, which is costly in terms of the required velocity change (ΔV). In contrast, adjusting the mean anomaly is more fuel efficient and enables interferometric revisits without altering the longitude of the ascending node when $\Delta\Omega = 2k\pi$, where $k \in \mathbb{Z}$. This holds if the desired revisit time satisfies

$$T_{\text{rev}} = k \cdot T_{\text{day}} = k \cdot \frac{2 \cdot \pi}{\omega_E - \dot{\Omega}}, \quad \text{for } k \in \mathbb{Z} \tag{7.22}$$

where T_{day} is the orbital day, defined in (2.6). In the case of a SSO, the nodal regression ($\dot{\Omega}$) is deliberately designed to match Earth's rotation rate, ensuring that the orbital day aligns with the solar day of 86 400 s.

7.3 Equivalent Constellations to High-Altitude Systems

A constellation of N_{sat} narrow-swath, high-efficiency satellites can generally be designed to achieve equivalence with a wide-swath SAR system operating at different altitudes. This section examines LEO constellations equivalent to three reference high-altitude SAR concepts introduced in Chapters 5 and 6. The first reference system is designed for global coverage from an orbit at 5952 km, the second targets local and continental coverage from a higher orbit at 20 181 km, and the third aims for sub-daily interferometric revisits from a geosynchronous orbit.

This section provides detailed design parameters, including constellation sizes and system specifications, derived from the analysis of the distributed designs.

7.3.1 Global MEO-SAR Equivalent

The reference global MEO-SAR mission, serving as the baseline for the equivalent design developed below, is detailed in Section 5.2. Table 7.1 summarizes the key parameters of the reference C-band MEO system operating at an altitude of 5952 km in full swath mode (Mode D). These parameters are compiled from Tables 5.2, 5.4, and 5.5 in Section 5.2. Apart from the reduced launch efficiency, the proposed C-band SAR instrument

Parameter	Value
Frequency [GHz]	5.405
Orbit cycle length [d]	3
Altitude at equator [km]	5952
Average eclipse duration [%]	< 8
Antenna diameter [m]	22
Transmit duty cycle [%]	8
Two-way losses [dB]	4
Noise figure [dB]	3
Swath width [km]	1667
Incident-angle range [°]	20 – 47
Average transmit power [W]	350
Resolution ($\delta x \times \delta g$) [m^2]	$< 57 \times 20$
NESN [dB]	< -22
AASR [dB]	< -25
RASR [dB]	< -25

Table 7.1: Relevant parameters of the reference MEO-SAR system at 5952 km targeting global coverage.

presents a high level of complexity. It incorporates a 22-m reflector antenna with an extensive feed network, utilizes elevation beamforming, and employs a ScanSAR imaging mode to achieve the wide swath coverage of 1667 km.

The design of the LEOs for the constellation is based on the analysis presented in Section 7.2. SSOs are selected for their energy efficiency and near-polar inclinations, which enable the constellation to meet the global coverage requirements of the reference mission. Additionally, for deformation monitoring in targeted regions, the accuracy of North-South deformation measurements can be enhanced using squinted or bistatic acquisitions, as explained in Section 7.2.

Figure 7.5 illustrates the total swath width needed to achieve gap-free equatorial coverage within a three-day cycle using low-Earth RGT SSOs. Alternative orbital cycles (e.g., one- or six-day repeats) offer greater flexibility for sampling LEO altitudes but introduce trade-offs, such as the need for roll maneuvers or adjustments to orbital insertion strategy.

Regarding altitude implications on instrument performance, Figure 7.6 displays the variation in the minimum required antenna area (a) and average

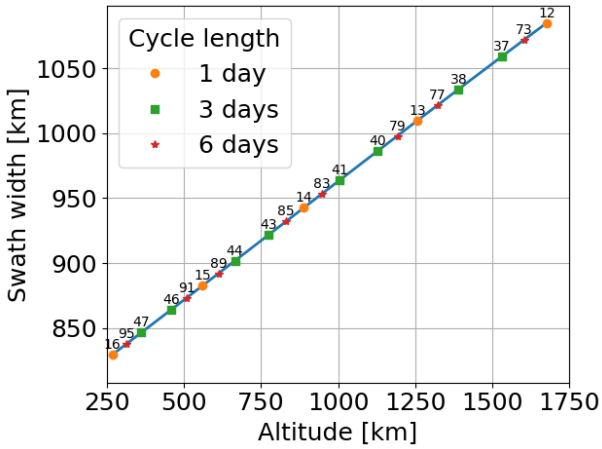

Figure 7.5: Required swath width for gap-free equatorial coverage within three days for one-, three-, and six-day low-Earth RGT SSOs. The annotations on the graph indicate the number of orbital revolutions per repeat cycle.

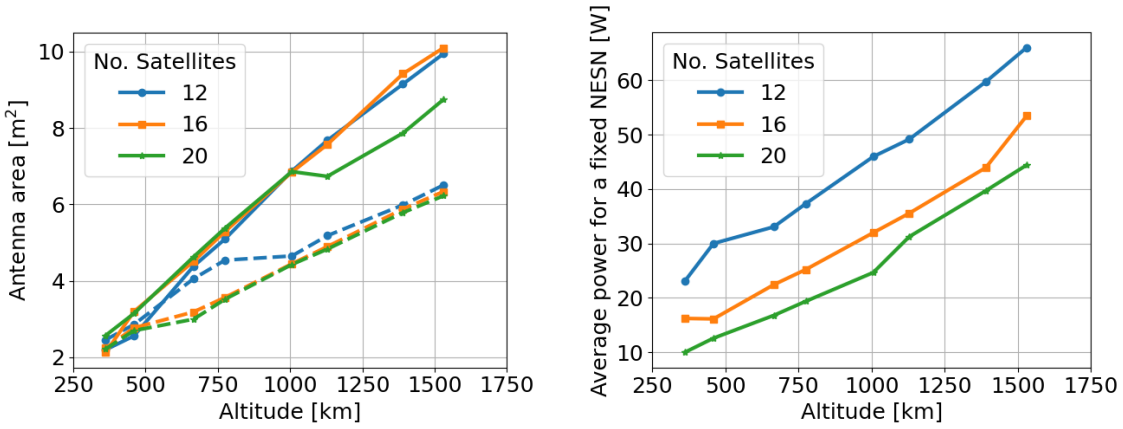

(a) (b)

Figure 7.6: Variation of (a) antenna area and (b) average transmit power with orbital altitude for SAR constellations comprising 12, 16, and 20 satellites in SSOs. Panel (a) compares planar (solid lines) and parabolic (dashed lines) antenna designs. The data represent C-band SAR systems designed for global coverage, delivering performance equivalent to the reference global MEO-SAR system.

transmit power (b) for a single satellite operating in stripmap mode within constellations of 12, 16, or 20 satellites. These variations correspond to the three-day repeat orbits and swath configurations depicted in Figure 7.5, assuming a 25-degree incidence at near range. The performance of the satellites in the constellation aligns with the reference MEO system outlined in Table 7.1, achieving a worst-case AASR of $-25\,\mathrm{dB}$, a worst-case RASR of $-25\,\mathrm{dB}$, worst-case NESN of $-22\,\mathrm{dB}$, and a 2-D SLC resolution of $1140\,\mathrm{m}^2$. The required swath width per satellite (W_g) ranges from 40 to 90 km, derived using (7.11) with an overlap factor (α_ol) of 1%, and can be

achieved without gaps in the provided designs. Given the moderate resolution requirements and correspondingly low average power demands, the antenna areas presented were derived by processing only a subset of the full Doppler bandwidth—corresponding to a 0.3 dB drop instead of the nominal 3 dB—to prioritize minimizing overall antenna size. Additional reductions in antenna area may be achieved through further optimization, such as the use of burst-mode operation.

The antenna areas shown in Figure 7.6(a) are plotted for two design scenarios: (i) planar antennas with low complexity and sinc patterns (solid lines) and (ii) parabolic antenna surfaces with tapered illumination (dashed lines). The parabolic design achieves approximately a 30% reduction in antenna area, primarily due to its superior control over side-lobe levels compared to sinc patterns. Similar, or potentially greater, reductions in antenna area could be achieved by optimizing planar antennas (e.g., by tapering) to improve side-lobe suppression. In both cases, the decrease in antenna area comes at the cost of increased average transmit power requirements (due to lower peak gain) and possibly higher system complexity.

For both cases, antenna area increases linearly with altitude due to the requirement for effective ambiguity suppression. Deviations from this linear trend, such as those observed for the 20-satellite configuration represented by the green curve in Figure 7.6(a), are caused by variations in the power of range ambiguities. These trends can be generalized to other constellation sizes; however, the three configurations presented here represent feasible systems regarding gap-free swath coverage, antenna dimensions, and power requirements.

Based on these trends, an orbit at 460 km altitude was selected for the equivalent constellation. Although this altitude leads to instrument and power requirements exceeding the minimum values shown in Figure 7.6, it offers advantages regarding the spacecraft's wet mass. At lower altitudes, the increased atmospheric drag and orbit decay rate may necessitate more frequent ground operations and maneuvers, which could outweigh the mass reduction benefits of smaller instruments. Figure 7.7(a) shows the variation in antenna dimensions, derived using the methodology in the flow chart in Figure 7.4, required to cover the corresponding 866-km swath for gap-free coverage as the constellation size increases. The HPBW ($\theta_{3\text{dB}}$) determines the antenna height needed to cover the swath portion. The PRF is then optimized to achieve range ambiguity ratios better than -25 dB for the antenna height. The antenna length is derived from the resulting PRF, ensuring compliance with the azimuth ambiguity ratio requirements, assuming processing of only a subset of the full Doppler bandwidth (corresponding to a 0.3 dB drop). The resulting antenna areas for the

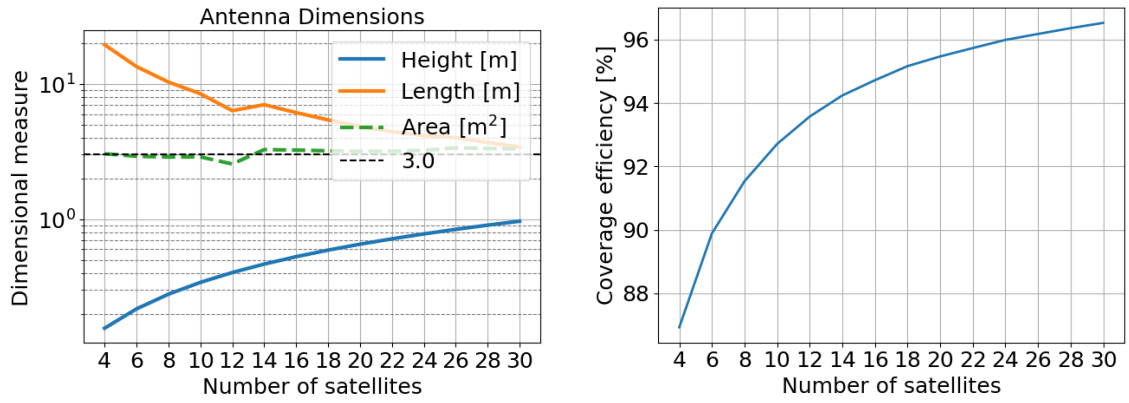

(a) (b)

Figure 7.7: (a) Required antenna dimensions to achieve worst-case AASR and RASR of −25 dB each for LEO constellations at 460 km, compared to the reference global MEO-SAR satellite at 5952 km. (b) Coverage efficiency of the constellation. The analysis assumes a near-range incident angle of 25°.

planar designs have a mean of 3.1 m^2 and a standard deviation of 0.3 m, influenced by variations in range ambiguity power and timing optimizations to accommodate transmission events. Figure 7.7(b) illustrates the increase in average coverage efficiency for larger constellations, calculated using (7.19). This improvement results from more efficient management of overlap regions at higher latitudes, enabling better spatial coverage and reduced redundancy.

Table 7.2 presents the key system parameters and performance metrics for the 12-, 16-, and 20-satellite constellations operating in stripmap mode. Timing parameters have been adjusted to avoid nadir returns at equatorial latitudes. If needed, nadir echoes at different latitudes can be effectively suppressed without additional cost using the dual-focusing nadir suppression technique, which utilizes up- and down-chirps [210].

All constellations meet the AASR, RASR, and NESN requirements specified in the reference, assuming a similar noise figure. The system losses are improved by 2.5 dB relative to the reference to account for simplifications in the antenna front-end and electronics. The instrument transmit duty cycle is constrained by nadir echoes and transmission events for the desired swaths and geometry, resulting in peak power requirements below 115 W across all three examples. The range resolution has been adjusted to maintain consistency with the 2-D resolution cell area of the reference design. The narrower swath width reduces power consumption and allows shorter antenna lengths due to improved ambiguity ratios at higher PRFs. However, this advantage comes at the expense of a larger constellation and asymmetrical resolution cells. The time offset between satellites in

Parameter	12 Sat.	16 Sat.	20 Sat.
Individual swath width [km]	73	55	44
Incident-angle range [°]	25 – 32.7	25 – 30.9	24.3 – 29.1
Antenna length [m]	7.33	6.22	5.63
Antenna height [m]	0.37	0.5	0.62
PRF [Hz]	1888	2150	2435
Doppler bandwidth [Hz]	593	698	772
Azimuth resolution [m]	15.6	13.3	12
Range resolution [m]	73	86	95
Average transmit power [W]	25	16	11
Transmit duty cycle [%]	< 22	< 14	< 12
Two-way losses [dB]	1.5	1.5	1.5
Single-plane time offset [min]	2.6	2	1.6

Table 7.2: System and performance metrics for 12-, 16- and 20-satellite constellations at an altitude of 460 km in stripmap mode.

a single-plane formation (see Figure 7.2 (b)) is on the order of several minutes. Estimated satellite mass for these systems ranges from 50 to 150 kg, with high orbit duty cycles.

A detailed acquisition plan over regions of interest for true 3-D deformation enables precise assessment of the required increase in constellation size for bistatic acquisitions, or the feasibility of squinted acquisitions at the cost of an increased orbit duty cycle.

7.3.2 Sub-daily Continental MEO-SAR Equivalent

The reference sub-daily continental MEO-SAR mission, serving as the baseline for the equivalent design developed below, is detailed in Section 5.2. Table 7.3 summarizes the key parameters of the reference L-band MEO system operating at an altitude of 20181 km in full swath mode (Mode A). These parameters are compiled from Tables 5.11, 5.12, and 5.13 in Section 5.2. Like the global mission, the proposed L-band SAR instrument is highly complex. It incorporates a 25-meter reflector antenna with an advanced feed network, utilizes elevation beamforming, and employs a ScanSAR imaging mode to achieve a wide swath coverage of 2115 km. Moreover, the higher orbital altitude further reduces launch efficiency and complicates navigation solutions, mainly due to the proximity to available global navigation satellite systems (GNSS).

Parameter	Value
Frequency [GHz]	1.2575
Orbit cycle length [d]	1
Altitude at equator [km]	20181
Average eclipse duration [%]	< 1.5
Antenna diameter [m]	25
Transmit duty cycle [%]	8
Two-way losses [dB]	4
Noise figure [dB]	3
Swath width [km]	2115
Incident-angle range [°]	18 – 42
Average transmit power [W]	100
Resolution ($\delta x \times \delta g$) [m^2]	$< 25 \times 500$
NESN [dB]	< -25
AASR [dB]	< -28
RASR [dB]	< -28

Table 7.3: Relevant parameters of the reference MEO-SAR system at 20181 km targeting sub-daily continental coverage.

The orbit design for the equivalent constellation follows the trends illustrated previously in Figure 7.5. The one-day repeat SSO at 561 km, with the 15 orbital revolutions per cycle, provides a good trade-off between the required instrument size and frequency of ground operations and maneuvers. Furthermore, the accuracy of North-South deformation measurements can be enhanced for deformation monitoring over specific regions, as explained in Section 7.2.

To achieve twice-daily, gap-free coverage of Europe, a total swath width of 2172 km is required, which is then distributed among the satellites in the constellation. Figure 7.8 shows the corresponding antenna dimensions for various constellation sizes, derived using the methodology outlined in the flow chart of Figure 7.4, ensuring that both AASR and RASR remain better than -28 dB. Deviations from the exponential trend in the required antenna length result from variations in range ambiguity power and timing optimizations to accommodate transmission events. The mean antenna area for the planar designs is approximately 17 m^2.

Table 7.4 presents the key system parameters and performance metrics for the 18-, 24-, and 30-satellite constellations operating in stripmap mode. These configurations are a subset of the designs shown in Figure 7.8. All

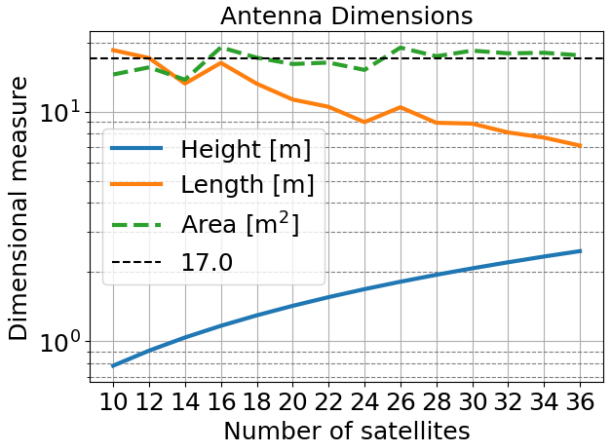

Figure 7.8: Required antenna dimensions to achieve worst-case AASR and RASR of −28 dB each for LEO constellations at 561 km, compared to the reference continental MEO-SAR satellite at 20 181 km. The analysis assumes a near-range incident angle of 25°.

Parameter	**18 Sat.**	**24 Sat.**	**30 Sat.**
Individual swath width [km]	122	91.5	73.1
Incident-angle range [°]	25 – 35.5	25 – 33	25 – 31.5
Antenna length [m]	13.22	9.15	8.87
Antenna height [m]	1.3	1.7	2.1
PRF [Hz]	1065	1540	1585
Doppler bandwidth [Hz]	325	470	485
Azimuth resolution [m]	28.1	19.4	18.9
Range resolution [m]	356	514	531
Average transmit power [W]	2.9	1.8	1.3
Transmit duty cycle [%]	< 20	< 20	< 27
Two-way losses [dB]	1.5	1.5	1.5
Single-plane time offset [min]	5.4	3.3	2.6

Table 7.4: System and performance metrics for 18-, 24- and 30-satellite constellations at an altitude of 561 km in stripmap mode.

constellations meet the AASR, RASR, and NESN requirements specified in the reference, assuming a similar noise figure and improved system losses of 1.5 dB. Larger constellation sizes offer advantages, particularly when platform or fairing constraints limit the antenna dimensions. The range resolution is adjusted to maintain the reference resolution cell area. However,

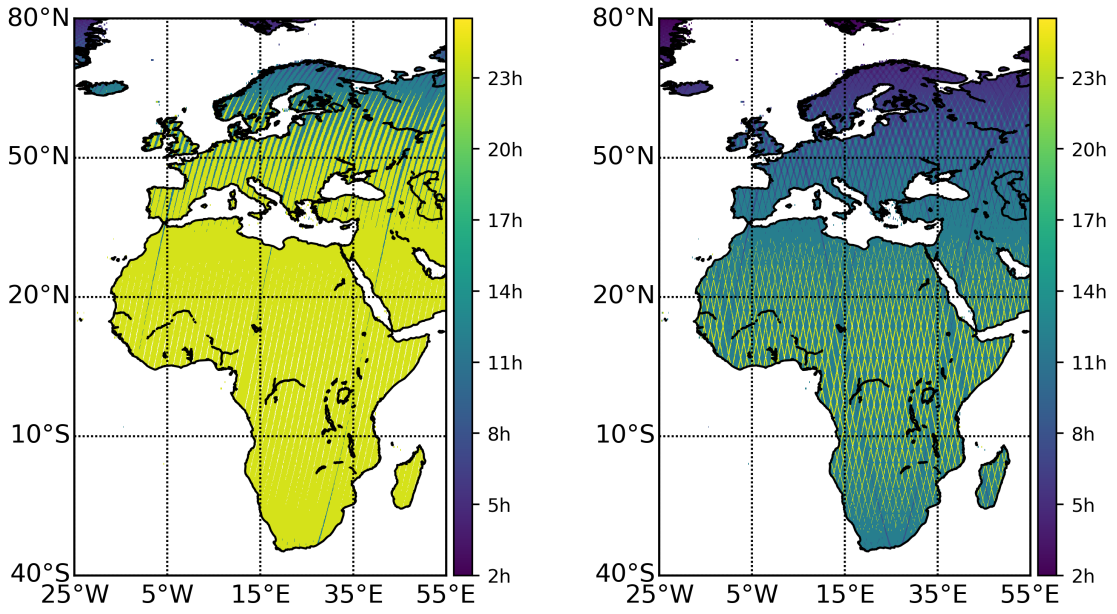

Figure 7.9: Potential coverage frequency maps—or average revisit time, in hours—for a constellation of 18 satellites in a SSO at an altitude of 561 km, optimized for sub-daily gap-free coverage over Europe. Panel (a) shows coverage from descending passes only, while panel (b) includes ascending and descending passes.

the low power demand and orbit duty cycle required to cover Europe (approximately 22%) provides an opportunity to enhance both range resolution and system capacity compared to the reference. For instance, increasing the average transmit power to approximately 36 W, 56 W, and 37 W would result in squared resolution cell areas of approximately $(28.1\,\mathrm{m})^2$, $(19.4\,\mathrm{m})^2$, and $(18.9\,\mathrm{m})^2$ for the three configurations, respectively.

In terms of coverage, Figure 7.9 shows the achievable coverage over land within the latitude-longitude region from 25°W to 55°E and 40°S to 80°N. The longer average revisit times at lower latitudes are due to the swath and orbital design prioritizing sub-daily coverage over Europe, particularly at $\phi_{\mathrm{lat}} = 35°\mathrm{N}$, to enable a fair comparison with the reference system.

Compared to the reference MEO-SAR mission, the equivalent LEO constellations, with their low power requirements and extensive coverage, can provide sub-daily global coverage with minor optimizations to swath overlap at equatorial latitudes. However, this comes at the expense of using larger constellations with antenna areas of approximately $17\,\mathrm{m}^2$. The comparison of constellation management and overall mission costs depends on the available technology and is primarily influenced by antenna design and launch technologies.

For scientific missions that can tolerate systematic gaps at the global scale, or that allow coverage of distinct Earth regions during separate mission phases, the proposed system designs can be implemented with smaller constellations. For example, instead of a 24-satellite constellation, a 6-satellite configuration could be employed to achieve sub-daily revisit over at least one-fourth of the globe.

7.3.3 Interferometric GEO-SAR Equivalent

The reference sub-daily interferometric geosynchronous SAR (GEO-SAR) mission, which serves as the baseline for the equivalent design described below, is detailed in Section 6.3. The reference C-band GEO-SAR system prioritizes sub-daily interferometric revisits over specific target regions in Europe (e.g., the Western Mediterranean and the Alpine region) and Africa (e.g., the Sahel and South Africa). The proposed SAR payload for this mission is relatively modest in size, utilizing mechanical steering of the spacecraft to enable seasonal coverage of the distinct target regions. However, the mission's complexity arises from the low launch efficiency and the high fuel budget requirements for orbital insertion and maintenance.

For a given geosynchronous orbit and predefined performance requirements (e.g., the standard deviation of the interferometric phase error, $\sigma_\varphi < 0.5$ rad), the number of achievable interferometric lags results from a trade-off with product resolution and scene size. The reference GEO-SAR system can provide interferometric lags of 1, 3, 6, and 12 hours, with product resolutions ranging from 25 km^2 to 0.01 km^2. Additionally, it offers radiometric products with the available revisit opportunities.

The orbit design for an equivalent LEO constellation of simple SAR satellites is illustrated in Figure 7.10. The proposed concept involves deploying multiple satellite clusters in one-day repeat orbits, typically sun-synchronous. Each cluster consists of several satellites that collectively achieve wide-swath coverage. The clusters are positioned in different orbital planes with offsets in their longitude of the ascending node (RAAN, $\Delta\Omega$) and mean anomaly (ΔM) to ensure the required interferometric lags, as detailed in Section 7.2.

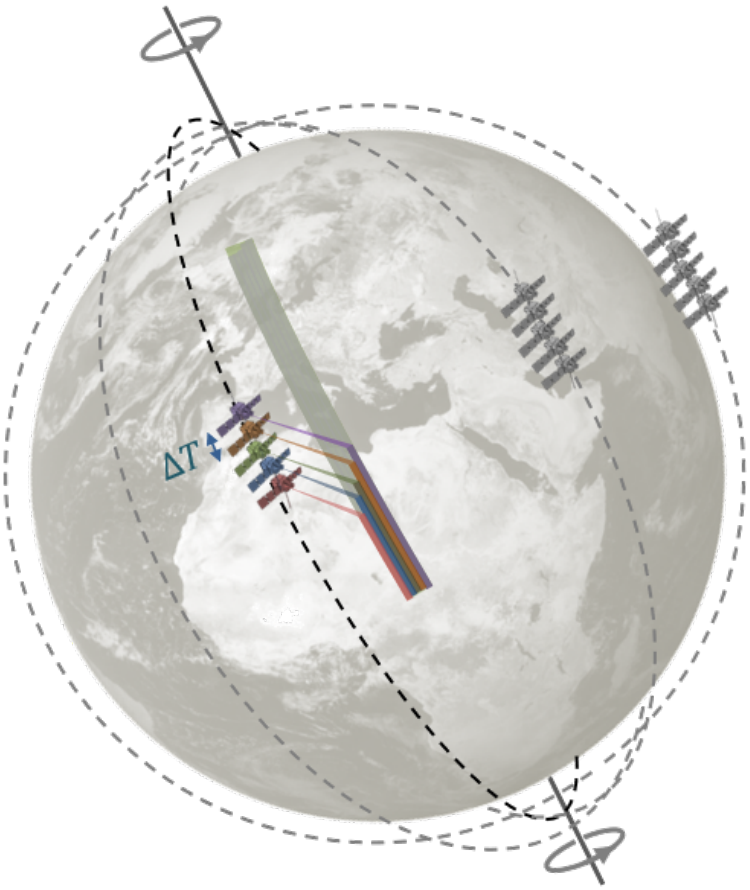

Figure 7.10: A realization of a LEO constellation of simple SAR satellites capable of wide-swath coverage and sub-daily interferometric acquisitions.

Interferometric Lags

The achievable number of sub-daily interferometric lags (L_{sub}) for a constellation with C LEO-satellite clusters is given by

$$L_{\text{sub}} = C \cdot (C - 1)\,. \tag{7.23}$$

Figure 7.11 illustrates the distribution of these lags for two cluster configurations: (a) a 4-cluster configuration providing 12 sub-daily lags, and (b) a 5-cluster configuration providing 20 sub-daily lags. The required $\Delta\Omega$ and ΔM values between a reference cluster (C_0) and the other clusters (C_i) can be derived from (7.20) and (7.21), respectively. Example values are provided in Table 7.5, assuming an orbit's nodal period (T_{N}) of 1.6 h for the estimation of ΔM.

The discrete placement of clusters, as shown in Figure 7.11, influences the distribution of interferometric lags, which is critical for characterizing

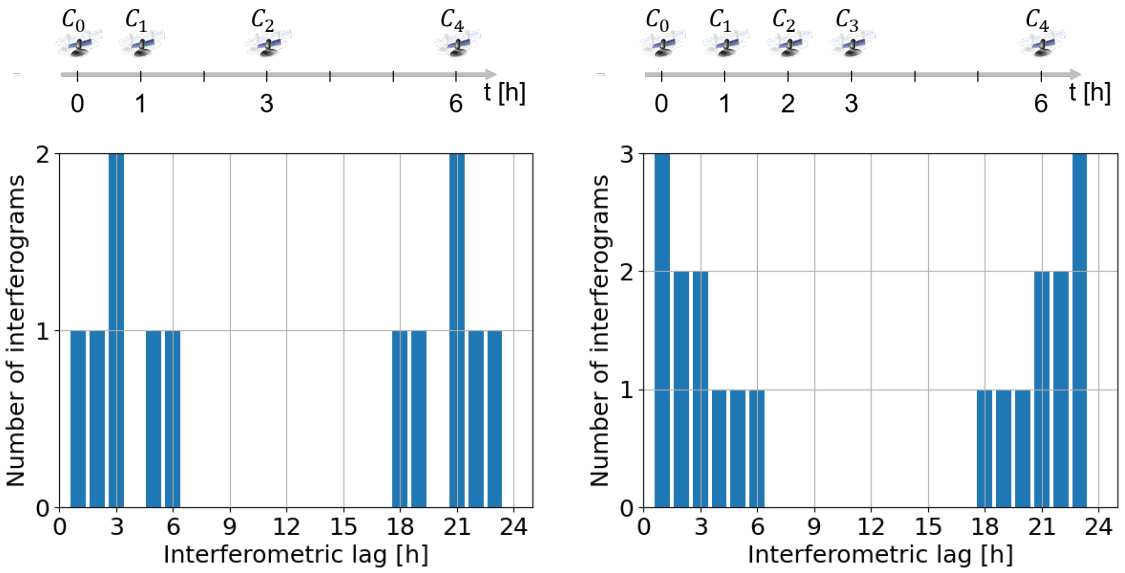

(a) (b)

Figure 7.11: Distribution of sub-daily interferometric lags for LEO SAR constellation configurations. (a) A 4-cluster configuration providing 12 sub-daily lags. (b) A 5-cluster configuration providing 20 sub-daily lags.

Revisit (T_{rev}) [h]	**1**	**2**	**3**	**6**
RAAN offset ($\Delta\Omega$) [°]	15	30	45	90
Mean anomaly offset (ΔM) [°]	135	270	45	90

Table 7.5: Required relative offsets in RAAN and mean anomaly for example revisit intervals.

physical parameters such as vegetation water content and soil moisture variation [219, 220]. This configuration also supports the simultaneous fulfillment of radiometric revisit requirements.

Notably, generating a single differential interferogram with the reference GEO-SAR mission requires four acquisitions, whereas its LEO-constellation counterpart needs only three. Additionally, the overlapping nature of the GEO sub-daily interferograms—with one being a subset of another, may increase the complexity of the inversion process. Considering this factor, and under the assumption of achieving 20 sub-daily lags for Hydroterra, a smaller LEO-SAR formation with four clusters—providing twelve sub-daily lags as depicted in Figure 7.11(a)—could potentially yield similar information for the inversion process.

Coverage Distribution

LEO provides exceptional coverage rates compared to GEO; however, its accessibility, in terms of spatial coverage and latitude reach, strongly depends on the orbital altitude and inclination. The six observation scenarios for Hydroterra, shown in Figure 6.13, each require exclusive coverage with varying spatial and temporal resolutions. Among these, the Western Mediterranean (WM) scenario poses a significant challenge in terms of coverage area, requiring a swath width of 1420 km from a single pass (either ascending or descending) in a near-polar orbit.

This required swath width can be reduced to approximately 890 km if the overlap between ascending and descending passes is optimized to align with the target region. The degree of overlap depends on the orbital altitude and observation geometry for the considered SSOs. Alternatively, adjusting the orbital inclination to match the target region's latitude and incident angle could reduce the single-pass swath width to 1200 km. However, this adjustment would result in a loss of sun-synchronicity, leading to deviations in the local time of repeat passes.

Although SARs in low-altitude orbits benefit from significantly improved power efficiency compared to those in GEO, primarily due to reduced free-space path loss (approximately 60 dB), the constellation design is based on a SSO with a one-day repeat cycle at an altitude of 561 km. This orbit is selected for its favorable trade-offs in instrument size and orbital insertion cost. As indicated by Equation (7.15) and Figure 7.5, the constellation offers substantial coverage potential, with a designed swath width of 890 km enabling daily coverage of one-third of the equator in a single-pass geometry. This suggests that global coverage can be achieved through three mechanical rolls or by selecting an orbit with a three-day repeat cycle. The orbital parameters for the central satellite in each of the clusters (in the four-cluster configuration) are listed in Table 7.6. These parameters are referenced to the epoch 2040-03-21T12:00:00.000Z UTC and are expressed in the true of date (TOD) frame. The insertion of C clusters with distinct RAAN is associated with increased costs but can be achieved in a straightforward manner using N_{lo} launchers, provided that $N_{\text{lo}} \geq C$. When fewer launchers are available ($N_{\text{lo}} < C$) and payload capacity is not a constraint, the RAAN offset ($\Delta\Omega$) can be obtained by deploying the clusters into orbits at different altitudes. By leveraging the differential nodal drift rates, the required $\Delta\Omega$ can be reached over a predefined time window, after which the clusters can be maneuvered into their designated formation. Such strategies are already employed by existing constellations like Starlink.

Parameter	C_0	C_1	C_2	C_3
Orbit type		1/15 SSO		
Semi-major axis (a) [km]		6939.1		
Eccentricity (e)		0.001065		
Inclination (i) [°]		97.635		
Argument of perigee (ω) [°]		90		
Time offset to reference [h]	-	1	3	6
RAAN (Ω) [°]	102	117	147	192
Mean anomaly at epoch (M_0) [°]	0	135	45	90
Average eclipse duration [%]	< 6.5	< 21.5	< 35	< 37

Table 7.6: Key parameters of the sun-synchronous RGT LEO designed for the equivalent constellation to the interferometric GEO-SAR mission. The reference epoch is 2040-03-21T12:00:00.000Z UTC, with all parameters expressed in the TOD frame.

The sun-synchronous nature of the orbits ensures systematic revisits at similar solar times, as the orbit's repeat cycle is a multiple of the solar day (in this case, precisely one solar day). However, achieving the desired sub-daily revisit distribution results in eclipse durations ranging from 6.5% to 37%. An interesting formation occurs with a 12-hour revisit interval and a two-cluster solution, where the satellites are out of phase, enabling the eclipse duration for both clusters to be kept below 6.5%, similar to the configuration of Sentinel-1A and Sentinel-1C.

In terms of cluster size, Figure 7.12 shows the corresponding antenna dimensions for various constellation sizes, derived using the methodology outlined in the flow chart of Figure 7.4, ensuring that both AASR and RASR remain better than -25 dB. The mean antenna area for the planar designs is approximately 3.5 m^2. Variations from this mean are attributed to variations in range ambiguity power and timing optimizations necessary to accommodate transmission events.

Table 7.7 presents the key system parameters and performance metrics for the 8-, 10-, and 12-satellite constellation designs operating in stripmap mode. These configurations are a subset of the designs shown in Figure 7.12. The antenna lengths have been further optimized compared to the results in Figure 7.12 to avoid nadir returns in the received echoes, resulting in antenna areas below 3.55 m^2 across all designs. Each constellation achieves an AASR and RASR better than -25 dB.

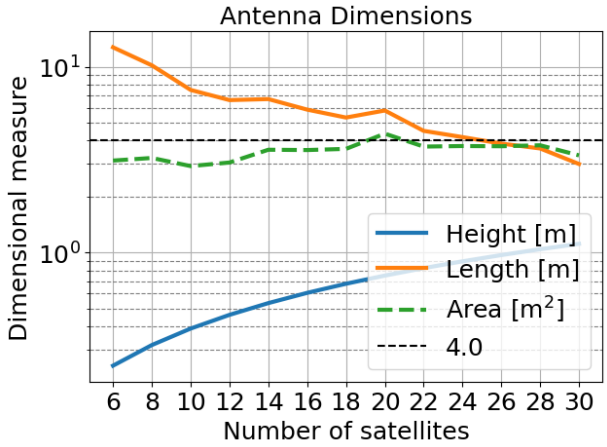

Figure 7.12: Required antenna dimensions to achieve worst-case AASR and RASR of −25 dB each for LEO constellations at 561 km. The analysis assumes a near-range incident angle of 24°.

Parameter	8 Sat.	10 Sat.	12 Sat.
Individual swath width [km]	113.2	90.6	75.5
Swath overlap [km]	2.2	1.8	1.5
Incident-angle range [°]	24 – 34	24 – 32.1	24 – 30.8
Antenna length [m]	10.35	8.62	7.7
Antenna height [m]	0.32	0.39	0.46
PRF [Hz]	1342	1595	1800
Doppler bandwidth [Hz]	415	508	571
Azimuth resolution [m]	22	18.	16
Range resolution [m]	110	90	80
Average transmit power [W]	18	19	17
Transmit duty cycle [%]	10	10	20
Two-way losses [dB]	1.5	1.5	1.5
Single-plane time offset [min]	5.2	4	3.3

Table 7.7: System and performance metrics for 8-, 10- and 12-satellite constellations at an altitude of 561 km in stripmap mode.

The 2-D SLC resolution is governed by the azimuth resolution and a resolution-aspect ratio (RAR) design limit of 0.2, yielding resolution cell areas of 2420 m^2, 1620 m^2, and 1280 m^2 for the 8-, 10-, and 12-satellite configurations, respectively. The specified average transmit power levels ensure a worst-case NESN of −20 dB for the given resolutions. Regarding radiometric resolution ($\delta_{\text{rad,dB}}$), all configurations achieve $\delta_{\text{rad,dB}} < 0.5$ dB for a ML resolution of 500 m. Similarly, for interferometric products, the required

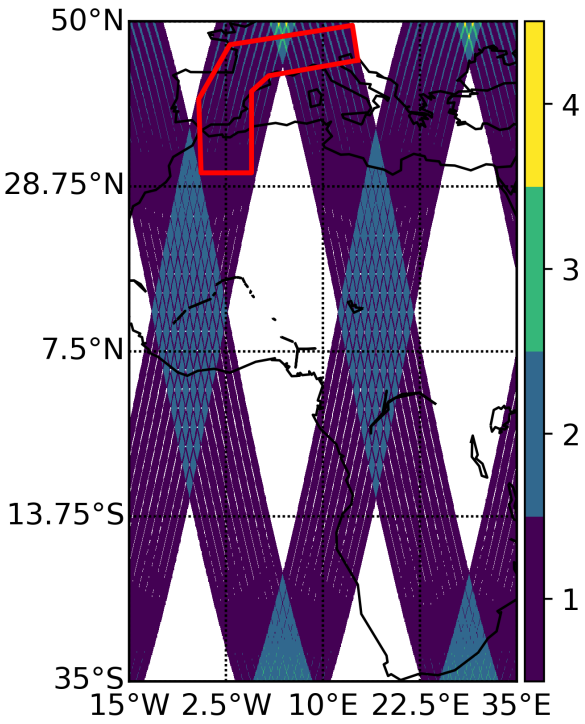

Figure 7.13: Potential daily coverage frequency map for a single cluster of 10 satellites in a SSO at an altitude of 561 km. The accumulated swath width at a latitude of 40° is 890 km, providing full coverage of the Western Mediterranean observation scenario.

standard deviation of the interferometric phase error ($\sigma_\varphi < 0.5\,\text{rad}$) is met for a ML resolution of 150 m. Higher-resolution products over smaller regions, such as the Alpine Center (AC) or South Africa (SA2) scenarios, necessitate additional looks. These can be achieved by increasing the system bandwidth or redirecting selected satellites within the cluster to focus on narrower regions, enhancing sensitivity rather than coverage.

Figure 7.13 shows the potential daily coverage frequency map for a single 10-satellite cluster deployed in a SSO at an altitude of 561 km. The accumulated swath width of 890 km at a latitude of 40° provides complete coverage of the Western Mediterranean observation scenario.

An analysis of the achievable resolutions and required transmit powers indicates that the equivalent LEO-SAR constellation offers superior resolution at larger scales. However, this improvement comes with challenges related to the number of interferometric lags and the flexibility of localized coverage. These limitations often necessitate large constellation sizes, defined as the product of the number of clusters and the number of satellites per cluster—for example, a total of 40 satellites in the case of 10 satellites per cluster.

Science-focused SAR missions in LEO could benefit from observation scenarios aligned with the near-polar swaths of SAR satellites in SSO and a relaxed requirement for systematic interferometric revisit, potentially enabling a reduction in overall constellation size as proposed in [219].

Conversely, a GEO-SAR mission provides greater flexibility in managing interferometric lags and adapting the size and orientation of coverage zones, enabling access to up to one-third of the Earth's surface. Nevertheless, GEO-SAR systems face significant inefficiencies in system capacity due to high propagation losses and low coverage rates.

7.4 Chapter Remarks

This chapter explored the equivalence between constellations of compact SAR systems in LEO and complex monostatic SAR systems in high Earth orbits. The analysis demonstrated that wide-swath, fast-revisit high-orbit systems could be effectively replaced by constellations of highly efficient LEO-SAR systems, providing deeper insights into the required system complexities and offering a viable alternative for diverse mission requirements.

Section 7.1 introduced a novel equivalence framework based on generic performance metrics with a focus on system capacity. This framework enables fair and consistent assessments of mission complexities and facilitates the design of equivalent constellations for various applications.

Section 7.2 presented distribution concepts for system capacity, addressing a broad spectrum of SAR mission objectives, including wide-swath coverage, fast revisit times, sub-daily interferometry, and both global and localized coverage. The section provided design guidelines emphasizing the use of simple SAR payloads and underscored the advantages of LEO constellations in achieving high coverage efficiency.

Finally, Section 7.3 validated the equivalence framework through realistic examples of MEO- and GEO-SAR systems from Chapters 5 and 6. The provided design metrics included antenna sizes, swath widths, and achievable SAR performance, highlighting the strengths and challenges of equivalent systems.

Instead of evaluating the full mission cost, which can vary significantly with technological advancements, this chapter adopted a timeless approach to assess mission complexity. The proposed methodology allows

for evaluating complexity based on key parameters, including constellation size, SAR payload characteristics (antenna dimensions, power requirements, radar electronics complexity), and orbital requirements. This approach offers a robust framework for mission planning that remains relevant regardless of future technological shifts.

8 Conclusions

8.1 Summary and Discussion of Results

Earth observation (EO) provides essential insights into the physical, chemical, and biological systems of our planet. The increasing availability of data from diverse EO satellite missions has advanced our understanding of these systems. However, significant observational and knowledge gaps remain, while the impacts of climate change and anthropogenic pressures continue to intensify.

Spaceborne SAR missions play a key role in addressing these gaps by delivering high-resolution imagery on a global scale, independent of daylight or weather conditions. Despite these advantages, conventional SAR missions are limited by infrequent temporal revisit. To address this, emerging missions are deploying LEO constellations designed to reduce revisit times to a few days over specific regions. Nevertheless, a critical gap persists for EO applications that demand both high temporal sampling—on the order of few days or sub-daily—and moderate spatial resolution at continental to global scales. Bridging this gap is essential for capturing various transient, rapidly evolving, or diurnally varying Earth processes.

This thesis investigated the potential of high-orbit SAR systems to address the existing gap in EO data for high-temporal, moderate-spatial sampling of large-scale dynamic Earth processes. Adopting a mission-level perspective, the thesis examined how key mission components could be optimized to exploit the expanded field of view inherent to high-altitude operations. The overarching objective was to enable frequent revisit capabilities while mitigating the significant loss in sensitivity associated with higher altitudes, thereby providing a viable solution to the identified spatio-temporal sampling gap.

The work contributed an in-depth quantitative analysis of high-orbit SAR missions, addressing a significant gap in the existing literature. It explored fundamental mission design trade-offs, including orbital configurations, energy availability, radiation environment, launch strategies, SAR payload design, and imaging performance.

The analysis identified orbital regimes that offer high coverage efficiency suitable for global-scale missions. It demonstrated that sufficient solar energy is available even in the absence of sun-synchronous conditions and characterized radiation environments that necessitate only moderate shielding, for example, approximately 8 mm of aluminum at altitudes above 5500 km, sufficiently distant from the inner Van Allen belt peak. Furthermore, electric propulsion was found to be a viable solution to mitigate the increased launch costs to higher orbital altitudes.

The sensitivity loss at higher altitudes was rigorously analyzed and shown to remain a challenge, even though partial compensation is possible by leveraging the nominal trajectory curvature of MEO. Two operational concepts were proposed for monostatic MEO-SAR systems:

A. a LEO-like swath width and resolution, with a broader accessible swath; and

B. an extended swath width, potentially spanning the entire accessible swath, with moderate resolution.

Both concepts exploit the expanded field of view (referred to as accessible swath) at higher altitudes to achieve frequent revisit times. Concept (A) is particularly well suited for event-triggered applications, whereas concept (B) supports a broader range of scientific applications that benefited from higher coverage rates and frequent recurring acquisitions, directly addressing the spatio-temporal EO gap motivating this research.

The thesis showed that antenna requirements are a primary factor driving SAR payload complexity in MEO. Large apertures are essential to suppress ambiguities and enhance sensitivity. With current technology, large deployable reflector antennas on the order of 22 m in diameter, combined with digital beamforming, were found to offer sufficient sensitivity, although such designs approach the edge of current engineering capabilities—for example, compared to the 15-m reflector proposed for the Tandem-L mission [61].

In contrast, geosynchronous orbits present an even greater sensitivity challenge. However, their instantaneous accessibility permits extended dwell times, enabling noise reduction through averaging of statistically independent looks. This trade-off allows the use of conventional LEO-like SAR payloads, albeit at the cost of significantly reduced system capacity.

The thesis revealed new concepts for EO from high Earth orbits, including:

- global-scale true 3-D deformation mapping using monostatic SAR in inclined MEO, e.g., an orbital altitude of 5952 km and inclination of 122°;
- sub-daily revisit using a single satellite in high MEO, e.g., at an altitude of 13 890 km or 20 200 km; and
- hourly revisit using equatorial MEO configurations, e.g., 6-hour revisit from 8035 km.

Two exemplary MEO-SAR mission concepts were developed in detail for the first two cases, including orbit design, SAR payload configuration, imaging modes, and resulting performance.

Additionally, the thesis introduced a novel geosynchronous orbit concept tailored for sub-daily interferometric observations, with a focus on minimizing baseline decorrelation—an approach that holds significant promise for future GEO-SAR missions. A systematic framework was developed to support the efficient allocation of GEO-SAR mission resources and was demonstrated through the derivation of observation scenarios for a third mission concept, analogous to Hydroterra, a GEO-SAR mission previously proposed under ESA's Earth Explorer 10 program.

Finally, the thesis introduced a novel comparative framework for evaluating the complexity of high-orbit SAR missions relative to their equivalent monostatic LEO-SAR constellations. This framework was complemented by introducing concepts for distributed SAR configurations that enabled the derivation of equivalent LEO constellation architectures corresponding to distinct high-orbit mission designs. These were applied to the three proposed MEO- and GEO-SAR missions, allowing a systematic assessment of relative complexity based on key parameters such as constellation size, SAR payload characteristics, and orbital requirements. The proposed timeless methodology offers a robust foundation for future mission planning and evaluation, maintaining relevance across evolving technological landscapes.

8.2 Outlook of Further Work

MEO-SAR Missions

This thesis has explored medium Earth orbits (MEO) in detail, with a particular focus on addressing the spatio-temporal Earth observation (EO) gap

by enabling frequent revisit rates at moderate spatial resolution. The sensitivity challenges inherent to MEO were evaluated within the broader objectives of the thesis. As demonstrated, the required antenna dimensions are predominantly driven by power limitations and ambiguity rejection requirements. For the specified mission objectives, this results in, for example, a reflector antenna diameter of 22 m for a C-band MEO-SAR system operating at an altitude of 5952 km.

Future investigations could examine the potential for system simplification by moderately reducing the spatial resolution or swath width, for example, by a factor of 2 to 3. Such a reduction would ease antenna design requirements and reduce overall system complexity, while still preserving a frequent revisit interval across the full accessible area. However, in the case of swath reduction, achieving this coverage would require mechanical roll maneuvers by the spacecraft. Given the inherently wide swath achievable from MEO, such an approach may still be sufficient to ensure frequent acquisitions over globally distributed active seismic regions.

These trade-off studies could substantially reduce the engineering challenges under current technological constraints and enhance the viability of MEO-SAR as a platform for future scientific EO missions.

Interferometric GEO-SAR Missions

This thesis introduced a novel geosynchronous orbit design optimized for sub-daily interferometric measurements. The proposed reference orbit enables minimal baselines when its geometric configuration is maintained. However, significant perturbations—particularly those induced by the Sun and Moon—lead to daily variations in the orbital plane. If left uncorrected, these perturbations increase the cross-track perpendicular baseline ($B_\perp$), thereby degrading SAR performance.

Counteracting these perturbations requires frequent orbital maneuvers, which are costly due to the high ΔV demand. A comparative assessment of maneuver strategies for the proposed optimized orbit versus current state-of-the-art low-inclination orbit designs is essential to quantify the trade-offs in maneuverability and performance. Further investigation into the trade-off between ΔV budget and observation capability is of particular interest. Specifically, higher ΔV consumption may shorten mission duration but enable broader observation scenarios (coverage or revisit), while a reduced ΔV budget could extend mission life at the expense of limited observation scenarios.

Furthermore, as discussed in Chapter 6, the numerous GEO-SAR sub-daily interferograms are subsets of one another. Therefore, an in-depth analysis of the required inversion processes to extract meaningful geophysical information from such differential interferograms is crucial for the development of future GEO-SAR missions.

Equivalent LEO-SAR Constellations

This work has introduced a robust comparative framework for assessing the relative complexity of monostatic SAR systems and their equivalent constellations, applicable to both low Earth orbit and high Earth orbit architectures. The complementary analysis for distributed SAR concepts emphasized high SAR payload efficiency across multiple dimensions, including coverage, propagation path, imaging mode, antenna architecture, and instrument design.

Throughout the analysis, constellation sizing was often dictated by antenna length requirements rather than power constraints or gap-free swath considerations, particularly for moderate-resolution products. This frequently led to relatively large constellation configurations, suggesting that optimizing for high SAR payload efficiency may inadvertently compromise overall mission efficiency. Larger constellations can introduce inefficiencies in terms of launch configuration, formation management, and production costs. Furthermore, long antenna apertures—extending several meters—pose challenges for the design of small satellite buses. They increase structural complexity, require more sophisticated deployment mechanisms, and contribute to higher overall system mass. These challenges ultimately result in inefficiencies in system integration and platform scalability.

Although the total antenna area remains nearly constant, increasing the constellation size could allow for the use of more symmetrical antenna designs, potentially simplifying individual payload architecture. However, this benefit comes at the cost of increased formation management complexity and perhaps production costs. Ultimately, the optimal constellation size is strongly dependent on available platform, antenna, and launch technologies.

A promising direction for future research involves investigating the use of burst-mode operations (such as ScanSAR or TOPS) to reduce antenna asymmetry. While this approach may lead to reduced imaging efficiency and impose stricter demands on onboard electronics, it offers advantages for systems with low power budgets and unfavorable resolution-aspect ratios. Incorporating this investigation into future assessments would enrich

the complexity analysis and provide further insight into the potential of LEO-SAR constellations to address the spatio-temporal EO gap that motivates this research.

List of Figures

List of Tables

Bibliography

[1] European Space Agency. Earth science in action for tomorrow's world - Earth observation science strategy, 2024. URL https://esamultimedia.esa.int/docs/EarthObservation/ESA_Earth_Observation_Science_Strategy_issued_Sept_2024.pdf. Accessed: March 22, 2025.

[2] European Space Agency (ESA). Copernicus: the European Earth observation programme, 2021. URL https://www.copernicus.eu. Accessed: March 18, 2025.

[3] NASA. Earth observing system (EOS), 2022. URL https://eospso.nasa.gov/. Accessed: March 18, 2025.

[4] C. A. Wiley. Pulsed Doppler radar methods and apparatus, U.S. Patent 3196436, filed 1954, published 1965.

[5] L. J. Cutrona, W. E. Vivian, E. N. Leith, and G. O. Hall. A high-resolution radar combat-surveillance system. *IRE Transactions on Military Electronics*, MIL-5(2):127–131, 1961.

[6] C. W. Sherwin, J. P. Ruina, and R. D. Rawcliffe. Some early developments in synthetic aperture radar systems. *IRE Transactions on Military Electronics*, MIL-6(2):111–115, 1962.

[7] W. M. Brown. Synthetic aperture radar. *IEEE Transactions on Aerospace and Electronic Systems*, AES-3(2):217–229, 1967.

[8] D. L. Evans, W. Alpers, A. Cazenave, C. Elachi, T. G. Farr, D. Glackin, B. Holt, L. Jones, W. T. Liu, W. McCandless, Y. Menard, R. Moore, and E. Njoku. Seasat—A 25-year legacy of success. *Remote Sensing of Environment*, 94(3):384–404, 2005.

[9] C. Elachi, W. E. Brown, J. B. Cimino, T. Dixon, D. L. Evans, J. P. Ford, R. S. Saunders, C. Breed, H. Masursky, J. F. McCauley, et al. Shuttle imaging radar experiment. *Science*, 218(4576):996–1003, 1982.

[10] J. Cimino, C. Elachi, and M. Settle. SIR-B-the second shuttle imaging radar experiment. *IEEE Transactions on Geoscience and Remote Sensing*, GE-24(4):445–452, 1986.

[11] R. L. Jordan, B. L. Huneycutt, and M. Werner. The SIR-C/X-SAR synthetic aperture radar system. *IEEE Transactions on Geoscience and Remote Sensing*, 33(4):829–839, 1995.

[12] T. G. Farr, P. A. Rosen, E. Caro, R. Crippen, R. Duren, S. Hensley, M. Kobrick, M. Paller, E. Rodriguez, L. Roth, D. Seal, S. Shaffer, J. Shimada, J. Umland, M. Werner, M. Oskin, D. Burbank, and D. Alsdorf. The shuttle radar topography mission. *Reviews of geophysics*, 45(2), 2007.

[13] E. P. W. Attema. The active microwave instrument on-board the ERS-1 satellite. *Proceedings of the IEEE*, 79(6):791–799, 2002.

[14] C. R. Francis, G. Graf, P. G. Edwards, M. McCraig, C. McCarthy, A. Lefebvre, B. Pieper, P. Y. Pouvreau, R. Wall, and F. Weschler. The ERS-2 spacecraft and its payload. *Esa Bulletin*, 83:13–31, 1995.

[15] Y. L. Desnos, C. Buck, J. Guijarro, G. Levrini, J. L. Suchail, R. Torres, H. Laur, J. Closa, and B. Rosich. The ENVISAT advanced synthetic aperture radar system. In *IGARSS 2000; IEEE International Geoscience and Remote Sensing Symposium*, volume 3, pages 1171–1173. IEEE, 2000.

[16] M Shimada. SAR programmes in JAXA: from JERS-1 to the future. *IEE Proceedings-Radar, Sonar and Navigation*, 153(2):122–128, 2006.

[17] A. Rosenqvist, M. Shimada, N. Ito, and M. Watanabe. ALOS PALSAR: A pathfinder mission for global-scale monitoring of the environment. *IEEE Transactions on Geoscience and Remote Sensing*, 45(11): 3307–3316, 2007.

[18] M. Ohki, T. Motooka, T. Abe, H. Nagai, T. Tadono, Y. Kankaku, and M. Shimada. ALOS-2 mission status updates. In *IGARSS 2018; IEEE International Geoscience and Remote Sensing Symposium*, pages 4166–4168. IEEE, 2018.

[19] Y. Kankaku, Y. Arikawa, S. Miura, T. Motohka, and Y. Kojima. ALOS-4 system design and PFM current status. In *IGARSS 2023; IEEE International Geoscience and Remote Sensing Symposium*, pages 1998–2001. IEEE, 2023.

[20] A. Mahmood. RADARSAT-1 background mission implementation and accomplishments. *Canadian Journal of Remote Sensing*, 40(6):385–395, 2014.

[21] L. C. Morena, K. V. James, and J. Beck. An introduction to the RADARSAT-2 mission. *Canadian Journal of Remote Sensing*, 30(3):221–234, 2004.

[22] G. Kroupnik, D. De Lisle, S. Côté, M. Lapointe, C. Casgrain, and R. Fortier. RADARSAT constellation mission overview and status. In *2021 IEEE Radar Conference*, pages 1–5, 2021.

[23] F. Caltagirone, G. De Luca, F. Covello, G. Marano, G. Angino, and M. Piemontese. Status, results, potentiality and evolution of COSMO-SkyMed, the Italian Earth observation constellation for risk management and security. In *IGARSS 2010; IEEE International Geoscience and Remote Sensing Symposium*, pages 4393–4396. IEEE, 2010.

[24] L. Pulvirenti, G. Squicciarino, E. Fiori, L. Candela, and S. Puca. Analysis and processing of the COSMO-SkyMed second generation images of the 2022 marche (Central Italy) flood. *Water*, 15(7):1353, 2023.

[25] Italian Space Agency (ASI). COSMO-SkyMed second generation: Space infrastructure for Earth observation, 2024. URL `https://www.asi.it/en/earth-science/cosmo-skymed/`. Accessed: September 23, 2024.

[26] R. Werninghaus and S. Buckreuss. The TerraSAR-X mission and system design. *IEEE Transactions on Geoscience and Remote Sensing*, 48(2): 606–614, 2010.

[27] S. Buckreuss, B. Schättler, T. Fritz, J. Mittermayer, R. Kahle, E. Maurer, J.s Böer, M. Bachmann, F. Mrowka, E. Schwarz, H. Breit, and U. Steinbrecher. Ten years of TerraSAR-X operations. *Remote Sensing*, 10(6): 873, 2018.

[28] A. Moreira, G. Krieger, I. Hajnsek, D. Hounam, M. Werner, S. Riegger, and E. Settelmeyer. TanDEM-X: A TerraSAR-X add-on satellite for single-pass SAR interferometry. In *IGARSS 2004; IEEE International Geoscience and Remote Sensing Symposium*, volume 2, pages 1000–1003. IEEE, 2004.

[29] G. Krieger, A. Moreira, H. Fiedler, I. Hajnsek, M. Werner, M. Younis, and M. Zink. TanDEM-X: A satellite formation for high-resolution SAR interferometry. *IEEE Transactions on Geoscience and Remote Sensing*, 45(11):3317–3341, 2007.

[30] B. Rizzoli, P. and Martone, M. and Gonzalez, C. and Wecklich, C. and Tridon, D. B. and others, M. Huber, B. Wessel, G. Krieger, M. Zink, and A. Moreira. Generation and performance assessment of the global TanDEM-X digital elevation model. *ISPRS Journal of Photogrammetry and Remote Sensing*, 132:119–139, 2017.

[31] M. Zink, M. Bachmann, B. Brautigam, T. Fritz, I. Hajnsek, A. Moreira, B. Wessel, and G. Krieger. TanDEM-X: The new global DEM takes shape. *IEEE Geoscience and Remote Sensing Magazine*, 2(2):8–23, 2014.

[32] T. Misra and A. S. Kirankumar. RISAT-1: configuration and performance evaluation. In *2014 XXXIth URSI General Assembly and Scientific Symposium (URSI GASS)*, pages 1–4. IEEE, 2014.

[33] X. Bian, Y. Shao, W. Tian, and C. Zhang. Estimation of shallow water depth using HJ-1C S-band SAR data. *The Journal of Navigation*, 69(1): 113–126, 2016.

[34] S. G. Lee, S. J. Lee, H. Kim, T. B. Chea, and D. Ryu. Status of the Kompsat-5 SAR mission, utilization and future plans. In *IGARSS 2020; IEEE International Geoscience and Remote Sensing Symposium*, pages 3552–3555, 2020.

[35] R. Torres, P. Snoeij, D. Geudtner, D. Bibby, M. Davidson, E. Attema, P. Potin, B. Rommen, N. Floury, M. Brown, et al. GMES Sentinel-1 mission. *Remote Sensing of Environment*, 120:9–24, 2012.

[36] L. Zhao, Q. Zhang, Y. Li, Y. Qi, X. Yuan, J. Liu, and H. Li. China's Gaofen-3 satellite system and Its application and prospect. *IEEE Journal of Selected Topics in Applied Earth Observations and Remote Sensing*, 14:11019–11028, 2021.

[37] S. Xue, X. Geng, L. Meng, T. Xie, L. Huang, and X. H. Yan. HISEA-1: The first C-band SAR miniaturized satellite for ocean and coastal observation. *Remote Sensing*, 13(11), 2021.

[38] J. Zheng, Q. Chen, X. Yan, and W. Ren. HISEA-1: China's first miniaturized mommercial C-Band SAR satellite. In *IGARSS 2022; IEEE International Geoscience and Remote Sensing Symposium*, pages 4133–4136, 2022.

[39] Spacety Co., Ltd. Imagery from Chaohu-1 SAR satellite unveiled, 2022. URL `https://en.spacety.com/index.php/2022/03/09/imagery-from-chaohu-1-sar-satellite-unveiled/`. Accessed: May 29, 2025.

[40] T. Li, X. Tang, X. Zhang, J. Lu, and X. Zhang. Current status and prospects of the LuTan-1 mission. In *2024 IEEE International Conference on Signal, Information and Data Processing (ICSIDP)*, pages 1–4, 2024.

[41] Space News 35. China launches first geosynchronous orbit radar satellite, 2022. URL `https://spacenews.com/China-launches-first-geosynchronous-orbit-radar-satellite/`. Accessed: March 21, 2025.

[42] L. Chang, A. Kulshrestha, B. Zhang, and X. Zhang. Extraction and analysis of radar scatterer attributes for PAZ SAR by combining time series InSAR, PolSAR, and land use measurements. *Remote Sensing*, 15(6):1571, 2023.

[43] M. Cohen, A. Larkins, P. L. Semedo, and G. Burbidge. NovaSAR-S low cost spaceborne SAR payload design, development and deployment of a new benchmark in spaceborne radar. In *2017 IEEE Radar Conference*, pages 0903–0907, 2017.

[44] M. Palomeque, J. Ferreyra, and M. Thibeault. Monitoring results of the SAOCOM-1 constellation: a mission overview and summary of results. *IEEE Geoscience and Remote Sensing Magazine*, pages 2–11, 2024.

[45] M. L. Battagliere, M. G. Daraio, F. Lenti, A. R. Pisani, and A. Coletta. COSMO-SkyMed and the ASI-CONAE cooperation: The SIASGE programme. *Proc. 68th Int. Astronautical Cong*, 2018.

[46] DSO National Laboratories. Singapore launches its first locally developed synthetic aperture radar (SAR) microsatellite, 2022. URL `https://www.dso.org.sg/media-centre/media-release/1606`. Accessed: May 29, 2025.

[47] ST Engineering. ST Engineering launches its first SAR satellite, 2023. URL `https://www.stengg.com/en/newsroom/news-releases/st-engineering-launches-its-first-sar-satellite/`. Accessed: May 29, 2025.

[48] V. Ignatenko, P. Laurila, A. Radius, L. Lamentowski, O. Antropov, and D. Muff. ICEYE microsatellite SAR constellation status update: Evaluation of first commercial imaging modes. In *IGARSS 2020; IEEE International Geoscience and Remote Sensing Symposium*, pages 3581–3584, 2020.

[49] D. Castelletti, G. Farquharson, C. Stringham, M. Duersch, and D. Eddy. Capella space first operational SAR satellite. In *IGARSS 2021; IEEE International Geoscience and Remote Sensing Symposium*, pages 1483–1486, 2021.

[50] D. Faizullin, M. Uetsuhara, R. Takahira, J. Murayama, M. Katayama, S. Onishi, and T. Yasaka. Attitude determination and control system for the first SAR satellite in a constellation of iQPS. In *71st International Astronautical Congress (IAC)*, 2020.

[51] K. Orzel, A. Fujita, M. M. D'Alessandro, G. Baier, H. Sugino, M. Kontto, S. Garsva, J. Krecke, J. Imber, A. Fukuda, and S. Fujimaru. Synspective SAR constellation status update: recent calval activities and the automatic data quality assessment. In *IGARSS 2023; IEEE International Geoscience and Remote Sensing Symposium*, pages 1517–1520, 2023.

[52] Umbra Space. Umbra product guide: Umbra satellites, 2024. URL `https://help.umbra.space/product-guide/umbra-satellites`. Accessed: September 23, 2024.

[53] ESA eoPortal. Umbra SAR constellation, 2024. URL `https://www.eoportal.org/satellite-missions/umbra-sar#launch`. Accessed: May 29, 2025.

[54] H. Li, H. Zhang, Q. Chen, Y. Gao, X. Shi, and L. Zhang. Accuracy analysis of radiometric calibration in-orbit for SuperView Neo-2 SAR satellite. *IEEE Journal of Selected Topics in Applied Earth Observations and Remote Sensing*, 17:2234–2244, 2024.

[55] Y. Deng, H. Zhang, K. Liu, W. Wang, N. Ou, H. Han, R. Yang, J. Ren, J. Wang, X. Ren, H. Fan, and S. Guo. Hongtu-1: The first spaceborne single-pass multibaseline SAR interferometry mission. *IEEE Transactions on Geoscience and Remote Sensing*, 63:1–18, 2025.

[56] European Space Agency. Biomass launched to count forest carbon, 2025. URL `https://www.esa.int/Applications/Observing_the_Earth/FutureEO/Biomass/Biomass_launched_to_count_forest_carbon`. Press release. Accessed: May 29, 2025.

[57] M. Sedehi, A. Carbone, E. Imbembo, F. Heliere, B. Rommen, M. Fehringer, K. Scipal, A. Leanza, T. Simon, and P. Willemsen. BIOMASS - A fully polarimetric P-band SAR ESA mission. In *EUSAR 2021; 13th European Conference on Synthetic Aperture Radar*, pages 1–5, 2021.

[58] P. A. Rosen and R. Kumar. NASA-ISRO SAR (NISAR) mission status. In *2021 IEEE Radar Conference*, pages 1–6, 2021.

[59] M. Davidson and R. Furnell. ROSE-L: Copernicus L-Band SAR mission. In *IGARSS 2021; IEEE International Geoscience and Remote Sensing Symposium*, pages 872–873, 2021.

[60] O. Pappas, J. Biggs, P. Prats-Iraola, A. Pulella, A. Stinton, and A. Achim. Measuring topographic change after volcanic eruptions using multistatic SAR satellites: Simulations in preparation for ESA's Harmony mission. *Remote Sensing of Environment*, 317:114528, 2025.

[61] A. Moreira, G. Krieger, I. Hajnsek, K. Papathanassiou, M. Younis, P. Lopez-Dekker, S. Huber, M. Villano, M. Pardini, M. Eineder, et al. Tandem-L: A highly innovative bistatic SAR mission for global observation of dynamic processes on the Earth's surface. *IEEE Geoscience and Remote Sensing Magazine*, 3(2):8–23, 2015.

[62] IPCC. Summary for Policymakers. In *Climate Change 2023: Synthesis Report. Contribution of Working Groups I, II and III to the Sixth Assessment Report of the Intergovernmental Panel on Climate Change* [Core Writing Team, H. Lee and J. Romero (eds.)], pages 35–115. IPCC, Geneva, Switzerland, 2023.

[63] World Meteorological Organization (WMO). Observing systems capability analysis and review tool (OSCAR), 2024. URL `https://www.wmo-sat.info/oscar`. Accessed: September 17, 2024.

[64] Copernicus Cultural Heritage Task Force. Report on the user requirements in the Copernicus domain to support cultural heritage management, conservation and protection. Technical report, Copernicus Programme, 2020. URL `https://www.copernicus.eu/sites/default/files/2020-10/CC-2020-37_Copernicus-Cultural-Heritage-Task-Force-Report_0.pdf`. Accessed: March 22, 2025.

[65] E. Lancheros, A. Camps, H. Park, P. Sicard, A. Mangin, H. Matevosyan, and I. Lluch. Gaps analysis and requirements specification for the evolution of copernicus system for polar regions monitoring: Addressing the challenges in the horizon 2020–2030. *Remote Sensing*, 10(7):1098, 2018.

[66] W. Dorigo et al. ESA CCI soil moisture for improved Earth system understanding: State-of-the art and future directions. *Remote Sensing of Environment*, 203:185–215, 2017.

[67] P. Bally. *Satellite Earth Observation for Geohazard Risk Management: The Santorini Conference, Santorini, Greece, 21-23 May 2012*. European Space Agency, 2014.

[68] European Space Agency (ESA). ESA's living planet programme: scientific achievements and future challenges–scientific context of the Earth observation science strategy for ESA (ESA SP-1329/2), 2015.

[69] K. Tomiyasu. Synthetic aperture radar in geosynchronous orbit. In *1978 Antennas and Propagation Society International Symposium*, volume 16, pages 42–45, 1978.

[70] K. Tomiyasu and J. L. Pacelli. Synthetic aperture radar imaging from an inclined geosynchronous orbit. *IEEE Transactions on Geoscience and Remote Sensing*, GE-21(3):324–329, 1983.

[71] Madsen, S. N. and Edelstein, W. and DiDomenico, L. D. and LaBrecque, J. A geosynchronous synthetic aperture radar; for tectonic mapping, disaster management and measurements of vegetation and soil moisture. In *IGARSS 2001; IEEE International Geoscience and Remote Sensing Symposium*, volume 1, pages 447–449, 2001.

[72] W. Edelstein, S. Madsen, A. Moussessian, and C. Chen. Concepts and technologies for synthetic aperture radar from MEO and geosynchronous orbits. *Proceedings of SPIE - The International Society for Optical Engineering*, pages 195–203, 01 2005.

[73] C. Chen and A. Moussessian. MeoSAR system concepts and technologies for Earth remote sensing. In *Space 2004 Conference and Exhibit*, page 5904, 2004.

[74] A. Moussessian, C. Chen, W. Edelstein, S. Madsen, and P. A. Rosen. System concepts and technologies for high orbit SAR. In *IEEE MTT-S International Microwave Symposium Digest 2005*, pages 1–4, June 2005.

[75] D. Tralli, W. Foxall, and C. Schultz. Concept for a High MEO InSAR seismic monitoring system. In *Aerospace Conference 2007 IEEE*, pages 1–7. IEEE, 2007.

[76] C. Prati, F. Rocca, D. Giancola, and A. M. Guarnieri. Passive geosynchronous SAR system reusing backscattered digital audio broadcasting signals. *IEEE Transactions on Geoscience and Remote Sensing*, 36(6): 1973–1976, 1998.

[77] S. E. Hobbs. *GeoSAR: Summary of the Group Design Project MSc in Astronautics and Space Engineering 2005/06 Cranfield University*. Cranfield University UK, 2006.

[78] Bruno.D, S. E. Hobbs, and G. Ottavianelli. Geosynchronous synthetic aperture radar: concept design, properties and possible applications. *Acta Astronautica*, 59(1):149–156, 2006.

[79] A. Monti Guarnieri, L. Perletta, F. Rocca, D. Scapin, S. Tebaldini, A. Broquetas, and J. Ruiz. Design of a geosynchronous SAR system for water-vapour maps and deformation estimation. *Fringe, Paris, France*, 2011.

[80] A. Monti Guarnieri, S. Tebaldini, F. Rocca, and A. Broquetas. GEMINI: geosynchronous SAR for Earth monitoring by interferometry

and imaging. In *IGARSS 20012; IEEE International Geoscience and Remote Sensing Symposium*, pages 210–213, 2012.

[81] A. Monti Guarnieri, F. Djelaili, D. Schulz, V. T. Khang, A. Recchia, F. Rocca, D. Giudici, S. E. Hobbs, T. Strozzi, C. Werner, R. Venturini, A. Broquetas, J. Ruiz-Rodon, and G. Wadge. Wide coverage, fine resolution, geosynchronous SAR for atmospheric and terrain observations. In *Living Planet Symp., paper no. ESA SP-722*, 2013.

[82] J. Ruiz Rodon, A. Broquetas, E. Makhoul, A. Monti Guarnieri, and F. Rocca. Nearly zero inclination geosynchronous SAR mission analysis With long integration time for Earth observation. *IEEE Transactions on Geoscience and Remote Sensing*, 52(10):6379–6391, 2014.

[83] S. E. Hobbs, C. Mitchell, B. Forte, R. Holley, B. Snapir, and P. Whittaker. System design for geosynchronous synthetic aperture radar missions. *IEEE Transactions on Geoscience and Remote Sensing*, 52(12): 7750–7763, 2014.

[84] A. Broquetas, D. Casado, R. Martin, M. Fernández, A. Monti Guarnieri, and A. Leanza. Track compensation and calibration of continuous monitoring GEOSAR missions. In *IGARSS 2016; IEEE International Geoscience and Remote Sensing Symposium*, pages 1408–1411, 2016.

[85] J. Nicolas, X. Carreño-Megias, E. Ferrer, M. Albert, A. Garcia, A. Garcia, J.A. Travieso-Rodríguez, B. Garcia, A. Aguasca, and A. Broquetas. Simultaneous interferometric tracking of a multi-satellite geosynchronous constellation for GEOSAR missions. In *International Astronautical Congress*, 2021.

[86] A. Monti Guarnieri, F. Rocca, and A. Broquetas. Impact of atmospheric water vapor on the design of a Ku band geosynchronous SAR system. In *IGARSS 2009; IEEE International Geoscience and Remote Sensing Symposium*, volume 2, pages II–945. IEEE, 2009.

[87] J. Ruiz Rodon, A. Broquetas, E. Makhoul, A. Monti Guarnieri, and F. Rocca. Results on spatial-temporal atmospheric phase screen retrieval from long-term GEOSAR acquisition. In *IGARSS 2012; IEEE International Geoscience and Remote Sensing Symposium*, pages 3289–3292, 2012.

[88] J. Ruiz Rodon, A. Broquetas, A. Monti Guarnieri, and F. Rocca. Atmospheric phase screen retrieval from GEOSAR long term acquisition. In *EUSAR 2012; 9th European Conference on Synthetic Aperture Radar*, pages 79–82, 2012.

[89] J. Ruiz Rodon, A. Broquetas, A. Monti Guarnieri, and F. Rocca. Geosynchronous SAR focusing with atmospheric phase screen retrieval and compensation. *IEEE Transactions on Geoscience and Remote Sensing*, 51(8):4397–4404, Aug 2013.

[90] M. Belotti, A. Broquetas, A. Leanza, A. Monti Guarnieri, A. Recchia, F. Rocca, J. Ruiz, and S. Tebaldini. An efficient method for the azimuth compression of geosynchronous SAR data through subapertures processing. In *IGARSS 2013; IEEE International Geoscience and Remote Sensing Symposium*, pages 2047–2050, 2013.

[91] D. Li, M. Rodriguez-Cassola, P. Prats-Iraola, Z. Dong, M. Wu, and A. Moreira. Modelling of tropospheric delays in geosynchronous synthetic aperture radar. *Science China Information Sciences*, 60:1–18, 2017.

[92] A. Monti Guarnieri, A. Leanza, A. Recchia, S. Tebaldini, and G. Venuti. Atmospheric phase screen in GEO-SAR: Estimation and compensation. *IEEE Transactions on Geoscience and Remote Sensing*, 56 (3):1668–1679, 2018.

[93] D. Bruno and S. E. Hobbs. Radar imaging from geosynchronous orbit: temporal decorrelation aspects. *IEEE Transactions on Geoscience and Remote Sensing*, 48(7):2924–2929, 2010.

[94] S. E. Hobbs, B. Snapir, R. Corstanje, C. Mitchell, B. Forte, R. Holley, P. Whittaker, K. Graham, and R. Burren. Simulation of geosynchronous radar and atmospheric phase compensation constraints. In *IET International Radar Conference 2013*, page C0737. IET, 2013.

[95] A. Recchia, A. M. Guarnieri, A. Broquetas, and A. Leanza. Impact of scene decorrelation on geosynchronous SAR data focusing. *IEEE Transactions on Geoscience and Remote Sensing*, 54(3):1635–1646, 2016.

[96] Y. Li, A. Monti Guarnieri, C. Hu, and F. Rocca. Performance and requirements of GEO SAR systems in the presence of radio frequency interferences. *Remote Sensing*, 10(1):82, 2018.

[97] A. Leanza, M. Manzoni, A. Monti-Guarnieri, and M. di Clemente. LEO to GEO-SAR interferences: Modelling and performance evaluation. *Remote Sensing*, 11(14):1720, 2019.

[98] V. Gracheva, P. Prats, R. Scheiber, R. Horn, M. Keller, J. Fischer, A. Reigber, and A. Moreira. Simulation of geosynchronous Hydroterra image products with airborne SAR data. In *EUSAR 2021; 13th European Conference on Synthetic Aperture Radar*, pages 1–6. VDE, 2021.

[99] A. Aguasca, A. Broquetas, X Fàbregas, J. J. Mallorquí Franquet, P. Vilalvilla, J. Biscamps, J. Llop, M. Gallart, E. Gil, and A. Gras. Hydrosoil, soil moisture and vegetation parameters retrieval with a C-Band GB-SAR: Campaign implementation and first results. In *IGARSS 2021; IEEE International Geoscience and Remote Sensing Symposium*, pages 6685–6687, 2021.

[100] R. Haagmans et al. Earth explorer 10 candidate mission Hydroterra. *ESA Report Assessment*, 2020.

[101] S. E. Hobbs and A. Monti Guarnieri. Geosynchronous continental land-atmosphere sensing system (G-Class): persistent radar imaging for Earth science. In *IGARSS 2018; IEEE International Geoscience and Remote Sensing Symposium*, pages 8621–8624, 2018.

[102] S. E. Hobbs, J. Calvet, G. Boni, R. Haagmans, G. Halloran, R. Hanssen, J. Kubanek, F. Mattia, A. Monti Guarnieri, A. Moreira, et al. Hydroterra: exploring the science of rapid water cycle processes over land. In *ESA Living Planet Symposium 2022*, 2022.

[103] J. Fischer, R. Scheiber, and J. Kubanek. First comparative analysis of simulated low and high resolution Hydroterra and conventional SAR data. In *EUSAR 2024; 15th European Conference on Synthetic Aperture Radar*, pages 260–265, 2024.

[104] European Space Agency. Phase 0/A system studies of the Hydroterra+ mission, 2024. URL `https://esastar-publication-ext.sso.esa.int/ESATenderActions/details/93025`. Accessed: March 22, 2025.

[105] M. Bao, Y. Liao, Z. J. Tian, M. D. Xing, and Y. C. Li. Imaging algorithm for GEO SAR based on series reversion. In *Proceedings of 2011 IEEE CIE international conference on radar*, volume 2, pages 1493–1496. IEEE, 2011.

[106] X. Dong, Y. Gao, C. Hu, T. Zeng, and C. Dong. Effects of Earth rotation on GEO SAR characteristics analysis. In *Proceedings of 2011 IEEE CIE international conference on radar*, volume 1, pages 34–37. IEEE, 2011.

[107] T. Long, C. Hu, Z. Ding, X. Dong, W. Tian, and T. Zeng. *Geosynchronous SAR: System and Signal Processing*. Springer, 2018.

[108] W. Liu, G. C. Sun, X. G. Xia, D. You, M. Xing, and Z. Bao. Highly squinted MEO SAR focusing based on extended Omega-K algorithm and modified joint time and Doppler resampling. *IEEE Transactions on Geoscience and Remote Sensing*, 57(11):9188–9200, 2019.

[109] G. C. Sun, Y. Liu, J. Xiang, W. Liu, M. Xing, and J. Chen. Spaceborne synthetic aperture radar imaging algorithms: an overview. *IEEE Geoscience and Remote Sensing Magazine*, 10(1):161–184, 2022.

[110] L. Kou, M. Xiang, X. Wang, and M. Zhu. Tropospheric effects on L-band geosynchronous circular SAR imaging. *IET Radar, Sonar and Navigation*, 7(6):693–701, 2013.

[111] X. Dong, C. Hu, and T. Zeng. Antenna area constraint in GEO SAR. In *IET International Radar Conference 2013*, pages 1–4, 2013.

[112] C. Hu, X. Li, T. Long, and Y. Gao. GEO SAR interferometry: Theory and feasibility study. In *IET International Radar Conference 2013*, pages 1–5. IET, 2013.

[113] D. A. Vallado. *Fundamentals of Astrodynamics and Applications*, volume 12. Springer Science & Business Media, 4th edition, 2013.

[114] J. R. Wertz and W. Larson. *Space Mission Analysis and Design*, volume 8. Springer, 1999.

[115] O. Montenbruck and E. Gill. *Satellite Orbits: Models, Methods, and Applications*. Springer, 2000.

[116] V. A. Chobotov. *Orbital Mechanics*. American Institute of Aeronautics and Astronautics (AIAA), 3rd edition, 2002.

[117] W. E Wiesel. *Spaceflight Dynamics*. New York: McGrawHill Book Company, 1996.

[118] C. Pickover. *Archimedes to Hawking: Laws of Science and the Great Minds Behind Them*. Oxford University Press, 2008.

[119] International Telecommunication Union. *Radio Regulations Articles*. ITU, 2020.

[120] A. Milani, A. M. Nobili, and P. Farinella. Non-gravitational perturbations and satellite geodesy. *Astronomische Nachrichten*, 309:38, 1988.

[121] NOAA, NASA, USAF. *US Standard Atmosphere, 1976*. US Government Printing Office (GPO), 1976.

[122] R. Boain. A-B-Cs of sun-synchronous orbit mission design. *14th AAS/AIAA Space Flight Mechanics Conference*, 2004.

[123] W. D. McClain. A recursively formulated first-order semianalytic artificial satellite theory based on the generalized method of averaging. Vol. 2. Technical Report CSC/TR-78/6001, Computer Sciences Corporation, 1978.

[124] C. R. Ortiz Longo and S. L. Rickman. Method for the calculation of spacecraft umbra and penumbra shadow terminator points. *NASA Technical Paper 3547*, April 1995.

[125] NASA. NASA's Van Allen probes reveal previously undetected radiation belt around Earth, 2013. URL `https://www.nasa.gov/news-release/nasas-van-allen-probes-reveal-a-new-radiation-belt-around-earth/`. Accessed: January 31, 2025.

[126] G Furano, R Jansen, and A Menicucci. Review of radiation hard electronics activities at European Space Agency. *Journal of Instrumentation*, 8(02):C02007, 2013.

[127] H. H. Andersen, J. F. Bak, H. Knudsen, and B. R. Nielsen. Stopping power of Al, Cu, Ag, and Au for MeV hydrogen, helium, and lithium ions. Z_1^3 and Z_1^4 proportional deviations from the Bethe formula. *Physical Review A*, 16(5):1929, 1977.

[128] M. Burrell, J. Watts, and J. Wright. An analysis of energetic space radiation and dose rates. *NASA Technical Note TN D-4404*, 4404, 1968.

[129] W. R. Johnston, T. P. O'Brien, G. P. Ginet, S. L. Huston, T. B. Guild, and J. A. Fennelly. AE9/AP9/SPM: New models for radiation belt and space plasma specification. In *Sensors and Systems for Space Applications VII*, volume 9085, pages 42–50. SPIE, 2014.

[130] R. Lagier. VEGA C user's manual. Technical report, Arianespace, 2018.

[131] R. Lagier. Ariane 6 user's manual. Technical report, Arianespace, 2016.

[132] R. Lagier. Ariane 5 user's manual. Technical report, Arianespace, 2021.

[133] SpaceX. Falcon user's guide. Technical report, SpaceX, 2021. URL `https://www.spacex.com/media/falcon-users-guide-2021-09.pdf`. Accessed: December 17, 2024.

[134] E. Perez. Soyuz at the Guiana Space Centre user's manual. Technical report, Technical report Arianespace, 2012.

[135] Roscosmos State Corporation. Soyuz-2 launch vehicle overview. Technical report, Roscosmos, 2020.

[136] R. Bate, D. Mueller, and J. White. *Fundamentals of Astrodynamics*. Courier Corporation, 1971.

[137] M. Turner. *Rocket and Spacecraft Propulsion: Principles, Practice and New Developments*. Springer Science & Business Media, 2009.

[138] J. Curlander and R. McDonough. *Synthetic Aperture Radar: Systems and Signal Processing*, volume 11. Wiley, New York, 1991.

[139] I. G. Cumming and F. H. Wong. *Digital Processing of Synthetic Aperture Radar Data*, volume 1. Boston, 2005.

[140] A. Moreira, P. Prats-Iraola, M. Younis, G. Krieger, I. Hajnsek, and K. Papathanassiou. A tutorial on synthetic aperture radar. *IEEE Geoscience and Remote Sensing Magazine*, 1(1):6–43, 2013.

[141] A. Moreira, J. Mittermayer, and R. Scheiber. Extended chirp scaling algorithm for air- and spaceborne SAR data processing in stripmap and ScanSAR imaging modes. *IEEE Transactions on Geoscience and Remote Sensing*, 34(5):1123–1136, 1996.

[142] C. Prati, A. M. Guarnieri, and F. Rocca. Spot mode SAR focusing with the omega-k technique. In *IGARSS 1991; IEEE International Geoscience and Remote Sensing Symposium*, volume 2, pages 631–634, 1991.

[143] R. Bamler. A comparison of range-Doppler and wavenumber domain SAR focusing algorithms. *IEEE Transactions on Geoscience and Remote Sensing*, 30(4):706–713, 1992.

[144] W. G. Carrara, R. S. Goodman, and R. M. Majewski. *Spotlight Synthetic Aperture Radar: Signal Processing Algorithms*. Artech House., 1995.

[145] P. Prats, R. Scheiber, J. Mittermayer, A. Meta, and A. Moreira. Processing of sliding spotlight and TOPS SAR data using baseband azimuth scaling. *IEEE Transactions on Geoscience and Remote Sensing*, 48 (2):770–780, 2010.

[146] J. Mittermayer, R. Lord, and E. Borner. Sliding spotlight SAR processing for TerraSAR-X using a new formulation of the extended chirp scaling algorithm. In *IGARSS 2003; IEEE International Geoscience and Remote Sensing Symposium*, volume 3, pages 1462–1464. IEEE, 2003.

[147] P. A. Rosen, S. Hensley, L. Veilleux, M. Chakraborty, T. Misra, and Bhan R. ScanSAR and SweepSAR performance in next generation Earth science missions. In *IGARSS 2015; IEEE International Geoscience and Remote Sensing Symposium*, July 2015.

[148] F. De Zan and A. Monti Guarnieri. TOPSAR: Terrain observation by progressive scans. *IEEE Transactions on Geoscience and Remote Sensing*, 44(9):2352–2360, 2006.

[149] N. Gebert, G. Krieger, and A. Moreira. Multichannel azimuth processing in ScanSAR and TOPS mode operation. *IEEE Transactions on Geoscience and Remote Sensing*, 48(7):2994–3008, 2010.

[150] F. Rocca. Modeling interferogram stacks. *IEEE Transactions on Geoscience and Remote Sensing*, 45(10):3289–3299, 2007.

[151] R. F. Hanssen. *Radar Interferometry: Data Interpretation and Error Analysis*, volume 2. Springer Science & Business Media, 2001.

[152] P. A. Rosen, S. Hensley, I. R. Joughin, F. K. Li, S. N. Madsen, E. Rodriguez, and R. M. Goldstein. Synthetic aperture radar interferometry. *Proceedings of the IEEE*, 88(3):333–382, 2000.

[153] R. Bamler and P. Hartl. Synthetic aperture radar interferometry. *Inverse problems*, 14(4):R1, 1998.

[154] D. Massonnet and K. L. Feigl. Radar interferometry and its application to changes in the Earth's surface. *Reviews of geophysics*, 36(4): 441–500, 1998.

[155] L. C. Graham. Synthetic interferometer radar for topographic mapping. *Proceedings of the IEEE*, 62(6):763–768, 1974.

[156] H. A. Zebker and R. M. Goldstein. Topographic mapping from interferometric synthetic aperture radar observations. *Journal of Geophysical Research: Solid Earth*, 91(B5):4993–4999, 1986.

[157] P. Rizzoli, L. Dell'Amore, J. Bueso-Bello, N. Gollin, D. Carcereri, and M. Martone. On the derivation of volume decorrelation from TanDEM-X bistatic coherence. *IEEE Journal of Selected Topics in Applied Earth Observations and Remote Sensing*, 15:3504–3518, 2022.

[158] D. C. Ghiglia and M. D. Pritt. *Two-Dimensional Phase Unwrapping: Theory, Algorithms, and Software*. New York: John Wiley & Sons., 1998.

[159] A. Monti Guarnieri and S. Tebaldini. Hybrid Cramér–Rao bounds for crustal displacement field estimators in SAR interferometry. *IEEE Signal Processing Letters*, 14(12):1012–1015, 2007.

[160] T. J. Wright, B. E. Parsons, and Z. Lu. Toward mapping surface deformation in three dimensions using InSAR. *Geophysical Research Letters*, 31(1), 2004.

[161] H. Ansari, F. De Zan, A. Parizzi, M. Eineder, K. Goel, and N. Adam. Measuring 3-D surface motion with future SAR systems based on reflector antennae. *IEEE Geoscience and Remote Sensing Letters*, 13(2): 272–276, 2016.

[162] P. Prats-Iraola, P. Lopez-Dekker, F. De Zan, N. Yagüe-Martínez, M. Zonno, and M. Rodriguez-Cassola. Performance of 3-D surface deformation estimation for simultaneous squinted SAR acquisitions. *IEEE Transactions on Geoscience and Remote Sensing*, 56(4):2147–2158, 2018.

[163] F. Giudicepietro, F. Casu, M. Bonano, C. De Luca, P. De Martino, F. Di Traglia, M. A. Di Vito, G. Macedonio, M. Manunta, F. Monterroso, P. Striano, and R. Lanari. First evidence of a geodetic anomaly in the Campi Flegrei caldera (Italy) ground deformation pattern revealed by DInSAR and GNSS measurements during the 2021–2023 escalating unrest phase. *International Journal of Applied Earth Observation and Geoinformation*, 132:104060, 2024.

[164] F. De Zan, P. Prats, and G. Krieger. Mission design and performance for systematic deformation measurements with a spaceborne SAR system. In *IGARSS 2009; IEEE International Geoscience and Remote Sensing Symposium*, volume 2, pages II–793–796, 2009.

[165] J.-S. Lee, K. W. Hoppel, S. A. Mango, and A. R. Miller. Intensity and phase statistics of multilook polarimetric and interferometric SAR imagery. *IEEE Transactions on Geoscience and Remote Sensing*, 32(5): 1017–1028, 1994.

[166] M Abramowitz and IA Stegun. *Handbook of Mathematical Functions*. New York: Dover, 1965.

[167] E. Rodriguez and J. M. L. Martin. Theory and design of interferometric synthetic aperture radars. *IEE Proc. Inst. Electr. F–Radar and Signal Processing*, 139:147, 1992.

[168] F. Gatelli, A. Monti Guarnieri, F. Parizzi, P. Pasquali, C. Prati, and F. Rocca. The wavenumber shift in SAR interferometry. *IEEE Transactions on Geoscience and Remote Sensing*, 32(4):855–865, 1994.

[169] H. A. Zebker and J. Villasenor. Decorrelation in interferometric radar echoes. *IEEE Transactions on Geoscience and Remote Sensing*, 30(5):950–959, 1992.

[170] R. N. Treuhaft and P. R. Siqueira. Vertical structure of vegetated land surfaces from interferometric and polarimetric radar. *Radio science*, 35(1):141–177, 2000.

[171] A. Olesk, J. Praks, O. Antropov, K. Zalite, T. Arumäe, and K. Voormansik. Interferometric SAR coherence models for characterization of hemiboreal forests using TanDEM-X data. *Remote Sensing*, 8(9):700, 2016.

[172] A. Parizzi, X. Cong, and M. Eineder. First results from multifrequency interferometry. A comparison of different decorrelation time constants at L, C, and X band. In *(SP-677), ESA Scientific Publications*, pages 1–5, 2009.

[173] L. J. Porcello. Turbulence-induced phase errors in synthetic-aperture radars. *IEEE Transactions on Aerospace and Electronic Systems*, AES-6 (5):636–644, 1970.

[174] V. I. Tatarski. *Wave Propagation in a Turbulent Medium*. McGraw-Hill, New York, Translated from Russian, 1961.

[175] F. Onn. *Modeling Water Vapor Using GPS with Application to Mitigating InSAR Atmospheric Distortions*. Ph.D. Dissertation, Stanford University, Stanford, CA, USA, 2006.

[176] A. Rucci, A. Ferretti, A. Monti Guarnieri, and F. Rocca. Sentinel 1 SAR interferometry applications: the outlook for sub millimeter measurements. *Remote Sensing of Environment*, 120:156–163, 2012.

[177] E. Pichelli, R. Ferretti, D. Cimini, G. Panegrossi, D. Perissin, N. Pierdicca, F. Rocca, and B. Rommen. InSAR water vapor data assimilation into mesoscale model MM5: technique and pilot study. *IEEE Journal of Selected Topics in Applied Earth Observations and Remote Sensing*, 8(8):3859–3875, 2014.

[178] Y. Shoji, H. Yamauchi, W. Mashiko, and E. Sato. Estimation of local-scale precipitable water vapor distribution around each GNSS station using slant path delay. *Sola*, 10:29–33, 2014.

[179] J. Billingsley. Exponential decay in windblown radar ground clutter Doppler spectra: multifrequency measurements and model. Technical report, Lincoln Laboratory, Massachusetts Institute of Technology, 1996.

[180] J. Billingsley. *Low-Angle Radar Land Clutter: Measurements and Empirical Models*. IET, 2002.

[181] A. Monti Guarnieri, M. Manzoni, D. Giudici, A. Recchia, and S. Tebaldini. Vegetated target decorrelation in SAR and interferometry: models, simulation, and performance evaluation. *Remote Sensing*, 12(16): 2545, 2020.

[182] S. Gantert, A. Kern, R. Düring, J. Janoth, L. Petersen, and J. Hermann. The future of X-band SAR: TerraSAR-X next generation and WorldSAR constellation. In *APSAR 2013; Asia-Pacific Conference on Synthetic Aperture Radar*, pages 20–23. IEEE, 2013.

[183] Airbus Defence and Space. Airbus-built Earth observation satellite (SARah-1) ready for launch, 2022. URL https://www.airbus.com/en/newsroom/press-releases/2022-06-airbus-built-earth-observation-satellite-sarah-1-ready-for-launch. Accessed: May 29, 2025.

[184] F. Covello, F. Battazza, A. Coletta, E. Lopinto, C. Fiorentino, L. Pietranera, G. Valentini, and S. Zoffoli. COSMO-SkyMed an existing opportunity for observing the Earth. *Journal of Geodynamics*, 49 (3):171–180, 2010.

[185] S. Cote, M. Lapointe, D. De Lisle, E. Arsenault, and M. Wierus. The RADARSAT constellation: Mission overview and status. In *EUSAR 2021; 13th European Conference on Synthetic Aperture Radar*, pages 1–5, 2021.

[186] G. Heiming. Satellitenaufklärungssysteme SARah komplett im All, 2023. URL https://esut.de/2023/12/meldungen/46421/satellitenaufklaerungssysteme-sarah-komplett-im-all/. Accessed: May 29, 2025.

[187] M. Naranjo, A. Montesano, F. Monjas, M. Gomez, R. Manrique, F. Heliere, and K. Van't Klooster. BIOMASS P-Band SAR reflector antenna - Feed S/S breadboarding. In *EUSAR 2014; 10th European Conference on Synthetic Aperture Radar*, pages 1–4, 2014.

[188] P. Xaypraseuth, R. Satish, and A. Chatterjee. NISAR spacecraft concept overview: Design challenges for a proposed flagship dual-frequency SAR mission. In *2015 IEEE Aerospace Conference*, pages 1–11, 2015.

[189] J. Matar, M. Rodriguez-Cassola, G. Krieger, P. López-Dekker, and A. Moreira. MEO SAR: system concepts and analysis. *IEEE Transactions on Geoscience and Remote Sensing*, 58(2):1313–1324, 2020.

[190] J. Matar and Marc Rodriguez-Cassola. Mission considerations for future MEO-SAR systems. In *EUSAR 2018; 12th European Conference on Synthetic Aperture Radar*, pages 1240–1244, 2018.

[191] Avio S.p.A. Zefiro 9 - Solid rocket motor for the Vega launch vehicle, 2024. URL https://www.avio.com/zefiro-9. Accessed: December 05, 2024.

[192] P. J. Alliot, J. Delange, and A. Lekeux. VINCI, the European reference for Ariane 6 upper stage cryogenic propulsive system. In *51st AIAA/SAE/ASEE Joint Propulsion Conference*, page 4063, 2015.

[193] Safran Group. PPS5000 - Safran spacecraft propulsion - Datasheet, 2022. URL https://www.safran-group.com/sites/default/files/2022-09/PPS5000-SafranSpacecraftPropulsion-Datasheet.pdf. Accessed: December 05, 2024.

[194] H. Fiedler, E. Boerner, J. Mittermayer, and G. Krieger. Total zero Doppler steering–A new method for minimizing the Doppler centroid. *IEEE Geoscience and Remote Sensing Letters*, 2(2):141–145, 2005.

[195] W. Emery and A. Camps. *Introduction to Satellite Remote Sensing: Atmosphere, Ocean, Land and Cryosphere applications*. Elsevier, 2017.

[196] A. Freeman, W. Johnson, B. Huneycutt, R. Jordan, S. Hensley, P. Siqueira, and J. Curlander. The "Myth" of the minimum SAR antenna area constraint. *IEEE Transactions on Geoscience and Remote Sensing*, 38(1):320–324, 2000.

[197] Harris Corporation. Unfurlable mesh reflector antennas, 2025. URL https://www.l3harris.com/all-capabilities/unfurlable-mesh-reflector-antennas. Accessed: January 19, 2025.

[198] M. Suess and W. Wiesbeck. Side-looking synthetic aperture radar system. *European Patent EP*, 1(241):487, 2002.

[199] A. Freeman, G. Krieger, P. A. Rosen, M. Younis, W. Johnson, S. Huber, R. Jordan, and A. Moreira. SweepSAR: Beam-forming on receive using a reflector-phased array feed combination for spaceborne SAR. In *2009 IEEE Radar Conference*, pages 1–9. IEEE, 2009.

[200] G. Krieger, N. Gebert, and A. Moreira. Multidimensional waveform encoding: a new digital beamforming technique for synthetic aperture radar remote sensing. *IEEE Transactions on Geoscience and Remote Sensing*, 46(1):31–46, 2008.

[201] R. Moore, J. Claassen, and Y. Lin. Scanning spaceborne synthetic aperture radar with integrated radiometer. *IEEE Transactions on Aerospace and Electronic Systems*, AES-17(3):410–421, 1981.

[202] J. Matar, M. Rodriguez-Cassola, G. Krieger, M. Zonno, and A. Moreira. Potential of MEO SAR for global deformation mapping. In *EUSAR 2021; 13th European Conference on Synthetic Aperture Radar*, pages 876–880, 2021.

[203] D. Geudtner, M. Tossaint, M. Davidson, and R. Torres. Copernicus Sentinel-1 next generation mission. In *IGARSS 2021; IEEE International Geoscience and Remote Sensing Symposium*, pages 874–876, 2021.

[204] P. Valle, G. Orlando, R. Mizzoni, F. Hélière, and K. van't Klooster. P-band feedarray for BIOMASS. In *EUCAP 2012; 6th European Conference on Antennas and Propagation*, pages 3426–3430, March 2012.

[205] S. Huber, F. de Almeida, M. Villano, M. Younis, G. Krieger, and A. Moreira. Tandem-L: A technical perspective on future spaceborne SAR sensors for Earth observation. *IEEE Transactions on Geoscience and Remote Sensing*, 56(8):4792–4807, 2018.

[206] GRASP Team. GRASP - Reflector antenna design analysis software, 2024. URL `https://www.ticra.com/software/grasp/`.

[207] G. Krieger, N. Gebert, M. Younis, F. Bordoni, A. Patyuchenko, and A. Moreira. Advanced concepts for ultra-wide-swath SAR imaging. In *EUSAR 2008; 7th European Conference on Synthetic Aperture Radar*, pages 1–4, June 2008.

[208] G. Krieger, M. Younis, N. Gebert, S. Huber, F. Bordoni, A. Patyuchenko, and A. Moreira. Advanced digital beamforming concepts for future SAR systems. In *IGARSS 2010; IEEE International Geoscience and Remote Sensing Symposium*, pages 245–248, 2010.

[209] M. Villano, G. Krieger, and A. Moreira. Staggered SAR: High-resolution wide-swath imaging by continuous PRI variation. *IEEE Transactions on Geoscience and Remote Sensing*, 52(7):4462–4479, July 2014.

[210] M. Villano, G. Krieger, and A. Moreira. Nadir echo removal in synthetic aperture radar via waveform diversity and dual-focus post-processing. *IEEE Geoscience and Remote Sensing Letters*, 15(5):719–723, 2018.

[211] F. Ulaby, M. Dobson, and J. Álvarez-Pérez. *Handbook of Radar Scattering Statistics for Terrain*. Artech House, 2019.

[212] D. Small. Flattening gamma: radiometric terrain correction for SAR imagery. *IEEE Transactions on Geoscience and Remote Sensing*, 49(8): 3081–3093, 2011.

[213] J. Kellndorfer, O. Cartus, M. Lavalle, C. Magnard, P. Milillo, S. Oveisgharan, B. Osmanoglu, P. A. Rosen, and U. Wegmüller. Global seasonal Sentinel-1 interferometric coherence and backscatter data set. *Scientific Data*, 9(1):73, 2022.

[214] E. J. Amin, G. Krieger, M. Younis, F. Bordoni, A. da Silva, and A. Moreira. A 2-D range ambiguity suppression method based on blind source separation for multichannel SAR systems. *IEEE Transactions on Geoscience and Remote Sensing*, 62:1–17, 2024.

[215] V. Queiroz de Almeida, J. Matar, M. Rodriguez–Cassola, A. Moreira, R. Haagmans, P. Bensi, and D. Petrolati. Orbit, performance and observation scenarios for ESA's Earth explorer mission proposal Hydroterra. In *IGARSS 2021; IEEE International Geoscience and Remote Sensing Symposium*, pages 7740–7743, 2021.

[216] F. Delgado, T. Shreve, S. Borgstrom, P. León-Ibáñez, J. Castillo, and M. Poland. A global assessment of SAOCOM-1 L-Band stripmap data for InSAR characterization of volcanic, tectonic, cryospheric, and anthropogenic deformation. *IEEE Transactions on Geoscience and Remote Sensing*, 62:1–21, 2024.

[217] J. Matar, M. Rodriguez-Cassola, G. Krieger, M. Zonno, and A. Moreira. On the equivalence of LEO-SAR constellations and complex high-orbit SAR systems for the monitoring of large-scale processes. *IEEE Geoscience and Remote Sensing Letters*, 21, 2023.

[218] J. Matar, M. Rodriguez-Cassola, E. Silva Filho, N. Sakar, V. Gracheva, M. Suess, G. Krieger, and A. Moreira. A LEO-SAR constellation equivalent to an interferometric geosynchronous mission. In *IGARSS 2023; IEEE International Geoscience and Remote Sensing Symposium*, pages 4706–4709, 2023.

[219] J. Matar, M. J. Sanjuan-Ferrer, M. Rodriguez-Cassola, S. Steele-Dunne, and F. De Zan. A concept for an interferometric SAR mission with sub-daily revisit. In *EUSAR 2024; 15th European Conference on Synthetic Aperture Radar*, pages 18–22, 2024.

[220] S. Steele-Dunne, A. Basto, F. de Zan, W. Dorigo, S. Lhermitte, C. Massari, J. Matar, D. Milodowski, D. Miralle, A. Monteith, M. Rodriguez Cassola, C. Taylor, S. Tebaldin, and L. Ulander. SLAINTE: a SAR mission concept for sub-daily microwave remote sensing of vegetation. In *EUSAR 2024; 15th European Conference on Synthetic Aperture Radar*, pages 870–872, 2024.

Appendices

Appendix A: GEO Concept for Sub-daily SAR Interferometry

This appendix presents the derivation of the orbital inclination for a geosynchronous orbit (GEO) concept designed to enable efficient sub-daily synthetic aperture radar (SAR) interferometry.

The proposed design features a low-inclination, low-eccentricity GEO optimized to minimize cross-track perpendicular baselines ($B_\perp$) between sub-daily interferometric acquisition pairs. The optimization strategy focuses on 12-hour acquisition pairs, specifically those captured near the apogee and perigee of the orbit. This configuration yields zero $B_\perp$ for the 12-hour pair and maintains low baseline values for other sub-daily combinations, as illustrated in Figure 6.4.

The cross-track perpendicular baseline can be estimated as

$$B_\perp = \frac{\vec{B} \cdot (\vec{r}_{\text{at}} \times \vec{v}_{\text{a}})}{|\vec{r}_{\text{at}} \times \vec{v}_{\text{a}}|}, \tag{A.1}$$

where $\vec{B}$ represents the baseline vector between the apogee and perigee, $\vec{r}_{\text{at}}$ denotes the line-of-sight vector from the apogee to a target of interest, and $\vec{v}_{\text{a}}$ is the velocity vector at the apogee.

The position vectors of the perigee and apogee with respect to the Earth's center, expressed in the Earth-Centered Inertial (ECI) frame, are given by

$$\begin{aligned} \vec{r}_{\text{p,ECI}} &= a \cdot (1 - e) \cdot \vec{P}, \\ \vec{r}_{\text{a,ECI}} &= -a \cdot (1 + e) \cdot \vec{P}, \end{aligned} \tag{A.2}$$

where a is the semi-major axis, e is the orbital eccentricity, and $\vec{P}$ is a unit vector pointing from the Earth's center toward the perigee. The vector $\vec{P}$ is defined as

$$\vec{P} = \begin{pmatrix} \cos\omega \cdot \cos\Omega - \sin\omega \cdot \cos i \cdot \sin\Omega \\ \cos\omega \cdot \sin\Omega + \sin\omega \cdot \cos i \cdot \cos\Omega \\ \sin\omega \cdot \sin i \end{pmatrix}, \tag{A.3}$$

where Ω is the right ascension of the ascending node, i is the inclination, and ω is the argument of perigee.

The velocity vector at apogee in the ECI frame can be expressed as

$$\vec{v}_{\mathrm{a,ECI}} = |\vec{v}_{\mathrm{a}}| \cdot \vec{Q}, \tag{A.4}$$

where $|\vec{v}_{\mathrm{a}}|$ denotes the magnitude of the orbital velocity at apogee, expressed as

$$|\vec{v}_{\mathrm{a}}| = \sqrt{\mu_{\mathrm{E}} \cdot \left(\frac{1-e}{a \cdot (1+e)} \right)}, \tag{A.5}$$

with μ_{E} denoting the Earth's standard gravitational constant. The unit vector $\vec{Q}$, which specifies the direction of motion at apogee, is given by

$$\vec{Q} = \begin{pmatrix} -\sin\omega \cdot \cos\Omega - \cos\omega \cdot \cos i \cdot \sin\Omega \\ -\sin\omega \cdot \sin\Omega + \cos\omega \cdot \cos i \cdot \cos\Omega \\ \cos\omega \cdot \sin i \end{pmatrix}. \tag{A.6}$$

The transformation of the above vectors from the ECI frame to the Earth-Centered, Earth-Fixed (ECEF) frame is achieved through a rotation about the Earth's rotational axis. This transformation is described by the rotation matrix

$$\vec{R}_{\mathrm{ECI}\to\mathrm{ECEF}}(\theta) = \begin{pmatrix} \cos\theta & \sin\theta & 0 \\ -\sin\theta & \cos\theta & 0 \\ 0 & 0 & 1 \end{pmatrix}. \tag{A.7}$$

The corresponding vectors in the ECEF frame are obtained via

$$\vec{r}_{\mathrm{ECEF}} = \vec{R}_{\mathrm{ECI}\to\mathrm{ECEF}}(\Theta(t)) \cdot \vec{r}_{\mathrm{ECI}}, \tag{A.8}$$

where $\Theta(t)$ denotes the right ascension of the Greenwich meridian at time t, representing the Earth's rotation relative to the inertial frame. An approximate expression for $\Theta(t)$ can be formulated as

$$\Theta(t) \approx \Omega + \omega + M(t) - \lambda_{\mathrm{lon},0}, \tag{A.9}$$

where $M(t)$ is the mean anomaly at time t, and $\lambda_{\mathrm{lon},0}$ is the central longitude of the ground track.

To achieve a zero cross-track perpendicular baseline, the following geometric condition must be satisfied:

$$\vec{B} \cdot (\vec{r}_{\mathrm{at}} \times \vec{v}_{\mathrm{a}}) = 0. \tag{A.10}$$

This condition imposes a constraint on the satellite's orbital configuration, which can be exploited to derive a trigonometric relationship between the orbit's Keplerian elements.

For the class of low-inclination, low-eccentricity geosynchronous orbits considered, certain assumptions can be made to simplify the derivation of a reference orbit. Specifically, the semi-major axis can be fixed by enforcing an orbital period equal to one sidereal day. The eccentricity can be bounded by the desired east-west extent of the ground track. The argument of perigee can be initially set to 90°, while the mean central longitude of both the ground track and the target region can be aligned at 0°.

Under these assumptions, the inclination can be analytically derived to ensure that the perigee and apogee align with the latitude and altitude of the region of interest. Once the required inclination is determined, the orbit can be rotated in the inertial frame by adjusting the argument of perigee. This enables the alignment of the apogee and perigee with the exact geographic location of the target region.

Assuming the perigee occurs at time t_p such that $\Theta(t_\mathrm{p}) = 0$, and using the relation $\Theta(t_\mathrm{a}) = \Theta(t_\mathrm{p}) + \pi$, the ECEF coordinates of the perigee and apogee, under the condition $\omega = 90^\circ$, simplify to

$$\vec{r}_{\mathrm{p,ECEF}} = \begin{pmatrix} a \cdot (1-e) \cdot \cos i \\ 0 \\ a \cdot (1-e) \cdot \sin i \end{pmatrix}, \tag{A.11}$$

$$\vec{r}_{\mathrm{a,ECEF}} = \begin{pmatrix} a \cdot (1+e) \cdot \cos i \\ 0 \\ -a \cdot (1+e) \cdot \sin i \end{pmatrix}. \tag{A.12}$$

Consequently, the baseline vector is given by

$$\vec{B} = \begin{pmatrix} -2 \cdot a \cdot e \cdot \cos i \\ 0 \\ 2 \cdot a \cdot \sin i \end{pmatrix}, \tag{A.13}$$

and the line-of-sight vector from the apogee to a target located at coordinates $(x_\mathrm{t}, y_\mathrm{t}, z_\mathrm{t})$ is expressed as

$$\vec{r}_{\mathrm{at}} = \begin{pmatrix} x_\mathrm{t} - a \cdot (1+e) \cdot \cos i \\ y_\mathrm{t} \\ z_\mathrm{t} + a \cdot (1+e) \cdot \sin i \end{pmatrix}. \tag{A.14}$$

The ECEF coordinates of the target can be obtained from its geodetic coordinates (ϕ_{lat}, λ_{lon}, h) using the transformation equations

$$\begin{aligned} x_{\text{t}} &= (N(\phi_{\text{lat}}) + h) \cdot \cos\phi_{\text{lat}} \cdot \cos\lambda_{\text{lon}} \\ y_{\text{t}} &= (N(\phi_{\text{lat}}) + h) \cdot \cos\phi_{\text{lat}} \cdot \sin\lambda_{\text{lon}} \\ z_{\text{t}} &= \left(N(\phi_{\text{lat}}) \cdot \frac{R_{\text{P}}^2}{R_{\text{E}}^2} + h \right) \cdot \sin\phi_{\text{lat}}, \end{aligned} \tag{A.15}$$

where $N(\phi_{\text{lat}})$ is the radius of curvature in the prime vertical at latitude ϕ_{lat}, given by

$$N(\phi_{\text{lat}}) = \frac{R_{\text{E}}^2}{\sqrt{R_{\text{E}}^2 - \left(R_{\text{E}}^2 - R_{\text{P}}^2\right) \cdot \sin\phi_{\text{lat}}{}^2}}. \tag{A.16}$$

Finally, the velocity vector at the apogee in the ECEF frame, under the same assumptions, is given by

$$\vec{v}_{\text{a,ECEF}} = |\vec{v}_{\text{a}}| \cdot \begin{pmatrix} 0 \\ -1 \\ 0 \end{pmatrix}. \tag{A.17}$$

Substituting (A.13), (A.14), and (A.17) into (A.10), the condition can be reformulated as the trigonometric equation

$$x_{\text{t}} \cdot \sin i + e \cdot z_{\text{t}} \cdot \cos i - a \cdot \left(1 - e^2\right) \cdot \sin i \cdot \cos i = 0. \tag{A.18}$$

This equation allows for the determination of the required inclination by solving for i.

Appendix B: Efficiency of SAR Modes

The efficiency of a SAR operation mode can be defined as

$$\eta_{\mathrm{SAR}} = \eta_{\mathrm{data}} \cdot \eta_{\mathrm{inst}}, \tag{B.1}$$

where η_{data} represents the ratio of focused image samples to raw samples, and η_{inst} is a radiometric term that accounts for the increased power consumption and losses associated with a given mode. The basic SAR operation modes were introduced in Chapter 3.

Stripmap

Stripmap is the fundamental SAR imaging mode, characterized by its straightforward processing and hardware implementation. Since η_{inst} quantifies additional instrument inefficiencies, it is normalized to stripmap mode, implying $\eta_{\mathrm{inst}} = 1$ for this case. The efficiency of stripmap mode can thus be approximated as

$$\eta_{\mathrm{strip}} \approx \eta_{\mathrm{a}} \cdot \eta_{\mathrm{r}} = \frac{T_{\mathrm{a}} - T_{\mathrm{SA}}}{T_{\mathrm{a}}} \cdot \frac{T_{\mathrm{ewl}} - \tau_{\mathrm{p}}}{T_{\mathrm{ewl}}}, \tag{B.2}$$

where η_{a} and η_{r} denote efficiencies in the along- and cross-track directions, respectively. Here, T_{a} is the total acquisition duration, and T_{ewl} is the echo window length. For stripmap mode, η_{a} is close to unity. For instance, in the case of TerraSAR-X, a 30-s acquisition and an illumination time of 0.5 s yield $\eta_{\mathrm{a}} \approx 0.984$. The value of η_{r} depends on the swath width and degrades for narrower swaths and higher transmit duty cycles. For example, with a pulse duration of 47 µs and an echo window length corresponding to a 30-km swath, η_{r} is approximately 0.7.

ScanSAR

Analogously to the stripmap mode, the efficiency of ScanSAR can be approximated as

$$\eta_{\mathrm{scan}} \approx \frac{\sum_{i=1}^{N_{\mathrm{B}}} T_{\mathrm{B}}[i] \cdot \left(T_{\mathrm{ewl}}[i] - \tau_{\mathrm{p}}[i]\right) \cdot \eta_{\mathrm{ol}}[i] \cdot \eta_t[i]}{T_{\mathrm{SA}} \cdot \sum_{i=1}^{N_{\mathrm{B}}} T_{\mathrm{ewl}}[i]} \cdot \eta_{\mathrm{inst}} \tag{B.3}$$

where η_{ol} accounts for the azimuth overlap losses between consecutive bursts of the same sub-swath and is close to unity. The factor η_{t} represents efficiency losses due to increased PRF, which is constrained by blind ranges, nadir echoes, swath continuity, and ambiguity suppression requirements. The factor η_{inst} is below unity for this mode and incorporates efficiency losses due to scalloping, operation at the antenna pattern edges, and additional inefficiencies from the more complex radar electronics required for multi-sub-swath imaging.

The efficiency of TOPS mode can be also approximated using (B.3). Compared to ScanSAR, TOPS typically uses longer bursts, leading to a higher efficiency in azimuth. However, range and overlap efficiencies remain similar. While TOPS reduces scalloping losses, its η_{inst} is expected to be comparable to ScanSAR due to the increased density of transmit-receive modules required for azimuth beam steering.